The reactive nitrogen budget throughout the diel cycle investigated via thermal dissociation cavity ring-down spectroscopy

Dissertation

zur Erlangung des Grades

“Doktor der Naturwissenschaften“ (Dr. rer. nat.)

im Promotionsfach Chemie

am Fachbereich Chemie, Pharmazie und Geowissenschaften der Johannes Gutenberg-Universität in Mainz

erarbeitet am Max-Planck-Institut für Chemie

als Mitglied im Max Planck Graduate Center

Nils Friedrich

geb. in Berlin am 22. April 1990

Mainz, im Juli 2021

1. Berichterstatter:

2. Berichterstatter:

Tag der mündlichen Prüfung:

I hereby declare that I wrote the dissertation submitted without any unauthorized external assistance and used only sources acknowledged in the work. All textual passages which are appropriated verbatim or paraphrased from published and unpublished texts as well as all information obtained from oral sources are duly indicated and listed in accordance with bibliographical rules. In carrying out this research, I complied with the rules of standard scientific practice as formulated in the statutes of Johannes Gutenberg-University Mainz to insure standard scientific practice.

Nils Friedrich

Mainz, 18 June 2021

Table of contents

1 Abstract / Zusammenfassung

Total reactive nitrogen (NO_y) denominates a group of atmospheric nitrogen species which consists of primary emitted NO_x (= NO + NO_2) and of the products of NO_x sequestering (NO_z). The processing of NO_x into NO_z during the ageing process of an air mass is responsible for the transport of harmful NO_x into regions of the planet where anthropogenic emissions are sparse. The reactive nitrogen budget is undergoing constant changes due to increased efforts in mitigating NO_x emissions. NO_y species contribute strongly to the production and loss of HO_x radicals, and therefore to the oxidation capacity of the atmosphere.

This work emphasises on *a)* the development and laboratory characterisation of a new instrument capable of following the partitioning between NO_x and NO_z, *b)* the reactive nitrogen budget in the Mediterranean Sea, the Red Sea, and the Arabian Gulf through measurements from a ship campaign, and *c)* chamber study results on the efficiency of organic nitrate formation following the nighttime isoprene oxidation by the nitrate radical NO_3.

An instrument was developed which detects NO_x and NO_y at 40 pptv detection limits (2σ confidence and 1 minute averaging). Complete thermal dissociation to NO_x was demonstrated for all relevant NO_z species. The NO_x detection was validated against a chemiluminescence detector under demanding and versatile field conditions. Memory effects were found to bias measurements of particulate nitrates when the activated carbon denuder is exposed to water, with potential strong implications for other instruments employing this method.

Median NO_z mixing ratios of up to 1.5 ppbv were observed in the Arabian Gulf, originating from high temperatures, strong photochemical activities, and the unique atmospheric mixture involving hydrocarbons related to petroleum production. An assessment of the NO_x source strengths under background conditions revealed the photolysis of nitrous acid (HONO) as an important source, presumably associated with the processing of ship plume black carbon to nitrate particles. In all regions of the AQABA campaign, shifts in the NO_y composition were successfully explained by varying air mass origins, using the corresponding back trajectories. The ratio between NO_z and NO_y mixing ratios is overall a valuable tracer for the processing state of an air parcel.

Investigations of the nighttime isoprene oxidation in a chamber study resulted in organic nitrate yields (relative to the lost isoprene) between 77 % and 109 %. These numbers are in good agreement with previous publications and highlight the key role of NO_3 in the oxidation of

biogenic volatile organic compounds (BVOCs), leading ultimately to the formation of secondary organic aerosol.

Die Summe aller atmosphärischen reaktiven Stickstoffverbindungen (NO_y) setzt sich zusammen aus primär emittiertem NO_x (= NO + NO_2) und den Umsetzungsprodukten von NO_x (= NO_z). Diese Prozessierung von NO_x hin zu NO_z während dem Alterungsprozesses einer Luftmasse ermöglicht den Transport von gesundheitsschädlichem NO_x in abgelegene, weniger von direkten anthropogenen Emissionen beeinflusste, Regionen. Das Budget reaktiver Stickstoffverbindungen unterliegt einem konstanten Wandel, aufgrund von gestiegenen Bemühungen zur Vermeidung von NO_x-Emissionen. NO_y-Spezies haben einen starken Einfluss auf die Produktion und den Verlust von HO_x-Radikalen, und damit auf die Oxidationskapazität der Atmosphäre.

Die Hauptaspekte dieser Arbeit sind *a)* die Entwicklung und Charakterisierung einen neuen Messinstruments, welches die Nachverfolgung der NO_x/NO_z-Verteilung erlaubt, *b)* das Stickstoffbudget im Mittelmeer, dem Roten Meer, und dem Arabischen Golf, anhand von Messdaten einer Schiffskampagne, und *c)* Resultate einer Kammerstudie zur Effizienz der Bildung organischer Nitrate im Rahmen der nächtlichen Isopren-Oxidation durch das Nitratradikal NO_3.

Ein Messinstrument wurde entwickelt welches NO_x und NO_y mit Detektionslimits (2σ Konfidenzintervall und eine Minute Mittelung) von 40 pptv bestimmen kann. Vollständige thermische Dissoziation zu NO_x wurde für die relevantesten NO_z-Spezies nachgewiesen. Die NO_x-Detektion wurde durch Vergleichsmessungen mit einem Chemilumineszenz-Detektor validiert, die im Rahmen einer anspruchsvollen und vielfältigen Feldkampagne durchgeführt wurden. Gedächtniseffekte beeinflussen die Messung von Partikelnitraten mithilfe von Aktivkohleoberflächen, insbesondere unter feuchten Bedingungen. Diese Entdeckung könnte bedeutende Implikationen für ähnlich operierende Messmethoden nach sich ziehen.

Median NO_z-Mischverhältnisse von bis zu 1.5 ppbv wurden im Arabischen Golf beobachtet. Grund hierfür waren hohe Temperaturen, ausgeprägte Photochemie, sowie die einmalige atmosphärische Mischung aus Kohlenwasserstoffen petrochemischen Ursprungs. Eine Analyse der NO_x-Quellstärken identifizierte die Photolyse von Salpetriger Säure (HONO) als eine bedeutende Quelle. Dieser Umstand könnte mit der Prozessierung schwarzen Kohlenstoffs zu Partikelnitraten in Schiffsabgasfahnen zusammenhängen. Verschiebungen in der NO_y-Komposition konnten in allen AQABA-Regionen erfolgreich mit Änderungen der Luftmassenherkunft erklärt werden. Hierzu wurden auch Rückwärtstrajektorien eingesetzt. Das Verhältnis der NO_z- und NO_y-Mischverhältnisse stellt zusammenfassend einen wertvollen Marker für den Reifegrad eines Luftpakets dar.

Untersuchungen der nächtlichen Isopren-Oxidation mittels einer Kammerstudie ergaben Organische-Nitrat-Ausbeuten (bezogen auf die umgesetzten Isopren-Mengen) zwischen 77 % und 109 %. Diese Werte sind in guter Übereinstimmung mit früheren Literatur-Quellen und heben die herausragende Rolle des Nitratradikals bei der Oxidation von biogenen Kohlenwasserstoffen hervor, welche abschließend die Bildung sekundären Aerosols begünstigt.

2 Introduction

2.1 Influence of reactive nitrogen species on air quality and climate

This work centres on a group of atmospheric species defined as *total reactive nitrogen* (abbreviated commonly as NO_y). The most important components of NO_y are listed in Eq. 1. As nitrogen monoxide (NO) and nitrogen dioxide (NO_2) are products of direct emissions or interconversion between each other (see Section 2.4), they are summarised under the term NO_x (see Eq. 2). Sequestering of NO_x leads to the formation of NO_z species (see Sections 2.4 and 2.5). NO_y is thus the sum of primarily-emitted or re-formed NO_x, and of the processed NO_z species (see Eq. 3).

$$NO_y = NO + NO_2 + HNO_3 + NO_3 + 2N_2O_5 + HONO + RO_2NO_2 + RONO_2$$
$$+XONO_2 + XNO_2 + particulate\ nitrates \qquad \text{Eq. 1}$$
$$(R = organic\ fragment;\ X = halogen\ or\ H\ atom)$$

$$NO_x = NO + NO_2 \qquad \text{Eq. 2}$$

$$NO_z = NO_y - NO_x \qquad \text{Eq. 3}$$

The term NO_y was originally introduced by Logan (1983), including also peroxynitric acid (HO_2NO_2), which, however, is thermally labile at 298 K with a lifetime of only ca. 10 s (Gierczak et al., 2005; Veres et al., 2015). Nitrous oxide (N_2O), ammonia (NH_3), and acetonitrile (CH_3CN), other prominent atmospheric nitrogen compounds, are not considered to belong to NO_y (Wild et al., 2014).

This introductory section serves to highlight exemplary effects of individual NO_y components onto aspects of air quality and climate change. Direct negative effects on the human health have been found for e.g. NO_x. An increased mortality following short- and long-term exposure to NO_2 is strongly associated with respiratory and cardiovascular diseases (Faustini et al., 2014; Mills et al., 2015). Indirectly, NO_x is involved in the generation of ozone (O_3) and airborne particles (see Section 2.4), which are estimated to be the predominant health risk related to air pollution (e.g. in Europe (Guerreiro et al., 2014), China (Chen et al., 2020), and the United States (Zhang et al., 2018)).

Worldwide, ca. 3.3 million yearly premature deaths can be attributed to $PM_{2.5}$ (particulate matter with < 2.5 µm aerodynamic diameter) and O_3 (Lelieveld et al., 2015). According to Lelieveld et al. (2015), the individual sources of air pollution vary by region: in India and China, residential energy uses are the dominating sources, whereas other countries are more affected by power plants, traffic, or agriculture. Global crop yields reductions by up to 26 % might occur in the year 2030, due to then projected surface O_3 levels (Avnery et al., 2011). The interplay between NO_x, O_3, hydrocarbons, particles, sunlight, and high temperatures leading to reduced visibility, eye irritation, and crop damage is also known as "photochemical smog" or "Los Angeles smog" and was first postulated by Haagensmit (1952).

In specific cases, NO_x emissions can be responsible for visibility impairment without concurrently elevated O_3 concentrations (Spicer, 1982; Watson et al., 1994; Barthelmie and Pryor, 1998; Finlayson-Pitts and Pitts, 2000). Such a situation occurs when NO_x is processed to nitric acid (HNO_3) and reaches areas with strong agricultural activities downwind the emission source, resulting in the formation of particulate ammonium nitrate (NH_4NO_3) in the reaction between HNO_3 and NH_3. This example highlights that sequestering of NO_x in form of HNO_3 or other longer-lived NO_z species (specifically organic nitrates (Horowitz et al., 1998)) allows the transport of reactive nitrogen into remote areas of the troposphere, which are not directly influenced by strong NO_x emission sources (Day et al., 2002).

Together with sulfuric acid (H_2SO_4) and organic acids, HNO_3 is also a major constituent of acid deposition (also popularly known as "acid rain"). The abundancy of the individual components depends on the respective regional emissions of SO_2, NO_x, volatile organic compounds (VOCs), and CO_2. In remote tropospheric areas, formic and acetic acids are the dominant carboxylic acids in the aqueous phase (Chebbi and Carlier, 1996). Recently, the formation of formic acid from oxidation of formaldehyde has been demonstrated to be mediated by cloud droplets (Franco et al., 2021). Acids can deposit via two mechanisms to the earth's surface: either via direct transport to the surface and subsequent adsorption (dry deposition), or after dissolving in the aqueous phase (wet deposition) (Finlayson-Pitts and Pitts, 2000). Acid deposition has adverse effects on e.g. soils, forests, aquatic lifeforms, and water quality (Driscoll et al., 2007). Mitigation strategies for SO_2 and NO_x were imposed in the 1970s and 1980s by legislators in Europe and Northern America, resulting in an 85 % decrease in the hydrogen ion content of precipitation in the north-eastern United States between 1981 and 2017 (Likens et al., 2021).

Tropospheric NO_x additionally influences the climate through its interaction with greenhouse gases, i.e. the generation of O_3 and N_2O (via denitrification in soils) as well as the destruction

of methane (CH_4), leading overall to warming effects (Lammel and Grassl, 1995; Grewe et al., 2012), particularly when NO_x is emitted by airplanes (Grewe et al., 2019). When considering the formation of particle nitrates, however, NO_x emissions are expected to globally have a net cooling effect (Shindell et al., 2009). Control strategies for short-lived reactive nitrogen species are therefore more relevant for improving regional air quality than for mitigating the effects of global warming, compared to long-lived greenhouse gases such as CO_2 and CH_4.

2.2 Oxidation capacity of the troposphere through the hydroxyl radical and connection to reactive nitrogen

The hydroxyl radical (OH) is responsible for large parts of the oxidation capacity of the atmosphere and for removal of both biogenic and anthropogenic trace gases (Levy, 1971; Crutzen, 1973; Logan et al., 1981; Lelieveld et al., 2016). At an assumed global OH concentration of 0.6 x 10^6 molecules cm^{-3}, for example, 90 % of isoprene, 50 % of α-pinene, 50 % of NO_2, and 30 % of SO_2 are removed in the reaction with OH (Ehhalt et al., 1990). Chemical processes involving the OH radical are discussed in this section in terms of their connections to NO_x and other NO_y species.

Sources of OH are classified as "primary" and "secondary" (Monks, 2005). The primary source of OH is photolysis of O_3 by UV light and the subsequent reaction of excited oxygen atoms with water molecules (see reactions R1 and R2), resulting in a water dependence for the OH formation. Primary production accounts for 33 % of the tropospheric OH (Lelieveld et al., 2016).

$$O_3 + h\nu \rightarrow O(^1D) + O_2 \qquad \text{R1}$$

$$O(^1D) + H_2O \rightarrow 2\,OH \qquad \text{R2}$$

Secondary OH production is dominated by the reaction of NO and the hydroperoxyl radical HO_2 (30 % of the tropospheric production term), followed by O_3 + HO_2 (14 %), chain reactions of oxygenated VOCs including the photolysis of hydroperoxides (13 %), and hydrogen peroxide photolysis (10 %) (Lelieveld et al., 2016). Production from NO + HO_2 has a larger impact in polluted environments. The most important sink of OH is the reaction with CO (39 % of the total annual sink flux), leading to CO_2 formation, whereas reactions with NO_y species only account for 1.5 % of the global tropospheric OH loss (Lelieveld et al., 2016).

The OH sink caused by CO, however, also leads to the formation of HO_2. Interconversion between these two radicals therefore enables recycling of OH (see secondary sources of OH above). HO_2 and OH are also summarised under the term "HO_x". The HO_x cycling is schematically illustrated together with source and sink processes of HO_x in Figure 1 (adapted from Monks (2005)).

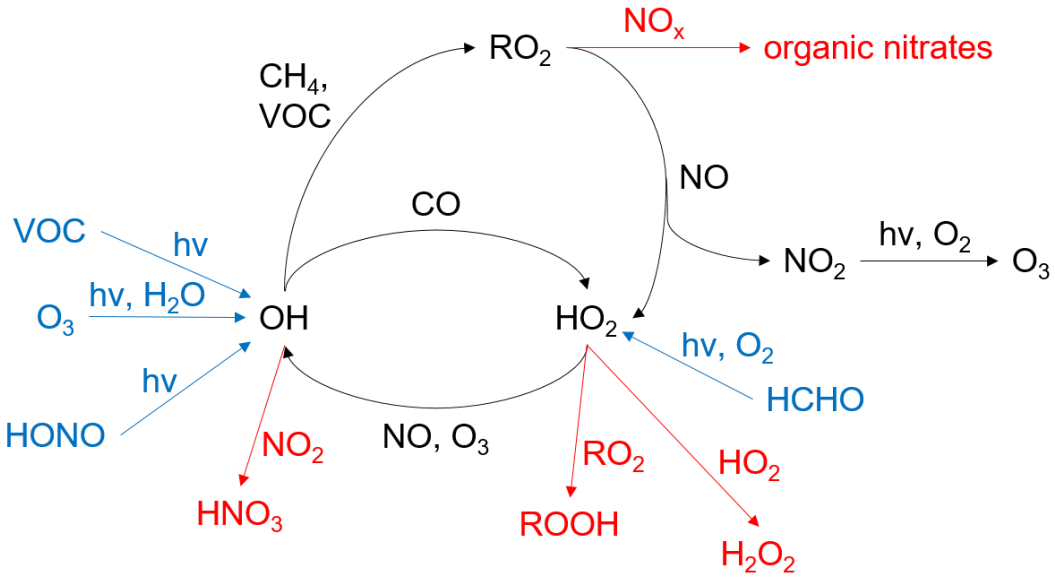

Figure 1: Schematic representation of cycling between HO_x radicals (= OH + HO_2), adapted from Monks (2005). Sources of HO_x are marked in blue, processes that terminate the radical chain reactions in red.

In urban environments, photolysis of nitrous acid (HONO) represents another potential source of OH (Lammel and Cape, 1996). OH to HO_2 interconversion through the oxidation of VOCs is a multistep process, involving intermediately formed organic peroxy (RO_2) and alkoxy radicals (RO), and requiring the presence of NO (Lightfoot et al., 1992). Exemplarily, the individual steps are shown for CH_4 in reactions R3-R6 (M is an inert collision partner).

$$CH_4 + OH \rightarrow CH_3 + H_2O \qquad \text{R3}$$

$$CH_3 + O_2 + M \rightarrow CH_3O_2 + M \qquad \text{R4}$$

$$CH_3O_2 + NO \rightarrow CH_3O + NO_2 \qquad \text{R5}$$

$$CH_3O + O_2 \rightarrow HCHO + HO_2 \qquad \text{R6}$$

NO oxidation to NO_2 occurs twice in Figure 1, allowing additional photochemical generation of O_3 and hence additional primary OH production. This circumstance highlights the self-sustaining nature of the HO_x cycle, in environments with regular NO emissions. There are, however, reactions involving NO_x (i.e. formation of HNO_3 or organic nitrates), which lead to

termination of the radical chain reactions and which damp the OH production (marked in red in Figure 1). Additionally, $HO_2 + RO_2$ and $HO_2 + HO_2$ are radical termination processes, despite the fact that hydroperoxide (ROOH) and hydrogen peroxide (H_2O_2) photolysis are also strong HO_x sources (see above).

Both OH concentrations and the O_3 production rate are classically considered to exhibit a large dependence on present NO_x mixing ratios, with maxima at ca. 1 ppbv NO_x under typical atmospheric conditions, as found in areas with moderate anthropogenic emissions (Poppe et al., 1993; Kleinman, 1994). Up to these maxima, an increase in NO_x leads to higher OH and O_3, due to the stronger HO_2 + NO cycling. At NO_x mixing ratios in excess of ca. 1 ppbv, the termination via OH + NO_2 dominates, resulting in decreased radical production and the counterintuitive case where mitigation of NO_x emissions initially increases the O_3 burden.

Using formaldehyde (HCHO) as a surrogate for VOC emissions, O_3 formation was found to be VOC-limited in air masses where the HCHO/NO_2 ratio is < 1, and NO_x-limited where the ratio is > 2, respectively (Duncan et al., 2010). Recently, OH concentrations largely exceeding traditional model predictions were observed in rural environments characterised by low NO_x emissions and a large abundance of biogenic VOCs (BVOCs), suggesting an unknown OH source which does not require NO and does not result in O_3 production (Rohrer et al., 2014). This source has been attributed to unimolecular decomposition or autoxidation reactions of peroxy radicals formed from BVOCs, such as e.g. isoprene (Crounse et al., 2013; Fuchs et al., 2013).

Overall, NO_x has a strong impact on the part of the tropospheric oxidation capacity which is connected to HO_x cycling. Modelled global OH concentrations would decrease by 76 % when excluding NO_x processes (Lelieveld et al., 2016), whereas VOC chemistry is mainly relevant in areas with pronounced biogenic activity. Together with the predominant O_3, longer-lived NO_z species (i.e. NO_x reservoirs), such as organic nitrates, can show a minor contribution to the buffering of global OH concentrations (Lelieveld et al., 2016).

2.3 Anthropogenic and natural emissions of reactive nitrogen

In this section primary emissions of NO_x and of other precursor species for NO_z formation are discussed. Most anthropogenic NO_y is emitted in form of NO produced in combustion processes (Finlayson-Pitts and Pitts, 2000). Depending on the combustion conditions, minor amounts of

NO_2 are also co-emitted, accounting for between < 1% and > 30 % of NO_x (Lenner, 1987). Roadside detected NO_2/NO_x ratios in London were exhibiting an increasing trend up to 2010 (25 %), and are now decreasing (15 % in 2014), due to revised exhaust gases after-treatment in motor vehicles (main effect from heavy duty vehicles and buses) (Carslaw et al., 2016). The generation of NO at combustion temperatures was first postulated by Zel'dovich (1946) and proceeds via the mechanism depicted in R7-R9:

$$O_2 \rightarrow 2\,O \qquad \text{R7}$$

$$N_2 + O \rightarrow NO + N \qquad \text{R8}$$

$$N + O_2 \rightarrow NO + O \qquad \text{R9}$$

Combustion processes are mainly anthropogenic sources of NO_x and are related generally to traffic, power generation, and other industrial processes. Biomass burning follows the same mechanism but can be considered as both an anthropogenic and a natural emission source. Denitrification of soils represents another natural emission of NO_x, despite the fact that soil processes can also be affected by anthropogenic activities. The term “denitrification” in this context signifies the bacterial reduction of nitrate anions (NO_3^-), via nitrite (NO_2^-), leading to the release of NO, together with N_2O and N_2 (Oertel et al., 2016). NO emissions from agricultural soils are increased under the usage of nitrogen-based fertilizers (Li, 2013).

High altitude sources of NO_x include aircraft emissions (see Section 2.1) and lightning (Chameides et al., 1977; Lange et al., 2001). In the upper troposphere, lightning represents the predominant source of NO_x (Schumann and Huntrieser, 2007). Estimates of the NO_x emission rates (in teragram nitrogen per year) from the aforementioned individual sources, in the decade between 2000 and 2010, were published by IPCC (2013) (IPCC = Intergovernmental Panel on Climate Change) and are listed in Table 1.

Table 1: NO_x emission rates from anthropogenic and natural sources according to IPCC (2013) for the decade between the years 2000 and 2010.

Anthropogenic source	**NO_x emissions (TgN yr^{-1})**
Fossil fuel combustion, industrial processes	28.3
Agriculture	3.7
Biomass and biofuel burning	5.5
Natural source	
Soils under natural vegetation	7.3
Lightning	4
Total sources	**48.8**

Table 1 demonstrates that anthropogenic sources dominate the total NO_x emissions and exceed natural sources by a factor of ca. 3.3. This imbalance also explains the increase of the total NO_x emission rate from 13.1 TgN yr^{-1} in preindustrial times, i.e. in the year 1860 (Galloway et al., 2004), to 48.8 TgN yr^{-1} in the 21st century. Natural emissions accounted for 80 % of the total emissions in 1860 (Galloway et al., 2004).

The current IPCC's "Representative Concentration Pathways" (RCPs) predict a decrease in NO_x emissions from 38 TgN yr^{-1} in 2000 to a range between 16 TgN yr^{-1} and 26 TgN yr^{-1} in 2100, due to increased efforts in air pollution control resulting from higher income levels and stricter climate policies (Lamarque et al., 2011; van Vuuren et al., 2011). Some regions are, however, still experiencing increasing NO_x pollution, specifically the Asian continent. India is expected replace China as the largest global NO_x emitter by 2024 (Itahashi et al., 2019).

2.4 Daytime reactive nitrogen chemistry

NO_x emitted into the atmosphere can undergo several transformation reactions, enabling the transport of reactive nitrogen into regions with sparse direct emissions. The sequestering reactions differ between day- and nighttime due to the presence or absence of sunlight. Nighttime chemistry of NO_y species is therefore discussed separately in Section 2.5. This section provides an overview over daytime processes. Additional information, in respect to the performed analyses, are given in the introductory parts of Sections 5, 6 and 7. Figure 2 graphically summarises tropospheric NO_y reactions.

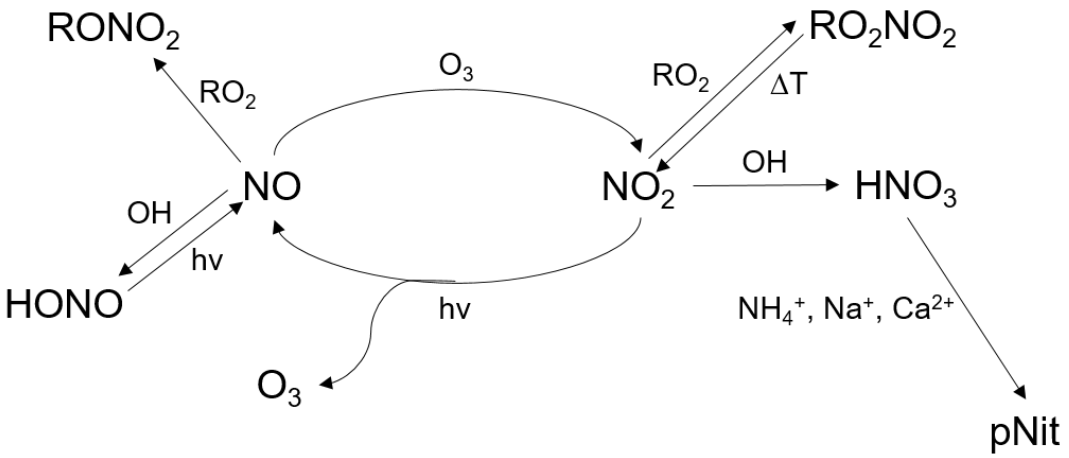

Figure 2: Daytime interconversion processes between NO_x and NO_z species. R = organic fragment; pNit = particulate nitrates; hν = photolysis reaction; ΔT = thermal decomposition.

NO and NO_2 rapidly convert into each other and are considered to enter a photostationary state at daytime, as described by reactions R10-R12 (Leighton, 1961). Following the photolysis of NO_2, the ground-state oxygen atom $O(^3P)$ facilitates the generation of O_3 through reaction with molecular oxygen. NO_2 is finally reformed in the oxidation of NO by O_3. This circular process does not lead to the consumption of O_3.

$$NO_2 + h\nu \rightarrow NO + O(^3P) \quad \text{R10}$$

$$O(^3P) + O_2 + M \rightarrow O_3 + M \quad \text{R11}$$

$$NO + O_3 \rightarrow NO_2 + O_2 \quad \text{R12}$$

Under photostationary state conditions, the ratio between the NO_2 loss rate through photolysis and the NO_2 production rate through NO + O_3 is expected to be 1. This relationship is known as Leighton ratio Φ (see Eq. 4). In Eq. 4, J_{NO2} signifies the NO_2 photolysis rate constant, and k_{NO+O3} the rate constant for the NO + O_3 reaction.

$$\Phi = \frac{J_{NO_2}[NO_2]}{k_{NO+O_3}[NO][O_3]} \quad \text{Eq. 4}$$

Deviations in Φ from unity under low-NO_x conditions are associated with additional oxidation of NO by HO_2, RO_2 (reactions R13 and R14; see Section 2.2), or halogen monoxides (XO; reaction R15) (Nakamura et al., 2003; Hosaynali Beygi et al., 2011). Reed et al. (2016), however, suggested that unexpectedly high NO_2/NO ratios might also result from the interfering

detection of NO_y species (specifically peroxyacetyl nitrate (PAN) in cold regions) in the NO_2 channel of chemiluminescence-based instruments (CLD).

$$NO + HO_2 \rightarrow NO_2 + OH \quad \text{R13}$$

$$NO + RO_2 \rightarrow NO_2 + RO \quad \text{R14}$$

$$NO + XO \rightarrow NO_2 + X \quad \text{R15}$$

Formation of HNO_3 represents an important sink for both NO_x and HO_x radicals (R16). Reaction R16 accounts globally for ca. 60 % of the total NO_x sink (Stavrakou et al., 2013). HNO_3 is additionally prone to adsorb to wet surfaces and is characterised by a high deposition velocity between ca. 1 and 5 cm s^{-1} (Finlayson-Pitts and Pitts, 2000). Deposition of HNO_3 can explain up to 40 % of the total nitrogen flux towards the surface (Russell et al., 1993). Mitigation of NO_x emissions with parallel increases in agricultural NH_3 emissions has, however, led to a situation where in large parts of the United States the majority of total reactive inorganic nitrogen deposition (wet + dry) is now caused by reduced nitrogen (i.e. ammonium-based species) (Li et al., 2016). Through heterogeneous processing, gaseous HNO_3 is also partly responsible for the formation of particulate nitrates (pNit). Nitrate particles can be found in both the accumulation (0.5-2 µm) and the coarse mode (> 2.5 µm) and have a tropospheric lifetime of ca. one week (Seinfeld and Pandis, 2016).

$$NO_2 + OH + M \rightarrow HNO_3 + M \quad \text{R16}$$

$$NO_2 + RO_2 + M \rightarrow RO_2NO_2 + M \quad \text{R17}$$

$$NO + RO_2 + M \rightarrow RONO_2 + M \quad \text{R18}$$

$$NO + OH + M \rightarrow HONO + M \quad \text{R19}$$

Organic nitrates (ONs) are other important reservoir species of NO_x and are principally produced by the reaction of NO_2 or NO with RO_2 (see R17 and R18), resulting in peroxy nitrates (RO_2NO_2, PNs) and alkyl nitrates ($RONO_2$, ANs). The formation of ANs competes with the dominating NO to NO_2 oxidation (see R5 and Figure 1), leading to ANs yields between 1 % and 35 % (Perring et al., 2013). ANs yields increase with the carbon chain length due to more vibrational modes stabilising the excited reaction intermediate. This reaction intermediate is deactivated in a collision with an inert partner, resulting in a positive correlation of the yield

with pressure, and a negative correlation with temperature (Perring et al., 2013). Large, multifunctional ANs also have the ability to condense and to form particulate organic nitrates (Rollins et al., 2010).

The stability and tropospheric abundancy of PNs depends largely on whether they possess an alpha acyl group or not (peroxyacyl nitrates are also abbreviated as PANs). The activation energy for thermal decomposition of non-acyl PNs amounts ca. 100 kJ mol^{-1} whereas PANs require ca. 120 kJ mol^{-1} (Nault et al., 2015). Methyl peroxy nitrate ($CH_3O_2NO_2$) and peroxynitric acid (HO_2NO_2) have been successfully detected in the colder upper troposphere (Kim et al., 2007; Nault et al., 2015). The formation of the most abundant PANs species, peroxyacetyl nitrate (PAN), is demonstrated exemplarily from ethane in Figure 3. After the H-abstraction by OH, the ethyl peroxy radical is formed. Via the respective alkoxy radical, acetaldehyde is intermediately obtained. Finally, PAN is formed in the analogue oxidation of acetaldehyde and under the presence of NO_2. PAN is an important constituent of photochemical smog and is responsible for the typical eye irritation during smog periods (Stephens and Price, 1969).

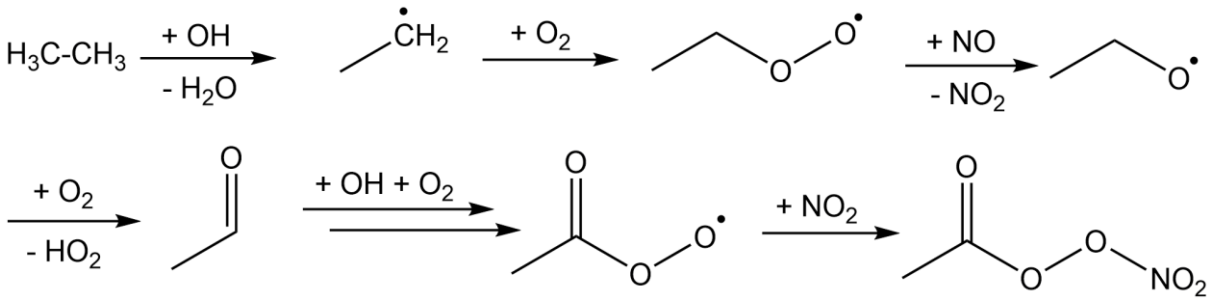

Figure 3: Atmospheric formation of peroxyacetyl nitrate (PAN) starting from ethane. The formation of the peroxyacetyl radical from acetaldehyde proceeds analogue to the ethane oxidation.

HONO constitutes another minor inorganic NO_y component, which is formed from the reaction of NO and OH (R19). The rapid photolysis of HONO limits its midday lifetime to ca. 20-30 minutes (Stutz et al., 2000). In regions of the marine boundary layer impacted by strong shipping emission, however, HONO might lead to enhanced concentrations of RO_x radicals, and therefore increased O_3 and $PM_{2.5}$ (Dai and Wang, 2021).

2.5 Nighttime reactive nitrogen chemistry

Nighttime NO_y chemistry differs significantly from the daytime mechanism described in Section 2.4, due to missing photolysis reactions. Therefore, no additional O_3 is formed from photolysis of NO_2 after sunset, and NO disappears in regions unaffected by fresh emissions.

Dominant nighttime processes are summarised schematically in Figure 4. The nitrate radical NO_3 is a key component in this scheme, despite being usually present in only low pptv amounts (Khan et al., 2015). NO_3 is formed in the oxidation of NO_2 by O_3 (R20). At daytime, NO_3 is rapidly lost due to photolysis (R21) or titration by NO (R22). The nocturnal lifetime of NO_3 can exceed one hour (Sobanski et al., 2016b).

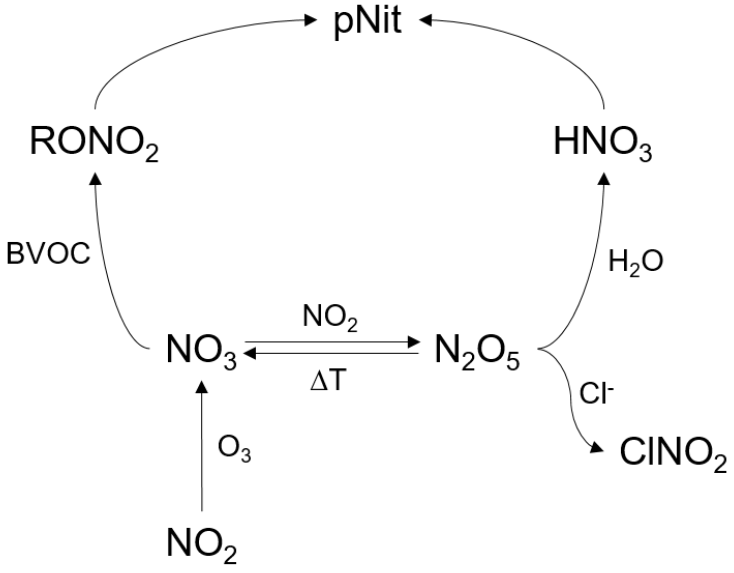

Figure 4: Nighttime chemistry of NO_y species. BVOC = biogenic volatile organic compounds; pNit = particulate nitrates; ΔT = thermal decomposition.

NO_3 also reacts with further NO_2 to form dinitrogen pentoxide (N_2O_5; R23). The back-reaction of R23, i.e. the decomposition of N_2O_5, has a strong temperature dependence. A thermal equilibrium hence evolves between N_2O_5, NO_3, and NO_2. N_2O_5 undergoes heterogeneous uptake onto aqueous aerosol, resulting in the formation of HNO_3 (R24), which again represents loss process for atmospheric NO_x. The formation of nitrate aerosol via R24 competes with the formation of nitryl chloride ($ClNO_2$; R25), which possesses a > 30 hours lifetime in the marine boundary layer (Osthoff et al., 2008). After sunrise, the photolysis of $ClNO_2$ acts as a source for chlorine atoms and NO_2 (R26).

$$NO_2 + O_3 \rightarrow NO_3 + O_2 \quad \text{R20}$$

$$NO_3 + h\nu \rightarrow NO_2 + O \quad \text{R21}$$
$$\rightarrow NO + O_2$$

$$NO_3 + NO \rightarrow 2\,NO_2 \quad \text{R22}$$

Unsaturated hydrocarbons, i.e. BVOCs and alkenes, are highly reactive towards NO_3, making NO_3 the predominant VOC oxidant at nighttime, also exceeding O_3 in importance (Wayne et al., 1991; Brown et al., 2011). The mechanism of the NO_3 addition to a BVOC double bond is discussed in detail in Section 7.1, on the example of isoprene. NO_3 oxidation of unsaturated hydrocarbons produces ANs more efficiently than the respective OH-initiated oxidation, with ANs yields reaching up to 100 % (see Section 7.3.3 and Perring et al. (2013)). As mentioned in Section 2.4, highly-functionalised ANs also partition into the particle phase, contributing to the pNit fraction detectable via TD-CRDS.

$$NO_3 + NO_2 + M \rightarrow N_2O_5 + M \quad \text{R23}$$

$$N_2O_5 + H_2O \rightarrow 2\,HNO_3 \quad \text{R24}$$

$$N_2O_5 + Cl^- \rightarrow ClNO_2 + NO_3^- \quad \text{R25}$$

$$ClNO_2 + h\nu \rightarrow Cl + NO_2 \quad \text{R26}$$

2.6 Previous maritime measurements of reactive nitrogen

Field measurements of NO_y presented in this work were primarily conducted during the AQABA ship campaign (see Section 6). This section therefore explores previous exemplary reactive nitrogen data sets from the literature, in order to give a perspective on the expected typical amounts of NO_y present in marine environments (see Table 2).

Total NO_y and individual NO_y species have been measured in numerous previous studies, with various instrumental approaches and in diverse marine locations, either on ships or at coastal sites. In these studies, NO_x and NO_y were detected via Chemiluminescence (CLD) (Carsey et al., 1997; Peterson and Honrath, 1999; Rickard et al., 2002; Dibb et al., 2004; Takiguchi et al., 2008; Yuba et al., 2014), NO_2 via Laser Induced Fluorescence (LIF) (Matsumoto et al., 2001) and Differential Optical Absorption Spectroscopy (DOAS) (Leser et al., 2003; Peters et al., 2012; Takashima et al., 2012), PAN via Gas Chromatography (GC) (Muller and Rudolph, 1992; Osthoff et al., 2006), NO_3 and N_2O_5 via Cavity Ring-Down Spectroscopy (CRDS) (Brown et al., 2004; Osthoff et al., 2006), or HNO_3 after collection in the aqueous phase (Brown et al., 2004; Dibb et al., 2004; Večeřa et al., 2008).

The measurement locations included the coasts of Japan and China (Matsumoto et al., 2001; Takiguchi et al., 2008; Yuba et al., 2014), England and Ireland (Rickard et al., 2002), the Northern and Southern Atlantic Ocean (Muller and Rudolph, 1992; Carsey et al., 1997; Peterson

and Honrath, 1999; Leser et al., 2003; Brown et al., 2004; Dibb et al., 2004; Osthoff et al., 2006), the Western Pacific and Indian Ocean (Peters et al., 2012; Takashima et al., 2012), and the Mediterranean Sea (Večeřa et al., 2008). Apparently, in situ coastal or shipborne measurements of NO_y have not yet been conducted in the Red Sea and Arabian Gulf regions.

Table 2: Exemplary literature studies with measurements of NO_y or individual NO_y species in marine environments (coastal or ship-based).

Location	**Species / Techniques**	**Typical mixing ratios (ppbv)**	**Max. mixing ratios (ppbv)**	**Source**
China, Japan ground based	NO_2 / LIF	1-3	8	Matsumoto et al. (2001)
	NO_x, NO_y / CLD	NO_y: 0.5-1.5	NO_y: 15	Takiguchi et al. (2008)
		NO_y: 1-5	9	Yuba et al. (2014)
North and South Atlantic Ocean	PAN / GC	< 0.2	1.1	Muller and Rudolph (1992)
	NO_x, NO_y / CLD	NO_y: < 0.2	NO_y: 0.3	Carsey et al. (1997)
		NO_y: < 0.6	NO_y: 1.6	Peterson and Honrath (1999)
	NO_x, NO_y / CLD; HNO_3 / IC	NO_y: 6-8 HNO_3: 0.5-2.5	NO_y: 87 HNO_3: 7	Dibb et al. (2004)
	NO_2 / Max-DOAS	< 0.1	3.7	Leser et al. (2003)
	NO_3, N_2O_5 / CRDS; HNO_3 / IC	N_2O_5: 1 HNO_3: 0.5-1.5	N_2O_5: 2 HNO_3: 2	Brown et al. (2004)
	NO_3, N_2O_5 / CRDS; PAN / GC	PAN: 1-2 ppbv	PAN: 4	Osthoff et al. (2006)
Western Pacific and Indian Ocean	NO_2 / Max-DOAS	< 0.05	0.8	Peters et al. (2012)
		< 0.2	0.4	Takashima et al. (2012)
England and Ireland	NO_x, NO_y / CLD	NO_z: < 1.0	NO_z: 1.5	Rickard et al. (2002)
Mediterranean Sea	NO_2, HONO, HNO_3 / Luminol CLD	HNO_3: < 2 HONO: < 1	HNO_3: 12 HONO: 2.5	Večeřa et al. (2008)

Maximum observed NO_y concentrations ranged from 0.2 ppbv in the remote centre of the Atlantic Ocean (Carsey et al., 1997) to 87 ppbv (campaign median = 6 ppbv) off the coast of New England (Dibb et al., 2004). This wide range in NO_y concentrations highlights the diversity of chemical conditions encountered at measurement sites on coasts or ships. The amounts of detected NO_y largely depend on the presence of nearby shipping lanes, harbours, or on-shore industrial activities. Consistent sub-ppbv levels are only expected in remote oceanic locations, and data sets require a thorough identification of NO_x plume events, to allow investigating the background composition of total reactive nitrogen.

2.7 Cavity-ringdown-spectroscopy detection of NO_2

The TD-CRDS instrument presented and employed in this work relies on the detection of gaseous NO_2 via the Cavity-ringdown-spectroscopy method at a wavelength of 405 nm. This method was conceived more than 30 years ago by Herbelin et al. (1980) and Anderson et al. (1984) in order to assess the reflectance of mirror coatings. Okeefe and Deacon (1988) later introduced the usage of pulsed lasers and demonstrated the ability to collect absorption spectra of gas phase molecules (e.g. O_2), present inside the cavity. Further information on the development and variations of cavity-based techniques are given in reviews e.g. by Berden et al. (2000) and Brown (2003). This section focusses on basic CRDS principles relevant for the detection of NO_2 in the TD-CRDS instrument.

A modulated laser diode inserts light at 405 nm into the cavity, where the laser beam is reflected multiple times between highly reflective hemispherical mirrors (reflectivity R > 99.9965 %), resulting in a path length which exceeds 10 km (Thieser et al., 2016). The long path length is an essential feature, allowing the detection of trace amounts of NO_2 (i.e. in the pptv range), as the optical path length is a variable in the Beer-Lambert law. A small amount of light exits the cavity and is detected by a photomultiplier tube (PMT). The trace of the detected light intensity after the diode is switched off is displayed schematically in Figure 5.

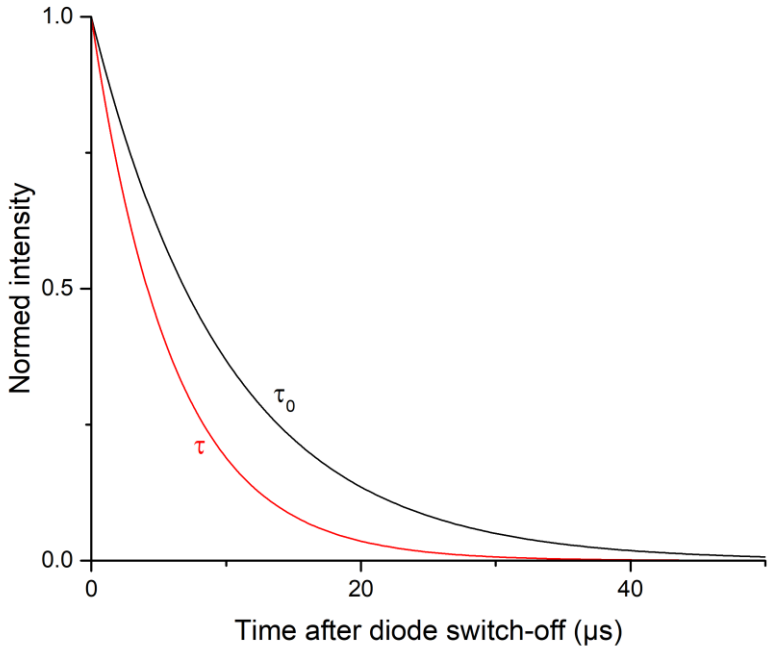

Figure 5: Exponential decay of the detected light intensity after the laser diode is switched off. The exponential decay rate increases with the mixing ratio of NO_2 present inside the cavity.

An exponential decay in the intensity I is observed, with a decay constant τ (see Eq. 5). This constant declines upon insertion of absorbing gas molecules into the cavity, due to a faster exponential decay. The mixing ratio of NO_2 is derived from this change in τ via Eq. 6, where c represents the speed of light, σ the effective absorption cross section of NO_2 (see below), and l/d the ratio between the distance separating the mirrors and the effective optical path, which is shorter due to a protective stream of synthetic air added in front of the mirrors.

$$I(t) = I_0 \cdot exp\left(-\frac{t}{\tau}\right) \qquad \text{Eq. 5}$$

$$[NO_2] = \frac{l}{d} \cdot \frac{1}{\sigma c}\left(\frac{1}{\tau} - \frac{1}{\tau_0}\right) \qquad \text{Eq. 6}$$

The absorption spectrum of NO_2 is displayed in Figure 6, as published by Vandaele et al. (1998). A local maximum in the absorption cross section σ is observed at 405 nm, which however does not represent the global maximum of the NO_2 spectrum. In contrast, absorption spectroscopy of NO_3 at 662 nm exploits a clear Gaussian-type peak in the respective spectrum (Orphal et al., 2003). The NO_2 absorption cross section at 405 nm and room temperature is ca. 6 x 10^{-}

^{19} cm^2 molec.$^{-1}$. Inserting this value and an *l/d* ratio of 1.05 in Eq. 6, a τ_0-τ change of 0.5 µs is obtained as equivalent to 1 ppbv of detected NO_2, when τ_0 was 35 µs.

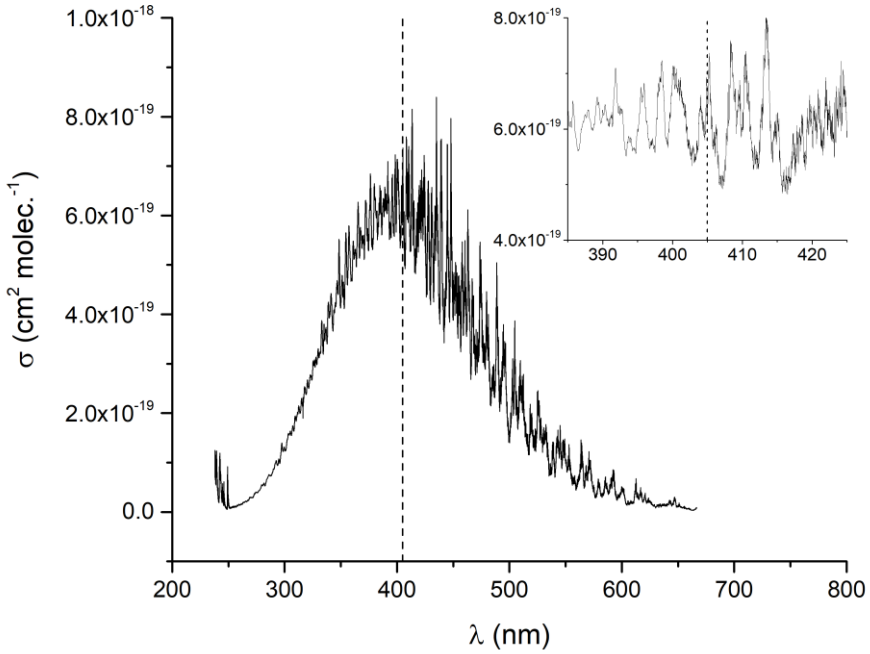

Figure 6: Absorption spectrum of NO_2 according to Vandaele et al. (1998) and a zoom onto the wavelength area between 385 and 425 nm. Dashed lines indicate the TD-CRDS laser diode wavelength of 405 nm. Units of the inset axes are identical to the main plot.

In conclusion, the CRDS technique represents a versatile method for detection of trace gas species at a high time resolution. Due to the relation to the NO_2 literature spectrum, the measurement is highly selective, absolute and in principle calibration-free. Some interferences in the NO_2 detection still exist (e.g. absorption of water molecules), and are discussed together with the associated corrections in Section 5.

3 Motivation

As elaborated in Section 2, reactive nitrogen species play crucial roles in important aspects of modern-day atmospheric chemistry. High concentrations of NO_x are a direct health risk for large parts of earth's population. This effect is enhanced by the indirect involvement in the production of O_3 and $PM_{2.5}$. NO_y species are associated in key locations with the HO_x and RO_x radical budget of the troposphere. The NO_3 radical acts itself as an important oxidising agent at nighttime. Processing and sequestering of NO_x leads to highly oxidised NO_z species which transport NO_x to remote locations and promote the formation of secondary organic aerosol. A main current question is, in how far the NO_y budget and chemistry evolve in an environment where NO_x emissions from transport and industry are mitigated in some parts of the world, while emissions from other sectors and regions continue to increase. Answering this question requires the development of precise, well-characterised, state-of-the-art equipment for the measurements of the total NO_y and the NO_y composition.

Previous measurements of NO_y relied mostly on the chemiluminescence method (see introduction of Section 5). This method, however, requires a precise characterisation of the conversion efficiencies of NO_2 and NO_z species to NO in their respective catalytic converter. In high-NO_z and low-NO_x environments, separation between NO_x and NO_z might be perturbed by the interfering detection of NO_z species in the NO_2 channel (see Section 2.4). The main goal of this project was to develop a TD-CRDS instrument capable of parallel NO_x and NO_y measurements, based on the TD principles described by Day et al. (2002) (with LIF detection) and Wild et al. (2014). Development started from the instrument presented by Thieser et al. (2016), which detected NO_2, PNs, and ANs.

Novel warranted features included the conversion of ambient NO to NO_2 (for NO_x detection) and separation between gas-phase and particulate-phase NO_z via a charcoal denuder. These new aspects of the instrument and the higher-temperature TD inlet required careful characterisation, in order to guarantee quantitative detection of NO_x and NO_z and to assess potential interferences originating from the hot inlet's radical chemistry or the adsorption of gas-phase NO_y on the denuder surface.

The ultimate goal was to deploy the characterised instrument on the AQABA ship campaign to the Mediterranean Sea and around the Arabian Peninsula. Especially the Arabian Gulf represents an intriguing area considering the concurrent emissions of NO_x and anthropogenic VOCs (e.g. from oil and gas production), while the area misses previous in-situ data sets which

allow the analysis of the NO_y budget. A second campaign (NO3ISOP) was planned to investigate the nighttime organic nitrate formation from NO_3 + isoprene, under controlled conditions at the SAPHIR simulation chamber.

Section 4 summarises the main results from the instrument development and characterisation, the AQABA campaign, and the NO3ISOP campaign. Detailed analyses and discussions of the data sets and experiments are presented in Sections 5, 6 and 7.

4 Results

4.1 Instrumental developments

A two-channel TD-CRDS was successfully developed, detecting NO_x, NO_y, NO_z (via NO_y-NO_x), and pNit. The heated inlet operates at a nominal temperature of 850 °C. Actual temperatures measured in the centre of the sampled gas stream are, however, significantly lower. A second heated inlet is equipped with an activated carbon denuder, which removes only NO_y components in the gas phase, resulting in a reading for pNit. NO is converted into detectable NO_2 by the addition of O_3. An addition of 12-20 ppmv O_3 to the sampling flow was found to result in quantitative conversion, confirmed by box model simulations showing that higher concentration lead to lower conversion efficiencies due to the formation of NO_3 and N_2O_5. Detection limits (1 min averages, 2σ) are 40 pptv for both NO_x and NO_y. The uncertainty of NO_x measurements amounts 11 %, whereas NO_z mixing ratios have a higher uncertainty of 16 %, as they are derived from the difference between the NO_y and the NO_x channels.

4.2 Characterisation of the instrument

At the nominal oven inlet temperature of 850 °C, stoichiometric conversion to NO_x (within the associated experimental uncertainties) was confirmed for PAN, isopropyl nitrate (iPN), HNO_3, N_2O_5, HONO, and $ClNO_2$. Thermal dissociation of NH_4NO_3 particles (ca. 200 nm diameter) was also observed, while $NaNO_3$ particles are detected with an efficiency < 25 %. High particle transmission (> 80 %) through the denuder was demonstrated for particles in a size range between 30 and 400 nm. An interfering detection of NH_3 was found to be supressed in ambient or ambient-mimicking mixtures. Secondary radical processes of dissociated organic nitrates are circumnavigated by the O_3 addition and the resulting NO_x detection, instead of NO_2.

The denuder-based pNit measurements are potentially biased from a humidity-induced direct breakthrough of NO and a re-release of previously deposited gas-phase NO_y species in humid synthetic air. This finding might have direct implications for other instruments which differentiate between gas- and particulate phase NO_z via denuder-techniques, under certain conditions.

The NO_x detection of the TD-CRDS was validated by a comparison of AQABA field data with an independent CLD. In a range from < 20 pptv up to 25 ppbv NO_x, a correlation slope of 0.996 ± 0.003 was obtained. Ambient measurements in Mainz, Germany, conducted for testing

purposes, revealed strong diel cycles in both NO_x and the NO_z/NO_y ratio, caused by the changing intensity in road traffic over the day.

4.3 Sources and sinks of NO_x in the Mediterranean Sea and around the Arabian Peninsula

During the AQABA campaign, ship emissions had a strong impact on detected NO_x mixing ratios, as concluded from the correlation with SO_2 in fresh and aged air masses. HONO photolysis was identified as another important source of NO. Observed HONO was potentially connected to the processing of black carbon emitted via ship plumes to pNit.

Mean NO_2 lifetimes, in respect to reaction with OH and O_3, were longest in the Red Sea (5.0 hrs), followed by the Arabian Gulf (4.0 hrs), and the Mediterranean Sea (3.9 hrs). The Mediterranean Sea was the only AQABA region where daytime losses via OH dominated over nighttime losses via O_3, due to consistently elevated daytime OH concentrations.

4.4 Reactive nitrogen budget

The reactive nitrogen budget was assessed both during the AQABA and the NO3ISOP campaign, by combing the NO_x and NO_z measurements of the TD-CRDS with other data sets from ancillary instruments. Contribution of NO_x to NO_y varied drastically depending on the location of the ship and the origins and transport paths of the sampled air masses (as inferred from back trajectories). The Mediterranean Sea was least influenced by fresh emissions (average NO_x/NO_y = 41 %), followed by the Arabian Gulf (46 %), and the Red Sea (47 %). HNO_3 was the dominant non-NO_x component of NO_y in all regions, reaching up to 39 % in the Arabian Gulf. The highest organic nitrates contribution was found in the Red Sea with 16 %, likely associated with NO_x and VOC emissions from oil and gas production. Overall, sampled air masses on AQABA were always influenced by shipping and other anthropogenic pollution sources, and cannot be classified as strictly remote marine.

In the simulated nighttime chemistry initiated by the oxidation of isoprene by NO_3 during the NO3ISOP campaign, organic nitrates (ONs) were, as expected, the dominant component of NO_z, contributing typically > 50 %. Closure on the reactive nitrogen budget was mostly achieved, by deriving a mean NO_z yield, relative to NO_x lost, of 90 ± 7 %. Under-stoichiometric detection of NO_z was likely related to losses of HNO_3 to the chamber wall.

4.5 Organic nitrate yields

The NO3ISOP experiments were also used determine the yields of ONs relative to consumed isoprene. Yields were corrected for other losses of isoprene, i.e. ozonolysis and dilution. ONs yields in a range between 77 % and 109 % were derived, largely in accordance with previous literature studies. The observed variability in the ONs yields was not connected to the fate of the initially formed RO_2 radicals, but rather to uncertainties associated with the measurements and the subtraction of HNO_3 from NO_z to obtain ONs mixing ratios.

4.6 List of publications

- **Friedrich, N.**, Tadic, I., Schuladen, J., Brooks, J., Darbyshire, E., Drewnick, F., Fischer, H., Lelieveld, J., and Crowley, J. N.: Measurement of NO_x and NO_y with a thermal dissociation cavity ring-down spectrometer (TD-CRDS): instrument characterisation and first deployment, *Atmos. Meas. Tech.*, 13, 5739-5761, 10.5194/amt-13-5739-2020, **2020**.

- **Friedrich, N.**, Eger, P., Shenolikar, J., Sobanski, N., Schuladen, J., Dienhart, D., Hottmann, B., Tadic, I., Fischer, H., Martinez, M., Rohloff, R., Tauer, S., Harder, H., Pfannerstill, E. Y., Wang, N., Williams, J., Brooks, J., Drewnick, F., Su, H., Li, G., Cheng, Y., Lelieveld, J., and Crowley, J. N.: Reactive nitrogen around the Arabian Peninsula and in the Mediterranean Sea during the 2017 AQABA ship campaign, *Atmos. Chem. Phys.*, 21, 7473-7498, 10.5194/acp-21-7473-2021, **2021**.

- **Celik, S.**, Drewnick, F., Fachinger, F., Brooks, J., Darbyshire, E., Coe, H., Paris, J. D., Eger, P. G., Schuladen, J., Tadic, I., Friedrich, N., Dienhart, D., Hottmann, B., Fischer, H., Crowley, J. N., Harder, H., and Borrmann, S.: Influence of vessel characteristics and atmospheric processes on the gas and particle phase of ship emission plumes: in situ measurements in the Mediterranean Sea and around the Arabian Peninsula, *Atmos. Chem. Phys.*, 20, 4713-4734, 10.5194/acp-20-4713-2020, **2020**.

- **Dewald, P.**, Liebmann, J. M., Friedrich, N., Shenolikar, J., Schuladen, J., Rohrer, F., Reimer, D., Tillmann, R., Novelli, A., Cho, C. M., Xu, K. M., Holzinger, R., Bernard, F., Zhou, L., Mellouki, W., Brown, S. S., Fuchs, H., Lelieveld, J., and Crowley, J. N.: Evolution of NO_3 reactivity during the oxidation of isoprene, *Atmos. Chem. Phys.*, 20, 10459-10475, 10.5194/acp-20-10459-2020, **2020**.

- **Eger, P. G.**, Friedrich, N., Schuladen, J., Shenolikar, J., Fischer, H., Tadic, I., Harder, H., Martinez, M., Rohloff, R., Tauer, S., Drewnick, F., Fachinger, F., Brooks, J., Darbyshire, E., Sciare, J., Pikridas, M., Lelieveld, J., and Crowley, J. N.: Shipborne measurements of $ClNO_2$ in the Mediterranean Sea and around the Arabian Peninsula during summer, *Atmos. Chem. Phys.*, 19, 12121-12140, 10.5194/acp-19-12121-2019, **2019**.

5 First publication: Measurement of NO_x and NO_y with a thermal dissociation cavity ring-down spectrometer (TD-CRDS): instrument characterisation and first deployment

The following chapter has been published as a research article in the peer-reviewed journal "Atmospheric Measurement Techniques":

Friedrich, N., Tadic, I., Schuladen, J., Brooks, J., Darbyshire, E., Drewnick, F., Fischer, H., Lelieveld, J., and Crowley, J. N.: Measurement of NO_x and NO_y with a thermal dissociation cavity ring-down spectrometer (TD-CRDS): instrument characterisation and first deployment, Atmos. Meas. Tech., 13, 5739-5761, 10.5194/amt-13-5739-2020, 2020.

The thesis author developed the presented instrument, performed all laboratory characterisation experiments, and operated the instrument during the campaigns. Additional contributions by the author were the data set analyses and the writing of the manuscript.

The paper presents the newly developed TD-CRDS instrument for the measurement of NOx and NO_y, together with the respective laboratory characterisation. Validations of the instrument included the collection of thermograms from various NO_z species, and the comparison of campaign NO_x measurements with an independent CLD instrument. The identification of potential humidity-induced biases for TD methods employing activated carbon denuders has widespread implications for previously published campaign data sets which saw significant discrepancies between pNit measured via TD-CRDS/LIF or via aerosol mass spectrometry (see e.g. Lee et al. (2016)).

Atmos. Meas. Tech., 13, 5739–5761, 2020
https://doi.org/10.5194/amt-13-5739-2020

Atmospheric Measurement Techniques
Open Access
EGU

Measurement of NO_x and NO_y with a thermal dissociation cavity ring-down spectrometer (TD-CRDS): instrument characterisation and first deployment

Nils Friedrich[1], Ivan Tadic[1], Jan Schuladen[1], James Brooks[2], Eoghan Darbyshire[2], Frank Drewnick[3], Horst Fischer[1], Jos Lelieveld[1], and John N. Crowley[1]

[1]Atmospheric Chemistry Department, Max Planck Institute for Chemistry, Mainz, 55128, Germany
[2]Centre for Atmospheric Science, University of Manchester, Manchester, M13 9PL, UK
[3]Particle Chemistry Department, Max Planck Institute for Chemistry, Mainz, 55128, Germany

Correspondence: John N. Crowley (john.crowley@mpic.de)

Received: 12 May 2020 – Discussion started: 25 May 2020
Revised: 17 August 2020 – Accepted: 11 September 2020 – Published: 29 October 2020

Abstract. We present a newly constructed, two-channel thermal dissociation cavity ring-down spectrometer (TD-CRDS) for the measurement of NO_x ($NO + NO_2$), NO_y ($NO_x + HNO_3 + RO_2NO_2 + 2N_2O_5$ etc.), NO_z ($NO_y - NO_x$) and particulate nitrate (pNit). NO_y-containing trace gases are detected as NO_2 by the CRDS at 405 nm following sampling through inlets at ambient temperature (NO_x) or at 850 °C (NO_y). In both cases, O_3 was added to the air sample directly upstream of the cavities to convert NO (either ambient or formed in the 850 °C oven) to NO_2. An activated carbon denuder was used to remove gas-phase components of NO_y when sampling pNit. Detection limits, defined as the 2σ precision for 1 min averaging, are 40 pptv for both NO_x and NO_y. The total measurement uncertainties (at 50 % relative humidity, RH) in the NO_x and NO_y channels are 11 %+10 pptv and 16 %+14 pptv for NO_z respectively. Thermograms of various trace gases of the NO_z family confirm stoichiometric conversion to NO_2 (and/or NO) at the oven temperature and rule out significant interferences from NH_3 detection (< 2 %) or radical recombination reactions under ambient conditions. While fulfilling the requirement of high particle transmission (> 80 % between 30 and 400 nm) and essentially complete removal of reactive nitrogen under dry conditions (> 99 %), the denuder suffered from NO_x breakthrough and memory effects (i.e. release of stored NO_y) under humid conditions, which may potentially bias measurements of particle nitrate.

Summertime NO_x measurements obtained from a ship sailing through the Red Sea, Indian Ocean and Arabian Gulf (NO_x levels from < 20 pptv to 25 ppbv) were in excellent agreement with those taken by a chemiluminescence detector of NO and NO_2. A data set obtained locally under vastly different conditions (urban location in winter) revealed large diel variations in the NO_z to NO_y ratio which could be attributed to the impact of local emissions by road traffic.

1 Introduction

1.1 Atmospheric NO_x and NO_y

Total reactive nitrogen NO_y ($= NO_x + NO_z$) consists of nitrogen oxide, NO; nitrogen dioxide, NO_2 ($NO + NO_2 = NO_x$); and their reservoir species, NO_z ($NO_3 + 2N_2O_5 + HNO_3 + HONO + RONO_2 + RO_2NO_2 + XONO_2 + XNO_2 +$ pNit), where X is a halogen atom. HCN and NH_3 are generally not considered to be components of NO_y (Logan, 1983).

The formation of both peroxy nitrates (PNs; RO_2NO_2) and alkyl nitrates (ANs; $RONO_2$) requires the presence of organic peroxy radicals (RO_2), which are formed by processes such as the reaction of OH radicals with volatile organic compounds (VOCs) and oxygen (Reaction R1). RO_2 radicals subsequently react with NO_2 or NO to form peroxy nitrates (PNs; RO_2NO_2) or alkyl nitrates (ANs; $RONO_2$, Re-

actions R2 and R3). Reaction (R3) competes with the formation of an alkoxy radical (RO) and the oxidation of NO to NO_2 (Reaction R4), which consumes the dominant fraction of RO_2. The branching ratio between these two pathways depends on atmospheric conditions such as pressure and temperature and on the structure and length of the organic backbone (Lightfoot et al., 1992). HNO_3 is produced mainly via the reaction of NO_2 with OH (Reaction R5).

$$OH + RH + O_2 \rightarrow RO_2 + H_2O \quad (R1)$$
$$RO_2 + NO_2 + M \rightarrow RO_2NO_2 + M \quad (R2)$$
$$RO_2 + NO + M \rightarrow RONO_2 + M \quad (R3)$$
$$RO_2 + NO \rightarrow RO + NO_2 \quad (R4)$$
$$OH + NO_2 + M \rightarrow HNO_3 + M \quad (R5)$$

The lifetimes of peroxy nitrates in the low troposphere are mainly governed by the temperature. PNs with an additional acyl group (PANs), such as peroxyacetyl nitrate (PAN), are generally more stable than PNs without an acyl group (e.g. pernitric acid, HO_2NO_2), which are observed only in cold regions (Slusher et al., 2002). Thus, of the peroxy nitrates, only PANs are considered able to act as transportable reservoirs for NO_x. At higher altitudes in the troposphere (above ca. 7 km) photolysis becomes the most important loss process for PAN, while the reaction with OH is negligible throughout the troposphere (Talukdar et al., 1995).

The absence of photolysis reactions and low levels of the OH radical at night-time provide alternative pathways for the formation of NO_z species. NO_2 is oxidised by O_3 to produce the nitrate radical NO_3, which exists in thermal equilibrium with N_2O_5 (Reactions R6 and R7). The reaction of NO_3 with hydrocarbons represents a night-time source of alkyl nitrates (Reaction R8), and N_2O_5 can be hydrolysed on aqueous aerosol, resulting in the formation of HNO_3 (Reaction R9) and $ClNO_2$ (Reaction R10) if particulate chloride is available (Finlayson-Pitts et al., 1989).

$$NO_2 + O_3 \rightarrow NO_3 + O_2 \quad (R6)$$
$$NO_3 + NO_2 \rightleftharpoons N_2O_5 \quad (R7)$$
$$NO_3 + R{=}R(+O_2) \rightarrow\rightarrow RONO_2 \quad (R8)$$
$$N_2O_5 + H_2O \rightarrow 2HNO_3 \quad (R9)$$
$$N_2O_5 + Cl^- \rightarrow ClNO_2 + NO_3^- \quad (R10)$$

Nitric acid formation via the reaction of NO_2 and OH (Reaction R5), followed by wet or dry deposition of HNO_3, is considered to be the dominant daytime loss process for atmospheric NO_x (Roberts, 1990), although the reduction of NO_x may result in an increasingly important role for organic nitrates (e.g. in the USA; Romer Present et al., 2020). As some organic nitrates have longer lifetimes than HNO_3, the atmospheric transport of NO_x to remote locations would lead to a more even distribution of NO_x, instead of hotspots in polluted regions close to emission sources. Atmospheric removal processes for ANs include oxidation by OH or O_3 (which may lead to a loss of the nitrate functionality), deposition to the Earth's surface and photolysis. Additionally, partitioning into the aerosol phase is possible for large and multifunctional ANs (Perring et al., 2013). Alkyl nitrates possessing no further functionality (e.g. double bonds or hydroxyl groups) can be unreactive and have long lifetimes (Talukdar et al., 1997). On the global average, $RONO_2$ has a lifetime of close to 3 h (2.6–3 h) with $\sim 30\,\%$ being lost by hydrolysis (Zare et al., 2018).

The formation of NO_z in the lower atmosphere reduces the NO_x lifetime, and the partitioning of NO_y into NO_x and NO_z can provide information about the chemical history of an air mass (Day et al., 2002; Wild et al., 2014). In regions impacted by biogenic emissions, the sources and sinks of ANs account for a large fraction of NO_x lost both during the day and night and, thus, control the lifetime of NO_x (Romer et al., 2016; Sobanski et al., 2017).

Laboratory experiments have shown that particulate nitrates (pNits) are formed at high yields in the atmospheric degradation of terpenoids in the presence of NO_x and play an important role in the formation and growth of secondary organic aerosol (SOA; Ng et al., 2017; Ammann et al., 2019). This has been confirmed in field studies, which provide evidence for the partitioning of organic nitrate to the aerosol phase both during day- and night-time (Rollins et al., 2012; Fry et al., 2013; Palm et al., 2017) with the formation of highly functionalised molecules and large contributions (up to 25 %) of particulate organic nitrates to the total aerosol mass (Xu et al., 2015; Lee et al., 2016; Huang et al., 2019).

1.2 Detection of NO_x

Methods for the detection of NO and NO_2 include chemiluminescence (CLD), differential optical absorption spectroscopy (DOAS), laser-induced fluorescence (LIF) and cavity ring-down spectroscopy (CRDS). A description and intercomparison of these methods is given in Fuchs et al. (2010), and we restrict the following discussion to an outline of the basic principles. The CLD method detects NO by chemiluminescent emission in its reaction with O_3; detection of ambient NO_2 by CLD follows its catalytic or photolytic conversion to NO. The best CLD devices have detection limits for NO and NO_2 in the single-digit parts per trillion by volume (pptv) range (Hosaynali Beygi et al., 2011; Reed et al., 2016; Tadic et al., 2020). Detection of NO_2 via LIF involves photoexcitation in its visible absorption band at wavelengths > 400 nm and detection of fluorescent emission at wavelengths > 600 nm, with detection limits of the order of parts per trillion by volume achieved for an integration time of a few seconds (Day et al., 2002; Javed et al., 2019). The structured spectrum of NO_2 between ≈ 400 and 600 nm is used to detect light absorption by ambient NO_2 by DOAS, using either broadband light sources (long-path DOAS, with a path length of more than a few kilometres) or natural sun-

light (Platt et al., 1979; Leser et al., 2003; Pohler et al., 2010; Merten et al., 2011).

The CRDS detection method for NO_2 also utilises its visible absorption spectrum, with high sensitivity being reached by achieving very long path lengths for optical extinction in an optical resonator (see Sect. 2.1). Limits of detection for NO_2 with CRDS of < 20 pptv with a 1 s integration time have been reported (Wild et al., 2014). NO can be detected as NO_2 following its oxidation by O_3 (Reaction R6; Fuchs et al., 2009).

1.3 Detection of NO_y

The first NO_y measurements were based on the conversion of all reactive nitrogen trace gases (apart from NO) to NO on catalytic metal surfaces of gold at $\sim$ 300–320 °C or of molybdenum oxide (MoO) at $\sim$ 350–400 °C (Fahey et al., 1985; Williams et al., 1998), with subsequent CLD detection of NO. Au converters were designed to exclude particulate nitrates, whereas MoO set-ups aimed at a response towards pNit (Williams et al., 1998). In recent years, the thermal decomposition of NO_z to NO_2 has been employed to detect NO_z using inlets held at temperatures high enough ($>$ 650–700 °C) to thermally dissociate the most strongly bound reactive nitrogen trace gas, HNO_3, to NO_2 (Day et al., 2002; Rosen et al., 2004; Wooldridge et al., 2010; Perring et al., 2013; Wild et al., 2014) and/or using multiple inlets at intermediate temperatures (Paul et al., 2009; Paul and Osthoff, 2010; Sadanaga et al., 2016; Sobanski et al., 2016; Thieser et al., 2016). Following thermal decomposition, the NO_2 product can be detected using LIF (Day et al., 2002, 2003; Rosen et al., 2004; Murphy et al., 2006; Wooldridge et al., 2010) or cavity-enhanced absorption spectroscopy (Paul et al., 2009; Wild et al., 2014; Sadanaga et al., 2016; Sobanski et al., 2016; Thieser et al., 2016). These techniques are impacted to various degrees by secondary reactions at high temperatures, including the loss of NO_2 via recombination with α-carbonyl peroxy radicals or reaction with $O(^3P)$ atoms (formed by the thermolysis of ambient O_3) and the generation of extra NO_2 from the oxidation of NO via reactions with peroxy radicals (Day et al., 2002; Sobanski et al., 2016; Thieser et al., 2016; Womack et al., 2017). Measures to reduce potential measurement artefacts and avoid excessive data correction include operation at low pressures (Day et al., 2002; Womack et al., 2017) and the addition of surfaces to scavenge peroxy radicals (Sobanski et al., 2016). Nonetheless, data correction may still be necessary and may involve laboratory characterisation and chemical simulation of the chemical reactions within the heated inlet (Sobanski et al., 2016; Thieser et al., 2016).

In this paper we present a two-channel TD-CRDS instrument for the detection of NO_x, NO_y, NO_z and pNit that overcomes these limitations. Compared with the set-ups described by Thieser et al. (2016), the following changes were implemented: (1) the addition of O_3 for NO_x detection, (2) use of an oven that was located directly at the front of the inlet and which was operated at a higher temperature (to detect HNO_3), and (3) the use of a charcoal denuder for separate measurement of pNit and gas-phase NO_z. The addition of O_3 (after the TD inlet) ensures that we detect NO as well as NO_2 and, thus, removes bias caused by factors such as the pyrolysis of O_3 and reactions of $O(^3P)$ which reduce NO_2 to NO.

2 Experimental

Our TD-CRDS instrument consists of two identically constructed cavities to monitor NO_2 at 405 nm which are largely unchanged compared to those described by Thieser et al. (2016). In the present set-up, the two cavities are connected to three different inlets. One cavity monitors NO_x via an inlet at ambient temperature, and the second samples air via one of two heated inlets (one equipped with a denuder, see below), thereby monitoring either NO_y or particle nitrate. A schematic diagram (not to scale) of the instrument is given in Fig. 1.

2.1 CRDS operation principals

The optical resonator consists of two mirrors (1 m radius of curvature) with a nominal 0.999965 reflectivity at 405 nm (Advanced Thin Films), which are mounted 70 cm apart. The cavity volumes are defined by Teflon (FEP) coated DURAN glass tubes with an inner diameter of 10 mm.

Under normal operating conditions each cavity samples 3.0 L (STP) min^{-1} (slpm; standard litres per minute) of ambient air (where STP refers to 0 °C and 1013 hPa). Additional purge flows (0.14 slpm dry synthetic air) are introduced directly in front of each mirror to prevent surface degradation by atmospheric trace gases. The cavities are operated at pressures of 540 to 580 Torr (1 Torr = 1.333 hPa), resulting in a residence time of $\sim$ 1.2 s. A 405 nm laser light (square-wave modulated at 1666 Hz and a 50 % duty cycle) is provided by a laser diode (LASER COMPONENTS), the emission of which is coupled into an optical fibre with a Y piece for splitting into both cavities. Temperature and current control of the laser diode are achieved by a Thorlabs ITC502 control unit. The laser emission spectrum is monitored continuously by coupling scattered light from one of the cavity mirrors into a 3648 pixel CCD (charge-coupled device) spectrograph (OMT, $\sim$ 0.1 nm resolution).

The intensity of light exiting the cavity is measured with a photomultiplier (Hamamatsu Photonics), with ring-up and ring-down profiles recorded by a digital oscilloscope (PicoScope 3000). NO_2 mixing ratios are derived from the decay constant (k or k_0) describing the exponential decrease in light intensity after the laser has been switched off:

$$[NO_2] = \frac{l}{d} \cdot \frac{1}{\sigma c} (k - k_0), \quad (1)$$

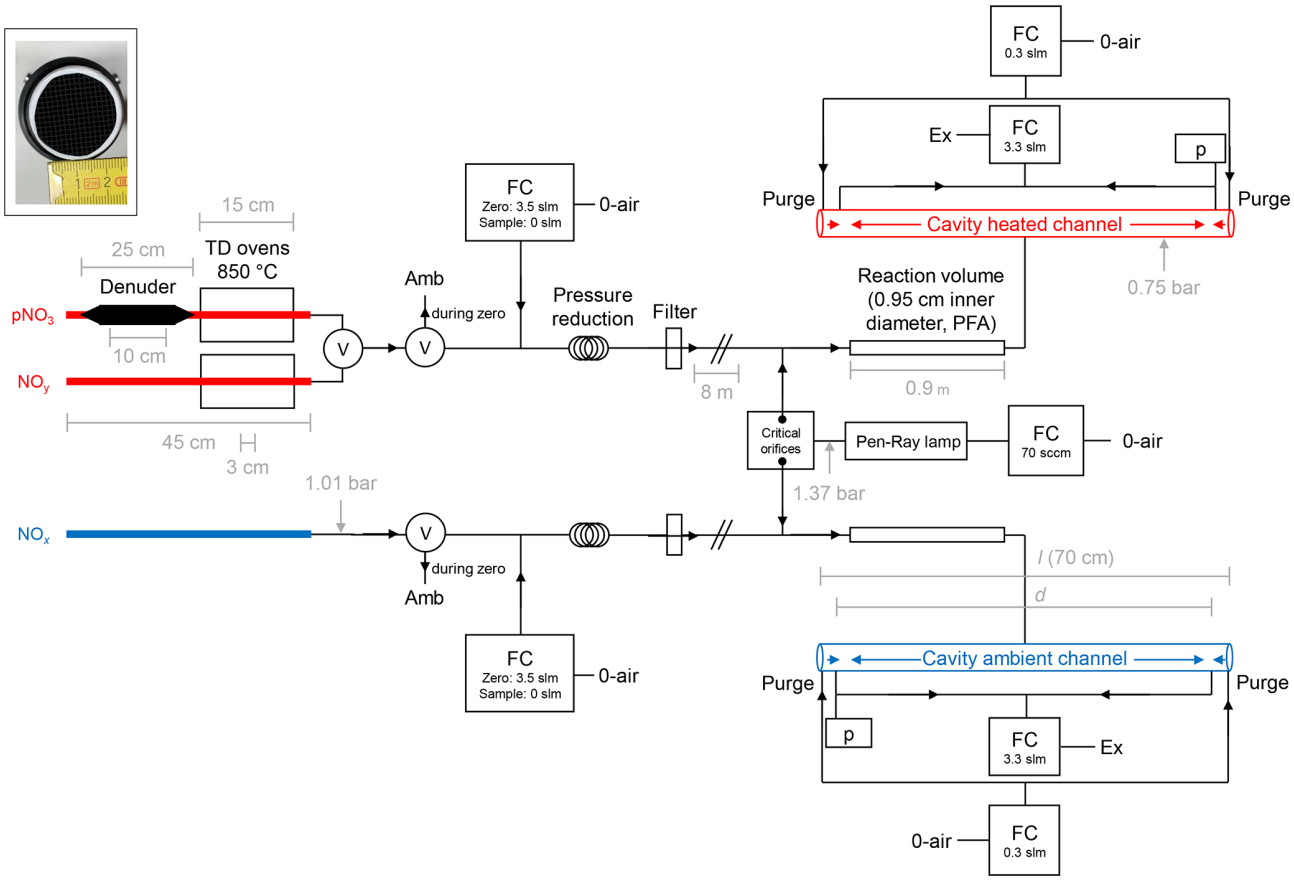

Figure 1. Schematic diagram of the TD-CRDS instrument (not to scale). NO_y and pNit are detected via the heated channel, and NO_x is detected via the ambient channel. Ozone is generated via a Pen-Ray lamp (185 nm) and serves to convert NO to NO_2. TD denotes thermal dissociation, and FC denotes flow controller. The flows listed are those used under normal operating conditions. p denotes a pressure sensor, Ex denotes a membrane pump and exhaust, Amb denotes ambient air and V denotes an electronically switchable PTFE valve. "Filter" is a PTFE filter, 2 µm pore size. O-air refers to zero air. The inset (photo) shows the honeycomb structure of the activated carbon denuder. The critical orifices have diameters of ≈ 0.05 mm. ("slm" is used to refer to standard litres per minute in this figure.)

where c is the speed of light, σ is the effective absorption cross section of NO_2 over the emission spectrum of the laser (Vandaele et al., 2002), and k and k_0 are the decay constant with and without NO_2 present in the cavity respectively. Thus, k_0 is defined by the mirror reflectivity and light scattering by the dry, synthetic air.

The ratio l/d accounts for the difference between the physical length of the cavity (l) and the effective optical path length (d) in which NO_2 is present as well as for dilution effects. d is shorter than l due to the purge flows of zero air in front of the mirrors, and a value of $l/d = 1.02 \pm 0.01$ was determined by adding a constant flow of NO_2 and varying the purge-gas flow rate (Schuster et al., 2009; Thieser et al., 2016). k_0 is typically determined every 5 min (for 1 min) by overflowing the inlets with zero air from a commercial zero air generator (CAP 180, Fuhr GmbH) attached to a source of compressed ambient air. PTFE filters (47 mm diameter, 2 µm pore size) prevent particles from entering the cavities. The filter's efficiency, tested with laboratory air containing 1.8×10^3 particles cm^{-3} and a CPC (TSI 3025 A), was > 98 %.

Raw data sets (i.e. ring-down constants) undergo a few basic corrections before further analysis:

1. k_0 is interpolated onto the k time grid. The first three data points after switching from sampling to zeroing are discarded in order to enable the stabilisation of the zero signal. The remaining data points of each zero cycle are averaged. Finally, a linear interpolation between the averaged k_0 values is performed, allowing for the subtraction of k_0 for each individual data point.

2. Depending on conditions of flow, the pressure and the inlet set-up (see Sect. 2.2 and 2.3), changes in flow resistance between the zeroing and sampling periods result in slight changes in the cavity pressure. The resulting change in Rayleigh scattering of the 405 nm light owing to a pressure change of 6.5 Torr was found to be equivalent to a change of ca. 300 pptv in the NO_2 mixing ratio,

which is in accordance with earlier experiments using previous versions of this instrumental set-up (Thieser et al., 2016). We have also used an alternative set-up in which the inlet is overflowed with zero air added close to the tip of the inlet (downstream of the oven); this reduces the pressure difference but has the disadvantage that hot air is blown out of the instrument when zeroing, which may interfere with co-located inlets. The addition of zero air upstream of the quartz inlets would remove this problem, but it would also increase the complexity of the inlet and potentially result in the loss of sticky molecules such as HNO_3.

3. A further correction is associated with the difference in the Rayleigh scattering coefficient between dry air (during zeroing) and humid air (whilst taking ambient measurements). This effect was corrected using the H_2O scattering cross sections reported by Thieser et al. (2016), leading, for example, to a correction of 116 pptv at 70 % RH and 20 °C.

2.2 Detection of NO_x

In order to measure NO (which does not absorb at 405 nm), it is converted to NO_2 by reaction with an excess of ozone (O_3); the O_3 was generated by passing zero air over a Hg Pen-Ray lamp emitting at 185 nm, which was housed inside a glass vessel at ca. 980 Torr pressure. The gas stream containing O_3 is split up equally by critical orifices and directed into two identical reaction volumes made of 88 cm long PFA tubing (1/2 inch outer diameter, residence time 1.05 s). The concentration of O_3 (monitored by a commercial monitor, Model 202, 2B Technologies) was optimised in laboratory experiments in which the efficiency of the conversion of NO to NO_2 was varied by changing the flow of air over the Pen-Ray lamp. The maximum concentration of NO_2 (corresponding to 96 % of the NO in the gas bottle) was observed when the flow over the Pen-Ray lamp was between 60 and 80 cm^3 (STP) min^{-1} (hereafter sccm), which resulted in 19 ppmv O_3 in the reaction volumes. This result could be confirmed by numerical simulation (see Table S1 in the Supplement) of the reactions involved in the formation and loss of NO_2 when NO reacts with O_3. According to the simulation, the maximum conversion of NO to NO_2 during the 1.05 s residence time occurs between ca. 12 and 20 ppmv O_3. The conversion efficiency decreases at higher O_3 concentrations due to the formation of N_2O_5 and NO_3. The results from the experiments to determine the optimum parameters for O_3 generation are summarised in Fig. S1.

For NO_2, the performance of the instrument was first described by Thieser et al. (2016), who reported a measurement uncertainty of $6\,\% + (20\,\text{pptv} \times \text{RH}/100)$ that was dominated by uncertainty in the effective cross section of NO_2 and the wavelength stability of the laser diode. The NO_x detection limit of 40 pptv (2σ, 1 min average) for the present instrument (laboratory conditions) was derived from an Allan variance analysis and is worse than that reported by Thieser et al. (2016) (6 pptv at 40 s) due to degradation of the mirror reflectivity. Corrections applied to take humidity and pressure changes into account are discussed in Sect. 2.1. The total uncertainty in NO_y will depend on the uncertainty in the conversion of both gaseous and particulate nitrate to NO_x and, thus, depends on the individual components of NO_y in the air sampled. For purely gaseous NO_y, the major problem is likely to be related to the loss of sticky molecules at the inlet, and we choose to quote a "worst case" uncertainty of 15 %.

2.3 Thermal dissociation inlets: detection of NO_y

The thermal dissociation inlets used to dissociate NO_y to NO_2 are quartz tubes housed in commercial furnaces (Carbolite, MTF 10/15/130). The oven temperature was regulated with a custom-made electronic module, which enabled spatial separation between the heating elements and insulation and the control electronics. The distance between the heated section of the quartz tubes and the point at which air was taken into the inlet was kept short (ca. 30 cm) in order to minimise losses of trace gases with a high affinity for surfaces, especially HNO_3 (Neuman et al., 1999). Experiments characterising the thermal conversion of various trace gases to NO_2 are described in Sect. 3.1. An electronic, PTFE three-way valve (Neptune Research, Inc., type 648T032, orifice diameter 4 mm) under software control switches between the two heated inlets, one of which is equipped with a denuder. Memory effects on the valves' surfaces were not observed for NO_2. Bypassing the valve under normal sampling conditions led to a 0.6 Torr pressure change. The sampling flow through both heated inlets is 3.0 slpm. When sampling ambient air via the denuder, we expect to remove all gas-phase NO_y components and, thus, measure only particulate nitrate (pNit). Experiments to characterise the transmission of the denuder for particles and various trace gases are presented in Sect. 3.3.

2.4 Active carbon denuder

The active carbon denuder (Dynamic AQS) has a honeycomb structure with 225 quadratic channels (1 mm × 1 mm) of 10 cm length in a cylindrical form (diameter 3 cm) which is housed inside an aluminium casing with 1/2 inch connections (see Fig. 1). The geometric surface area of the denuder is $\sim 45\,cm^2$. Assuming a specific surface area for activated carbon of $1000\,m^2\,g^{-1}$ (Atsuko et al., 1996), we calculate a BET (Brunauer–Emmett–Teller, Brunauer et al., 1938) surface area of the order of $10^8\,cm^2$.

2.5 Chemicals

A stock, liquid sample of PAN in *n*-tridecane (> 98 %, Alfa Aesar) was synthesised according to the procedures described by Gaffney et al. (1984) and Talukdar et al. (1995).

Samples of lower concentration (as used in the experiments described below) were produced by diluting the original sample with additional *n*-tridecane. Acetone (> 99 %), isopropyl nitrate (> 98.0 %) and (R)-(+)-limonene (97 %) were obtained from Sigma-Aldrich. An ammonia permeation source (324 ng min^{-1}) was supplied by VICI Metronics. Methanol (> 99.9 %) was acquired from Merck, isoprene (98 %, stabilised) from Acros Organics, and ethanol from Martin and Werner Mundo oHG. Both nitric acid (65 %) and β-pinene (pure) were obtained from Carl Roth. N_2O_5 crystals were synthesised according to Davidson et al. (1978) by reacting NO (5 %) with excess O_3 in a glass reactor. O_3 was produced via electrical discharge through O_2 using a commercial ozone generator (Ozomat Com, Anseros). The crystals were trapped and stored at −78 °C in dry ice and ethanol.

3 Results and discussion

3.1 Trace gas thermograms

The fractional conversion of NO_z to NO_2 in the TD inlets was investigated in a series of experiments in which constant flows of various NO_z trace gases were passed through the heated inlet (bypassing the denuder) while the temperature was varied and NO_2 was monitored. NO_x impurity levels were determined either via the simultaneous operation of the NO_x channel or via the NO_y channel mixing ratio at room temperature, before and after heating the inlet. By inserting a thermocouple into the middle part of the heated section under normal sampling conditions, we were able to show that the temperature of the gas was ≈ 80 °C lower than that indicated by the oven's internal temperature sensor in the 200–300 °C temperature range and about 40 °C lower at a set temperature of 600 °C (see Fig. S3a). We were unable to measure the temperatures of the gas stream at oven temperatures above about 600 °C, and we refer only to the temperature indicated by the internal sensor of the oven throughout the paper.

In the following, we show that the thermograms (plots of fractional dissociation of NO_z to NO_x versus temperature) which we measure with this instrument are broader and are shifted in temperature compared with other examples found in the literature, including those from this laboratory. As this instrument is built for the measurement of NO_y and is not intended for separate measurement of species such as PNs, ANs and HNO_3, overlap of the individual thermograms does not represent a problem.

3.1.1 PAN

A stream of 200 sccm synthetic air was used to elute a constant supply of gaseous PAN from its solution (held at a constant temperature of 0 °C in a glass vessel) into the CRDS inlet. The thermogram is presented in Fig. 2, and the absolute NO_2 mixing ratios are depicted in Fig. S2a. In this experiment the maximum amount of NO_2 observed (at temperatures > 400 °C) was 2.2 ppbv. At temperatures < 100 °C, there was no measurable thermal decomposition of PAN to NO_2. Increasing the temperature from 100 °C to 300 °C resulted in a sharp increase in NO_2 which flattened off at temperatures > 380 °C. We conclude that PAN is stoichiometrically converted to NO_2 at temperatures above 400 °C in our oven. The steepest part of the isotherm at ∼ 200 °C, i.e. 50 % conversion of PAN to NO_2, is therefore shifted by ca. 80 °C compared with those reported in the literature by Wild et al. (2014), Thieser et al. (2016) and Sobanski et al. (2016). This is a consistent feature of our TD ovens and is related to the short time available for thermal decomposition (see below) and a significantly lower gas temperature than indicated by the oven's internal temperature sensor.

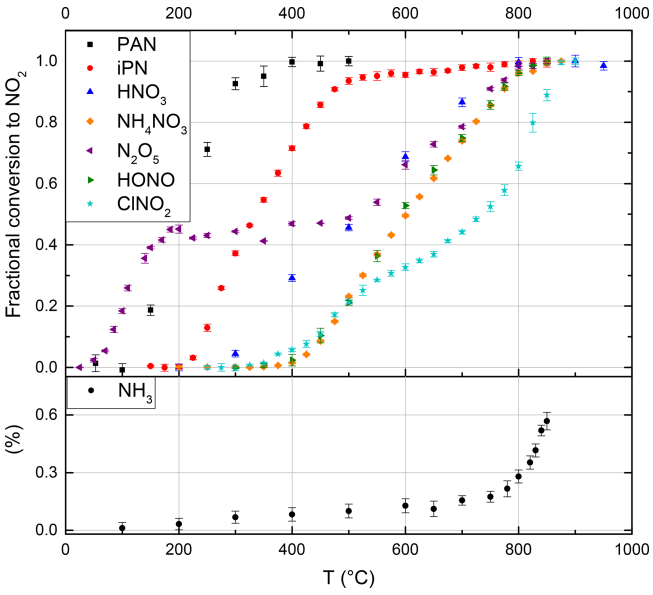

Figure 2. Thermograms of the NO_z species PAN, iPN (isopropyl nitrate), HNO_3, NH_4NO_3, N_2O_5, HONO, $ClNO_2$ and the potential interference from NH_3 (without added O_3). The NH_3 fractional conversion is calculated relative to the calibrated output of the permeation source, whereas all other species are calculated relative to the observed mixing ratio at maximum conversion. Error bars are derived from the standard deviations during the averaging intervals. At the set temperature of 850 °C, PAN, iPN, NH_4NO_3, N_2O_5 (x2), HONO and HNO_3 are converted quantitatively to NO_2, while the NH_3 interference is negligible under typical ambient conditions.

3.1.2 Isopropyl nitrate

A 10 L stainless-steel canister containing 10.3 ppmv of isopropyl nitrate (iPN) at a pressure of 4 bar N_2 was prepared using a freshly vacuum-distilled liquid sample utilising standard manometric methods. NO_x impurities were ∼ 4.7 ppbv, although we note that diluted iPN stored in stainless-steel canisters for periods of several weeks degrades to form NO_2 and HNO_3.

The thermogram is displayed in Fig. 2, and the absolute concentrations are shown in Fig. S2b. Based on the mixing ratio of iPN in the canister and the dilution flows, 10.7 ppbv represents (101 ± 11) % conversion. The shaded area around the expected iPN mixing ratio in Fig. S2b signifies the uncertainty of this value based on the propagation of the errors during the manometric and dilution procedures (2 % for flow rates, 5 % for pressures measured with digital pressure gauges and 10 % for the last dilution step using the analogue pressure gauge of the canister).

Between 550 and 850 °C, we observe a weak increase in NO_2 from 10.7 to 11.2 ppbv, which is likely due to small amounts of HNO_3 in the sample. For iPN, the temperature at 50 % conversion is 50 °C higher than those reported by Thieser et al. (2016) and Sobanski et al. (2016). Wild et al. (2014) employed a gaseous mixture of different alkyl nitrates and also observed an initial increase in NO_2 (up to 80 % conversion) for temperatures < 300 °C, followed by a slower increase up to 800 °C. The alkyl nitrates thermogram of Wild et al. (2014) has been included into Fig. S2b to illustrate this behaviour and to facilitate direct comparison.

3.1.3 HNO_3

A custom-made permeation source was used to provide a constant, known flow of HNO_3 (with ~ 8 % NO_x impurity) to the TD-CRDS inlet. The permeation source consisted of a length (≈ 1 m) of PFA tubing immersed in 66 % HNO_3 solution held at 50 °C through which 100 sccm of dry, zero air was passed. The concentration of HNO_3 and, thus, its permeation rate, $(1.62 \pm 0.2) \times 10^{-4}$ sccm, was derived by measuring the optical extinction of HNO_3 at 185 nm using the absorption cross section of Dulitz et al. (2018). The uncertainty is related to the uncertainty in the absorption cross section and the reproducibility of the output. The HNO_3 thermogram (Figs. 2 and S2c) has a plateau at temperatures above ≈ 800 °C. In the plateau region of Fig. 2, the HNO_3 mixing ratio measured is 13.0 ± 0.8 ppb, which (within combined uncertainties) is in agreement with the expected value (15.2 ± 1.98 ppbv) calculated from the permeation rate and uncertainty in the dilution factor. We cannot rule out some loss of HNO_3 in the tubing connecting the permeation source to the TD-CRDS, although previous studies have shown that irreversible losses are ~ 5 % or less under dry conditions (Neuman et al., 1999). We note that inlet loss of HNO_3 is minimised under ambient sampling conditions, as only a short section (~ 20 cm) of the quartz tubing at ambient temperature is upstream of the heated section in which HNO_3 is converted to NO_2. Therefore, our observations are in accord with previous studies that found the complete conversion of HNO_3 to NO_2 in similar set-ups (Day et al., 2002; Di Carlo et al., 2013; Wild et al., 2014; Womack et al., 2017).

3.1.4 N_2O_5

A sample of N_2O_5 was prepared by flowing 80 sccm of synthetic air over N_2O_5 crystals, kept at -70 °C, with further dilution with 20 slpm synthetic air. An 8.5 cm long nylon tube was used to reduce HNO_3 impurity. Two distinct dissociation steps can be observed in Fig. 2. The first step, between 50 and 185 °C (in which NO_2 increases to 4.2 ppbv, see Fig. S2d), is due to the dissociation of N_2O_5 to $NO_2 + NO_3$. In the second step, in which NO_3 is dissociated to NO_x between 450 and 800 °C, the NO_2 mixing ratio was 9.2 ppbv. As the amount of N_2O_5 derived from the first dissociation step was in accord with simultaneous measurements of N_2O_5 using a further TD-CRDS set-up (Sobanski et al., 2016), we conclude that some HNO_3 was present in the sample, which was presumably the result of N_2O_5 hydrolysis. Our thermogram is similar to that reported by Womack et al. (2017), who also observed two steps – the first with a plateau at $T > 100$ °C and the second at $T > 650$ °C. The shift in temperature (100–150 °C) compared with our results is rationalised in Sect. 3.1.8.

3.1.5 HONO

Gaseous HONO was produced by flowing HCl in air (22 ppbv; relative humidity, RH, ca. 50 %), over a bed of continuously stirred sodium nitrate crystals (Wollenhaupt et al., 2000). In our set-up, the thermal dissociation of HONO to NO starts at ~ 400 °C and reaches a plateau (6.2 ppbv) between ca. 800 and 850 °C (Fig. 2). We did not have access to independent instrumentation to characterise the concentrations of HONO and potential impurities generated using this method. Previous investigations have reported that HONO thermally dissociates between 450 and 650 °C (Perez et al., 2007) and between 200 and 700 °C (Wild et al., 2014). The reasons for such large divergence in the positions and widths of the thermograms may be partially related to the presence of impurities in the HONO samples used, although the details of the ovens used to thermally dissociated HONO also play an important role as described in see Sect. 3.1.8.

3.1.6 $ClNO_2$

$ClNO_2$ was generated by passing Cl_2 (33 ppbv in air) over sodium nitrate at room temperature. The thermogram, depicted in Fig. 2, has two steps – one with an apparent plateau at ~ 500 °C and a second at ~ 800 °C. The lower temperature plateau in which $ClNO_2$ dissociates to NO_2 corresponds to that reported previously (Thaler et al., 2011; Sobanski et al., 2016; Thieser et al., 2016). The observation of further NO_2 formation at higher temperature is consistent with the observations of Wild et al. (2014). We hypothesise, that the second dissociation step might be associated with the presence of ClNO which dissociates to NO (and would therefore not have been detected by instruments that monitor NO_2 rather

than NO_x). Even at temperatures $> 850\,°C$, we still see an increase in the NO_2 signal. However, as ClNO is not considered to be an important atmospheric trace gas, this has no repercussions for the deployment of the instrument.

3.1.7 NH_4NO_3 and $NaNO_3$ particles

NH_4NO_3 and $NaNO_3$ particles were generated from an aqueous solution (ca. 1 g in 500 mL deionised water) using an atomiser (TSI 3076). The particles were dried prior to size selection (DMA, TSI 3080) and were diluted in a total flow of 6 slpm synthetic air which was split between a condensation particle counter (CPC) and the heated TD-CRDS inlet (after further dilution). The relative thermogram for NH_4NO_3 is displayed in Fig. 2 and, similar to HNO_3, displays a plateau region at temperatures above 830 °C. The shift in the thermogram when comparing HNO_3 and NH_4NO_3 (which we expect to detect in a two-step process in which NH_4NO_3 first decomposes to HNO_3) may be related to the time required to fully thermally decompose particles (e.g. of 200 nm diameter) containing several million molecules. Particle numbers (in cm^{-3}) detected by the CPC were converted to molar mixing ratios via the diameters and densities of the dry particles ($1.72\,g\,cm^{-3}$ for NH_4NO_3 and $2.26\,g\,cm^{-3}$ for $NaNO_3$). The fraction of NH_4NO_3 detected as NO_x following passage through the oven is illustrated in Fig. S5, which indicates values between $\approx 60\,\%$ and 120 % depending on particle size. The total uncertainty in the concentration was estimated as 41 %, which includes 10 % uncertainty in the particle diameter (based on measured size distributions of latex calibration particles), 20 % uncertainty in the particle number (including the error in the multiple charge correction) and 10 % uncertainty in the density, due to possible differences between single crystal and bulk density. As the particle mass scales to the third order with the particle diameter, the correction for double-charged particles introduces a large uncertainty in the calculated mixing ratios, with the effect being largest in the size range between 100 and 150 nm, which probably explains the lower NH_4NO_3 detection efficiencies in this range. We consider the data obtained at 200 nm to be the most reliable and conclude that, similar to other TD instruments (Womack et al., 2017; Garner et al., 2020), our instrument also detects NH_4NO_3 particles as NO_2 with close to 100 % efficiency. In contrast, our experiments using $NaNO_3$ resulted in much smaller NO_x concentrations despite identical experimental conditions in back-to-back experiments and produced detection efficiencies of close to 25 %. While the inefficient detection of $NaNO_3$ is consistent with a previous reports suggesting that $NaNO_3$ would not be detected in TD inlets (Womack et al., 2017), it contrasts strongly with the very recent result of Garner et al. (2020), who observed quantitative conversion of $NaNO_3$ to NO_2 at 600 °C. This difference may be related to residence times in the heated section of the inlet.

3.1.8 Summary of thermograms

The thermograms obtained by the present instrument deviate from others reported in the literature, with the temperatures required for 50 % dissociation generally being higher by, for example, 80 °C for PAN, 50 °C for iPN and 150 °C for HNO_3 respectively (Day et al., 2002; Wild et al., 2014; Sobanski et al., 2016; Thieser et al., 2016; Womack et al., 2017). This lack of agreement with other set-ups is not unexpected, as the degree of dissociation of a trace gas at any temperature depends not only on the temperature but also on the time over which the molecule is exposed to that temperature (Womack et al., 2017). To illustrate this, based on rate coefficients (related to bond-dissociation energies, BDEs) for the thermal dissociation of PAN (Bridier et al., 1991), iPN (Barker et al., 1977), HNO_3 (Glänzer and Troe, 1974), N_2O_5 (Ammann et al., 2019), $ClNO_2$ (Baulch et al., 1981) and HONO (Tsang and Herron, 1991), we calculated the theoretical 50 % conversion temperature for each molecule as a function of residence time inside the oven (see Fig. S3b). At short residence times the dependence on temperature is very steep (especially for large BDEs) which partially explains the differences between our short heated section inlet and longer ones. However, in practise, we do not know the precise average temperature of the gas at the centre of the oven nor can we characterise the axial and radial gradients in temperature in the quartz tubes; thus, the calculations of fractional dissociation (or complete thermograms) based on bond-dissociation energies are only a rough guide at best. We note that the use of different flows, oven diameters and operational pressures will strongly affect heat transfer from the oven walls to the gas; therefore, reporting the temperature of the external oven wall (as done here and in all reports in the literature) to some extent precludes comparison between different set-ups. The width of the thermograms (i.e. the temperature difference between e.g. 10 % and 90 % dissociation) will also depend on details of axial and radial temperature gradients in the tubing located within the oven as well as in the downstream section of tubing, which represents a transition regime between oven and room temperature. The impact of temperature gradients inside the quartz tube was explored by calculating the HNO_3 thermogram using an Arrhenius expression for its thermal dissociation and the gas residence time within the quartz tube. We initially assumed that all HNO_3 molecules experience the same temperature and then compared this to the situation in which 20 % of the HNO_3 molecules experience an 80 °C lower temperature and 20 % experience an 80 °C higher temperature. The resultant thermograms are displayed in Fig. S3c and indicate that the presence of temperature gradients results in an increase in the width of the thermogram from 250 to 350 °C.

The thermograms we report here serve only to determine the temperature needed to ensure the maximum conversion of each trace gas to NO_2. This is achieved in the present set-up with a temperature of 850 °C. Where possible, we have veri-

fied that operation at the plateau of the thermogram resulted in quantitative conversion of the traces gases and particles studied, with one exception – $NaNO_3$ particles. We further note that, in an instrument designed only to measure NO_y, there is no need to ensure separation (in temperature) of the thermograms for different classes of molecules.

3.1.9 Detection of NH_3

As described previously (Wild et al., 2014; Womack et al., 2017) ammonia represents a potential interference in NO_y measurements. In order to quantify this interference, we measured NO_2 formation in air containing 131 ppbv NH_3 delivered by a calibrated permeation source (VICI METRONICS, permeation rate 324 ng min^{-1} at 45 °C). The results are summarised in Fig. 2. In NH_3–air mixtures, we observe a small NO_2 signal, increasing slowly at first and then (from $\approx$ 700 °C) rapidly with temperature; the amount of NO_2 observed at 850 °C corresponds to a fractional conversion of NH_3 to NO_2 of 0.006 ± 0.002. This result is in broad agreement with Wild et al. (2014), who found a conversion efficiency of < 0.01 at 700 °C. In experiments with NH_3 in zero air with relative humidities of 17 %, 31 % and 53 %, we were unable to observe the conversion of NH_3 to NO_2, which is again consistent with the humidity-related suppression of NO_2 formation observed by Wild et al. (2014).

In additional experiments, we investigated the potential influence of ozone on the NH_3 to NO_2 conversion efficiency in zero air containing O_3. The addition of O_3 results in a significant increase in NO_2 with a linear dependence on the O_3 mixing ratio (Fig. 3) and up to 11.4 % conversion of NH_3 to NO_2 at 200 ppbv O_3. This was not reduced measurably by the addition of water vapour to the air–O_3 mixture. In further experiments, we spiked air with the headspace of various organic liquids (acetone, methanol, ethanol, β-pinene, limonene and isoprene). The gas-phase mixing ratios of the organic trace gases were unknown, but the formation of NO_2 was suppressed or completely stopped in each case. A more quantitative investigation was carried out using a known concentration (1 ppmv gas bottle) of isoprene. We found that the addition of 30 ppbv isoprene to zero air (containing 330 ppbv O_3) did not significantly reduce the NH_3-to-NO_2 conversion efficiency under dry conditions, but it decreased it by a factor of 2 when the RH was increased to 50 %.

A tentative chemical mechanism, based partially on Womack et al. (2017), to explain the formation of NO_2 from NH_3 and O_3 at high temperatures and the processes that suppress it is given in Reactions (R11) to (R15). In this scheme, the oxidation of NH_3 is initiated and propagated by $O(^3P)$, which is formed from the thermal dissociation of O_3 (Peukert et al., 2013). This leads to the formation of NO and HNO (Reaction R13a and R13b), both of which can be oxidised to NO_2 (Reactions R14 and R15). Forward and reverse rate coefficients for Reaction (R11) indicate that O_3 is converted almost stoichiometrically to $O(^3P)$ in the

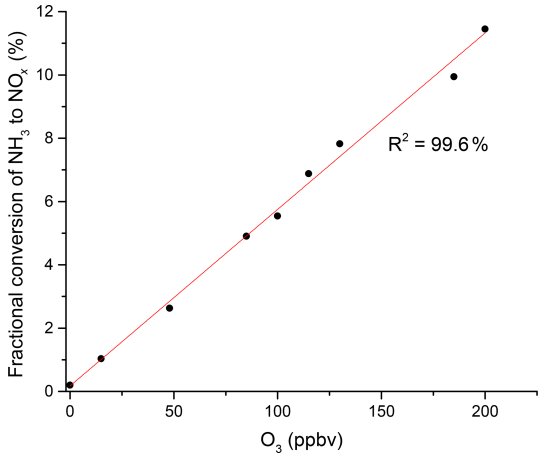

Figure 3. NH_3 to NO_x conversion in the heated inlet channel of the instrument in the presence of O_3. The fractional conversion of NH_3 to NO_x is calculated from the 13.1 ppmv of NH_3 from the permeation source.

$\approx$ 10 ms reaction time in the heated inlet. The rate constants (at 1123 K) for the subsequent reactions involving $O(^3P)$ are as follows: $k_{12} = 4.4 \times 10^{-13}$ cm^3 molec.$^{-1}$ s^{-1}, $k_{13a} = 8.3 \times 10^{-12}$ cm^3 molec.$^{-1}$ s^{-1} and $k_{13b} = 7.5 \times 10^{-11}$ cm^3 molec.$^{-1}$ s^{-1}) (Cohen and Westberg, 1991). Reaction (R12) converts 0.3 % of the initial NH_3 molecules to NH_2 within 10 ms (at 100 ppbv O_3 and 1123 K).

$$O_3 + M \rightarrow O(^3P) + O_2 + M \quad \text{(R11)}$$

$$O(^3P) + NH_3 \rightarrow NH_2 + OH \quad \text{(R12)}$$

$$NH_2 + O(^3P) \rightarrow NO + H_2 \quad \text{(R13a)}$$

$$\rightarrow HNO + H \quad \text{(R13b)}$$

$$HNO + O(^3P)/OH/H \rightarrow NO + OH/H_2O/H_2 \quad \text{(R14)}$$

$$NO + O(^3P) + M \rightarrow NO_2 + M \quad \text{(R15)}$$

The experimental results obtained in zero air indicate that reactions involving $O(^3P)$ from O_3 thermolysis can result in the conversion of NH_3 to NO and NO_2. These results could, however, not be reproduced when adding NH_3 to ambient air sampled from outside of the building. In this case, the addition of NH_3 (at 50–60 ppbv O_3) did not result in a measurable increase in NO_2, which was in accord with the observations of Womack et al. (2017). The scavenging of NH_2 radicals and $O(^3P)$ by both volatile organic compounds and H_2O provides a likely explanation for this. Womack et al. (2017) also found that the addition of 100 ppbv CO can reduce the conversion of NH_3 to NO_x.

In summary, our experiments indicate that the conversion of NH_3 to NO_2 is suppressed in ambient air samples, or in synthetic air with added VOCs and water. The ambient air used in these experiments was from an urban and polluted environment (typical NO_x levels between 10 and 50 ppbv; see

Sect. 4.2). As high levels of atmospheric NH_3 are associated with agricultural activity (Langford et al., 1992; Schlesinger and Hartley, 1992) and are often accompanied by high NO_x and VOC levels, the NH_3 interference under these conditions is most likely to be small compared with ambient NO_z levels. Long-term measurements of NH_3 have additionally found a positive correlation between NH_3 concentrations and ambient temperature (Yamamoto et al., 1988; Wang et al., 2015; Yao and Zhang, 2016), with the latter promoting the presence of high levels of biogenic VOCs, such as isoprene (Tingey et al., 1979), which would also help to minimise the NH_3-related interference.

3.2 Bias caused by secondary reactions in the TD ovens

Thermal dissociation techniques coupled to CRD systems for the measurement of organic nitrates suffer bias to different degrees owing to reactions of organic peroxy radicals with NO and NO_2 (Sobanski et al., 2016; Thieser et al., 2016). According to previous studies (Day et al., 2002; Rosen et al., 2004; Thieser et al., 2016), in experiments using iPN at an oven temperature of 450 °C, an overestimation of ANs in the presence of NO is caused by reactions of the initially formed alkoxy radical, C_3H_7O, which results in the formation of both HO_2 and CH_3O_2 (Reactions R16–R21).

$$C_3H_7ONO_2 + M \rightarrow C_3H_7O + NO_2 + M \quad \text{(R16)}$$
$$C_3H_7O + O_2 \rightarrow CH_3C(O)CH_3 + HO_2 \quad \text{(R17)}$$
$$C_3H_7O + M \rightarrow CH_3 + CH_3CHO + M \quad \text{(R18)}$$
$$CH_3 + O_2 + M \rightarrow CH_3O_2 + M \quad \text{(R19)}$$
$$CH_3O_2 + NO \rightarrow CH_3O + NO_2 \quad \text{(R20)}$$
$$HO_2 + NO \rightarrow HO + NO_2 \quad \text{(R21)}$$
$$CH_3C(O)O_2NO_2 + M \rightarrow CH_3C(O)O_2 + NO_2 + M \quad \text{(R22a)}$$
$$CH_3C(O)O_2 + NO_2 + M \rightarrow CH_3C(O)O_2NO_2 + M \quad \text{(R22b)}$$
$$CH_3C(O)O_2 + M \rightarrow CH_3CO + O_2 + M \quad \text{(R23a)}$$
$$CH_3C(O)O_2 \rightarrow CH_2C(O)OOH \quad \text{(R23b)}$$
$$OH + NO_2 + M \rightarrow HNO_3 + M \quad \text{(R24)}$$

In order to investigate the potential bias in the measurement of ANs under the present experimental conditions, a set of experiments was conducted in which NO (up to 12 ppbv) was added to various amounts of iPN. The NO mixing ratio was determined by modulating the addition of O_3. The results (Fig. 4a) show that NO_2 derived from the thermal decomposition of iPN increases with the amount of NO added and results in overestimation (factor of ∼1.6) at 12 ppbv NO, which is consistent with the observations by Thieser et al. (2016). This disappears when 19 ppmv ozone is added in front of the cavity so that NO_x rather than NO_2 is measured (blue data points). This is readily explained by the compensation of the additional NO_2 formed via reactions of NO with RO_2 by an equal loss in NO, which is only detected when introducing O_3. This is illustrated graphically in Fig. S4.

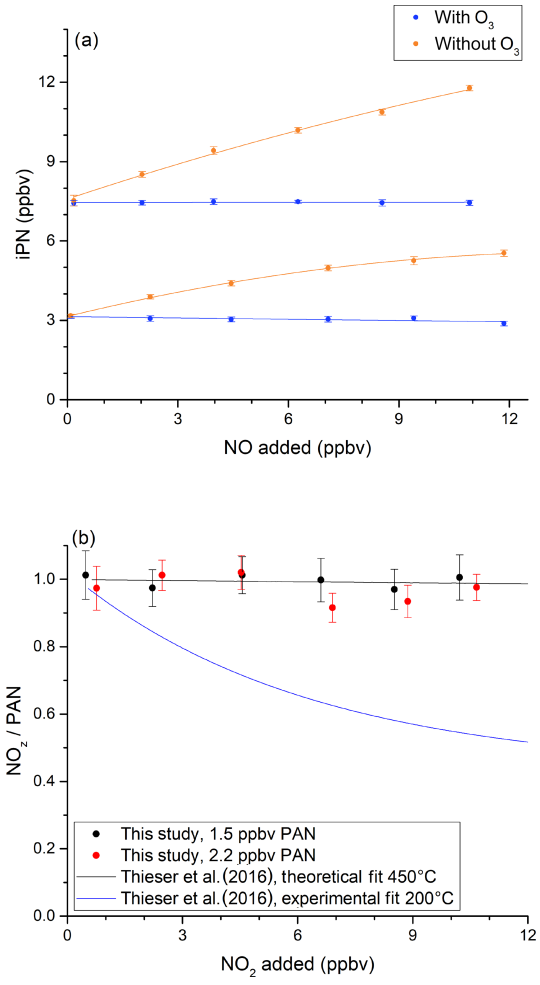

Figure 4. Investigation of bias caused by reactions of NO with HO_2 and RO_2 when measuring iPN. **(a)** NO varied for two initial iPN mixing ratios in the presence (blue data points) and absence (orange data points) of added O_3. The NO_x background signal from the iPN cylinder was subtracted from the iPN mixing ratios. **(b)** The investigation of bias caused by the recombination of RO_2 and NO_2 during the thermal decomposition of PAN. In both experiments, the oven temperature was 850 °C. In both plots, the error bars indicate the standard deviation over the averaging interval.

We also explored the potential for bias caused by the recombination of $CH_3C(O)O_2$ and NO_2 (Reaction R22b), following the thermal decomposition of PAN (Reaction R22a). Thieser et al. (2016) reported that PAN was underestimated by a factor 0.45 when adding 10 ppbv NO_2 to an air sample containing PAN at 200 °C. This behaviour was not apparent at 450 °C, which is related to the decomposition (Reaction R23a) or isomerisation (Reaction R23b) of $CH_3C(O)O_2$ at the higher temperature. The results of a similar experiment with our 850 °C inlet are presented in Fig. 4b. In this plot, the measured NO_z relative to the input PAN is plotted versus the mixing ratio of added NO_2. For PAN concentrations from 1.5 to 2.2 ppbv, no effect was observed for NO_2 concentrations

of up to 10 ppbv. This is consistent with the reaction scheme presented by Thieser et al. (2016) at 450 °C.

A potential source of bias when measuring HNO_3 includes its reformation via the reaction of OH and NO_2 (Reaction R24). Compared with the RO and RO_2 radicals formed in the thermal dissociation of PNs and ANs, OH exhibits a higher affinity for surfaces and is likely to be efficiently removed at the oven wall. Day et al. (2002) estimated that wall losses are the dominant OH sink and that the resulting underestimation of HNO_3 would be < 2 % for NO_y levels < 5 ppbv. At our oven temperature, the diffusion coefficient for OH (D_{OH}) can be calculated according to Tang et al. (2014):

$$D_{OH}(1123\,K) = D_{OH}(296\,K) \cdot \frac{296}{T}^{-1.75}. \quad (2)$$

Using an average of the literature values for D_{OH} at room temperature from Ivanov et al. (2007), 165 Torr cm^2 s^{-1}, and Bertram et al. (2001), 192 Torr cm^2 s^{-1}, a value of D_{OH} (1123 K) = 1841 Torr cm^2 s^{-1} was derived. The maximum rate constant for OH wall loss (assuming laminar flow) can subsequently be approximated according to Zasypkin et al. (1997):

$$k_{wall} = \frac{D_{OH} \cdot 3.66}{r^2 \cdot p} \quad (3)$$

With the radius of the oven quartz tube r (0.45 cm) and the pressure p (760 Torr), the maximum value of k_{wall} is 44 s^{-1}. The first-order loss rate coefficient for the reaction of OH with NO_2 is given by $k_{(OH+NO_2)}$ [NO_2], where $k_{(OH+NO2)}$ is the rate coefficient for the reaction between OH and NO_2 at 1123 K $\sim 5 \times 10^{-14}$ cm^3 molec.$^{-1}$ s^{-1} (Ammann et al., 2019) and [NO_2] = 6.5×10^{10} molec. cm^{-3} (the concentration of 10 ppb NO_2 at the pressure and temperature of the oven). The first-order loss rate of OH via reaction with NO_2 is then 3×10^{-3} s^{-1}. Clearly, the efficiency of uptake of OH to the wall would have to be very low in order to reduce the maximum value of 44 s^{-1} to values that are comparable to the reaction with NO_2, which is very unlikely. We conclude that reformation of HNO_3 via Reaction (R24) will not bias measurements of HNO_3 with the present set-up.

3.3 Denuder characterisation

The efficiency of the removal of NO_y trace gases and the transmission of submicron particles was determined in a series of experiments, which are described below.

3.3.1 Transmission of ammonium nitrate particles (10–414 nm)

In order to characterise the transmission of the denuder for particles of different diameter, a constant flow of particles was generated by passing 3.3 slpm of nitrogen through an atomiser (TSI 3076) containing an aqueous solution of ammonium nitrate. The flow rate (3.3 slpm) was matched to the typical sampling flow through the denuder. A total of 0.28 slpm of the flow was sampled into a scanning mobility particle sizer (SMPS)/CPC system (TSI 3080 and TSI 3025A) to measure the number density and size distribution (10–414 nm) of the ammonium nitrate particles. The flow was delivered either directly to the SMPS/CPC via straight metal tubing (length 27 cm, inner diameter 0.9 cm), for which we assume 100 % particle transmission, or via the denuder. Thus, the ratio of the particle numbers in each size bin represents the size-dependent denuder transmission. As shown in Fig. 5, the transmission of the denuder is > 80 % for particles between 30 and 400 nm in diameter. As expected, some diffusive loss is observed for particles < 20 nm in diameter and loss due to impaction and/or settling is observed for particles > 300 nm. The particle transmission T as a function of particle diameter D can be represented by the following empirical expression:

$$T(\%) = \frac{D(\mathrm{nm}) - 5.79}{0.035 + 0.010 \cdot (D - 5.79) + 1.78 \cdot 10^{-6} \cdot (D - 5.79)^2} \quad (4)$$

The particle transmission through the denuder channels was also calculated using the Particle Loss Calculator (PLC) developed by von der Weiden et al. (2009). The results of this calculation are plotted in Fig. 5. The observed loss of particles smaller than 40 nm is not replicated by the PLC, which was developed for cylindrical piping and not for the square honeycomb shape of the denuder; thus, it does not consider losses due to impact at the finite surface area which the gas and particle flow is exposed to at the entrance to the honeycomb. The PLC does a better job at predicting a reduction in transmission for the largest particles that we measured, indicating a transmission of 74 % at 1 µm and 45 % at 2 µm. Therefore, in certain environments, nitrate associated with coarse-mode particles represents a potential bias for TD-CRDS measurements of NO_y.

3.3.2 Efficiency of removal of NO_y trace gases

The efficiency of the removal of trace gases in the denuder under typical flow conditions (3.3 slpm) was investigated for NO, NO_2, PAN, iPN, HONO, N_2O_5, $ClNO_2$ and HNO_3 as representative NO_y species. The efficiency of removal of each trace gas (generally present at 5–40 ppbv) was determined by measuring its relative concentration when flowing through the denuder (pNit channel) and when bypassing the denuder (NO_y channel). The results (Fig. 6) indicate that, in dry air, all of these trace gases were removed with an efficiency of close to 100 %. However, when the main dilution flow was humidified, RH-dependent breakthrough of NO was observed, with only 60 % stripped from the gas phase at an RH close to 100 %. HONO was removed with 85 % efficiency at an RH of 46 %, and $ClNO_2$ was removed

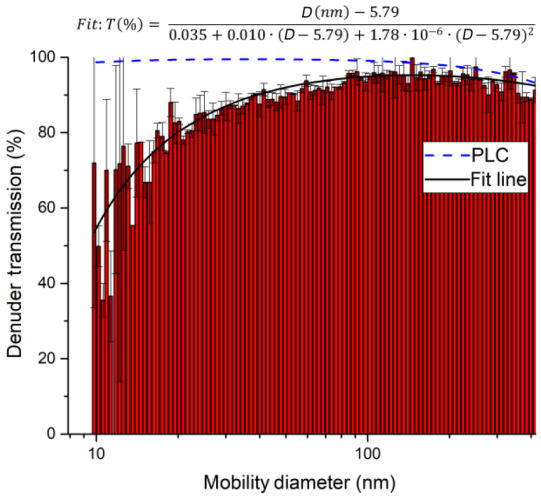

Figure 5. Transmission of ammonium nitrate particles through the denuder inlet. Relative transmissions are derived by dividing the number size distribution when sampling through the denuder by a size distribution obtained without the denuder. Error bars are based on the standard deviation of three consecutive measurements with and without the denuder. An aerosol flow of 3.3 slpm was directed through the denuder (diameter 3 cm, see Sect. 2.4), and a DMA subsequently sampled 0.3 slpm from the stream exiting the denuder. The plot also includes a fit of the experimental (solid, black line) data and a theoretical transmission distribution computed with the Particle Loss Calculator (PLC).

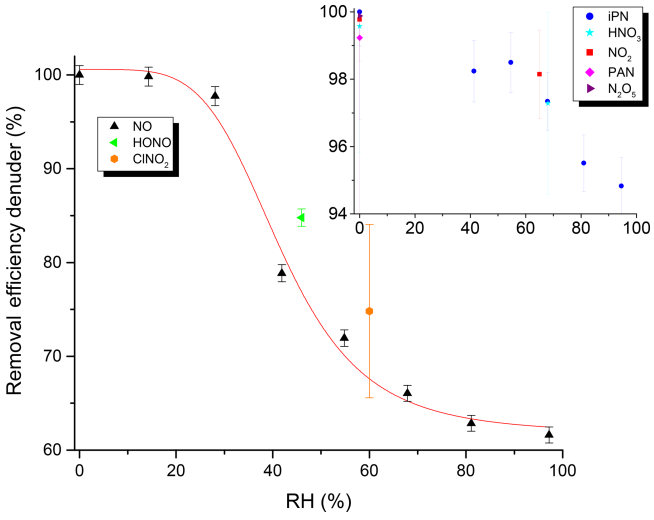

Figure 6. Removal efficiency of the denuder for various NO_y trace gases as a function of RH. Units of the inset are identical to the main graph. See Table S2 for the exact values and information on the error determination.

with a 75 % efficiency at an RH of 60 %. In contrast, humidification only had a marginal effect on the scrubbing efficiency for NO_2, iPN and HNO_3, for which an efficiency of ≥ 95 % was observed. The precise values that the removal efficiencies in Fig. 6 were determined from are listed in Table S2.

In further experiments, we examined the potential for re-release of NO_y that had previously been stored in the activated carbon substrate of the denuder. In these experiments, in which either NO_x or NO_y was continuously monitored, the denuder was exposed to a flow of 9.5 ppm iPN in dry nitrogen for 90 min during which 2.30×10^{17} molecules of iPN were stripped from the gas phase and deposited onto the denuder. This exposure is equivalent to a month-long exposure to 20 ppb of iPN. The air passing through the denuder was subsequently humidified to an RH of 65 %. The results (Fig. 7a) indicate a high initial (11:40–11:50 UTC) rate of release of NO_x under humid conditions (resulting in a maximum mixing ratio of 2 ppbv at 11:45 UTC). At 11:50 UTC, humidification of the air was stopped and the rate of release of NO_x dropped gradually towards zero. During a second period, in which the air was again humidified (from 11:50 UTC onwards), NO_x was released from the denuder, albeit at a lower rate than during the first humidification. From 12:25 UTC onwards, the oven behind the denuder was heated to 850 °C so that NO_y was added. No significant increase in NO_2 was observed, indicating that the trace gas(es) species released from the denuder surface upon humidification are predominantly NO_x. During this experiment, 2.55×10^{15} molecules of NO_x desorbed from the denuder, indicating that the major fraction of iPN molecules remained stored on the denuder surface upon humidification.

Similar denuder exposure experiments were performed with HNO_3 and NO_2. For HNO_3, no evidence for desorption of NO_x or NO_y during exposure to humidified air was observed, whereas NO_2 exhibited a similar behaviour to iPN (Fig. 7b). After loading the denuder with 5 sccm from a 0.831 ppm NO_2 gas bottle for 4.8 d (a total of 7.60×10^{17} molecules were deposited as derived from the flow rate, the exposure time and the gas bottle mixing ratio), the effect of passing humidified air through the denuder was to release NO_x, which was observed at concentrations up to ≈ 39 ppbv. While the relative humidity was kept constant at close to 100 %, the NO_x released decreased over time so that after 30 min, 3.2 ppbv of NO_x could still be detected. By switching the O_3 source off (at $\approx$ 10:45 UTC), the NO_2 measured went to ≈ 0, indicating that predominantly NO was released (and not NO_2). Integrating these results over time yielded a value of 1.63×10^{16} molecules desorbed NO from the denuder surface in humid air. Qualitatively similar results, i.e. humidity-induced formation and release of NO_x from the denuder, were observed when the denuder was exposed to variable levels of NO_x (i.e. up to 20 ppbv) under dry conditions for periods of weeks.

Clearly, adsorption of water molecules onto the denuder surface can initiate and/or catalyse chemical transformation at the surface that convert stored NO_z into forms which can desorb and be detected as NO_x. To further our understanding

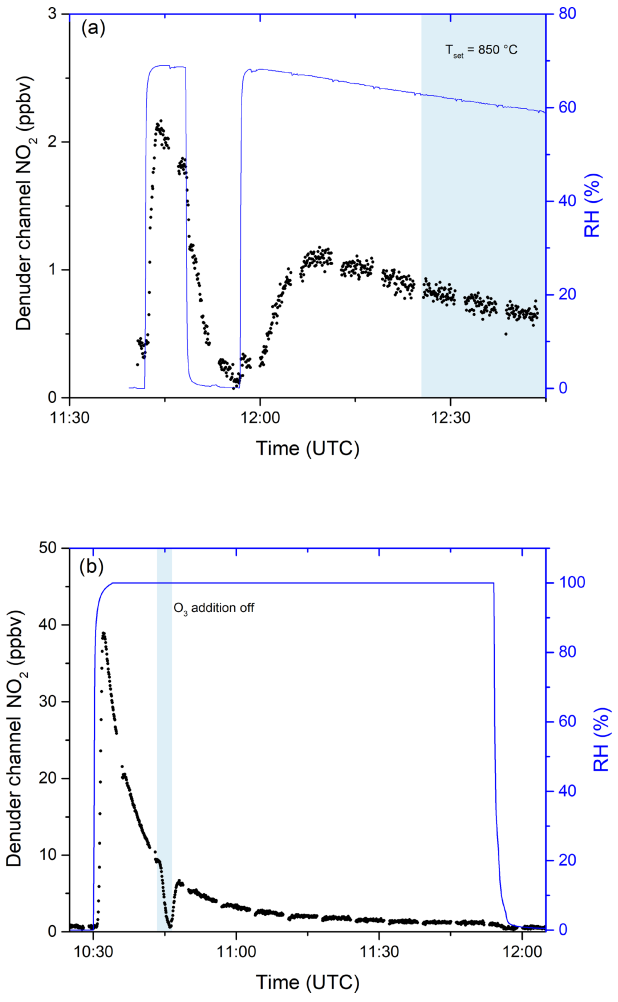

Figure 7. (a) Release of NO_x from the denuder in humid air after exposure to 9.5 ppmv iPN for 1.5 h. Relative humidity was measured before passing through the denuder. The blue shaded area signifies the period in which the inlet oven was heated to 850 °C. Changes in RH are achieved by flowing parts of the zero air stream through deionised water. **(b)** The release of NO_x from the denuder in humid air after exposure to 0.83 ppmv NO_2 for 4.8 d. O_3 addition was switched off during the blue shaded period.

of the underlying processes that occur upon humidification, a series of experiments were conducted to examine the adsorption of water on the denuder. In these experiments, the denuder was first dried by exposing it to dry air for several hours until the relative humidity of the air exiting the denuder was close to zero. Subsequently, humidified air was passed through the denuder and the RH of air exiting it was continuously monitored. The results of an experiment in which the air was humidified to 68 % are shown in Fig. 8a. After 77 min of exposure to this humidity, the RH of the air exiting the denuder acquired a maximum value of 64 %. After switching back to dry synthetic air (at 09:37 UTC), ∼ 60 minutes passed before the RH dropped to values close to zero. In this period, the RH did not decrease monotonically, with the rate of change of relative humidity exiting the denuder revealing a number of discreet steps. Figure 8b plots the derivatives (dRH/dt) of the drying phases of a series of experiments in which the initial RH was varied between 47 % and 75 %. A similar pattern emerges for each experiment with the greatest desorption rates occurring at the beginning of the drying phase followed by a minimum in the desorption rate and a second maximum (at ≈ 15 % relative humidity). This behaviour is a clear indication that H_2O is bound to more than one chemically or physically distinct surface sites on the activated carbon.

By measuring the change in the RH of the air flowing into and out of the denuder, we can derive an equilibrium adsorption isotherm for H_2O at the active carbon surface. An example is given in Fig. 9 where it is also compared to a literature isotherm for the adsorption of water vapour on activated carbon fibre (Kim et al., 2008). The data of Kim et al. (2008) have been scaled by matching the number of adsorbed water molecules at an RH of 65.9 % to our observed value at an RH of 67.2 %. The exposure of carbonaceous surfaces to inert gases at high temperatures (2000 °C) reduces the capacity for water uptake, whereas functionalising the carbon surface with oxygen-containing groups (e.g. from HNO_3) enhances the water adsorption capacity (Dubinin et al., 1982; Barton and Koresh, 1983; Liu et al., 2017). Thus, in our experiments, the uptake of gas-phase NO_y is expected to generate oxygenated sites on our denuder surface, which, in turn, will influence water uptake and subsequent further trace gas accommodation.

The chemistry leading to the formation of gas-phase NO_x from NO_y trace gases adsorbed at the denuder surface under humid conditions cannot be elucidated in detail with our experimental set-up. However, a strong humidity dependence in the heterogeneous generation of HONO and NO from NO_2 adsorbed on soot particles has been reported (Kalberer et al., 1999; Kleffmann et al., 1999). Formation of HONO from NO_x has also been observed on wet aerosol and ground surfaces in field studies (Lammel and Perner, 1988; Notholt et al., 1992). Previous investigations report the adsorption of NO_2 on activated carbon at ambient or close to ambient temperatures (30–50 °C), followed by its reduction to NO, with the simultaneous oxidation of the carbon surface (Shirahama et al., 2002; Zhang et al., 2008; Gao et al., 2011). These results are consistent with our observation of processes such as the conversion of NO_2 to NO at the denuder surface under humid conditions. In our experiments, we observed that NO_2 was converted to NO (rather than HONO) at the denuder surface. It is possible that the initial step is the formation of HONO (e.g. by the surface-catalysed hydrolysis of NO_2 or iPN) which undergoes further reduction on the surface to NO. The release of HONO and NO has also been observed from soil, after the nitrification of NH_3/NH_4^+ or the reduction of NO_3^- (Su et al., 2011; Pilegaard, 2013; Meusel et al., 2018). Oswald et al. (2013) found compara-

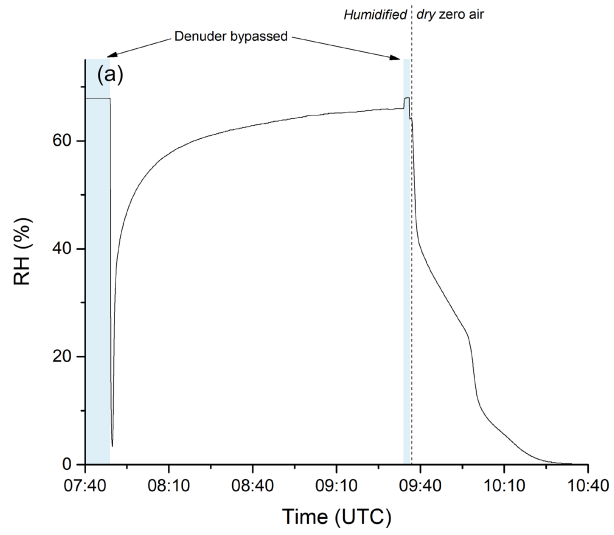

Figure 8. **(a)** RH of humidified zero air after passing through the denuder. The initial RH was determined by bypassing the denuder before and after the experiment. Zero air was humidified by flowing a fraction of the stream through deionised water stored in a glass vessel. The time at which the experiment was conducted is given on the x axis. Until ca. 09:35 UTC, zero air with constant humidity (RH ca. 68 %) was sent through the denuder. Afterwards the denuder was exposed to dry zero air. **(b)** Derivative of the measured RH during the drying period. The step during the drying phase occurs in a higher RH area when starting the drying from a larger RH value.

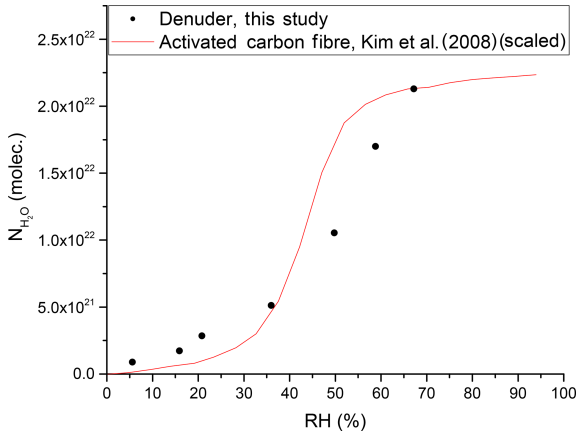

Figure 9. Number of adsorbed water molecules onto the denuder surface at equilibrium versus RH. The red line represents (scaled) results from a study on activated carbon fibre (Kim et al., 2008).

ble HONO and NO emission fluxes from non-acidic soils, providing another example of the heterogeneous formation of HONO from other atmospheric nitrogen species, followed by the gas-phase release of NO.

We conclude that the use of this denuder type (and the assumption of complete removal of gaseous NO_y) may potentially result in a positive bias in measurements of particle nitrate owing to the variable breakthrough and release of NO_x (dependent on the historical exposure of the denuder and relative humidity). Our findings may be applicable (at least in a qualitative sense) to similar denuders using activated carbon surfaces, and careful characterisation of the NO_y components' capacity to adsorb, breakthrough and release should be carried out prior to use in the field.

Reliable surface reactivation techniques for similar denuders would be useful to ensure continuous, efficient scrubbing of NO_y and NO_x and circumnavigate the potential overestimation of pNit. In this regard, attempts to "reactivate" the denuder by cleaning with distilled water, drying at 50 °C and exposure to ca. 300 ppbv O_3 for 1 h did not result in an improvement of the direct NO breakthrough or in the background pNit signal upon humidification. Surface-sensitive spectroscopic investigation of the water-induced transformation of organic and inorganic NO_y to NO_x (and its subsequent release to the gas phase) on denuder surfaces would be useful in resolving these issues.

3.4 Comparison of the TD-CRDS with existing methods for NO_x and NO_y and instruments

In this section, our instrument's performance is compared to other methods for NO_x and NO_y detection. We consider only instruments that measure NO_x and/or NO_y and not those that measure individual trace gases from each family.

NO_x has traditionally been measured by two-channel CLD instruments, which have one channel for NO and one channel for NO_2 respectively: NO is detected by chemiluminescence from its reaction with O_3, and NO_2 is converted to NO on a molybdenum converter or by photolysis at wavelengths close to 390 nm. Examples of this type of instrument as well as the reported levels of detection (LODs) and overall uncertainties are listed in Table 1. In Table 1, we also list the LOD and uncertainty of a recently developed CRDS set-up which is

Table 1. Comparison of NO_x and/or NO_y measurements.

Species	Reference	Method	2σ level of detection (integration time)	Uncertainty (%)
NO_x	Parrish et al. (2004)	CLD	20 pptv (1 s)	10
	Fuchs et al. (2009)	CRDS	22 pptv (1 s)	5
	Wild et al. (2014)	CRDS	< 30 pptv (1 s)	5
	Reed et al. (2016)	CLD lab CLD aircraft	2.5 pptv (60 s) ~ 1.0 pptv (60 s)	5 5
	This study	CRDS	40 pptv (60 s)	6
NO_y	Fischer et al. (1997)	CLD	200 pptv (6 s)	25
	Williams et al. (1998)	CLD "BNL" CLD "NOAA"	~ 50 pptv (1 s) 20 pptv (1 s)	10 18
	Day et al. (2002)	LIF	~ 10 pptv (10 s)	< 5
	Parrish et al. (2004)	CLD	36 pptv (1 s)	10
	Wild et al. (2014)	CRDS	< 30 pptv (1 s)	12
	Pätz et al. (2006)	CLD CLD	51 pptv (1 s) 100 pptv (1s)	13 9
	This study	CRDS	40 pptv (60 s)	15*

Note: * Refers to gas-phase NO_y only.

similar in principal of operation to the one described here (Fuchs et al., 2009).

NO_y has frequently been measured by CLD instruments with Au and/or MoO-coated thermal dissociation inlets that reduce NO_z to NO, which is detected as described above for CLD-NO_x instrument. Although such instruments have very low detection limits, they have been shown to be vulnerable to degradation of the NO_y conversion efficiency and suffer from interferences by HCN, CH_3CN and NH_3 (Kliner et al., 1997) as well as loss of NO_y in the inlet (Zenker et al., 1998; Parrish et al., 2004). Table 1 summarises the LODs and uncertainties reported by other NO_y instruments.

Table 1 indicates that the total uncertainty of the present instrument is comparable to those reported for both NO_x and NO_y. However, our present detection limit for both NO_x and NO_y is worse than that reported (for NO_2) for the same instrument in 2016 (Thieser et al., 2016), which is a result of mirror degradation since that study.

4 Application of the instrument in field experiments

4.1 NO_x intercomparison and pNit measurements during the AQABA campaign

The first deployment of the instrument was during the AQABA (Air Quality and climate change in the Arabian Basin) ship campaign in summer 2017. From 31 July to 2 September, the ship "*Kommander Iona*" followed a route from southern France via the Mediterranean Sea, the Suez Channel, the Red Sea, the Arabian Sea and the Arabian Gulf to Kuwait and back. The instrument was located in a container in front of the ship, with the inlet ovens located in an aluminium box on the roof of the container. The (unheated) tips of quartz inlet tubes protruded about 15 cm from the side of the aluminium box. Here, we compare the NO_x and pNit measurements with other measurements of these parameters made during the campaign.

During AQABA, NO_x levels ranged from a few parts per trillion by volume (maritime background) up to several tens of parts per billion by volume in heavily polluted air masses in shipping lanes or in harbours. In Fig. 10a, we compare NO_x measured with the TD-CRDS with the results of a chemiluminescence detector (CLD 790 SR, ECO PHYSICS; Tadic et al., 2020), which measured NO and NO_2. The data points represent 1 min averages for the entire campaign, excluding air masses that were contaminated by the ship's exhaust. Additionally, periods with very high NO_x variability were not included, with a data point being discarded whenever the differences in mean values exceeded 2 ppbv for consecutive data points.

A bivariate fit to the data sets (York, 1966), which incorporates total uncertainties for both instruments (CLD: 8.6 %; TD-CRDS: $11\,\% + 20\,\text{pptv} \times \text{RH}/100$) resulted in a slope of 0.996 ± 0.003 and an intercept of -1.3 pptv. This very good agreement serves to underline the general applicability of the

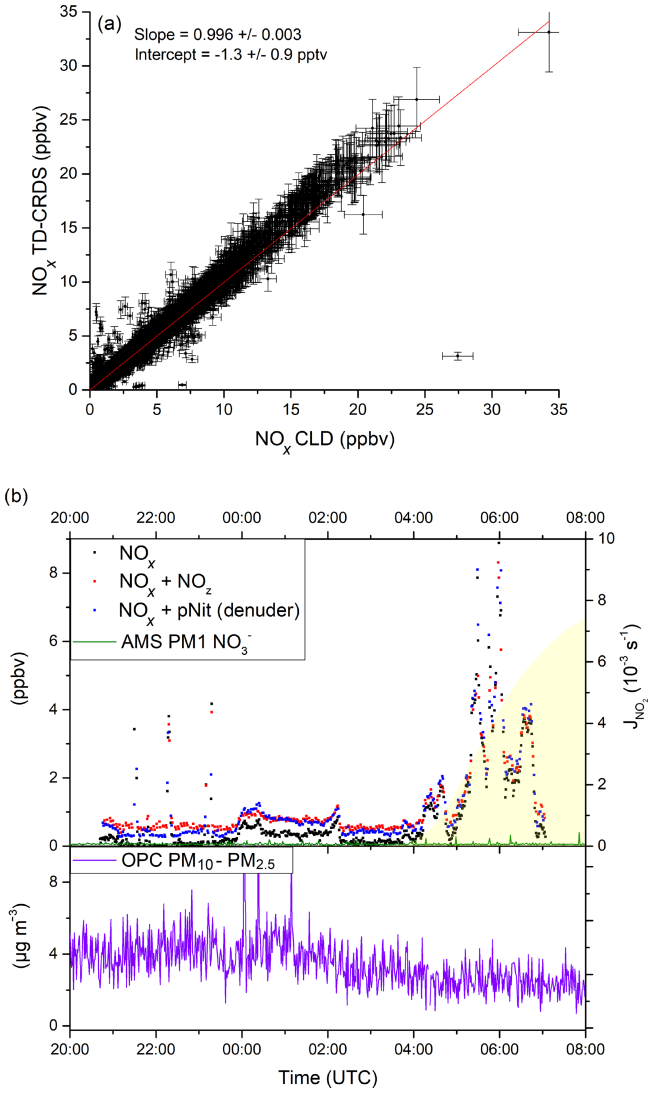

Figure 10. (a) Correlation between the TD-CRDS NO_x measurements (1 min averages) and an independent CLD NO_x instrument from the AQABA campaign. Data obtained during phases of very high NO_x variability have been excluded (see Sect. 4.1). See Fig. S6 for a histogram of the NO_x data points. **(b)** pNit measurements using the denuder channel (blue data points) during AQABA and comparison with particulate NO_3^- from an AMS (aerosol mass spectrometer). The discrepancy towards the AMS and the correlation with the NO_x mixing ratios indicate a positive bias in the pNit measurements, caused by humidity effects on the denuder surface. OPC (optical particle counter) measurements are added in the lower panel of **(b)** in order to assess the potential influence of coarse-mode aerosol nitrates.

TD-CRDS in NO_x measurements, even under difficult conditions (e.g. a non-static platform). In this context, we note that the deployment on a ship resulted in a degradation in performance (the LOD was ≈ 100 pptv) owing to the ship's motion, especially in heavy seas, which resulted in drifts in the instrument zero.

Figure 10b shows a ca. 10 h time frame with pNit measurements from the denuder channel of the TD-CRDS. Unfortunately, the TD oven of the denuder channel broke down very early in the campaign and was not operational afterwards. The data from the pNit channel are presented along with the NO_x and NO_y measurements as well as particulate nitrate mass concentrations measured by an aerosol mass spectrometer (Aerodyne HR-ToF-AMS; DeCarlo et al., 2006; Brooks et al., 2020). The night-to-day transition is indicated via the NO_2 photolysis rates J_{NO_2} derived from a spectral radiometer (Metcon GmbH). The relative humidity was $> 80\,\%$ throughout the period shown. During the two periods when, apart from some short spikes, NO_x was very low (21:10–23:45 and 02:20–03:40 UTC), TD-CRDS data indicate the presence of 300–400 pptv of pNit, which would then constitute $\sim 80\,\%$ NO_y. Such mixing ratios of particulate nitrate are not commensurate with those measured by the AMS, which, on average, are a factor of 6–8 lower. As the AMS does not detect particles larger than ~ 600 nm with high efficiency (Drewnick et al., 2005), the difference could potentially indicate that a significant fraction of the particulate nitrate is associated with coarse-mode aerosol. In the lower panel of Fig. 10b, we plot the coarse-mode aerosol mass concentration determined from measurements of an optical particle counter (OPC) that measures particles between 0.2 and 20 µm. In the two low-NO_x periods outlined above, the OPC-derived aerosol mass concentrations were between 3 and 5 µg m^{-3}. If 10 % of this coarse-mode aerosol mass concentration was nitrate, which is a typical value in the Mediterranean (Koulouri et al., 2008; Calzolai et al., 2015; Malaguti et al., 2015), this would account for 100–200 pptv of the pNit observed by the TD-CRDS and not by the AMS. However, the time profile of pNit measured by the TD-CRDS is not consistent with those of either the OPC or the AMS and rather resembles the NO_x mixing ratios. This strongly suggests that the large difference between pNit reported by the TD-CRDS and the AMS does not result from the non-detection or detection of supermicron particulate nitrate by the AMS but instead results from the denuder artefacts described in Sect. 3.3.2. This short case study serves to highlight the potential positive bias in denuder-based TD-CRDS measurements of pNit under humid field conditions.

4.2 Ambient NO_x and NO_y measurements in an urban environment (Mainz, Germany)

NO_x and NO_y mixing ratios were obtained in air sampled outside the Max Planck Institute for Chemistry (MPIC). The MPIC (49°59′27.5″ N 8°13′44.4″ E) is located on the outskirts of Mainz but within 200 m of two busy two- and four-lane roads and within 500 m of additional university buildings as well as commercial and residential areas. The city of Mainz (217 000 inhabitants) is located in the densely populated Rhine–Main area along with the cities of Frankfurt (753 000 inhabitants) and Wiesbaden (278 000 inhabitants);

the air in this region is strongly influenced by local pollution. The sampling location was on the top floor of a three-story building (ca. 12 m above ground level). Air was subsampled to the inlets of the instrument from a ∼ 1 m long 0.5 inch outer diameter PFA tube that was connected to a membrane pump and flow controller to generate a 20 slpm bypass flow. Aerosol transmission was probably < 100 % in these measurements.

Figure 11a summarises the 8 d of measurement (data coverage 82 %) as a time series for NO_x, NO_y, NO_z, (10 min averages) wind speed (1 h averages) and the NO_z/NO_y ratio. The NO_x and NO_y mixing ratios were highly variable throughout this period, with NO_x mixing ratios between 0.7 and 148.3 ppbv (mean and median values of 22.1 and 6.9 ppbv respectively). Traffic-related morning rush-hour peaks in NO_x were observed on all weekdays (14, 16, 17 and 20 January) between 05:00 and 10:00 UTC. The morning NO_x peak is reduced or absent on the weekends (18 and 19 January). NO_x levels stayed above 50 ppbv for nearly a full day from 18:00 UTC on 16 January until 18:00 UTC on 17 January, which coincides with constantly low wind speeds and the sampling of air masses that were predominantly local, and thus highly polluted. NO_z mixing ratios were usually between 0.5 and 2.5 ppbv (minimum < LOD, maximum 3.1 ppbv, mean 1.0 ppbv and median 0.9 ppbv), with NO_z/NO_y ratios below 0.5. These values indicate that the air masses had been impacted by recent (local) NO_x emissions.

The NO_z/NO_y ratio can be used as indicator of the degree of chemical processing of an air mass. In Fig. 11b, a median diel profile (including all measurement days) for the NO_z/NO_y ratio from the ambient measurement is shown. The diel profile displays two distinct minima in NO_z/NO_y during the morning and evening rush hours, where NO_z only makes up 5 %–10 % of the total NO_y. This fraction increases up to 15 % during midday and up to 25 % during night-time, when emissions of NO_x are reduced. The diel profiles of NO_z/NO_y are strongly influenced by fresh emissions of NO_x. As the measurement location is strongly influenced by traffic, there is a decrease in NO_x (and an increase in NO_z/NO_y) at night-time. Night-time increases in NO_z (13–14, 15–16, 18–19 and 19–20 January 2020) may also be partially caused by the formation of N_2O_5 as previously observed (Schuster et al., 2009) and which would have been favoured by the low night-time temperatures (< 10 °C) in winter.

These measurements serve to illustrate the applicability of our TD-CRDS over a wide range of NO_x and NO_y concentrations under realistic field conditions and in the investigation of processes that transform NO_x into its gas- and particle-phase reservoirs.

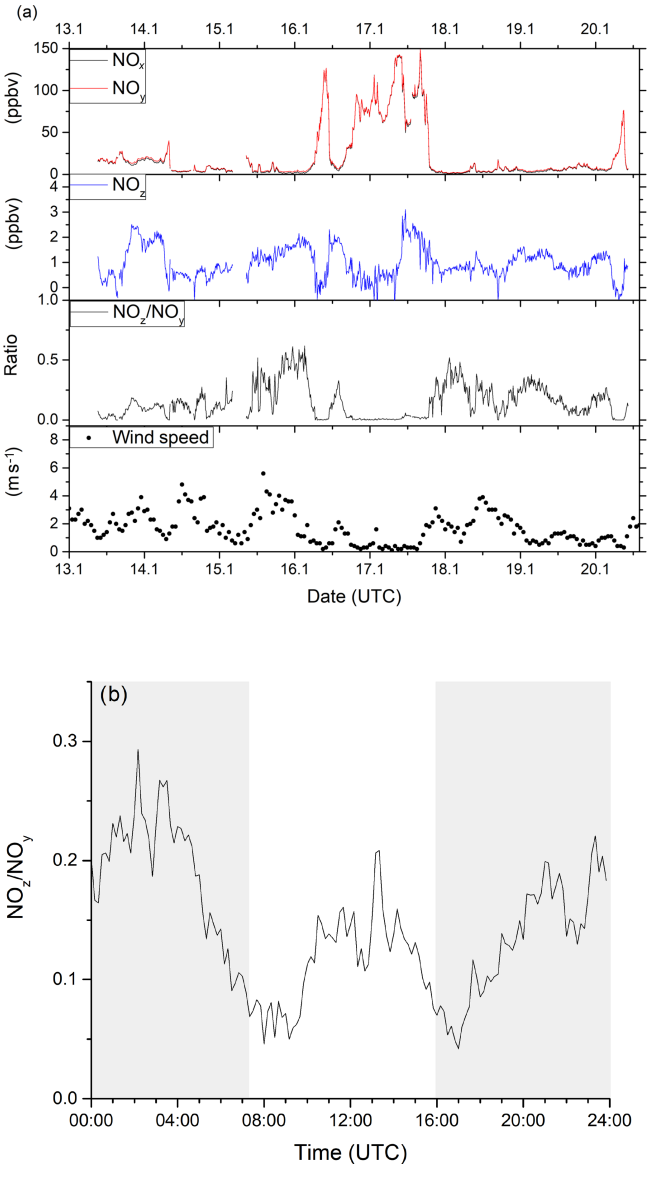

Figure 11. (a) Time series of NO_x, NO_y, NO_z, NO_z/NO_y and wind speed from ambient measurements in Mainz, Germany, in January 2020. Highly variable NO_x (between 0 and 150 ppbv) and moderate NO_z (between 0 and 3 ppbv) mixing ratios were observed, identifying the sampled air masses as being dominated by anthropogenic emissions. Wind speed data was obtained from Agrarmeteorologie Rheinland-Pfalz (http://www.wetter.rlp.de, last access: 20 October 2020). **(b)** Diel profile of the NO_z/NO_y ratio including all measurement days, showing distinct minima during the morning and evening rush hours. Shaded areas signify the time between sunset and sunrise.

5 Conclusions

We report on the development, characterisation and first deployment of a TD-CRDS instrument for the measurement of NO_x, NO_y, NO_z and pNit. Our laboratory experiments suggest that the different gas-phase NO_z species investigated

(PAN, iPN, N_2O_5, HONO, $ClNO_2$ and HNO_3) are converted with near-stoichiometric efficiency to NO_x at a nominal oven temperature of 850 °C. NH_4NO_3 particles of 200 nm in diameter are also detected quantitatively as NO_x, whereas the efficiency of detection of $NaNO_3$ particles of similar diameter was closer to 25 %. The efficiency of the detection of coarse-mode particles will be further reduced by their lower transmission through the denuder.

The potential for NH_3 to bias NO_y measurements was assessed and was found to be insignificant in ambient air or synthetic air containing VOCs and water. The conversion to NO_2 (by reaction with O_3) of atmospheric NO, as well as NO formed in the heated inlet, circumvents bias resulting from O_3 thermolysis (leading to an NO_2 overestimation) and secondary processes, which are initiated by the thermal dissociation of organic nitrates.

For our activated carbon denuder, we observed > 90 % transmission for ammonium nitrate particles with diameters between 40 and 400 nm. Under humid conditions, the denuder suffered from the direct breakthrough of NO and the re-release of previously stored iPN and NO_2 in the form of NO, indicating a potential bias of pNit measurements using this technique and potentially limiting its deployment to low-NO_x and low-NO_z environments. When using comparable denuders, we recommend regular checks with humidified zero air to characterise potential breakthrough. Our experiments demonstrated that the release of NO_x from the denuder exposed to humid zero air for several hours can decrease to values below 1 ppbv, which, in a first approximation, could be treated as an offset. Cycling between multiple denuders would help to reduce the size of any bias.

The performance of the instrument under field conditions was demonstrated by measurements in Mainz, Germany, and during the AQABA ship campaign. NO_x measurements with the new instrument were in good agreement with those from an established, independent CLD-based instrument.

Data availability. The NO_x data set from the AQABA campaign is available at https://doi.org/10.5281/zenodo.4134659 (Friedrich, 2020). Data used to generate the figures in this paper can be obtained upon request from the corresponding author.

Supplement. The supplement related to this article is available online at: https://doi.org/10.5194/amt-13-5739-2020-supplement.

Author contributions. NF developed the TD-CRDS, performed all laboratory and campaign measurements, evaluated the data sets and wrote the paper. IT and HF provided the AQABA CLD NO_x measurements. JS designed the heated inlet system and performed actinic flux measurements during AQABA. JB, ED and FD provided AMS and OPC measurements from AQABA. JL and JNC designed and supervised the study and the campaigns. JNC, JL and FD contributed to the paper.

Competing interests. The authors declare that they have no conflict of interest.

Acknowledgements. We thank Ezra Wood for providing us with the activated carbon denuder and Chemours for the provision of the FEP sample (FEPD 121) used to coat the cavity walls. This work was supported by the Max Planck Graduate Center with the Johannes Gutenberg-Universität Mainz (MPGC).

Financial support. The article processing charges for this open-access publication were covered by the Max Planck Society.

Review statement. This paper was edited by Dwayne Heard and reviewed by three anonymous referees.

References

Atsuko, N., Kazuya, S., Toshiaki, E., Kei-ichi, K., Morinobu, E., and Norifumi, S.: Electronic and Magnetic Properties of Activated Carbon Fibers, Bull. Chem. Soc. Jpn., 69, 333–339, https://doi.org/10.1246/bcsj.69.333, 1996.

Barker, J. R., Benson, S. W., Mendenhall, G. D., and Goldern, D. M.: Measurements of rate constants of importance in smog, Rep. PB-274530, Natl. Tech. Inf. Serv., Springfield, Va., USA, 1977.

Barton, S. S. and Koresh, J. E.: Adsorption Interaction of Water with Microporous Adsorbents 1. Water-Vapor Adsorption on Activated Carbon Cloth, J. Chem. Soc. Faraday Trans. I, 79, 1147–1155, https://doi.org/10.1039/f19837901147, 1983.

Baulch, D. L., Duxbury, J., Grant, S. J., and Montague, D. C.: Evaluated kinetic data for high temperature reactions. Volume 4 Homogeneous gas phase reactions of halogen- and cyanide-containing species, J. Phys. Chem. Ref. Data, 10, 1–721, 1981.

Bertram, A. K., Ivanov, A. V., Hunter, M., Molina, L. T., and Molina, M. J.: The reaction probability of OH on organic surfaces of tropospheric interest, J. Phys. Chem. A, 105, 9415–9421, 2001.

Bridier, I., Caralp, F., Loirat, H., Lesclaux, R., Veyret, B., Becker, K. H., Reimer, A., and Zabel, F.: Kinetic and Theoretical-studies of the Reactions $CH_3C(O)O_2 + NO_2 + M \leftrightarrow CH_3C(O)NO_2 + M$ between 248 K and 393 K and Between 30-torr and 760-torr, J. Phys. Chem., 95, 3594–3600, 1991.

Brooks, J., Darbyshire, E., Drewnick, F., Alfarra, R., Struckmeier, C., Fachinger, F., Borrmann, S., Allen, G., and Coe, H.: Characterisation of accumulation mode aerosol across the Middle East and Mediterranean during a ship campaign in the summer of 2017, in preperation, 2020.

Brunauer, S., Emmett, P. H., and Teller, E.: Adsorption of gases in multimolecular layers, J. Am. Chem. Soc., 60, 309–319, 1938.

Calzolai, G., Nava, S., Lucarelli, F., Chiari, M., Giannoni, M., Becagli, S., Traversi, R., Marconi, M., Frosini, D., Severi, M., Udisti, R., di Sarra, A., Pace, G., Meloni, D., Bommarito, C., Monteleone, F., Anello, F., and Sferlazzo, D. M.: Characterization of PM_{10} sources in the central Mediterranean, Atmos. Chem. Phys., 15, 13939–13955, https://doi.org/10.5194/acp-15-13939-2015, 2015.

Cohen, N. and Westberg, K. R.: Chemical Kinetic Data Sheets for High-Temperature Reactions .2., J. Phys. Chem. Ref. Data, 20, 1211–1311, https://doi.org/10.1063/1.555901, 1991.

Davidson, J. A., Viggiano, A. A., Howard, C. J., Dotan, I., Fehsenfeld, F. C., Albritton, D. L., and Ferguson, E. E.: Rate Constants for Reactions of O_2^+, NO_2^+, NO^+, H_3O^+, CO_3^-, NO_2^-, and Halide Ions with N_2O_5 at 300 K, J. Chem. Phys., 68, 2085–2087, 1978.

Day, D. A., Wooldridge, P. J., Dillon, M. B., Thornton, J. A., and Cohen, R. C.: A thermal dissociation laser-induced fluorescence instrument for in situ detection of NO_2, peroxy nitrates, alkyl nitrates, and HNO_3, J. Geophys. Res.-Atmos., 107, 4046, https://doi.org/10.1029/2001jd000779, 2002.

Day, D. A., Dillon, M. B., Wooldridge, P. J., Thornton, J. A., Rosen, R. S., Wood, E. C., and Cohen, R. C.: On alkyl nitrates, O_3, and the "missing NO_y", J. Geophys. Res.-Atmos., 108, 4501, https://doi.org/10.1029/2003jd003685, 2003.

DeCarlo, P. F., Kimmel, J. R., Trimborn, A., Northway, M. J., Jayne, J. T., Aiken, A. C., Gonin, M., Fuhrer, K., Horvath, T., Docherty, K. S., Worsnop, D. R., and Jimenez, J. L.: Field-deployable, high-resolution, time-of-flight aerosol mass spectrometer, Anal. Chem., 78, 8281–8289, https://doi.org/10.1021/ac061249n, 2006.

Di Carlo, P., Aruffo, E., Busilacchio, M., Giammaria, F., Dari-Salisburgo, C., Biancofiore, F., Visconti, G., Lee, J., Moller, S., Reeves, C. E., Bauguitte, S., Forster, G., Jones, R. L., and Ouyang, B.: Aircraft based four-channel thermal dissociation laser induced fluorescence instrument for simultaneous measurements of NO_2, total peroxy nitrate, total alkyl nitrate, and HNO_3, Atmos. Meas. Tech., 6, 971–980, https://doi.org/10.5194/amt-6-971-2013, 2013.

Drewnick, F., Hings, S. S., DeCarlo, P., Jayne, J. T., Gonin, M., Fuhrer, K., Weimer, S., Jimenez, J. L., Demerjian, K. L., Borrmann, S., and Worsnop, D. R.: A new time-of-flight aerosol mass spectrometer (TOF-AMS) – Instrument description and first field deployment, Aerosol Sci. Tech., 39, 637–658, https://doi.org/10.1080/02786820500182040, 2005.

Dubinin, M. M., Andreeva, G. A., Vartapetyan, R. S., Vnukov, S. P., Nikolaev, K. M., Polyakov, N. S., Seregina, N. I., and Fedoseev, D. V.: Adsorption of Water and the Micropore Structures of Carbon Adsorbents .5. Pore Structure Parameters of Thermally Treated Carbon Adsorbents and the Adsorption of Water-Vapor on These Materials, B. Acad. Sci. Ussr. Ch.+, 31, 2133–2137, https://doi.org/10.1007/Bf00958379, 1982.

Dulitz, K., Amedro, D., Dillon, T. J., Pozzer, A., and Crowley, J. N.: Temperature-(208–318 K) and pressure-(18–696 Torr) dependent rate coefficients for the reaction between OH and HNO_3, Atmos. Chem. Phys., 18, 2381–2394, https://doi.org/10.5194/acp-18-2381-2018, 2018.

Fahey, D. W., Eubank, C. S., Hubler, G., and Fehsenfeld, F. C.: Evaluation of a Catalytic Reduction Technique for the Measurement of Total Reactive Odd-Nitrogen Noy in the Atmosphere, J. Atmos. Chem., 3, 435–468, https://doi.org/10.1007/Bf00053871, 1985.

Finlayson-Pitts, B. J., Ezell, M. J., and Pitts, J. N. J.: Formation of chemically active chlorine compounds by reactions of atmospheric NaCl particles with gaseous N_2O_5 and $ClONO_2$, Nature, 337, 241–244, 1989.

Fischer, H., Waibel, A. E., Welling, M., Wienhold, F. G., Zenker, T., Crutzen, P. J., Arnold, F., Burger, V., Schneider, J., Bregman, A., Lelieveld, J., and Siegmund, P. C.: Observations of high concentrations of total reactive nitrogen (NO_y) and nitric acid (HNO_3) in the lower Arctic stratosphere during the stratosphere-troposphere experiment by aircraft measurements (STREAM) II campaign in February 1995, J. Geophys. Res.-Atmos., 102, 23559–23571, https://doi.org/10.1029/97jd02012, 1997.

Friedrich, N.: Measurement of NO_x and NO_y with a thermal dissociation cavity ring-down spectrometer (TD-CRDS): Instrument characterisation and first deployment [Data set], Zenodo, https://doi.org/10.5281/zenodo.4134659, 2020.

Fry, J. L., Draper, D. C., Zarzana, K. J., Campuzano-Jost, P., Day, D. A., Jimenez, J. L., Brown, S. S., Cohen, R. C., Kaser, L., Hansel, A., Cappellin, L., Karl, T., Hodzic Roux, A., Turnipseed, A., Cantrell, C., Lefer, B. L., and Grossberg, N.: Observations of gas- and aerosol-phase organic nitrates at BEACHON-RoMBAS 2011, Atmos. Chem. Phys., 13, 8585–8605, https://doi.org/10.5194/acp-13-8585-2013, 2013.

Fuchs, H., Dube, W. P., Lerner, B. M., Wagner, N. L., Williams, E. J., and Brown, S. S.: A Sensitive and Versatile Detector for Atmospheric NO_2 and NO_x Based on Blue Diode Laser Cavity Ring-Down Spectroscopy, Environ. Sci. Technol., 43, 7831–7836, https://doi.org/10.1021/es902067h, 2009.

Fuchs, H., Ball, S. M., Bohn, B., Brauers, T., Cohen, R. C., Dorn, H.-P., Dubé, W. P., Fry, J. L., Häseler, R., Heitmann, U., Jones, R. L., Kleffmann, J., Mentel, T. F., Müsgen, P., Rohrer, F., Rollins, A. W., Ruth, A. A., Kiendler-Scharr, A., Schlosser, E., Shillings, A. J. L., Tillmann, R., Varma, R. M., Venables, D. S., Villena Tapia, G., Wahner, A., Wegener, R., Wooldridge, P. J., and Brown, S. S.: Intercomparison of measurements of NO_2 concentrations in the atmosphere simulation chamber SAPHIR during the NO3Comp campaign, Atmos. Meas. Tech., 3, 21–37, https://doi.org/10.5194/amt-3-21-2010, 2010.

Gaffney, J. S., Fajer, R., and Senum, G. I.: An Improved Procedure for High-Purity Gaseous Peroxyacyl Nitrate Production – Use of Heavy Lipid Solvents, Atmos. Environ., 18, 215–218, https://doi.org/10.1016/0004-6981(84)90245-2, 1984.

Gao, X. A., Liu, S. J., Zhang, Y., Luo, Z. Y., Ni, M. J., and Cen, K. F.: Adsorption and reduction of NO_2 over activated carbon at low temperature, Fuel Process. Technol., 92, 139–146, https://doi.org/10.1016/j.fuproc.2010.09.017, 2011.

Garner, N. M., Matchett, L. C., and Osthoff, H. D.: Quantification of Non-refractory Aerosol Nitrate in Ambient Air by Thermal Dissociation Cavity Ring-Down Spectroscopy, Environ. Sci. Technol., 54, 9864–9861, https://doi.org/10.1021/acs.est.0c01156, 2020.

Glänzer, K. and Troe, J.: Thermal Decomposition of Nitrocompounds in Shock Waves. IV: Decomposition of Nitric Acid, Berichte der Bunsengesellschaft für physikalische Chemie, 78, 71–76, https://doi.org/10.1002/bbpc.19740780112, 1974.

Hosaynali Beygi, Z., Fischer, H., Harder, H. D., Martinez, M., Sander, R., Williams, J., Brookes, D. M., Monks, P. S., and Lelieveld, J.: Oxidation photochemistry in the Southern Atlantic boundary layer: unexpected deviations of photochemical steady state, Atmos. Chem. Phys., 11, 8497–8513, https://doi.org/10.5194/acp-11-8497-2011, 2011.

Huang, W., Saathoff, H., Shen, X. L., Ramisetty, R., Leisner, T., and Mohr, C.: Chemical Characterization of Highly Functionalized Organonitrates Contributing to Night-Time Organic Aerosol Mass Loadings and Particle Growth, Environ. Sci. Technol., 53, 1165–1174, https://doi.org/10.1021/acs.est.8b05826, 2019.

Ammann, M., Cox, R. A., Crowley, J. N., Herrmann, H., Jenkin, M. E., McNeill, V. F., Mellouki, A., Rossi, M. J., Troe, J., and Wallington, T. J.: Evaluated Kinetic and Photochemical Data for Atmospheric Chemistry, Task Group on Atmospheric Chemical Kinetic Data Evaluation, IUPAC, available at: http://iupac.pole-ether.fr/index.html (last access: 28 October 2020), 2019.

Ivanov, A. V., Trakhtenberg, S., Bertram, A. K., Gershenzon, Y. M., and Molina, M. J.: OH, HO_2, and ozone gaseous diffusion coefficients, J. Phys. Chem. A, 111, 1632–1637, 2007.

Javed, U., Kubistin, D., Martinez, M., Pollmann, J., Rudolf, M., Parchatka, U., Reiffs, A., Thieser, J., Schuster, G., Horbanski, M., Pöhler, D., Crowley, J. N., Fischer, H., Lelieveld, J., and Harder, H.: Laser-induced fluorescence-based detection of atmospheric nitrogen dioxide and comparison of different techniques during the PARADE 2011 field campaign, Atmos. Meas. Tech., 12, 1461–1481, https://doi.org/10.5194/amt-12-1461-2019, 2019.

Kalberer, M., Ammann, M., Arens, F., Gaggeler, H. W., and Baltensperger, U.: Heterogeneous formation of nitrous acid (HONO) on soot aerosol particles, J. Geophys. Res.-Atmos., 104, 13825–13832, 1999.

Kim, P., Zheng, Y. J., and Agnihotri, S.: Adsorption equilibrium and kinetics of water vapor in carbon nanotubes and its comparison with activated carbon, Ind. Eng. Chem. Res., 47, 3170–3178, https://doi.org/10.1021/ie0713240, 2008.

Kleffmann, J., Becker, K. H., Lackhoff, M., and Wiesen, P.: Heterogeneous conversion of NO_2 on carbonaceous surfaces, Phys. Chem. Chem. Phys., 1, 5443–5450, https://doi.org/10.1039/a905545b, 1999.

Kliner, D. A. V., Daube, B. C., Burley, J. D., and Wofsy, S. C.: Laboratory investigation of the catalytic reduction technique for measurement of atmospheric NO_y, J. Geophys. Res.-Atmos., 102, 10759–10776, https://doi.org/10.1029/96jd03816, 1997.

Koulouri, E., Saarikoski, S., Theodosi, C., Markaki, Z., Gerasopoulos, E., Kouvarakis, G., Makela, T., Hillamo, R., and Mihalopoulos, N.: Chemical composition and sources of fine and coarse aerosol particles in the Eastern Mediterranean, Atmos. Environ., 42, 6542–6550, https://doi.org/10.1016/j.atmosenv.2008.04.010, 2008.

Lammel, G. and Perner, D.: The Atmospheric Aerosol as a Source of Nitrous-Acid in the Polluted Atmosphere, J. Aerosol Sci., 19, 1199–1202, https://doi.org/10.1016/0021-8502(88)90135-8, 1988.

Langford, A. O., Fehsenfeld, F. C., Zachariassen, J., and Schimel, D. S.: Gaseous Ammonia Fluxes and Background Concentrations in Terrestrial Ecosystems of the United States, Global Biogeochem. Cy., 6, 459–483, https://doi.org/10.1029/92gb02123, 1992.

Lee, B. H., Mohr, C., Lopez-Hilfiker, F. D., Lutz, A., Hallquist, M., Lee, L., Romer, P., Cohen, R. C., Iyer, S., Kurten, T., Hu, W. W., Day, D. A., Campuzano-Jost, P., Jimenez, J. L., Xu, L., Ng, N. L., Guo, H. Y., Weber, R. J., Wild, R. J., Brown, S. S., Koss, A., de Gouw, J., Olson, K., Goldstein, A. H., Seco, R., Kim, S., McAvey, K., Shepson, P. B., Starn, T., Baumann, K., Edgerton, E. S., Liu, J. M., Shilling, J. E., Miller, D. O., Brune, W., Schobesberger, S., D'Ambro, E. L., and Thornton, J. A.: Highly functionalized organic nitrates in the southeast United States: Contribution to secondary organic aerosol and reactive nitrogen budgets, P. Natl. Acad. Sci. USA, 113, 1516–1521, https://doi.org/10.1073/pnas.1508108113, 2016.

Leser, H., Honninger, G., and Platt, U.: MAX-DOAS measurements of BrO and NO_2 in the marine boundary layer, Geophys. Res. Lett., 30, 1537, https://doi.org/10.1029/2002GL015811, 2003.

Lightfoot, P. D., Cox, R. A., Crowley, J. N., Destriau, M., Hayman, G. D., Jenkin, M. E., Moortgat, G. K., and Zabel, F.: Organic peroxy radicals – kinetics, spectroscopy and tropospheric chemistry, Atmos. Environ., A-Gen., 26, 1805–1961, 1992.

Liu, L. M., Tan, S. L., Horikawa, T., Do, D. D., Nicholson, D., and Liu, J. J.: Water adsorption on carbon – A review, Adv. Colloid Interf. Sci., 250, 64–78, https://doi.org/10.1016/j.cis.2017.10.002, 2017.

Logan, J. A.: Nitrogen-Oxides in the Troposphere – Global and Regional Budgets, J. Geophys. Res.-Oceans, 88, 78-5-807, https://doi.org/10.1029/JC088iC15p10785, 1983.

Malaguti, A., Mircea, M., La Torretta, T. M. G., Telloli, C., Petralia, E., Stracquadanio, M., and Berico, M.: Chemical Composition of Fine and Coarse Aerosol Particles in the Central Mediterranean Area during Dust and Non-Dust Conditions, Aerosol Air Qual. Res., 15, 410–425, https://doi.org/10.4209/aaqr.2014.08.0172, 2015.

Merten, A., Tschritter, J., and Platt, U.: Design of differential optical absorption spectroscopy long-path telescopes based on fiber optics, Appl. Optics, 50, 738–754, 2011.

Meusel, H., Tamm, A., Kuhn, U., Wu, D., Leifke, A. L., Fiedler, S., Ruckteschler, N., Yordanova, P., Lang-Yona, N., Pöhlker, M., Lelieveld, J., Hoffmann, T., Pöschl, U., Su, H., Weber, B., and Cheng, Y.: Emission of nitrous acid from soil and biological soil crusts represents an important source of HONO in the remote atmosphere in Cyprus, Atmos. Chem. Phys., 18, 799–813, https://doi.org/10.5194/acp-18-799-2018, 2018.

Murphy, J. G., Day, D. A., Cleary, P. A., Wooldridge, P. J., and Cohen, R. C.: Observations of the diurnal and seasonal trends in nitrogen oxides in the western Sierra Nevada, Atmos. Chem. Phys., 6, 5321–5338, https://doi.org/10.5194/acp-6-5321-2006, 2006.

Neuman, J. A., Huey, L. G., Ryerson, T. B., and Fahey, D. W.: Study of inlet materials for sampling atmospheric nitric acid, Environ. Sci. Technol., 33, 1133–1136, 1999.

Ng, N. L., Brown, S. S., Archibald, A. T., Atlas, E., Cohen, R. C., Crowley, J. N., Day, D. A., Donahue, N. M., Fry, J. L., Fuchs, H., Griffin, R. J., Guzman, M. I., Herrmann, H., Hodzic, A., Iinuma, Y., Jimenez, J. L., Kiendler-Scharr, A., Lee, B. H., Luecken, D. J., Mao, J., McLaren, R., Mutzel, A., Osthoff, H. D., Ouyang, B., Picquet-Varrault, B., Platt, U., Pye, H. O. T., Rudich, Y., Schwantes, R. H., Shiraiwa, M., Stutz, J., Thornton, J. A., Tilgner, A., Williams, B. J., and Zaveri, R. A.: Nitrate radicals and biogenic volatile organic compounds: oxidation, mechanisms, and organic aerosol, Atmos. Chem. Phys., 17, 2103–2162, https://doi.org/10.5194/acp-17-2103-2017, 2017.

Notholt, J., Hjorth, J., and Raes, F.: Formation of HNO_2 on Aerosol Surfaces During Foggy Periods in the Presence of NO and NO_2, Atmos. Environ. A-Gen., 26, 211–217, 1992.

Oswald, R., Behrendt, T., Ermel, M., Wu, D., Su, H., Cheng, Y., Breuninger, C., Moravek, A., Mougin, E., Delon, C., Loubet, B., Pommerening-Roser, A., Sorgel, M., Poschl, U.,

Hoffmann, T., Andreae, M. O., Meixner, F. X., and Trebs, I.: HONO Emissions from Soil Bacteria as a Major Source of Atmospheric Reactive Nitrogen, Science, 341, 1233–1235, https://doi.org/10.1126/science.1242266, 2013.

Palm, B. B., Campuzano-Jost, P., Day, D. A., Ortega, A. M., Fry, J. L., Brown, S. S., Zarzana, K. J., Dube, W., Wagner, N. L., Draper, D. C., Kaser, L., Jud, W., Karl, T., Hansel, A., Gutiérrez-Montes, C., and Jimenez, J. L.: Secondary organic aerosol formation from in situ OH, O_3, and NO_3 oxidation of ambient forest air in an oxidation flow reactor, Atmos. Chem. Phys., 17, 5331–5354, https://doi.org/10.5194/acp-17-5331-2017, 2017.

Parrish, D. D., Ryerson, T. B., Holloway, J. S., Neuman, J. A., Roberts, J. M., Williams, J., Stroud, C. A., Frost, G. J., Trainer, M., Hubler, G., Fehsenfeld, F. C., Flocke, F., and Weinheimer, A. J.: Fraction and composition of NO_y transported in air masses lofted from the North American continental boundary layer, J. Geophys. Res.-Atmos., 109, D09302, doi10.1029/2003jd004226, 2004.

Pätz, H.-W., Volz-Thomas, A., Hegglin, M. I., Brunner, D., Fischer, H., and Schmidt, U.: In-situ comparison of the NO_y instruments flown in MOZAIC and SPURT, Atmos. Chem. Phys., 6, 2401–2410, https://doi.org/10.5194/acp-6-2401-2006, 2006.

Paul, D. and Osthoff, H. D.: Absolute Measurements of Total Peroxy Nitrate Mixing Ratios by Thermal Dissociation Blue Diode Laser Cavity Ring-Down Spectroscopy, Anal. Chem., 82, 6695–6703, https://doi.org/10.1021/ac101441z, 2010.

Paul, D., Furgeson, A., and Osthoff, H. D.: Measurements of total peroxy and alkyl nitrate abundances in laboratory-generated gas samples by thermal dissociation cavity ring-down spectroscopy, Rev. Sci. Instrum., 80, 114101, https://doi.org/10.1063/1.3258204 2009.

Perez, I. M., Wooldridge, P. J., and Cohen, R. C.: Laboratory evaluation of a novel thermal dissociation chemiluminescence method for in situ detection of nitrous acid, Atmos. Environ., 41, 3993–4001, https://doi.org/10.1016/j.atmosenv.2007.01.060, 2007.

Perring, A. E., Pusede, S. E., and Cohen, R. C.: An observational perspective on the atmospheric impacts of alkyl and multifunctional nitrates on ozone and secondary organic aerosol, Chem. Rev., 113, 5848–5870, https://doi.org/10.1021/cr300520x, 2013.

Peukert, S. L., Sivaramakrishnan, R., and Michael, J. V.: High temperature shock tube studies on the thermal decomposition of O_3 and the reaction of dimethyl carbonate with O-Atoms, J. Phys. Chem. A, 117, 3729–3738, https://doi.org/10.1021/jp400613p, 2013.

Pilegaard, K.: Processes regulating nitric oxide emissions from soils, Philos. T. Roy. Soc. B, 368, 20130126, https://doi.org/10.1098/rstb.2013.0126, 2013.

Platt, U., Perner, D., and Patz, H. W.: Simultaneous Measurement of Atmospheric CH_2O, O_3, and NO_2 by Differential Optical-Absorption, J. Geophys. Res.-Oceans, 84, 6329–6335, https://doi.org/10.1029/JC084iC10p06329, 1979.

Pohler, D., Vogel, L., Friess, U., and Platt, U.: Observation of halogen species in the Amundsen Gulf, Arctic, by active long-path differential optical absorption spectroscopy, P. Natl. Acad. Sci. USA, 107, 6582–6587, https://doi.org/10.1073/pnas.0912231107, 2010.

Reed, C., Evans, M. J., Di Carlo, P., Lee, J. D., and Carpenter, L. J.: Interferences in photolytic NO_2 measurements: explanation for an apparent missing oxidant?, Atmos. Chem. Phys., 16, 4707–4724, https://doi.org/10.5194/acp-16-4707-2016, 2016.

Roberts, J. M.: The atmospheric chemistry of organic nitrates, Atmos. Environ. A-Gen., 24, 243–287, https://doi.org/10.1016/0960-1686(90)90108-y, 1990.

Rollins, A. W., Browne, E. C., Min, K.-E., Pusede, S. E., Wooldridge, P. J., Gentner, D. R., Goldstein, A. H., Liu, S., Day, D. A., Russell, L. M., and Cohen, R. C.: Evidence for NO_x Control over Nighttime SOA Formation, Science, 337, 1210–1212, 2012.

Romer, P. S., Duffey, K. C., Wooldridge, P. J., Allen, H. M., Ayres, B. R., Brown, S. S., Brune, W. H., Crounse, J. D., de Gouw, J., Draper, D. C., Feiner, P. A., Fry, J. L., Goldstein, A. H., Koss, A., Misztal, P. K., Nguyen, T. B., Olson, K., Teng, A. P., Wennberg, P. O., Wild, R. J., Zhang, L., and Cohen, R. C.: The lifetime of nitrogen oxides in an isoprene-dominated forest, Atmos. Chem. Phys., 16, 7623–7637, https://doi.org/10.5194/acp-16-7623-2016, 2016.

Romer Present, P. S., Zare, A., and Cohen, R. C.: The changing role of organic nitrates in the removal and transport of NO_x, Atmos. Chem. Phys., 20, 267–279, https://doi.org/10.5194/acp-20-267-2020, 2020.

Rosen, R. S., Wood, E. C., Wooldridge, P. J., Thornton, J. A., Day, D. A., Kuster, W., Williams, E. J., Jobson, B. T., and Cohen, R. C.: Observations of total alkyl nitrates during Texas Air Quality Study 2000: Implications for O_3 and alkyl nitrate photochemistry, J. Geophys. Res.-Atmos., 109, D07303, https://doi.org/10.1029/2003jd004227, 2004.

Sadanaga, Y., Takaji, R., Ishiyama, A., Nakajima, K., Matsuki, A., and Bandow, H.: Thermal dissociation cavity attenuated phase shift spectroscopy for continuous measurement of total peroxy and organic nitrates in the clean atmosphere, Rev. Sci. Instrum., 87, 074102, https://doi.org/10.1063/1.4958167, 2016.

Schlesinger, W. H. and Hartley, A. E.: A Global Budget for Atmospheric NH_3, Biogeochemistry, 15, 191–211, 1992.

Schuster, G., Labazan, I., and Crowley, J. N.: A cavity ring down/cavity enhanced absorption device for measurement of ambient NO_3 and N_2O_5, Atmos. Meas. Tech., 2, 1–13, https://doi.org/10.5194/amt-2-1-2009, 2009.

Shirahama, N., Moon, S. H., Choi, K. H., Enjoji, T., Kawano, S., Korai, Y., Tanoura, M., and Mochida, I.: Mechanistic study on adsorption and reduction of NO_2 over activated carbon fibers, Carbon, 40, 2605–2611, https://doi.org/10.1016/S0008-6223(02)00190-2, 2002.

Slusher, D. L., Huey, L. G., Tanner, D. J., Chen, G., Davis, D. D., Buhr, M., Nowak, J. B., Eisele, F. L., Kosciuch, E., Mauldin, R. L., Lefer, B. L., Shetter, R. E., and Dibb, J. E.: Measurements of pernitric acid at the South Pole during ISCAT 2000, Geophys. Res. Lett., 29, 2011, https://doi.org/10.1029/2002gl015703, 2002.

Sobanski, N., Schuladen, J., Schuster, G., Lelieveld, J., and Crowley, J. N.: A five-channel cavity ring-down spectrometer for the detection of NO_2, NO_3, N_2O_5, total peroxy nitrates and total alkyl nitrates, Atmos. Meas. Tech., 9, 5103–5118, https://doi.org/10.5194/amt-9-5103-2016, 2016.

Sobanski, N., Thieser, J., Schuladen, J., Sauvage, C., Song, W., Williams, J., Lelieveld, J., and Crowley, J. N.: Day and nighttime formation of organic nitrates at a forested mountain site

in south-west Germany, Atmos. Chem. Phys., 17, 4115–4130, https://doi.org/10.5194/acp-17-4115-2017, 2017.

Su, H., Cheng, Y. F., Oswald, R., Behrendt, T., Trebs, I., Meixner, F. X., Andreae, M. O., Cheng, P., Zhang, Y., and Poschl, U.: Soil Nitrite as a Source of Atmospheric HONO and OH Radicals, Science, 333, 1616–1618, https://doi.org/10.1126/science.1207687, 2011.

Tadic, I., Crowley, J. N., Dienhart, D., Eger, P., Harder, H., Hottmann, B., Martinez, M., Parchatka, U., Paris, J.-D., Pozzer, A., Rohloff, R., Schuladen, J., Shenolikar, J., Tauer, S., Lelieveld, J., and Fischer, H.: Net ozone production and its relationship to nitrogen oxides and volatile organic compounds in the marine boundary layer around the Arabian Peninsula, Atmos. Chem. Phys., 20, 6769–6787, https://doi.org/10.5194/acp-20-6769-2020, 2020.

Talukdar, R. K., Burkholder, J. B., Schmoltner, A. M., Roberts, J. M., Wilson, R. R., and Ravishankara, A. R.: Investigation of the loss processes for peroxyacetyl nitrate in the atmosphere: UV photolysis and reaction with OH, J. Geophys. Res.-Atmos., 100, 14163–14173, https://doi.org/10.1029/95jd00545, 1995.

Talukdar, R. K., Herndon, S. C., Burkholder, J. B., Roberts, J. M., and Ravishankara, A. R.: Atmospheric fate of several alkyl nitrates .1. Rate coefficients of the reactions alkyl nitrates with isotopically labelled hydroxyl radicals, J. Chem. Soc. Faraday T., 93, 2787–2796, 1997.

Tang, M. J., Cox, R. A., and Kalberer, M.: Compilation and evaluation of gas phase diffusion coefficients of reactive trace gases in the atmosphere: volume 1. Inorganic compounds, Atmos. Chem. Phys., 14, 9233–9247, https://doi.org/10.5194/acp-14-9233-2014, 2014.

Thaler, R. D., Mielke, L. H., and Osthoff, H. D.: Quantification of nitryl chloride at part per trillion mixing ratios by thermal dissociation cavity ring-down spectroscopy, Anal. Chem., 83, 2761–2766, https://doi.org/10.1021/ac200055z, 2011.

Thieser, J., Schuster, G., Schuladen, J., Phillips, G. J., Reiffs, A., Parchatka, U., Pöhler, D., Lelieveld, J., and Crowley, J. N.: A two-channel thermal dissociation cavity ring-down spectrometer for the detection of ambient NO_2, RO_2NO_2 and $RONO_2$, Atmos. Meas. Tech., 9, 553–576, https://doi.org/10.5194/amt-9-553-2016, 2016.

Tingey, D. T., Manning, M., Grothaus, L. C., and Burns, W. F.: Influence of Light and Temperature on Isoprene Emission Rates from Live Oak, Physiol. Plant., 47, 112–118, https://doi.org/10.1111/j.1399-3054.1979.tb03200.x, 1979.

Tsang, W. and Herron, J. T.: Chemical kinetic data base for propellant combustion. I. Reactions involving NO, NO_2, HNO, HNO_2, HCN and N_2O, J. Phys. Chem. Ref. Data, 20, 609–663, 1991.

Vandaele, A. C., Hermans, C., Fally, S., Carleer, M., Colin, R., Merienne, M. F., Jenouvrier, A., and Coquart, B.: High-resolution Fourier transform measurement of the NO_2 visible and near-infrared absorption cross sections: Temperature and pressure effects, J. Geophys. Res.-Atmos., 107, 4348, https://doi.org/10.1029/2001JD000971, 2002.

von der Weiden, S.-L., Drewnick, F., and Borrmann, S.: Particle Loss Calculator – a new software tool for the assessment of the performance of aerosol inlet systems, Atmos. Meas. Tech., 2, 479–494, https://doi.org/10.5194/amt-2-479-2009, 2009.

Wang, S. S., Nan, J. L., Shi, C. Z., Fu, Q. Y., Gao, S., Wang, D. F., Cui, H. X., Saiz-Lopez, A., and Zhou, B.: Atmospheric ammonia and its impacts on regional air quality over the megacity of Shanghai, China, Sci. Rep.-UK, 5, 15842, https://doi.org/10.1038/srep15842, 2015.

Wild, R. J., Edwards, P. M., Dube, W. P., Baumann, K., Edgerton, E. S., Quinn, P. K., Roberts, J. M., Rollins, A. W., Veres, P. R., Warneke, C., Williams, E. J., Yuan, B., and Brown, S. S.: A measurement of total reactive nitrogen, NO_y, together with NO_2, NO, and O_3 via cavity ring-down spectroscopy, Environ. Sci. Technol., 48, 9609–9615, https://doi.org/10.1021/es501896w, 2014.

Williams, E. J., Baumann, K., Roberts, J. M., Bertman, S. B., Norton, R. B., Fehsenfeld, F. C., Springston, S. R., Nunnermacker, L. J., Newman, L., Olszyna, K., Meagher, J., Hartsell, B., Edgerton, E., Pearson, J. R., and Rodgers, M. O.: Intercomparison of ground-based NO_y measurement techniques, J. Geophys. Res.-Atmos., 103, 22261–22280, https://doi.org/10.1029/98jd00074, 1998.

Wollenhaupt, M., Carl, S. A., Horowitz, A., and Crowley, J. N.: Rate coefficients for reaction of OH with acetone between 202 and 395 K, J. Phys. Chem. 104, 2695–2705, 2000.

Womack, C. C., Neuman, J. A., Veres, P. R., Eilerman, S. J., Brock, C. A., Decker, Z. C. J., Zarzana, K. J., Dube, W. P., Wild, R. J., Wooldridge, P. J., Cohen, R. C., and Brown, S. S.: Evaluation of the accuracy of thermal dissociation CRDS and LIF techniques for atmospheric measurement of reactive nitrogen species, Atmos. Meas. Tech., 10, 1911–1926, https://doi.org/10.5194/amt-10-1911-2017, 2017.

Wooldridge, P. J., Perring, A. E., Bertram, T. H., Flocke, F. M., Roberts, J. M., Singh, H. B., Huey, L. G., Thornton, J. A., Wolfe, G. M., Murphy, J. G., Fry, J. L., Rollins, A. W., LaFranchi, B. W., and Cohen, R. C.: Total Peroxy Nitrates (ΣPNs) in the atmosphere: the Thermal Dissociation-Laser Induced Fluorescence (TD-LIF) technique and comparisons to speciated PAN measurements, Atmos. Meas. Tech., 3, 593–607, https://doi.org/10.5194/amt-3-593-2010, 2010.

Xu, L., Suresh, S., Guo, H., Weber, R. J., and Ng, N. L.: Aerosol characterization over the southeastern United States using high-resolution aerosol mass spectrometry: spatial and seasonal variation of aerosol composition and sources with a focus on organic nitrates, Atmos. Chem. Phys., 15, 7307–7336, https://doi.org/10.5194/acp-15-7307-2015, 2015.

Yamamoto, N., Kabeya, N., Onodera, M., Takahahi, S., Komori, Y., Nakazuka, E., and Shirai, T.: Seasonal-Variation of Atmospheric Ammonia and Particulate Ammonium Concentrations in the Urban Atmosphere of Yokohama over a 5-Year Period, Atmos. Environ., 22, 2621–2623, https://doi.org/10.1016/0004-6981(88)90498-2, 1988.

Yao, X. and Zhang, L.: Trends in atmospheric ammonia at urban, rural, and remote sites across North America, Atmos. Chem. Phys., 16, 11465–11475, https://doi.org/10.5194/acp-16-11465-2016, 2016.

York, D.: Least-Squares Fitting of a Straight Line, Can. J. Phys., 44, 1079–1086, https://doi.org/10.1139/p66-090, 1966.

Zare, A., Romer, P. S., Nguyen, T., Keutsch, F. N., Skog, K., and Cohen, R. C.: A comprehensive organic nitrate chemistry: insights into the lifetime of atmospheric organic nitrates, Atmos. Chem. Phys., 18, 15419–15436, https://doi.org/10.5194/acp-18-15419-2018, 2018.

Zasypkin, A. Y., Grigoreva, V. M., Korchak, V. N., and Gershenson, Y. M.: A formula for summing of kinetic resistances for mobile and stationary media: 1. Cylindrical reactor, Kinet. Catal.+, 38, 772–781, 1997.

Zenker, T., Fischer, H., Nikitas, C., Parchatka, U., Harris, G. W., Mihelcic, D., Müsgen, P., Pätz, H. W., Schultz, M., Volz-Thomas, A., Schmitt, R., Behmann, T., Weißenmayer, M., and Burrows, J. P.: Intercomparison of NO, NO_2, NO_y, O_3, and RO_x measurements during the Oxidizing Capacity of the Tropospheric Atmosphere (OCTA) campaign 1993 at Izaña, J. Geophys. Res.-Atmos., 103, 13615–13634, https://doi.org/10.1029/97jd03739, 1998.

Zhang, W. J., Bagreev, A., and Rasouli, F.: Reaction of NO_2 with activated carbon at ambient temperature, Ind. Eng. Chem. Res., 47, 4358–4362, https://doi.org/10.1021/ie800249s, 2008.

Supplement of Atmos. Meas. Tech., 13, 5739–5761, 2020
https://doi.org/10.5194/amt-13-5739-2020-supplement

Atmospheric Measurement Techniques
Open Access
EGU

Supplement of

Measurement of NO_x and NO_y with a thermal dissociation cavity ring-down spectrometer (TD-CRDS): instrument characterisation and first deployment

Nils Friedrich et al.

Correspondence to: John N. Crowley (john.crowley@mpic.de)

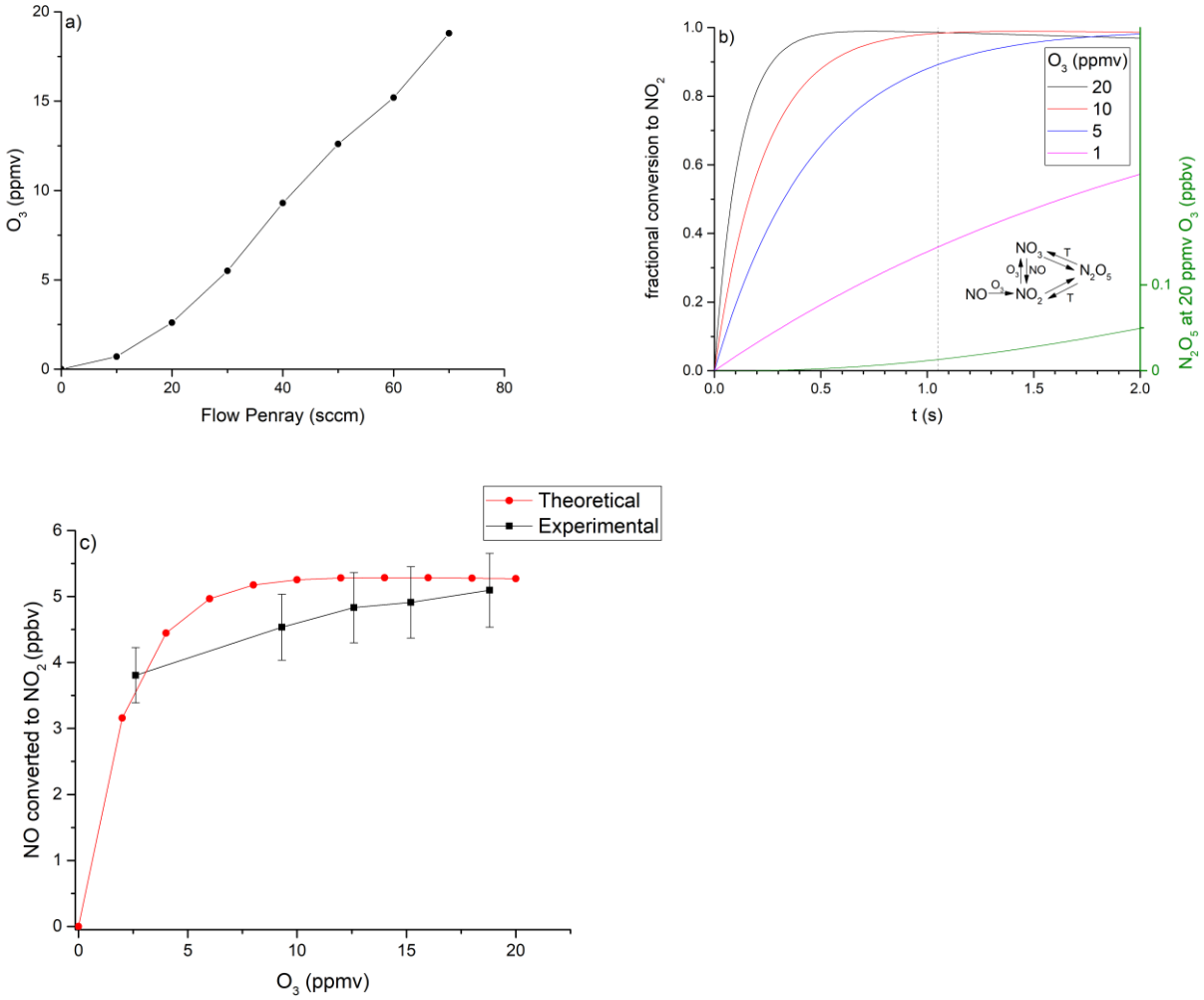

Figure S1: Optimisation of NO to NO_2 conversion via the addition of O_3. *a)* Ozone generated by passing synthetic air over the Pen-Ray lamp as a function of the flow rate. *b)* Numerical simulation of the fractional NO conversion as a function of reaction time and a chemical scheme showing reactions included in the model. High concentrations of O_3 can lead to the formation of significant amounts of N_2O_5 (50 pptv at 20 ppmv O_3 and 2 s reaction time). *c)* Conversion of 5.3 ppbv NO to NO_2 as a function of O_3 in 1.05 s reaction time. Both laboratory results and predictions of a numerical simulation are shown. Quantitative conversion is achieved for O_3 concentrations above 15 ppmv. The error bars indicate total overall uncertainty.

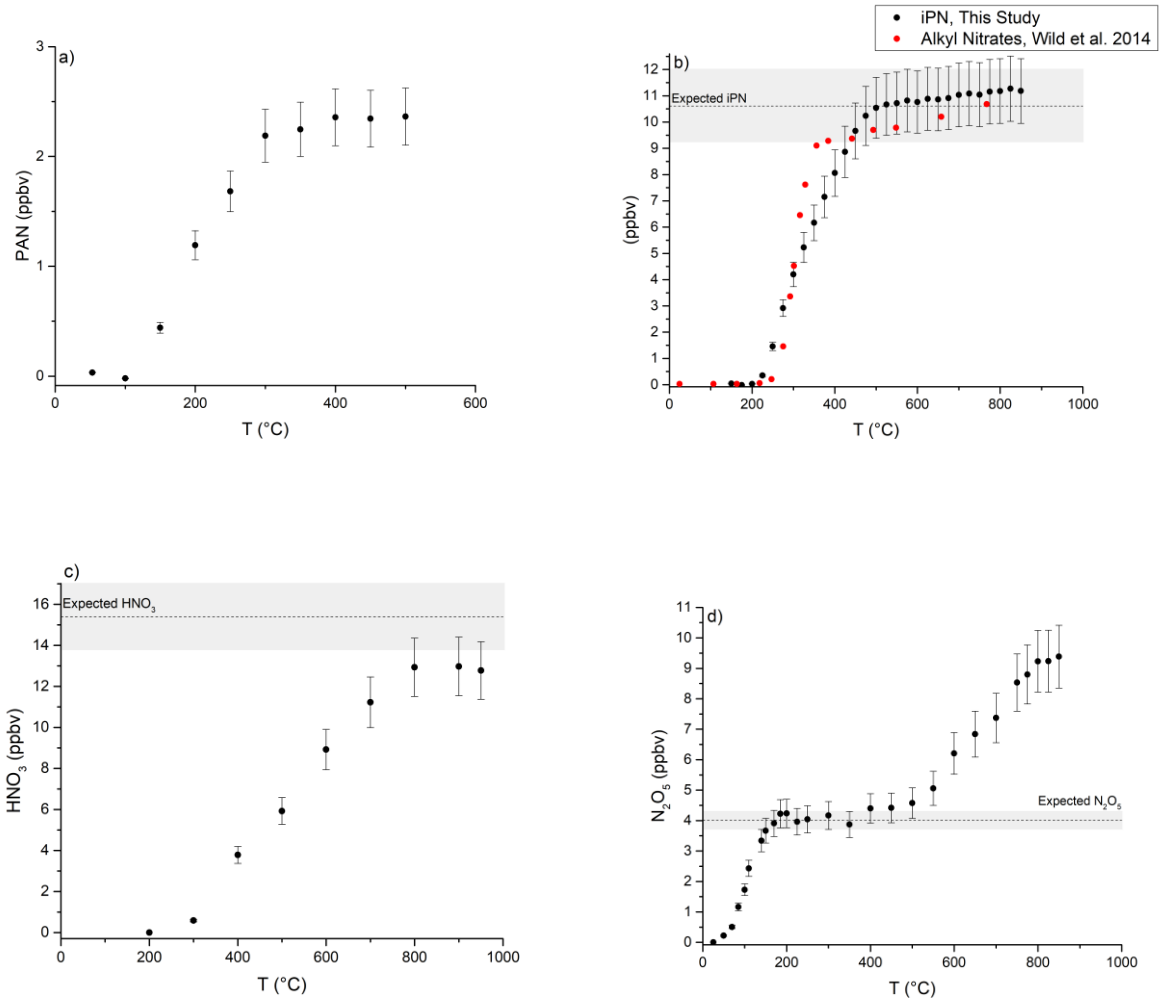

Figure S2: Absolute thermograms of PAN *(a)*, iPN *(b)*, HNO_3 *(c)*, and N_2O_5 *(d)*. Error bars represent the measurement uncertainty (see Sect. 2.2). Shaded areas show the estimated uncertainty ranges for the expected iPN and HNO_3 concentrations, based on errors during sample preparation and gas stream dilution. Within combined uncertainties we observe quantitative conversion of PAN, iPN, 2x N_2O_5 and HNO_3 to NO_2 at the TD-CRDS set temperature of 850 °C. *(b)* also includes data points for an alkyl nitrates mixtures from Wild et al. (2014), to illustrate the continuous increases in signal above 400 °C.

Wild, R. J., Edwards, P. M., Dube, W. P., Baumann, K., Edgerton, E. S., Quinn, P. K., Roberts, J. M., Rollins, A. W., Veres, P. R., Warneke, C., Williams, E. J., Yuan, B., and Brown, S. S.: A measurement of total reactive nitrogen, NOy, together with NO_2, NO, and O_3 via cavity ring-down spectroscopy, Env. Sci. Tech., 48, 9609-9615, doi:doi:10.1021/es501896w, 2014

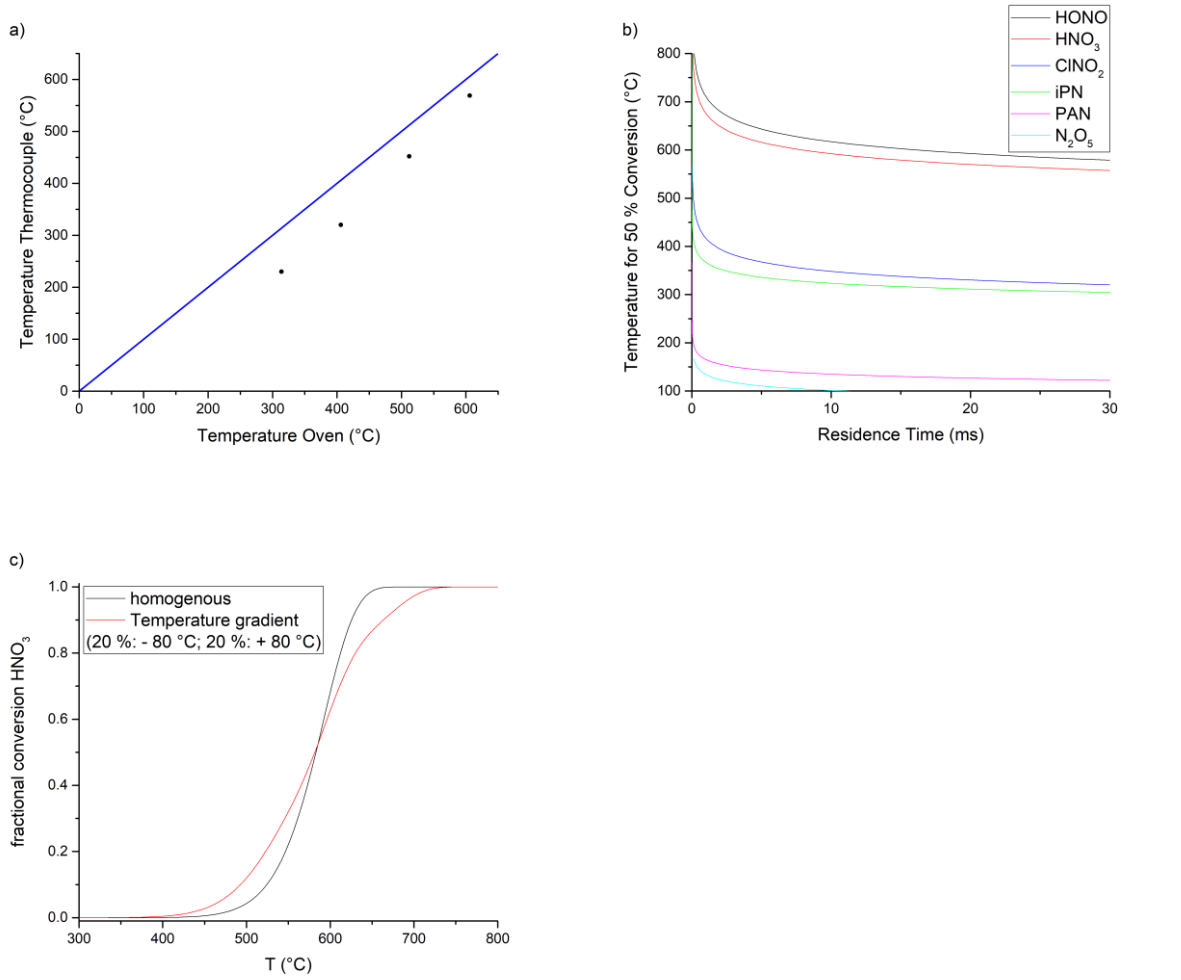

Figure S3: a) Plot of temperature from the internal reading of the TD-oven and a thermocouple located in the gas stream. The blue line shows a 1:1 correlation. b) Calculated threshold temperature for 50% conversion of N_2O_5, PAN, iPN, $ClNO_2$, HNO_3 and HONO to NO_x relative to the residence time in the heated inlet and based on kinetic parameters of their thermal dissociation (see Sect. 3.1.8). For HNO3, the threshold temperature increases by 40 °C when the residence time decreases from 30 to 10 ms. c) Impact of temperature gradients inside the TD-inlet on the shape of the calculated HNO_3 thermogram. The width of the thermogram increases by ca. 100 °C.

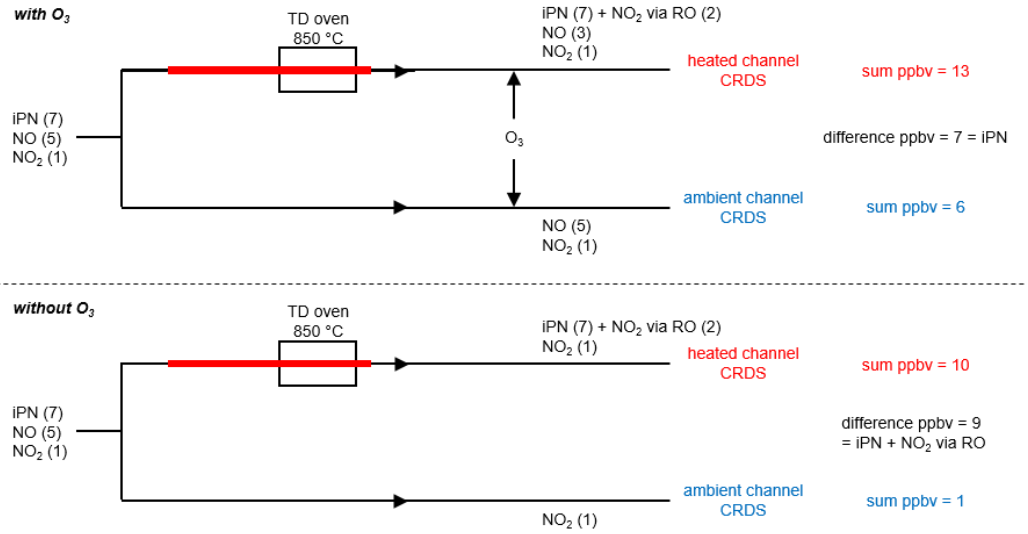

Figure S4: Graphical representation of the bias caused by RO_2 + NO reactions in detecting iPN. In both cases an initial mixing ratio of 7 ppbv iPN is present, along with 5 ppbv NO and 1 ppbv NO_2. When passed through the oven the iPN is converted to 7 ppbv NO_2 and (in this scenario) 2 ppbv of NO are converted to NO_2 via reaction with HO_2. In total 13 ppbv of NO_2 are detected in the cavity sampling via the oven. In the cavity at ambient temperature 6 ppbv of NO_2 are detected so that a (correct) iPN mixing ratio of 7 ppbv is derived. In the lower part of the figure, the same initial conditions apply, but O_3 is not added. The conversion of 2 ppbv NO to NO_2 occurs as above, so that 10 ppbv NO_2 are detected when sampling from the oven. The NO_2 mixing ratio in the cavity sampling at ambient is 1 ppbv, resulting in a derived (incorrect) NO_2 iPN mixing ratio of 9 ppbv.

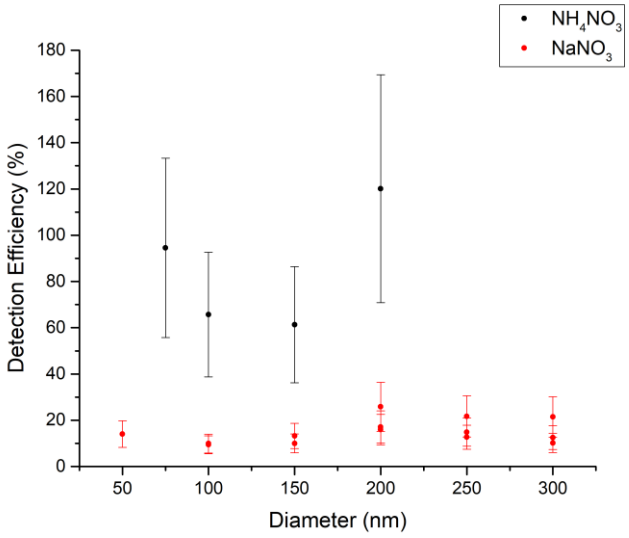

Figure S5: Detection efficiencies of NH_4NO_3 and $NaNO_3$ in the TD-CRDS, as a function of particle diameter. The CPC measured particle numbers were converted to mixing ratios and compared to the TD-CRDS. Errors imminent for this method are explained in Sect. 3.1.7. The particle conversion to NO_2 is clearly more efficient for NH_4NO_3, in direct comparison to $NaNO_3$.

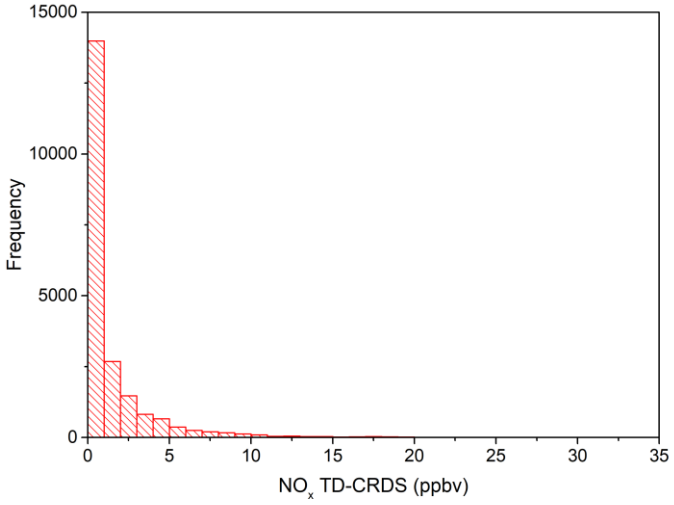

Figure S6: Histogram of the AQABA TD-CRDS NO_x mixing ratios shown in Fig. 10a). 92 % of the NO_x data points were at mixing ratios below 5 ppbv.

Table S1: Reactions included in the numerical simulations used to generate Fig. S1.

Reaction	**Rate coefficients (**Burkholder et al. (2015)
$NO_2 + O_3 \rightarrow NO_3 + O_2$	1.2E-13*exp(-2450/T)
$NO + NO_3 \rightarrow NO_2 + NO_2$	1.5E-11*exp(170/T)
$NO + O_3 \rightarrow NO_2 + O_2$	3.0E-12 *exp(-1500/T)
$N_2O_5 \rightarrow NO_3 + NO_2$	(((2.0E-30*(T/300)^-4.4)*M/(1+((2.0E-30*(T/300)^-4.4)*M/(1.4E-12*(T/300)^-0.7))))*0.6^((1+(LOG10((2.0E-30*(T/300)^-4.4)*M/(1.4E-12*(T/300)^-0.7)))^2)^-1))/(3.0E-27*exp(10990/T))
$NO_2 + NO_3 \rightarrow N_2O_5$	((2.0E-30*(T/300)^-4.4)*M/(1+((2.0E-30*(T/300)^-4.4)*M/(1.4E-12*(T/300)^-0.7))))*0.6^((1+(LOG10((2.0E-30*(T/300)^-4.4)*M/(1.4E-12*(T/300)^-0.7)))^2)^-1)

M = molecular density in molecule cm^{-3}, T = temperature in K.

Burkholder, J. B., Sander, S. P., Abbatt, J., Barker, J. R., Huie, R. E., Kolb, C. E., Kurylo, M. J., Orkin, V. L., Wilmouth, D. M., and Wine, P. H.: Chemical Kinetics and Photochemical Data for Use in Atmospheric Studies, Evaluation No. 18," JPL Publication 15-10, Jet Propulsion Laboratory, Pasadena, http://jpldataeval.jpl.nasa.gov., 2015.

Table S2: Denuder characterisation

NO_y species	**RH (%)**	**Reference mixing ratio (pptv) = $I_0 \pm \Delta I_0$**	**Mixing ratio with denuder (pptv) = $I \pm \Delta I$**	**Removal efficiency (%) = $(R \pm \Delta R) \times 100$**
NO	0	37036 ± 261	0 ± 43	100.0 ± 1.0
	14		62 ± 46	99.8 ± 1.0
	28		832 ± 94	97.8 ± 1.0
	42		7832 ± 60	78.9 ± 0.9
	55		10391 ± 65	71.9 ± 0.9
	68		12575 ± 45	66.0 ± 0.9
	81		13758 ± 51	62.9 ± 0.8
	97		14220 ± 74	61.6 ± 0.9
iPN	0	20181 ± 247	0 ± 22	100.0 ± 1.0
	14		-98 ± 91	100.5 ± 1.0
	27		-65 ± 58	100.3 ± 1.0
	41		355 ± 49	98.2 ± 0.9
	55		303 ± 41	98.5 ± 0.9
	68		537 ± 47	97.3 ± 0.9
	81		907 ± 46	95.5 ± 0.8
	95		1043 ± 33	94.8 ± 0.9
HNO_3	0	8224 ± 214	35 ± 58	99.6 ± 2.7
	68	9104 ± 173	247 ± 50	97.3 ± 3.7
NO_2	0	24259 ± 211	54 ± 45	99.8 ± 1.3
	65	24164 ± 225	448 ± 40	98.1 ± 1.2
PAN	0	7575 ± 93	58 ± 130	99.2 ± 2.4
N_2O_5	0	4179 ± 230	5 ± 48	99.9 ± 7.8
HONO	46	10000 ± 61	1521 ± 47	84.8 ± 0.9
$ClNO_2$	60	2068 ± 103	521 ± 141	74.8 ± 9.2

Mixing ratios (reference determined in heated inlet with bypassed denuder), standard deviations (1σ) during the averaging intervals and derived denuder removal efficiencies of various NO_y species, as a function of RH and as presented graphically in Fig. 6. $R = (I_0 - I) / I_o$. ΔR was determined by error propagation.

6 Second publication: Reactive nitrogen around the Arabian Peninsula and in the Mediterranean Sea during the 2017 AQABA ship campaign

The following chapter has been published as a research article in the peer-reviewed journal "Atmospheric Chemistry and Physics":

Friedrich, N., Eger, P., Shenolikar, J., Sobanski, N., Schuladen, J., Dienhart, D., Hottmann, B., Tadic, I., Fischer, H., Martinez, M., Rohloff, R., Tauer, S., Harder, H., Pfannerstill, E. Y., Wang, N., Williams, J., Brooks, J., Drewnick, F., Su, H., Li, G., Cheng, Y., Lelieveld, J., and Crowley, J. N.: Reactive nitrogen around the Arabian Peninsula and in the Mediterranean Sea during the 2017 AQABA ship campaign, Atmos. Chem. Phys., 21, 7473-7498, 10.5194/acp-21-7473-2021, 2021.

The thesis author operated the TD-CRDS during the campaign, analysed the data sets, and wrote the article.

This paper represents the first publication of shipborne NO_x and NO_y data sets from the Red Sea and Arabian Gulf regions. The observed dependence of the NO_2 lifetime on the present levels of OH and O_3 highlights the role of NO_x in the HO_x cycle and in O_3 production. The unique mixture of anthropogenic NO_x and VOC emissions allowed an assessment of the reactive nitrogen partitioning and the processing of air masses under intriguing and variable conditions. HONO was identified as an important NO_x source in marine environments which are strongly influenced by shipping emissions.

Atmos. Chem. Phys., 21, 7473–7498, 2021
https://doi.org/10.5194/acp-21-7473-2021

Atmospheric Chemistry and Physics
Open Access
EGU

Reactive nitrogen around the Arabian Peninsula and in the Mediterranean Sea during the 2017 AQABA ship campaign

Nils Friedrich[1], Philipp Eger[1], Justin Shenolikar[1], Nicolas Sobanski[1], Jan Schuladen[1], Dirk Dienhart[1], Bettina Hottmann[1], Ivan Tadic[1], Horst Fischer[1], Monica Martinez[1], Roland Rohloff[1], Sebastian Tauer[1], Hartwig Harder[1], Eva Y. Pfannerstill[1], Nijing Wang[1], Jonathan Williams[1], James Brooks[2], Frank Drewnick[3], Hang Su[4], Guo Li[5], Yafang Cheng[5], Jos Lelieveld[1], and John N. Crowley[1]

[1]Atmospheric Chemistry Department, Max Planck Institute for Chemistry, Mainz 55118, Germany
[2]Centre for Atmospheric Science, University of Manchester, Manchester, M13 9PL, UK
[3]Particle Chemistry Department, Max Planck Institute for Chemistry, Mainz 55118, Germany
[4]Multiphase Chemistry Department, Max Planck Institute for Chemistry, Mainz 55118, Germany
[5]Minerva Research Group, Max Planck Institute for Chemistry, Mainz 55118, Germany

Correspondence: John N. Crowley (john.crowley@mpic.de)

Received: 15 January 2021 – Discussion started: 21 January 2021
Revised: 19 March 2021 – Accepted: 8 April 2021 – Published: 18 May 2021

Abstract. We present shipborne measurements of NO_x ($\equiv NO + NO_2$) and NO_y ($\equiv NO_x +$ gas- and particle-phase organic and inorganic oxides of nitrogen) in summer 2017 as part of the expedition "Air Quality and climate change in the Arabian BAsin" (AQABA). The NO_x and NO_z ($\equiv NO_y$-NO_x) measurements, made with a thermal dissociation cavity ring-down spectrometer (TD-CRDS), were used to examine the chemical mechanisms involved in the processing of primary NO_x emissions and their influence on the NO_y budget in chemically distinct marine environments, including the Mediterranean Sea, the Red Sea, and the Arabian Gulf, which were influenced to varying extents by emissions from shipping and oil and gas production. Complementing the TD-CRDS measurements, NO and NO_2 data sets from a chemiluminescence detector (CLD) were used in the analysis. In all regions, we find that NO_x is strongly connected to ship emissions, both via direct emission of NO and via the formation of HONO and its subsequent photolytic conversion to NO. The role of HONO was assessed by calculating the NO_x production rate from its photolysis. Mean NO_2 lifetimes were 3.9 h in the Mediterranean Sea, 4.0 h in the Arabian Gulf, and 5.0 h in the Red Sea area. The cumulative loss of NO_2 during the night (reaction with O_3) was more important than daytime losses (reaction with OH) over the Arabian Gulf (by a factor 2.8) and over the Red Sea (factor 2.9), whereas over the Mediterranean Sea, where OH levels were high, daytime losses dominated (factor 2.5). Regional ozone production efficiencies (OPEs; calculated from the correlation between O_x and NO_z, where $O_x = O_3 + NO_2$) ranged from 10.5 ± 0.9 to 19.1 ± 1.1. This metric quantifies the relative strength of photochemical O_3 production from NO_x compared to the competing sequestering into NO_z species. The largest values were found over the Arabian Gulf, consistent with high levels of O_3 found in that region (10–90 percentiles range: 23–108 ppbv). The fractional contribution of individual NO_z species to NO_y exhibited a large regional variability, with HNO_3 generally the dominant component (on average 33 % of NO_y) with significant contributions from organic nitrates (11 %) and particulate nitrates in the PM_1 size range (8 %).

1 Introduction

The nitrogen oxides NO and NO_2 are emitted into the atmosphere in several natural and anthropogenic processes including lightning (Chameides et al., 1977; Lange et al., 2001), combustion (Lenner, 1987), and bacterial action in soil (Oertel et al., 2016). Due to their rapid interconversion, NO and NO_2 are often treated as a single chemical family (NO_x).

The chemical processing of NO_x in the atmosphere, initiated by ozone and the radicals OH, HO_2, and NO_3, leads to the formation of NO_z ($NO_z = HNO_3 +$

$NO_3 + 2N_2O_5 + RO_2NO_2 + RONO_2 + XONO_2 + XNO_2 +$ particulate nitrates), where R is an organic fragment and X represents a halogen atom or a H atom. The sum of NO_x and NO_z is referred to as total reactive nitrogen NO_y (Logan, 1983), which does not include N_2, N_2O, NH_3, or HCN.

OH, formed, for example, via the photolysis of O_3 in the presence of water (Reactions R1a and R1b), can directly convert both NO and NO_2 to more oxidised, acidic forms (R2, R3; where M is a collision partner). NO_x can be re-formed from HONO at daytime through photolysis, with a noon-time lifetime of ca. 20–30 min (Stutz et al., 2000).

$$O_3 + h\nu \rightarrow O(^1D) + O_2 \quad \text{(R1a)}$$

$$O(^1D) + H_2O \rightarrow 2OH \quad \text{(R1b)}$$

$$OH + NO + M \rightarrow HONO + M \quad \text{(R2)}$$

$$OH + NO_2 + M \rightarrow HNO_3 + M \quad \text{(R3)}$$

OH can also react with volatile organic compounds (VOCs) to generate peroxy radicals (RO_2, Reaction R4). Reaction with organic peroxy radicals converts NO to NO_2 (major channel; reaction R5a) or to organic nitrates $RONO_2$ (minor channel; Reaction R5b), and it sequesters NO_2 as peroxy nitrates RO_2NO_2 (Reaction R7).

$$OH + RH(+O_2) \rightarrow RO_2 + H_2O \quad \text{(R4)}$$

$$RO_2 + NO \rightarrow RO + NO_2 \quad \text{(R5a)}$$

$$RO_2 + NO + M \rightarrow RONO_2 + M \quad \text{(R5b)}$$

$$HO_2 + NO \rightarrow OH + NO_2 \quad \text{(R6)}$$

$$RO_2 + NO_2 + M \rightarrow RO_2NO_2 + M \quad \text{(R7)}$$

The formation of long-lived organic nitrates (R5b) and especially nitric acid (R3) represent daytime sinks for both NO_x and RO_x ($OH + HO_2 + RO + RO_2$).

At night-time, when the photolysis of NO_2 ceases, NO is sequentially converted to the NO_3 radical (Reaction R8). This radical can also be a source of $RONO_2$ species through the addition to unsaturated VOCs. NO_3 exists in thermal equilibrium with NO_2 and N_2O_5 (Reaction R9) and the heterogeneous loss of N_2O_5 to aqueous surfaces results in transfer of NO_y to the particle phase as HNO_3 (Reaction R10) or its loss via deposition. In some (especially marine) environments (Osthoff et al., 2008; Kercher et al., 2009), loss of N_2O_5 to particles can result in formation of $ClNO_2$ (R11) which, via photolysis, re-forms NO_2 the next day.

$$NO_2 + O_3 \rightarrow NO_3 + O_2 \quad \text{(R8)}$$

$$NO_3 + NO_2 + M \rightleftharpoons N_2O_5 + M \quad \text{(R9)}$$

$$N_2O_5 + H_2O \rightarrow 2HNO_3 \quad \text{(R10)}$$

$$N_2O_5 + Cl^- \rightarrow ClNO_2 + NO_3^- \quad \text{(R11)}$$

The above reactions illustrate that NO_x and VOCs provide the catalyst and fuel for photochemical ozone formation, the efficiency of which is determined by the competition between photolysis of NO_2 to ozone and its conversion to NO_z (Day et al., 2003; Wild et al., 2014, 2016; Womack et al., 2017). Modelling studies have identified the Arabian Gulf as a hotspot for O_3 pollution and photochemical smog, with O_3 mixing ratios exceeding 100 ppbv (Lelieveld et al., 2009).

The lack of measurements in the Arabian Gulf and the eastern Mediterranean, both of which are expected to be significantly impacted by climate change (Lelieveld et al., 2012), preclude accurate prognosis of air quality in these regions and provide the rationale for conducting the AQABA campaign (AQABA: Air Quality and climate change in the Arabian BAsin), in which a large suite of instruments were operated in regions that were influenced by anthropogenic emissions from megacities, petrochemical and shipping activity, and desert dust emissions and through regions that could be classified as maritime background conditions. Emissions from oil exploration provide a complex atmospheric mixture of NO_x and anthropogenic VOCs. The presence of desert dust can have a significant impact on the budget of inorganic acids such as HNO_3. Finally, the overall elevated temperatures and actinic fluxes during AQABA promoted rapid photochemical processing of NO_x. We therefore expect a more varied and complex chemistry than found in remote marine locations.

Previous analyses from this campaign focussed on sources and sinks of non-methane hydrocarbons (Bourtsoukidis et al., 2019); the role of OH reactivity in ozone chemistry (Pfannerstill et al., 2019); formation of $ClNO_2$ (Eger et al., 2019a), ethane, and propane emissions from the Red Sea (Bourtsoukidis et al., 2020); emission factors in ship plumes (Celik et al., 2020); marine emissions of methane sulfonamide (Edtbauer et al., 2020); rates of net O_3 production (Tadic et al., 2020); and the abundance of carbonyl compounds.

In this paper we present NO_x, NO_y, and NO_z mixing ratios obtained by a thermal dissociation cavity ring-down spectrometer (TD-CRDS), together with NO and NO_2 mixing ratios from a chemiluminescence detector, a comprehensive set of ancillary measurements, and an analysis of the results in terms of photochemical processing and ageing of air masses, chemical sources of NO_x (e.g. from the photolysis of HONO), and the efficiency of ozone formation.

The ozone production efficiency (OPE), a metric used in the analysis of the O_3 formation, quantifies the fractional transformation of primarily emitted NO_x to O_3 (Liu et al., 1987; Trainer et al., 1993) and thus reflects the relative importance of competing photochemical processes leading to O_3 and NO_z formation from NO_x. High values of OPE are favoured by low OH and VOC concentrations, and values exceeding 80 have been reported for remote marine environments. Low single-digit values have been observed in polluted urban environments (Rickard et al., 2002; Wang et al., 2018). The location dependence of the OPE can be further classified with previous observations from the literature. Minimal OPEs in urban environments between 1 and 2 have

been reported from the Beijing area (Lin et al., 2011; Ge et al., 2013) and from the USA (Daum et al., 2000; Sillman, 2000; Nunnermacker et al., 2004). In rural and suburban environments, the OPE can increase to values between 10 and 15, as demonstrated in North America (Olszyna et al., 1994; Roussel et al., 1996; Fried et al., 1997; Ninneman et al., 2017) and in China (Sun et al., 2010). From oceanic samples, OPEs of 65 and 87 were observed on the south-eastern coast of the UK (Rickard et al., 2002) and on Sable Island, Canada (Wang et al., 1996). Flights over the western Pacific Ocean found values of 102–246 in the tropical area (latitude 0–18° N) and of 73–209 further north (18–42° N) (Davis et al., 1996). For the AQABA campaign, we expect lower OPEs than those observed in remote oceanic locations, due to the variable influx from harbours, coastal pollution, and surrounding ship traffic.

2 Methods

The AQABA ship campaign followed a route from Toulon in southern France to Kuwait (and back) via the Mediterranean Sea, the Suez Canal, the Red Sea, the Arabian Sea, and the Arabian Gulf (see Fig. 1). Stops were made in Malta, Jeddah, Djibouti, and Fujairah on the first leg (24 June to 30 July 2017) and in Fujairah and Malta on the second leg (2 August to 30 August 2017). Most measurements started in the south-eastern Mediterranean Sea on the first leg and finished ca. halfway between Sicily and Corsica on the second leg. The instruments were located either in air-conditioned research containers aboard, or directly on the deck of, the 73 m long research vessel "*Kommandor Iona*". Periods during which instrument inlets were contaminated by ship-stack emissions from the ship (identified based on relative wind direction and speed and the variability in measured SO_2 and NO mixing ratios) were excluded from the analysis. This resulted in rejection of 38.4 % of the data points on the first leg, when the wind and ship direction were often similar, and rejection of 1.4 % on the second leg of the campaign, when sailing mainly into the wind.

2.1 TD-CRDS instrument for NO_x, NO_y, and NO_z detection

The TD-CRDS instrument, its operating principles, laboratory characterisation, and a validation of the NO_x measurements versus an independent chemiluminescence detector (CLD) instrument have recently been presented (Friedrich et al., 2020). The TD-CRDS (located in an air-conditioned research container on the front deck of the vessel) has two separate cavities operating at a wavelength of 405 nm and at sub-ambient pressure (720 to 770 hPa) to prevent condensation of water on inlet lines under humid conditions. One of the cavities is connected to an inlet (perfluoroalkoxy alkane (PFA) tubing) at ambient temperature, and the other cavity is connected to a tubular quartz inlet, which was heated to 850 °C to thermally dissociate NO_y trace gases to NO or NO_2. The TD oven was accommodated in an aluminium box on top of the container with the inlet ca. 1.2 m above the container roof. Air samples reached the TD area less than 30 cm behind the tip of the inlet, and we expect negligible inlet losses for NO_y species. Inlet lines of the heated and the ambient temperature channel were each overall ca. 4 m long (2 m located inside and 2 m outside the container). In the Red Sea and Arabian Gulf, the inlet heating of the NO_y channel was switched off occasionally during the hottest hours of the day to prevent damage to the oven electronics. The campaign data coverage for NO_y is 65 %, considering only time periods when the ship was moving.

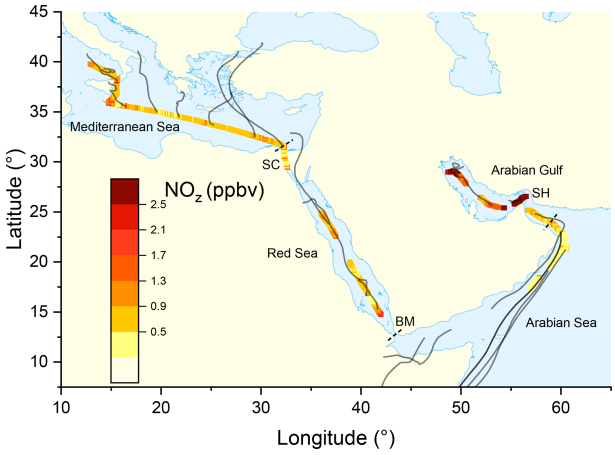

Figure 1. Mixing ratio of NO_z from the second leg of the campaign, colour-coded along the ship track. Each data point represents an average over 30 min. Grey lines represent HYSPLIT 48 h back-trajectories starting from the ship location at 100 m height. SH = Strait of Hormuz; BM = Strait of Bab al-Mandab; SC = Suez Canal.

The total uncertainty (at 50 % relative humidity and 1 min integration time) amounts to 11 % + 10 pptv for NO_x and to 16 % + 14 pptv for NO_z if we disregard the non-quantitative detection of coarse-mode non-refractory nitrate (see below). Detection limits (5 s integration time) during the AQABA campaign were 98 pptv for NO_x, 51 pptv for NO_y, and 110 pptv for NO_z and are higher than those reported for laboratory operation owing to problems with optical alignment due to the motion of the ship. Detection limits are defined as the 2σ standard deviation between consecutive zeroing periods. Under laboratory conditions, NO_x detection limits of 40 pptv (1 min average) were obtained (Friedrich et al., 2020); 6 pptv (40 s) has been achieved with undegraded mirrors (Thieser et al., 2016).

The NO_z mixing ratios obtained using the TD-CRDS were calculated from the difference between NO_y and NO_x measurements and thus contain a contribution from particulate nitrate. Friedrich et al. (2020) have shown that this instru-

ment measures ammonium nitrate quantitatively but detects only a fraction ($\approx 25\,\%$) of sodium nitrate ($NaNO_3$) of 200–300 nm diameter as NO_x. The inefficient detection of some non-refractory nitrate species (e.g. $NaNO_3$) means that the NO_y mixing ratios presented below are thus (potentially) lower limits. As $NaNO_3$ is usually associated with coarse-mode aerosol (particle diameter $> 1\,\mu m$), this also implies that the particle-phase nitrate measured by the TD-CRDS is comparable to that measured by an aerosol mass spectrometer (HR-ToF-AMS; see Sect. 2.3). In marine environments, sea salt aerosol can be the dominant aerosol component (Lewis and Schwartz, 2004). We therefore note that the definition of NO_y, in this work, is restricted to non-refractory nitrate particles which can be vaporised by the AMS or in the TD inlet of the CRDS. Nitrate detection by the AMS is further discussed in Sect. 3.2.2 and 3.4.

High loadings of coarse-mode particles are associated with high wind speeds, which were encountered on the first leg passing the Strait of Bab al-Mandab, through the Arabian Sea, and until the Gulf of Oman and on the second leg in the Arabian Sea and in the northern Red Sea. The fractional contribution of coarse-mode particles to the overall mass concentration were derived using data from an optical particle counter (OPC) and via the $(PM_{10}–PM_1)\,/\,PM_{10}$ ratio (both PM_1 and PM_{10} were measured with the OPC). We see from Fig. S1 that the impact of coarse-mode nitrate may have been largest on both legs in the transitional area between the southern Red Sea and Arabian Sea, where OPC PM_{10} mass concentrations exceeded $150\,\mu g\,m^{-3}$ and the coarse-mode fraction was consistently $>$ ca. 90 %.

2.2 CLD measurements of NO_x

NO and NO_2 were measured with a chemiluminescence detector (CLD 790 SR, ECO PHYSICS, 5 s time resolution) as described in Tadic et al. (2020), with total measurement uncertainties of 6 % (NO) and 23 % (NO_2) and detection limits of 22 pptv for NO and 52 pptv for NO_2, both calculated at a time resolution of 5 s and a confidence interval of 2σ. The CLD detection method is based on the chemiluminescence of electronically excited NO_2^* formed in the reaction of NO with O_3. Ambient NO_2 is photolytically converted to NO by exposure to UV light from LEDs emitting at wavelengths close to 398 nm. The CLD was calibrated every 6 h using a 2 ppmv NO gas standard.

2.3 Other measurements

An overview of the instruments deployed is given in Table 1. Total organic nitrates (ONs) were measured as the sum of peroxy nitrates (PNs, RO_2NO_2) and alkyl nitrates (ANs, $RONO_2$) in a five-channel thermal dissociation cavity-ring-down spectrometer (5C-TD-CRDS; Sobanski et al., 2016). SO_2 and $ClNO_2$ were measured with a chemical ionisation quadrupole mass spectrometer (CI-QMS) with 15 s time resolution (Eger et al., 2019a, b). The detection limits for SO_2 and $ClNO_2$ were 38 and 12 pptv, respectively; the total uncertainties were $20\,\% \pm 23$ pptv (SO_2) and $30\,\% \pm 6$ pptv ($ClNO_2$). Particulate-phase nitrate (pNit) and sulfate concentrations in the PM_1 size range were obtained by an aerosol mass spectrometer (Aerodyne HR-ToF-AMS; DeCarlo et al., 2006) with measurement uncertainties of 30 % and 35 %, respectively, for the mass concentrations of NO_3^- and SO_4^{2-}. Total aerosol mass concentrations in the PM_1 and PM_{10} size ranges were calculated from particle size distributions, detected with an optical particle counter (OPC, Grimm model 1.109; size range: 250 nm to 32 µm) in a 6 s time resolution and with a 35 % uncertainty. Ozone was measured by optical absorption at 253.65 nm in a commercial ozone monitor (2B Technologies model 202) with total measurement uncertainty of $2\,\% \pm 1$ ppbv and a detection limit of 3 ppbv (at 10 s integration time). HONO mixing ratios were measured by a long-path absorption photometer (LOPAP; Heland et al., 2001) with a 3–5 pptv detection limit and a measurement uncertainty of 20 %. The path length of the instrument was 1.9 m, and the inlet was also located on the foredeck of the ship at a ca. 5 m distance to the TD-CRDS inlets. A spectral radiometer (Metcon GmbH) measured wavelength-resolved actinic flux, which was converted to photolysis rate constants (J) for NO_2, NO_3 and HONO using evaluated quantum yields and cross sections (Burkholder et al., 2015). The overall uncertainty in J is ca. 15 %, which includes calibration accuracy (Bohn et al., 2008) and the neglect of upwelling radiation from the sea surface. OH concentrations were obtained from a custom-built laser-induced fluorescence (LIF) instrument (Martinez et al., 2010; Regelin et al., 2013) with an upper limit total uncertainty of 40 %. Total OH reactivity measurements were performed according to the comparative reactivity method (Sinha et al., 2008), with a 5 min detection limit of $5.4\,s^{-1}$ and a ca. 50 % total uncertainty, as described in Pfannerstill et al. (2019). HCHO was detected by a commercial instrument (AL4021, Aero-Laser GmbH) according to the Hantzsch method and had a relative uncertainty of 13 % (Stickler et al., 2006). Multi-pass absorption spectroscopy using a quantum cascade laser was used to measure CO mixing ratios with 20 % uncertainty and a limit of detection of 0.6 ppbv (Li et al., 2013).

2.4 Meteorological data

Temperature, wind direction, wind speed, and relative humidity were measured by a weather station (Neptune, Sterela), together with the GPS position and velocity of the ship. Back-trajectories were obtained using the HYSPLIT transport and dispersion model (Stein et al., 2015; Rolph et al., 2017). The trajectories were calculated backwards for 48 h from the GPS location of the ship with a starting height of 100 m a.m.s.l., using the Global Data Assimilation System (GDAS1) meteorological model. The back-trajectories were limited to 48 h as this exceeds the lifetimes of both

Table 1. Data sets used in the analysis and corresponding measurement characteristics.

Species	Instrument	Technique	Detection limit	Measurement uncertainty
NO_x	TD-CRDS	thermal dissociation cavity ring-down spectroscopy	98 pptv	11 %
NO_z			110 pptv	16 %
NO	CLD	chemiluminescence	22 pptv (5 s, 2σ)	6 %
NO_2			52 pptv (5 s, 2σ)	23 %
ONs	5C-TD-CRDS	thermal dissociation cavity ring-down spectroscopy	NA	NA
SO_2	CI-QMS	chemical ionisation mass spectrometry	38 pptv	20 % ± 23 pptv
$ClNO_2$			12 pptv	30 % ± 6 pptv
pNit (PM_1)	AMS	aerosol mass spectrometry	NA	30 %
SO_4^{2-} (PM_1)			NA	35 %
PM_1^*	OPC	optical particle counter	NA	35 %
PM_{10}^*				
O_3	O_3	optical absorption	3 ppbv (10 s)	2 % ± 1 ppbv
HONO	LOPAP	long-path absorption photometry	3–5 pptv	20 %
J_x^{**}	J_x	wavelength-resolved actinic flux	NA	10 %
OH	LIF	laser-induced fluorescence	variable	40 % (upper limit)
OH reactivity	OH reactivity	comparative reactivity method	5.4 s^{-1} (5 min)	ca. 50 %
HCHO	HCHO	Hantzsch method	0.128 ppbv (170 s, 2σ)	13 %
CO	CO	absorption spectroscopy with quantum cascade laser	0.6 ppbv	20 %

* represents total aerosol mass concentration. ** represents photolysis rate constants for NO_2, NO_3, and HONO. NA stands for not available.

NO_x and NO_z (see later) and is thus sufficient to indicate potential source regions. Back-trajectories displayed in graphs are considered to be representative for the prevailing atmospheric flow conditions when passing the respective areas along the AQABA ship track.

3 Results and discussion

In Fig. S2 we show the complete NO_x, NO_y, and NO_z time series from the campaign, averaged from the 5 s raw data time resolution onto a 5 min grid. Periods of contamination by the ship's own exhaust are indicated by grey background colouring. The regional variation in NO_x and NO_z during the second leg is illustrated in Figs. S3c and 1 which also delineates the campaign into the "Red Sea" (2–16 July and 17–24 August 2017), the "Arabian Sea" (16–24 July and 7–17 August 2017), the "Arabian Gulf" (24–31 July and 3–7 August 2017), and the "Mediterranean Sea" (24–31 August 2017).

Altogether, 4.8 % of the NO_x measurements during AQABA were below the ca. 100 ppt detection limit of the TD-CRDS instrument, indicating only sporadic occurrence of maritime background conditions. Similar observations were made by Tadic et al. (2020), with only 3.3 % of the NO_x data set below 50 pptv in the Arabian Sea, the southern Red Sea, and the eastern Mediterranean. In comparison, NO_x mixing ratios below 20 pptv were previously found, for example, over the South Atlantic (Fischer et al., 2015). The black lines in Fig. 1 represent 2 d back-trajectories (HYSPLIT; see Sect. 2.4). A similar figure for the first leg is given in Fig. S3. For the Mediterranean Sea, the Red Sea, and the Arabian Gulf, we present an analysis of the lifetimes and sources of NO_x and NO_z. Chemical sources of NO_x, e.g. from the photolysis of HONO or pNit, are discussed in Sect. 3.4. The chemically distinct regions are compared and contrasted in Sects. 3.5 and 4. Dividing the analysis into the three regions helps to highlight the chemically different environments encountered. An analysis of the Arabian Sea region was unfortunately not possible due to a gap in the NO_z measurements between 9 and 17 August 2017, caused by instrument failure during heavy seas and winds. The division of the regions was based on the prevalent NO_x mixing ratios displayed in Fig. S3c. In contrast to other AQABA publications (Eger et al., 2019a; Pfannerstill et al., 2019; Tadic et al., 2020), the Gulf of Oman, and the Suez Channel were included in the Arabian Gulf and the Red Sea regions, respectively, as a clear shift in NO_x to mixing ratios below ca. 1 ppbv occurred both upon leaving the Gulf of Oman into the Arabian Sea and upon exiting the Suez Channel to the north towards the Mediterranean Sea. The transitions between the Arabian Gulf and the Gulf of Oman, and between

the northern Red Sea and the Suez region are less obviously represented in the NO_x levels.

3.1 Mediterranean Sea

Owing to unfavourable winds resulting in contamination of the measurements by the ships own exhaust as well as instrument malfunction, very little useable data were obtained by the TD-CRDS during the first leg through the Mediterranean Sea, and we analyse only the data obtained on the return leg (24–31 August 2017). In this period, temperatures varied between 24 and 29 °C with relative humidity between 52 % and 89 % (see Fig. S2). During most of the transit through the Mediterranean Sea, winds were from the north. At the end of the cruise when approaching Sicily, we encountered a shift in wind direction with air arriving from the north-west. Back-trajectories (see Fig. 1) indicate that when sailing through the eastern Mediterranean Sea we encountered air masses that had passed over Turkey; the air we sampled in the central Mediterranean Sea had passed over the Balkan states, and in the western Mediterranean it had passed over Greece and Italy. The trajectories ending at the ships location were persistently located in the boundary layer (height < 1000 m) for the previous 48 h. An exception was the back-trajectory originating from the Black Sea, which was located at a height (above ground level) of up to 1740 m. The back-trajectory passing over the island of Crete was located at a maximum height of 3224 m, which may be the result of orographic uplift caused by the central Cretan mountain range.

3.1.1 NO_x

NO_x mixing ratios were generally low in the Mediterranean Sea (Fig. 2a). One-minute mean and median mixing ratios of NO_x as detected by the TD-CRDS were 1.3 and 0.3 ppbv, respectively. For the CLD measurements of NO_x, the equivalent values are 1.1 and 0.2 ppbv, respectively. For both instruments, the difference between mean and median values stems from the frequent occurrence of NO_x plumes resulting from emissions of nearby ships. The NO_x mixing ratios measured by TD-CRDS and CLD were in good agreement (see Friedrich et al., 2020) and the bias of the TD-CRDS to higher values reflects the exclusion of data below the detection limit. A histogram of the NO_x measurements made by the CLD is displayed in Fig. 2b), which indicates that 33 % of the NO_x data were between 100 and 250 pptv and 24 % were above 1 ppbv. The maximum mixing ratio of NO_x in the Mediterranean Sea of 84.7 ppbv was measured in the narrowest part of the Strait of Messina, which is a busy corridor for international shipping with ferry traffic between Italy and Sicily crossing the *Kommandor Iona*'s ship track. This observation highlights the importance of NO_x shipping emissions in some parts of the Mediterranean Sea, which we return to later.

Potential non-shipping sources of NO_x in this region can be identified via the back-trajectories plotted in Fig. 1. In the eastern part of the Mediterranean Sea, the air masses were influenced by emissions from the heavily populated and industrialised western Turkish coastal area, the island of Crete, and mainland Greece. However, as we show below, the lifetime of NO_x is generally less than 6 h, and the greater fraction of any land-based NO_x emissions would have undergone oxidation to NO_z during the 48 h transport time of the back-trajectory. In the western Mediterranean Sea, the 2 d back-trajectories end above the open ocean.

Our data can be compared to results from previous measurements of NO_x in the Mediterranean area. Excluding pollution events, Mallik et al. (2018) report NO and NO_2 levels below 0.05 and 0.25 ppbv, respectively, during the 2014 Cyprus-based CYPHEX (CYprus PHotochemical EXperiment 2014) campaign in the eastern Mediterranean Sea. Plume-like increases in NO_x were associated with enhanced SO_2 and related to emissions from shipping (Eger et al., 2019b). During the MINOS (Mediterranean INtensive Oxidant Study) campaign on the island of Crete, median NO_2 mixing ratios between 0.3 ppbv and 0.7 ppbv were reported (Berresheim et al., 2003). The lower mixing ratios were associated with air masses arriving from the western European free troposphere, whereas the higher values were air masses impacted by biomass burning in eastern Europe. In contrast, higher NO_2 mixing ratios (typically between 4 and 6 ppbv excluding plumes) were reported from shipboard measurements in the Aegean Sea (Večeřa et al., 2008). Satellite-based observations of NO_2 vertical column densities over Crete and in the region between Crete and Sicily, were used to derive near-surface NO_2 mixing ratios of up to ~ 0.4 ppbv (Ladstätter-Weißenmayer et al., 2003, 2007).

Our NO_x measurements are thus broadly consistent with previous measurements in the Mediterranean Sea which indicate mixing ratios of less than 1 ppbv in the absence of recent emissions from ships. The higher mixing ratios reported by Večeřa et al. (2008) are likely to be related to the close proximity of their ship to NO_x sources on the European continent and denser ship traffic compared to the more southerly AQABA route through the eastern Mediterranean Sea.

3.1.2 NO_z

Figure 2c and d show a time series and histogram, respectively, of NO_z for the Mediterranean Sea. The shape of the distribution indicates that NO_z mixing ratios close to the detection limit were rarely measured. The mean (0.8 ppbv), median (0.7 ppbv), maximum (2.8 ppbv), and minimum NO_z mixing ratios (< 0.1 ppbv) along with the narrower distribution indicate that, as expected, NO_z is significantly less variable than NO_x. The ratio of the median mixing ratios NO_z / NO_y in the Mediterranean Sea is ~ 0.8, and, concomitantly, that of NO_x / NO_y is ~ 0.2. A more detailed analysis of the relative contributions of NO_x and NO_z to NO_y,

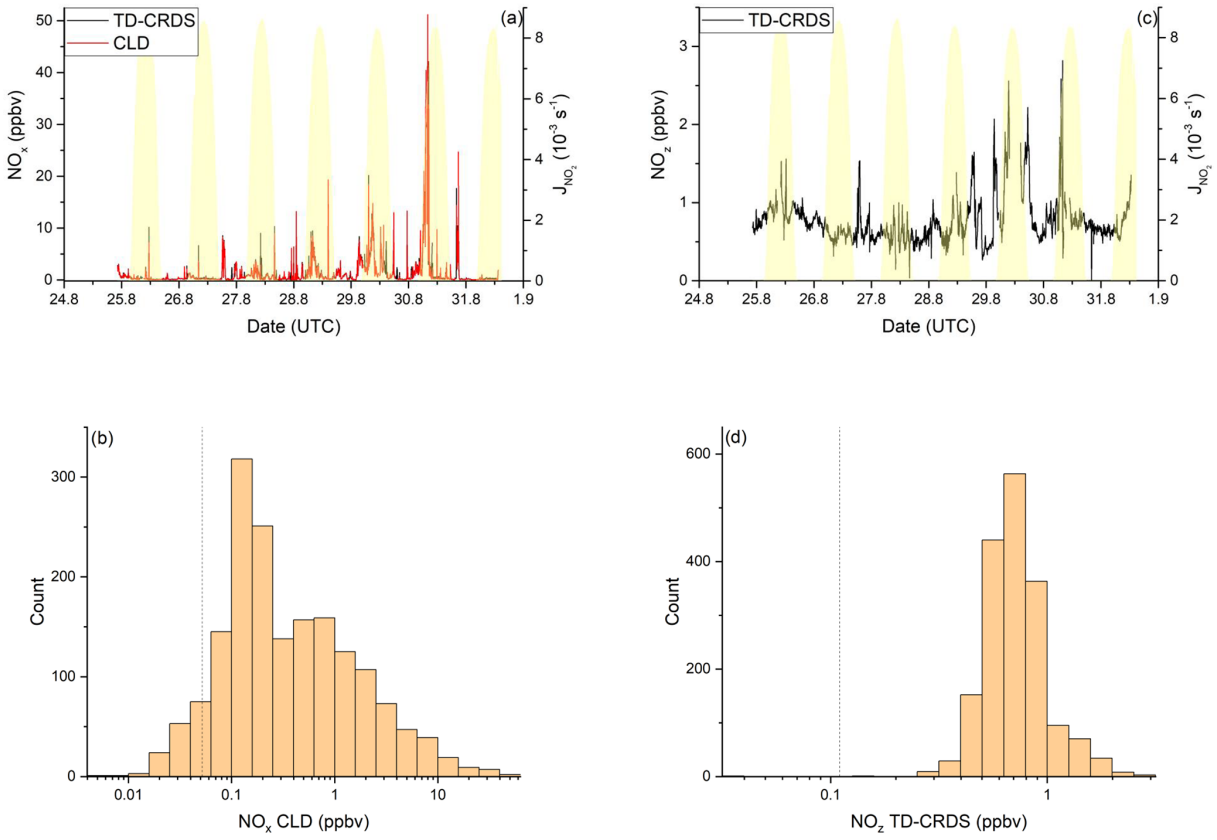

Figure 2. NO_y measurements in the *Mediterranean Sea*. Dashed lines signify the instrument detection limits. **(a)** NO_x mixing ratios by CLD and TD-CRDS. **(b)** Frequency distribution of NO_x mixing ratios between 25 August and 1 September 2017. **(c)** NO_z mixing ratios by TD-CRDS. **(d)** Frequency distribution of NO_z mixing ratios between 25 August and 1 September 2017. The yellow shaded regions show J_{NO_2}. The vertical dotted lines are the limits of detection of the respective measurements.

in which we divide the Mediterranean Sea into seven subregions, is presented in the following paragraphs. The choice of these subregions was based on the existence of homogeneous NO_z / NO_y ratios over periods of hours to days. This approach enabled us to compare subregions with substantially different chemical regimes along the ship track but does not lend itself to the derivation of a representative NO_y budget for the entire region.

The pie charts in Fig. 3 indicate the regional average contributions (in subregions M1 to M7) of reactive nitrogen species to NO_y. The fractional contributions are based on measurements of NO_x, NO_y, gas-phase organic nitrates (ON), particulate nitrate (pNit), $ClNO_2$, and HONO. HNO_3 was not measured directly but calculated from $HNO_3 = NO_y - (NO_x + ON + pNit + ClNO_2 + HONO)$, where pNit refers to submicron particulate nitrate as measured by the HR-ToF-AMS. Detection of coarse-mode pNit by the TD-CRDS (see Friedrich et al., 2020) would lead to an overestimation of HNO_3. However, given that the thermal dissociation to NO_2 of $NaNO_3$ particles with 300 nm diameter is inefficient ($\sim 20\,\%$) with this instrument, a significant bias by coarse-mode nitrate (e.g. associated with sea salt or mineral dust) appears unlikely. The data available in each subregion did not always cover an entire diurnal cycle, which will have an impact on the fractional contributions of individual NO_y species (see differences between day- and night-time chemistry in Sect. 1). We argue, however, that diurnal patterns in NO_y are likely overshadowed by the variability of air mass sources. The NO_y compositions presented are thus to be considered coarse estimates.

In all subregions, HNO_3 is the dominant component of NO_y besides NO_x and therefore the most important NO_z species. Contrastingly, submicron pNit only contributes between 5.4 % (M6) and 15.5 % (M2) to NO_y and ONs between 7.1 % (M4) and 16.9 % (M2). $ClNO_2$ only constitutes a minor part of NO_y with ca. 1 % contribution in all regions where $ClNO_2$ was measured (M1–M6). The low mixing ratios of $ClNO_2$ have been attributed to high night-time temperatures and high reactivity of NO_3 which reduce the interaction of N_2O_5 with chloride-containing particles (Eger et al., 2019a). Elevated HONO mixing ratios (up to 0.3 ppbv) were observed in regions M3 and M6 where its contributions to NO_z was 3.8 % and 4.2 %, respectively. As the daytime lifetime of HONO is short (a few minutes) due to its rapid

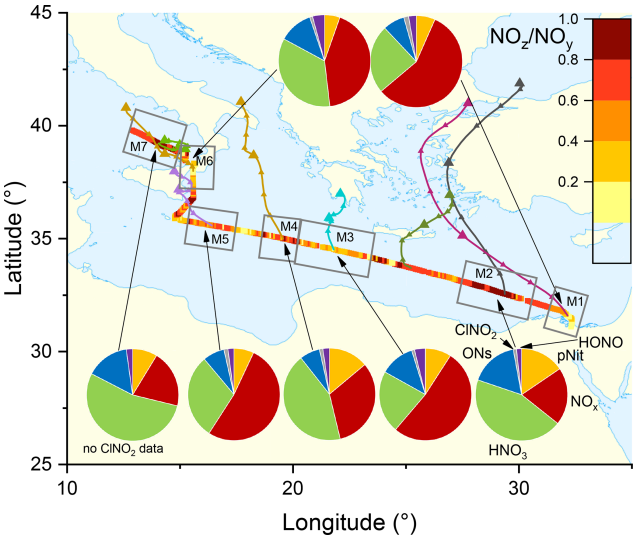

Figure 3. The NO_z / NO_y ratio over the *Mediterranean Sea*. Coloured lines are 2 d back-trajectories (HYSPLIT). The pie charts indicate the components of NO_y at various segments along the ship's track (ONs = organic nitrates, pNit = particulate nitrate). HNO_3 was calculated via $HNO_3 = NO_z$ – (ONs + pNit + $ClNO_2$ + HONO). The colours of the pie chart segments are assigned as follows (clockwise): pNit in yellow, NO_x in red, HNO_3 in green, ONs in blue, $ClNO_2$ in grey, and HONO in magenta.

photolysis (Platt et al., 1980), HONO levels up to 0.3 ppbv imply strong sources. Elevated HONO mixing ratios in ship plumes have been observed in previous field measurements (Večeřa et al., 2008; Sun et al., 2020) and could explain the presence of HONO in subregions M3 and M6. Other sources of HONO, summarised in Elshorbany et al. (2012), include heterogeneous or photochemical reactions of NO_x and NO_z on various surfaces and also the photolysis of particulate nitrate (Meusel et al., 2018).

Figure 3 also plots the NO_z / NO_y ratio along the ship's track. The highest values with median NO_z / $NO_y > 0.68$ were found in regions M2, M4, and M7, reflecting a lack of local NO_x sources as confirmed by the back-trajectories. For visual clarity, only the back-trajectories starting at the geographical centres of the respective subregions are displayed in Fig. 3. Back-trajectories starting at the ship's location 4 h before or after confirmed that the air mass origin was very similar. In contrast, the regions designated M3, M5, and M6 are influenced by fresh emissions from land-based sources and are characterised by low NO_z / NO_y ratios (medians < 0.55), reflecting the higher levels of NO_x which contributed 52 % (M3 and M5) and 43 % (M6) to total NO_y.

3.1.3 Lifetime and sources of NO_x

In the following section, the observations of NO_x in the Mediterranean Sea are analysed in terms of its production and loss. Following the considerations in Sect. 1, we compare the daytime loss of NO_x via the reaction between NO_2 and OH (Reaction R3; expected to dominate over other daytime NO_x loss processes in the marine environment) with night-time losses via the reaction between NO_2 and O_3 (Reaction R8):

$$k^{NO_2} = k_3[OH] + k_8[O_3], \quad (1)$$

where k^{NO_2} represents the total loss rate constant (in s^{-1}) for NO_2 and is the inverse of the NO_2 lifetime (τ^{NO_2}). The first term on the right-hand side of this expression is most important during the day when OH levels were high (up to 1.4×10^7 molec. cm^{-3} at local noon) but relatively unimportant at night. In contrast, the second term on the right is only important at night as the NO_3 product of R8 is rapidly photolysed back to NO_x during daytime so that NO_x is conserved.

By using Eq. (1) to approximate the NO_2 loss rate constant, we neglect two further processes which can, under some conditions, influence the lifetime of NO_2. Our approach assumes that the night-time formation of NO_3 leads to the removal of one NO_2 molecule. This approach would be invalid if a significant fraction of NO_3 would be lost via formation (and subsequent heterogeneous loss) of N_2O_5. Firstly, we note that formation of N_2O_5 was hindered during AQABA by the high gas-phase reactivity of NO_3 towards VOCs (Eger et al., 2019a) and that the transfer of N_2O_5 to the particle phase was hindered by high temperatures. For example, taking an N_2O_5 uptake coefficient $\gamma_{N_2O_5}$ of 0.03 (as found for polluted marine environments by Aldener et al., 2006) and the median night-time aerosol surface area (ASA) in the Mediterranean Sea of 1.78×10^{-6} cm^2 cm^{-3} (Eger et al., 2019a), we estimated a loss rate constant for uptake of N_2O_5 of 3.5×10^{-4} s^{-1}, which is 2 orders of magnitude lower than the rate constant (4.9×10^{-2} s^{-1}) for thermal decomposition at 25.7 °C (the mean, minimum night-time temperature in the Mediterranean Sea).

We also neglect the loss of NO_x via uptake of NO_2 onto black carbon (BC) particles. Using a literature uptake coefficient γ_{NO_2} of ca. 1×10^{-4} (Longfellow et al., 1999) and the aforementioned ASA, the first-order loss rate constant for the heterogeneous uptake would be 1.8×10^{-6} s^{-1}. Using an O_3 mixing ratio of 63.4 ppbv (equal to night-time median mixing ratio in the Mediterranean Sea), we calculate a first-order loss rate constant for the reaction of NO_2 and O_3 of 5.5×10^{-5} s^{-1}, which implies that > 95 % of total NO_2 loss at night-time NO_2 is due to O_3. Uptake of NO_2 might, therefore, be relevant for HONO formation (see Sect. 3.4) but does not constitute a relevant loss process for NO_x.

In order to fill gaps in the OH data set (daytime data coverage of 71 %), complete diel cycles of OH were generated by scaling measurements of J_{O^1D} to the OH noon-time maxima. Figure S4 compares the measured OH concentrations with the interpolated trace and shows that the thereby derived OH levels can be considered upper limits. Inserting these values and the measured O_3 concentration into Eq. (1) and using

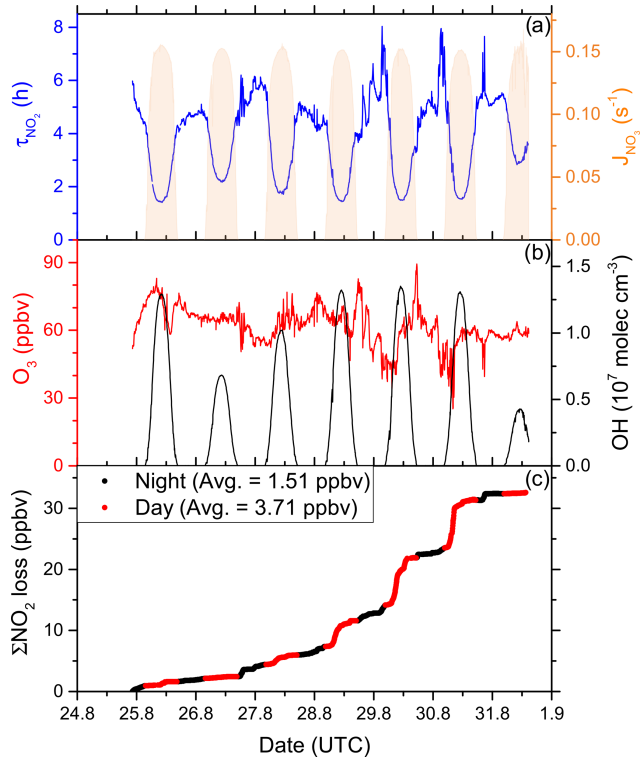

Figure 4. **(a)** Lifetime (τ) of NO_2 due to reactions with OH and O_3 in the *Mediterranean Sea*, together with concentrations of O_3 and OH. The OH trace is an interpolation based on OH measurements and J_{O^1D} (see Sect. 3.1.3). Daytime hours are indicated via J_{NO_3}. **(b)** Cumulative loss of NO_2 during the displayed time frame, based on the calculated lifetimes and measured NO_2.

preferred rate coefficients for k_3 and k_8 (IUPAC, 2020) we derive lifetimes (Fig. 4a) of ~ 2 h at local noon (largest OH levels) and 5–6 h at night. Loss of NO_x by deposition may be important in forested regions (Delaria et al., 2018; Delaria and Cohen, 2020) but is expected to be insignificant in a marine environment. The relative importance of day- and night-time losses of NO_2 in the Mediterranean Sea during AQABA was estimated by integrating the two loss terms using the available NO_2, O_3, and OH data. Averaged over the 6 d of measurements, 3.71 ppbv of NO_x was lost per 12 h day and 1.51 ppbv was lost per 12 h night (Fig. 4c).

Although our conclusion is based on a limited data set, we calculate that the OH-induced daytime loss of NO_x is most important in the Mediterranean Sea, reflecting the high levels of OH encountered during AQABA, but we note that night-time losses make a significant contribution. It is very likely that in other seasons with reduced photochemical activity and lower temperatures (which favour the formation of N_2O_5 which can remove two NO_2 molecules via heterogeneous processes), the night-time losses gain in relative importance. Averaged over the entire data set obtained in the Mediterranean Sea, we calculate a lifetime of NO_2 of 3.9 h. Chemical sources of NO_x in the Mediterranean Sea, i.e. from the photolysis of HONO and pNit, as well the reaction of OH and HNO_3, are discussed in detail in Sect. 3.4.

In the following, we examine the contribution of ship emissions to the NO_x budget in the Mediterranean region and especially along the track taken by the *Kommandor Iona* during the AQABA campaign. In Fig. S5 we plot a time series of NO_x and SO_2 data for the transit through the Mediterranean Sea. It is immediately apparent that large plume-like features in NO_x coincide with similar features in SO_2. We now separate the data set into two regimes in which the NO_z and NO_y measurements indicate either relatively "fresh" emissions (NO_z / NO_y ratio < 0.4) or relatively "aged" emissions (NO_z / NO_y ratio > 0.8). In Fig. 5a we show that, for fresh emissions, SO_2 and NO_x are highly correlated (Pearson's $R = 0.84$) with a slope of 4 ± 0.1 ppbv NO_x per ppbv SO_2 and an intercept (at zero SO_2) of -1.9 ± 0.3 ppbv. This strongly suggests that fresh NO_x emissions are generally accompanied by SO_2 and thus indicates that either ships or power plants, e.g. in coastal locations, are the likely sources of a large fraction of the NO_x. The slope is similar to that derived by Celik et al. (2020) (2.7 ± 0.8), who examined single ship plumes in a more detailed analysis and with literature values that range from 6.8 ± 6.3 near the coast of Texas (Williams et al., 2009) to 11.2 ± 10.9 (Diesch et al., 2013) at the Elbe river near Hamburg/Germany. In comparison to Celik et al. (2020), however, the two other literature studies only sampled very fresh and unprocessed ship plumes, from a distance of less than ca. 5 km to the emission source. Fig. 5a shows that NO_z and SO_2 are not correlated (Pearson's $R = 0.38$) in air masses impacted by fresh emissions.

In more aged air masses (Fig. 5b) the slope of NO_x per SO_2 is, as expected, much smaller (0.16 ± 0.01 ppbv NO_2 per ppbv SO_2) which reflects the significantly longer lifetime of SO_2 (~ 10 d) compared to NO_x. After a few days of transport an air mass containing co-emitted NO_x and SO_2 will still contain SO_2 but the initially emitted NO_x will, to a large extent, have been converted to NO_z. The intercept ($NO_x = 0.049 \pm 0.005$ ppbv at zero SO_2) is consistent with the re-generation of NO_x from NO_z (see above) but is also in the area of the detection limit of the NO_x measurement.

The plot of NO_z versus SO_2 for aged emissions indicates a significant intercept (at zero SO_2) of 0.4 ppbv NO_z. As the lifetime of SO_2 (~ 10 d) is longer than of NO_z ($\sim$ half a day) (Dickerson et al., 1999; Romer et al., 2016), the residual NO_z at zero SO_2 cannot stem directly from ship emissions (or combustion sources that generate both NO_x and SO_2) but represents the background level of NO_z in the Mediterranean Sea in aged air masses and is consistent with an average HNO_3 mixing ratio of 0.48 ppbv observed during the MINOS campaign at Finokalia on Crete (Metzger et al., 2006).

The analysis above, when combined with back-trajectory information, provides clear evidence that shipping emissions are responsible for a large fraction of NO_x in the Mediterranean Sea. The impact of shipping emissions on the atmospheric sulfur budget has been assessed in numerous stud-

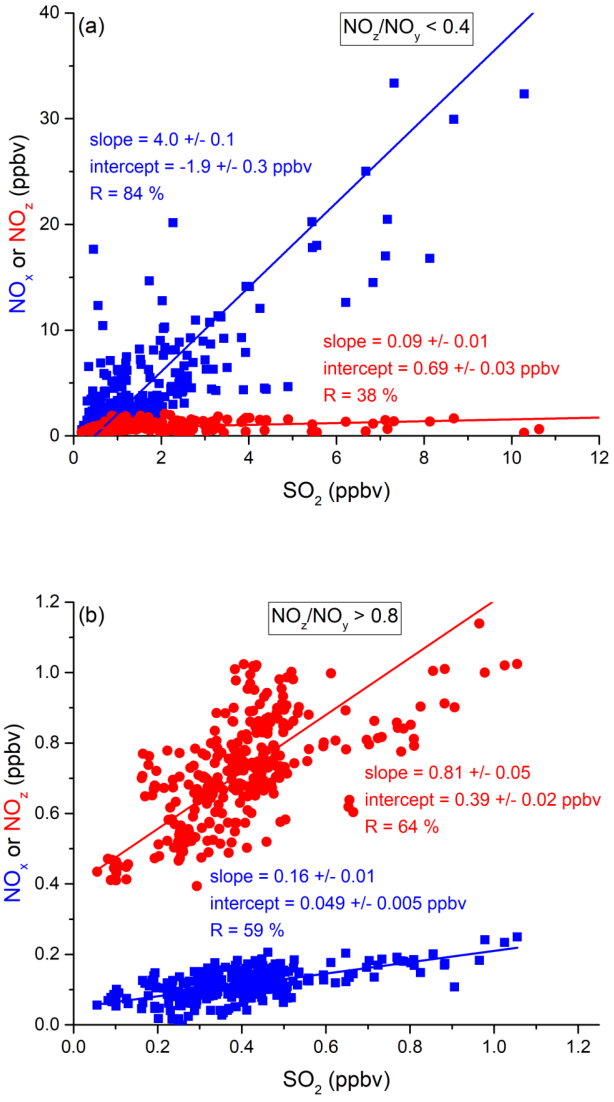

Figure 5. Correlation between SO_2 and NO_x or NO_z for **(a)** fresh and **(b)** aged NO_x emissions in the *Mediterranean Sea*.

ies which identify coastal areas and international shipping lanes as important hotspots for SO_2 emissions (Capaldo et al., 1999; Dalsøren et al., 2009; Eyring et al., 2010), with emissions of SO_2 severely impacting air quality in port regions (Isakson et al., 2001; Cooper, 2003; Saxe and Larsen, 2004; Marmer and Langmann, 2005; Ledoux et al., 2018). A detailed analysis of SO_2 data with regard to ship emissions during AQABA is provided by Celik et al. (2020), who analysed emission factors from individual ship plumes during the AQABA campaign.

3.2 Red Sea

Measurements over the Red Sea (from the Suez Canal and the Strait of Bab al-Mandab) were made from 2–16 July 2017 on the first leg and 17–25 August 2017 on the second leg. On the first leg, the *Kommandor Iona* reversed direction in the northern Red Sea three times (twice for 9 h and once for 6 h), in order to sail into the wind and avoid contamination by the ship's own stack. Additionally, there was a 3 d layover in Jeddah (10 to 13 July 2017). Temperatures on the first leg were usually above 27 °C, with maxima of 37–38 °C in the Suez Canal, in Jeddah, and on the approach to Bab al-Mandab. The relative humidity was usually between ca. 60 % and 80 % but dropped below 30 % in the Suez Canal and in Jeddah. Winds came predominantly from northerly directions with speeds generally between 2 and 10 m s^{-1}. On the second leg, temperatures were constantly above 30 °C in the southern Red Sea; relative humidities were similar to the first leg. The wind was consistently from the north, with wind speeds between 5 and 12 m s^{-1} until the ship reached the Suez region. During the first leg, the air masses intercepted above the northern Red Sea were impacted by emissions from Cairo and the Nile valley. Two-day back-trajectories for the southern Red Sea start in the centre of the Red Sea and do not indicate transport from the Suez region. Extended back-trajectories for the southern Red Sea showed that 3 to 4 d prior to sampling, the air parcel passed over southern Egypt, and 5 to 6 d before it was located over the Cairo area. Similar back-trajectories were obtained for the second leg. Air masses in the northern Red Sea were influenced by the Suez region, north-eastern Egypt, and Israel.

3.2.1 NO_x

NO_x mixing ratios in the Red Sea (excluding the 3 d layover in the port of Jeddah) as measured by the TD-CRDS and the CLD instruments are displayed in Fig. 6a. NO_x mixing ratios were highly variable and there were only short periods free of NO_x plumes > 10 ppbv (e.g. during the second leg on 19 and 20 August 2017). The mean NO_x mixing ratios (2.8 ppbv measured by the TD-CRDS and 3.2 ppbv measured by the CLD) were therefore significantly higher than the median values of 1.0 ppbv. Figure 6b indicates that the NO_x mixing ratios are broadly distributed around the median of 1.0 ppbv with 21 % of all data points > 3 ppbv. The highest NO_x levels during AQABA were found in narrow shipping corridors of the Suez region and the Strait of Bab al-Mandab. When excluding the Suez and Bab al-Mandab regions, a median NO_x mixing ratio of 0.7 ppbv can be derived for the maritime central part of the Red Sea.

To the best of our knowledge, in situ measurements in the Red Sea area are not available for comparison with our NO_x data. Satellite-based modelling studies show that high NO_2 column densities above the Red Sea are associated with shipping emissions (Richter et al., 2004; Alahmadi et al., 2019), which is consistent with our observation of a strong correlation between NO_x and SO_2 (see below). Johansson et al. (2017) have estimated a NO_x emission rate of 0.70 t km^{-2} yr^{-1} for the Red Sea (including the Suez region).

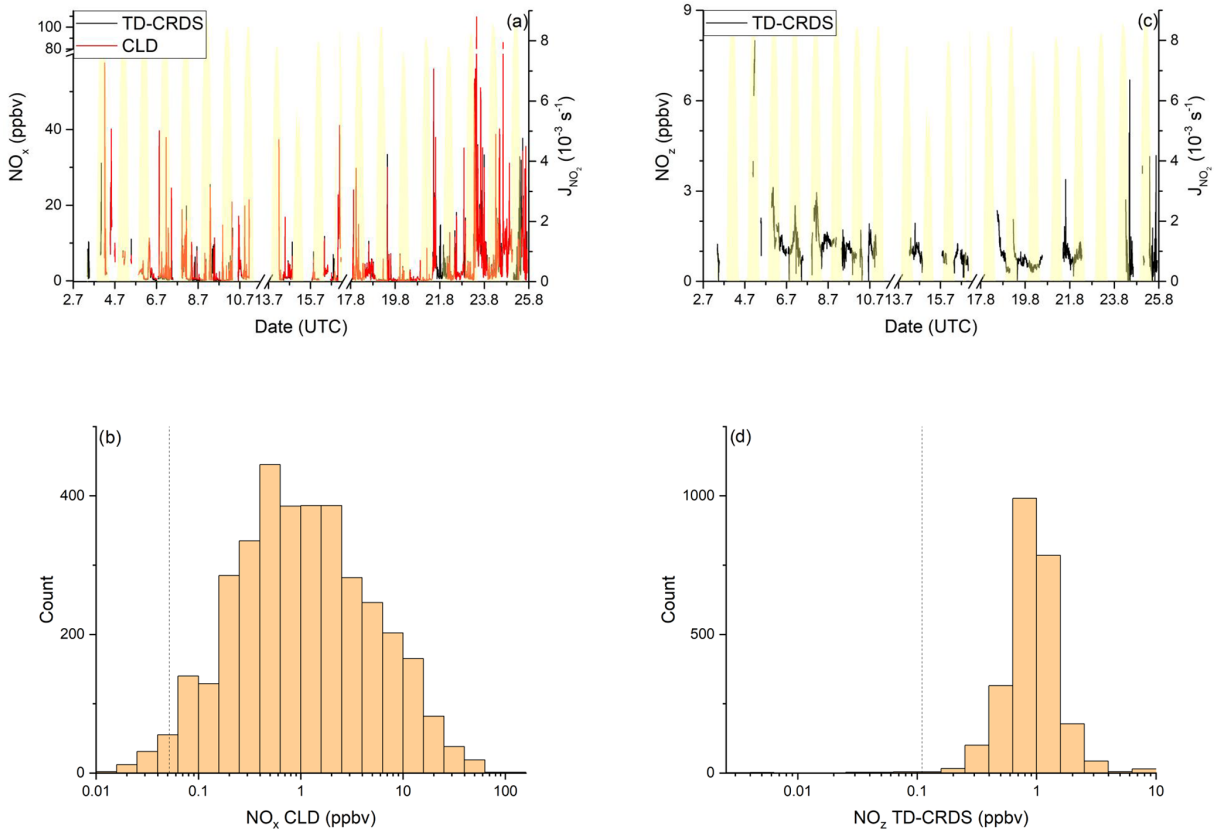

Figure 6. NO_y measurements in the *Red Sea*. Dashed lines signify the instrument detection limits. **(a)** NO_x mixing ratios by CLD and TD-CRDS. **(b)** Frequency distribution of NO_x mixing ratios during 2–16 July 2017 and 17–24 August 2017, excluding the layover in Jeddah. **(c)** NO_z mixing ratios by TD-CRDS. **(d)** Frequency of NO_z mixing ratios during 2–16 July 2017 and 17–24 August 2017. The yellow shaded regions show J_{NO_2}. The vertical dotted lines are the limits of detection of the respective measurements.

3.2.2 NO_z

The mean mixing ratio of NO_z over the Red Sea was 1.0 ppbv, with a maximum value of 8.0 ppbv measured in the Gulf of Suez on the first leg. NO_z mixing ratios are narrowly distributed (see Fig. 6d) around a median value of 0.7 ppbv, with 53 % of the measurements between 0.4 and 1.0 ppbv and 41 % between 1.0 and 4.0 ppbv.

The NO_z / NO_y ratios along the ship's track are plotted in Fig. 7: values > 0.6 were mostly observed over the northern Red Sea on the first leg, after leaving the Gulf of Suez. On the second leg, the NO_z / NO_y ratio was higher in the southern Red Sea. NO_z data coverage was limited in the Red Sea on both legs and the NO_z / NO_y ratio was more variable than values found in the Mediterranean Sea and the Arabian Gulf. The high variability in the NO_z / NO_y ratios is caused by the route of the *Kommandor Iona* along the main shipping lane connecting the Suez Canal and the Gulf of Aden and the frequent sampling of plumes from nearby ships. The observed NO_z / NO_y ratios of < 0.6 in the Red Sea highlight the impact of NO_x emissions from shipping on the reactive nitrogen budget and the air quality in the Red Sea region (as discussed in Sect. 3.2.1).

For the Red Sea, we have defined four subregions in which we calculate the contributions of NO_x and various NO_z species to NO_y: these are RS1 on the first leg and RS2, RS3, and RS4 on the second leg. Note that RS1 and RS4 are both located in the northern Red Sea, but the measurements ($\sim$ 5 weeks apart) revealed different chemical characteristics; hence the separate treatment.

Due to poor data coverage, mainly of organic nitrates, we were not able to perform this calculation in further subregions on the first leg. In all four regions, NO_x was the largest component of NO_y which results from continuous NO_x input from onshore and shipping emissions.

In RS1 we observed the lowest contribution (36.4 %) of NO_x to NO_y and the largest contribution of ONs (23.8 %) to NO_y, over the Red Sea. The latter value is the highest found during the entire AQABA campaign and is comparable to the contribution of HNO_3 (30.0 %). In roughly co-located RS4, but 5 weeks later, the NO_x contribution was much larger (69.5 %). The divergent median NO_x / NO_y and NO_z / NO_y for subregions RS1 and RS4 can be understood

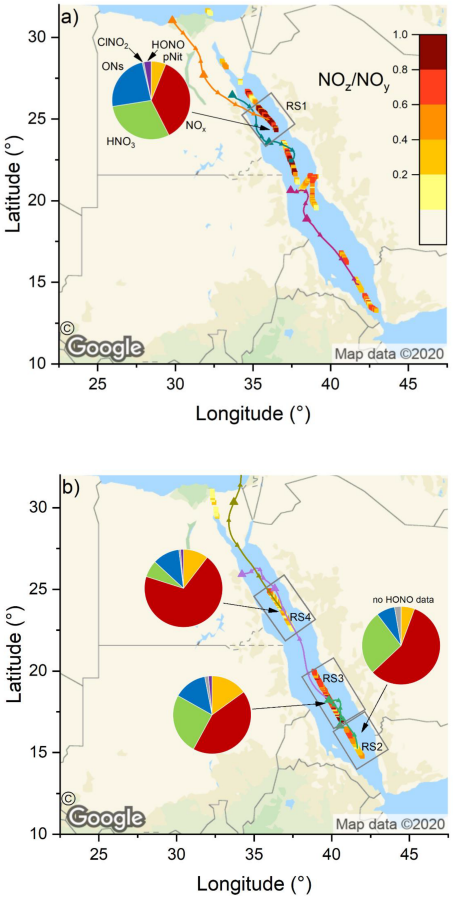

Figure 7. The NO_z / NO_y ratio over the Red Sea during the **(a)** first and **(b)** second leg. Coloured lines are 2 d back-trajectories (HYSPLIT). The pie charts indicate the components of NO_y at various segments along the ship's track (ONs = organic nitrates, pNit = particulate nitrate). HNO_3 was calculated via $HNO_3 = NO_z - (ONs + pNit + ClNO_2 + HONO)$. The colours of the pie chart segments are assigned as follows (clockwise): pNit in yellow, NO_x in red, HNO_3 in green, ONs in blue, $ClNO_2$ in grey, and HONO in magenta (© Google Maps).

when one examines the air mass back-trajectories for the two legs. On the second leg, strong northerly winds transported NO_x from the highly polluted southern end of the Gulf of Suez to RS4, whereas during the first leg the back-trajectory for RS1 passed (with lower wind speeds) mainly over eastern Egyptian deserts, with emissions from Cairo requiring 36 h to reach RS1 during which a significant fraction of NO_x was converted to NO_z. We expect that the large contribution of ONs in RS1 is a result of the unique chemical environment at the southern end of the Gulf of Suez and in the northern Red Sea. A large coherent oil field is located south of the Gulf of Suez and the coast of eastern Egypt (Alsharhan, 2003), and the numerous facilities for oil extraction result in abundant emissions of VOCs, while the proximity to the Gulf of Suez and the narrowing shipping corridor on the approach to Suez provides the NO_x required for formation of organic nitrates (ONs). Meteorological conditions additionally favoured a build-up of ONs during our passage through RS1: elevated wind speeds of up to 11 m s^{-1} coincided with temperatures below 30 °C, which slowed down the thermal decomposition of PAN (peroxyacetyl nitrate) compared to the ca. 35 °C regime in the Arabian Gulf. Average PAN mixing ratios, as measured by chemical ionisation mass spectroscopy (CIMS), were 190 pptv in this area, which constitutes ca. 20 % of the total ONs signal. On the second leg in RS4, the fractional contribution of ONs was overshadowed by the stronger impact of NO_x pollution from the Suez region (see above).

In RS1 and RS4 the contributions of HONO and $ClNO_2$ to NO_y were minor (≤ 3 %). RS2 and RS3 are both located in the southern half of the Red Sea. For RS3 we observed the highest contribution (15 %) of AMS-measured particulate nitrate to NO_y, and RS3 was characterised in large parts by coarse-mode OPC fractions > 85 % (i.e. (PM_{10}-PM_1) / PM_{10}; see 18 and 19 August 2017 in Fig. S1). It is reasonable to assume that the coarse-mode particle mass concentrations in this area was due to sea salt, which reacts heterogeneously with HNO_3 to form particle-phase nitrates (Mamane and Gottlieb, 1990). Refractory sea salt aerosol particles in the PM_1 size range are, however, not expected to be detectable via AMS (Jimenez et al., 2003) or with only very low efficiency (ca. 1 %) (Zorn et al., 2008).

Region RS2 shows a intermediate behaviour, as NO_z / NO_y increases after leaving Bab al-Mandab and transported air only came from the surrounding southern Red Sea without being influenced by shore-side anthropogenic activities. Here, NO_x and HNO_3 contribute 57 % and 27 %, respectively. The relatively high NO_x contribution, considering the remote area, can be explained by sampling ship plumes on the departure from Bab el-Mandab, which led to several NO_x peaks above 10 ppbv (see Fig. 6a). Consequently, background NO_x levels also did not fall below ca. 1.5 ppbv on the night from 17 to 18 August 2017. Overall, the fractional contributions of NO_x were positively biased by short-term spikes in NO_x mixing ratios caused by ship plumes in all Red Sea subregions. The use of mean values to assess the fractional contributions of NO_y species in certain subregions is thus a caveat of this analysis, as NO_z signals exhibit less variability during pollution events (see Fig. 6c). Employing the median values, however, would not allow the relative contributions to NO_y to be assessed.

3.2.3 Lifetime and sources of NO_x

Analogous to Sect. 3.1.3, we now investigate the day- and night-time chemical losses of NO_2 in the Red Sea (see Fig. 8). As described previously, we used an interpolated OH data set based on a scaling factor between the available OH data and J_{O^1D}.

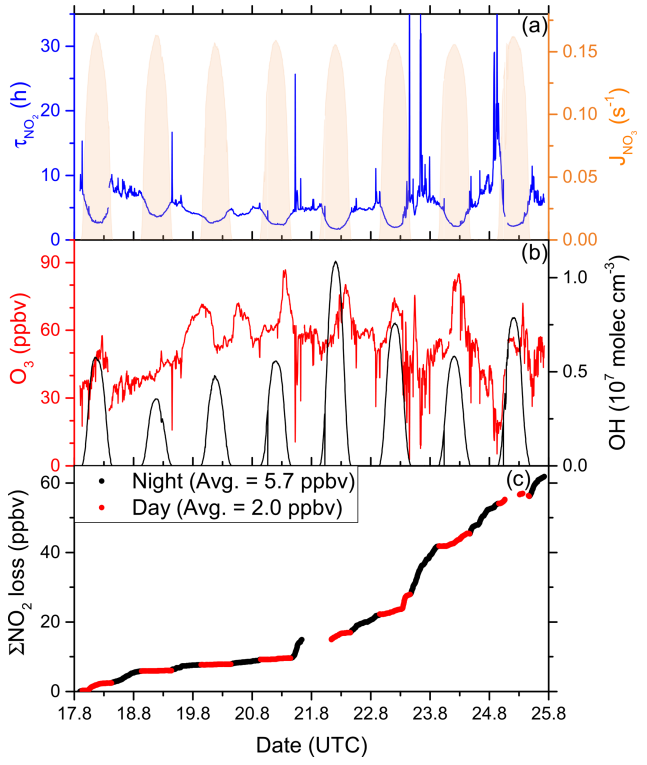

Figure 8. **(a)** Lifetime (τ) of NO_2 due to reactions with OH and O_3 along the second *Red Sea* leg, together with concentrations of O_3 and OH. The OH trace is an interpolation based on OH measurements and J_{O^1D} (see Sect. 3.2.3). Daytime hours are indicated via J_{NO_3}. **(b)** Cumulative loss of NO_2 during the displayed time frame, based on the calculated lifetimes and measured NO_2.

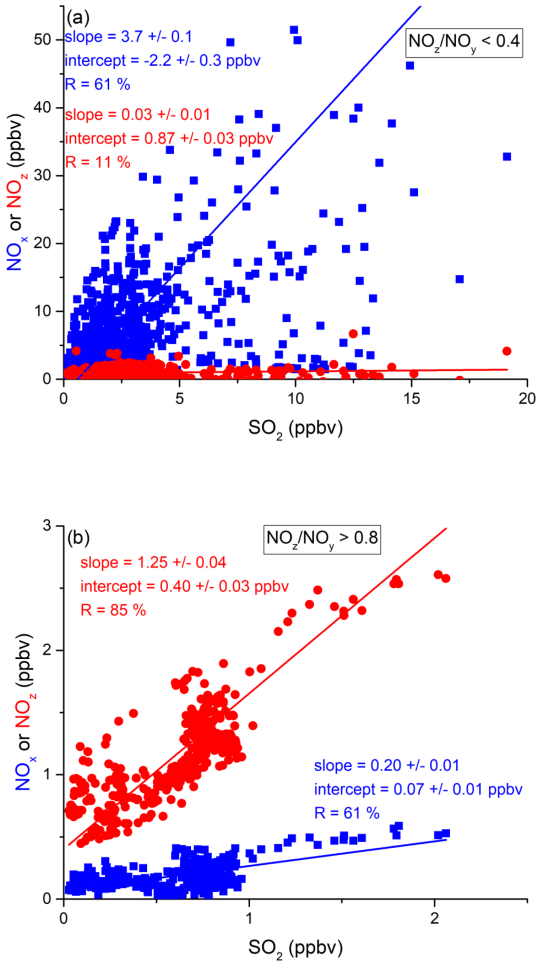

Figure 9. Correlation between SO_2 and NO_x or NO_z for **(a)** fresh and **(b)** aged NO_x emissions in the *Red Sea*.

As OH was not measured over the Red Sea on the first leg, our analysis is restricted to the second leg only. Daytime NO_2 lifetimes with respect to loss by reaction with OH were usually in a range between 2 and 4 h, with a minimum of 1.7 h on 21 August 2017, where the noon-time OH concentration peaked at 1.1×10^7 molec. cm^{-3}. Night-time NO_2 lifetimes (determined by O_3 levels) exhibited a larger variability but were mostly between 5 and 10 h. The average (day and night) NO_2 lifetime in the Red Sea was 5.0 h.

Over the entire period of measurements in the Red Sea (8 d and 8 nights) we calculate that a cumulative total of 62 ppbv of NO_2 were lost (Fig. 8c). Despite the shorter lifetime of NO_2 at noon, the greater integrated loss of NO_2 occurred during night-time (5.7 ppbv per night on average) when continually high O_3 levels (median 54 ppbv) were available. At midday, NO_2 mixing ratios are reduced due to the shift in the NO_2 / NO ratio caused by the rapid photolysis of NO_2 and also because the OH levels are highest then. On average, daytime loss rates were 2.0 ppbv per day.

In order to assess the contribution of shipping on NO_x emissions, we correlated NO_x and SO_2 mixing ratios for freshly emitted (NO_z / $NO_y < 0.4$) and chemically more aged (NO_z / $NO_y > 0.8$) air masses. The results are illustrated in Fig. 9 and summarised in Table 2, which reveal a positive correlation (slope of 3.7 ± 0.1 and a regression coefficient R of 0.61) between NO_x and SO_2 in air masses containing freshly emitted pollutants. Six data points far above 20 ppbv (range 43–128 ppbv SO_2) were excluded, as they would bias the linear regression result. Including these data points lowers the slope to 1.26 ± 0.04 and the correlation coefficient R to 0.40. The NO_x / SO_2 ratio is thus highly variable throughout the Red Sea, potentially reflecting variable NO_x / SO_2 emission ratios of different vessels, using various fuels, as well as the impact (on NO_x) of offshore oil-drilling rigs and shore-side oil refineries. The latter are most important in the northern Red Sea, whereas shipping emissions dominate in the narrow shipping lanes of the Suez Canal.

For chemically aged air masses, the NO_x / SO_2 ratio is 0.20 ± 0.01 with $R = 0.61$ and the reduction in slope reflecting the shorter lifetime of NO_x compared to SO_2. We find, however, that in chemically aged air masses, NO_z and SO_2 are highly correlated (Fig. 9b) with a slope NO_z / SO_2 of 1.25 ± 0.04 and $R = 0.85$. The intercept (see Fig. 9b) at an

Table 2. Summary of correlation results between NO_x / NO_z and SO_2 in all regions.

Region	NO_z / NO_y	Species	Slope	Intercept (ppbv)	R (%)
Mediterranean Sea	< 0.4	NO_x	4.0 ± 0.1	-1.9 ± 0.3	84
		NO_z	0.09 ± 0.01	0.69 ± 0.03	38
	> 0.8	NO_x	0.16 ± 0.01	0.049 ± 0.005	59
		NO_z	0.81 ± 0.05	0.39 ± 0.02	64
Red Sea	< 0.4	NO_x	3.7 ± 0.1	-2.2 ± 0.3	61
		NO_z	0.03 ± 0.01	0.87 ± 0.03	11
	> 0.8	NO_x	0.20 ± 0.01	0.07 ± 0.01	61
		NO_z	1.25 ± 0.04	0.40 ± 0.03	85
Arabian Gulf	< 0.4	NO_x	4.1 ± 0.2	-7.4 ± 0.7	41
		NO_z	0.20 ± 0.02	0.73 ± 0.06	46
	> 0.8	NO_x	0.11 ± 0.01	0.11 ± 0.04	72
		NO_z	0.88 ± 0.07	0.0 ± 0.3	68

SO_2 mixing ratio of zero is 0.40 ± 0.03 ppbv, which can be taken to be the regional NO_z background mixing ratio (i.e. NO_z formed from NO_x which was not emitted from SO_2-containing fuels).

3.3 Arabian Gulf

Data over the Arabian Gulf (see Fig. 10) were obtained from 24 to 31 July 2017 (first leg) and 31 July to 3 August 2017 (second leg). During the 4 d layover in the harbour of Kuwait, the TD-CRDS was not operational. The highest temperatures during the AQABA campaign were found in the Arabian Gulf with daytime temperatures up to 46 °C at Kuwait harbour and 38–39 °C offshore. Night-time temperatures were constantly above 30 °C on both legs. Offshore relative humidities were between 60 % and 90 % during both legs; wind speeds were generally below $6\,m\,s^{-1}$ and frequently 1–2 $m\,s^{-1}$. The Arabian Gulf crossing was divided into four subregions: A1 and A2 on the first leg and A3 and A4 on the second leg (see Fig. 11).

Air mass back-trajectories indicated that air sampled in the Gulf of Oman originated in Oman; the south-eastern Arabian Gulf was influenced by transport from the central Arabian Gulf and Saudi Arabia. Inside A1, samples were affected by the eastern coast of Saudi Arabia. When approaching Kuwait (area A2), back-trajectories originated from Iraq. During the second leg, the northern Arabian Gulf region was dominated by stagnating air masses, mainly containing emissions from local sources and from the direction of Iran. Air from this area was also transported to the central Arabian Gulf, which is covered by subregion A3. Local sources from inside the shipping lane were dominant when passing the Strait of Hormuz (A4). The Gulf of Oman experienced influx from the remote Arabian Sea in contrast to the first leg.

3.3.1 NO_x

Elevated NO_x mixing ratios were detected by both TD-CRDS and CLD throughout the Arabian Gulf (see Fig. 10a). The TD-CRDS measured mean and median NO_x mixing ratios of 3.3 and 1.6 ppbv, respectively. By comparison, the CLD measured an average of 4.1 ppbv and a median of 1.8 ppbv. The large difference between median and mean reflects the numerous plumes of high NO_x detected by both instruments (Fig. 10a). The deviation of the TD-CRDS and the CLD data is caused by different data coverage as the CLD continued measuring in the most polluted areas close to Fujairah and Kuwait, while the TD-CRDS was switched to zeroing mode, in order to avoid contamination of the inlet lines. When limiting the comparison to periods where both instruments were operating, very similar median values are obtained, with 1.6 ppbv from the TD-CRDS and 1.5 ppbv from the CLD. A histogram of the NO_x measurements (CLD data only) made in the Arabian Gulf (Fig. 10b) shows a broad distribution, reflecting high variability in the region, with 77 % of the data points falling into a range between 0.4 and 10 ppbv and a broad maximum at 1–3 ppbv. The highest NO_x daily maxima were observed near Fujairah (up to 34 ppbv on the first and 153 ppbv on the second leg), in the Strait of Hormuz (26 and 30 ppbv), and when approaching and departing Kuwait (43 and 90 ppbv). The locations of these maxima close to the shore or in narrow shipping corridors and the plume-dominated time series suggest the influence of mostly local pollution sources of NO_x, i.e. from ship traffic or from industrial activities in the shore-side areas of the neighbouring cities. NO_x mixing ratios < 0.5 ppbv were found exclusively in the central part of the Arabian Gulf, which is the widest part (least influence from onshore activity) with the largest spread of the shipping lanes.

The generally very high levels of NO_x in the Arabian Gulf are consistent with results from satellite measurements which have identified high NO_2 tropospheric vertical column den-

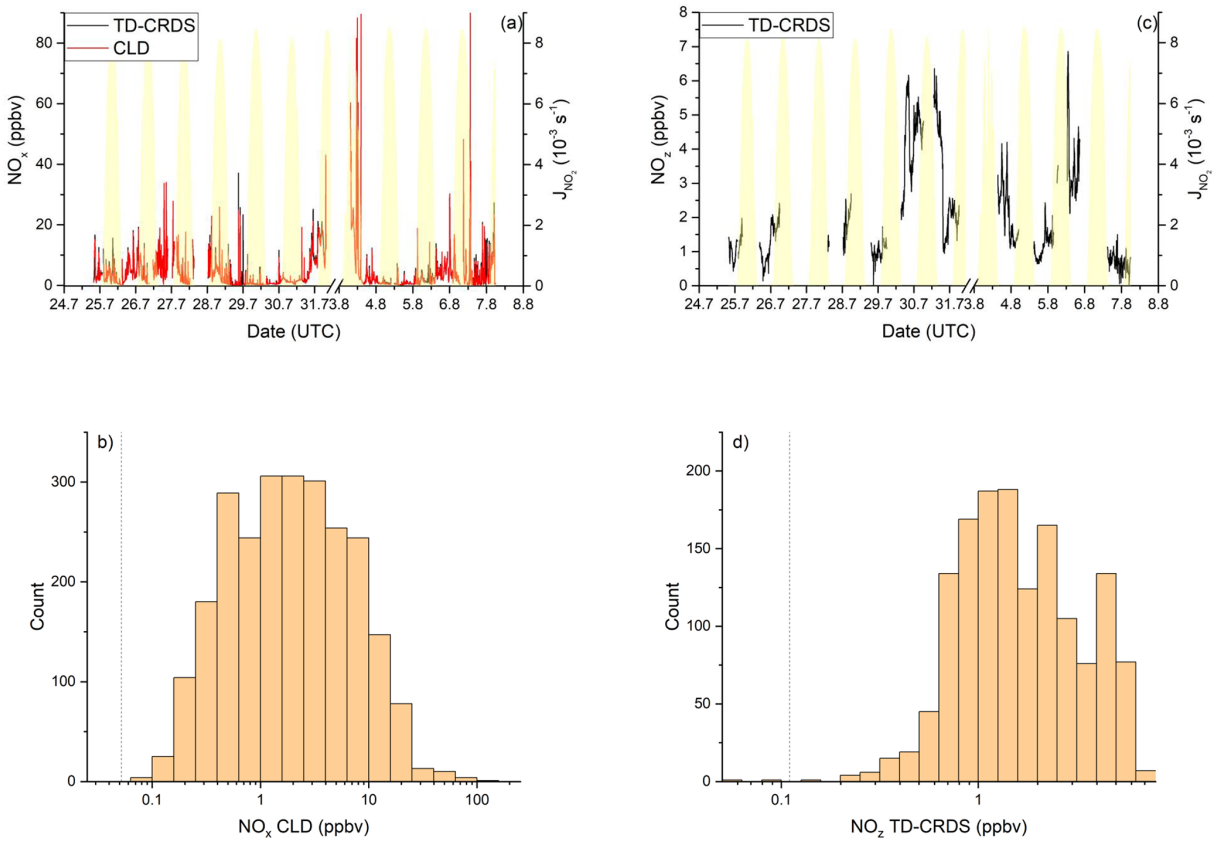

Figure 10. NO_y measurements in the *Arabian Gulf*. Dashed lines signify the instrument detection limits. **(a)** NO_x mixing ratios by CLD and TD-CRDS. The NO_x peak in the afternoon of 6 August 2017 reached 153 ppbv. **(b)** Frequency of NO_x mixing ratios between 24 July and 7 August 2017, excluding the layover in Kuwait. **(c)** NO_z mixing ratios by TD-CRDS. **(d)** Frequency of NO_z mixing ratios between 24 July and 7 August 2020. The yellow shaded regions show J_{NO_2}.

sities over the Gulf of Oman, the Strait of Hormuz, and the south-eastern Arabian Gulf (Beirle et al., 2004). Model studies estimate a NO_x emission rate of 1.13 t km^{-2} yr^{-1} for the Arabian Gulf (Johansson et al., 2017). With a NO_x lifetime of 4.0 h (see Sect. 3.3.3) and a boundary layer height of 1 km (Wu et al., 2008), this emission rate translates to a NO_x mixing ratio of 0.3 ppbv. The lower mixing ratio, compared to the median NO_x observed on AQABA (see above), is likely caused by the averaging of the model over the entire Arabian Gulf water surface area, whereas the *Kommandor Iona* followed common shipping routes with larger NO_x emissions. To the best of our knowledge, there are no in situ measurements of NO_x over the Arabian Gulf with which to compare our data.

3.3.2 NO_z

The Arabian Gulf featured the highest NO_z levels during the AQABA campaign (see Fig. 10c), with mixing ratios from < 0.1 ppbv up to 6.9 ppbv (mean 2.0 ± 1.5 ppbv (standard deviation) and median of 1.5 ± 0.7 ppbv (median absolute deviation)). The histogram of NO_z mixing ratios (Fig. 10d) shows a maximum in the frequency distribution at 1–3 ppbv, with 73 % of all data above 1 ppbv and 15 % above 4 ppbv. Our results thus indicate that the Arabian Gulf is a hotspot for NO_z formation, which is a result of high levels of the NO_x and VOCs precursors and also O_3. The spatial distribution of the NO_z / NO_y ratio for both legs is presented in Fig. 11. On both legs, NO_z / NO_y ratios above 0.8 were found in the central part of the Arabian Gulf, which results from the processing of NO_x emissions during transport from the shore to the centre of the Arabian Gulf.

We now examine the partitioning of NO_y into its various components in the four subregions (A1–A4) defined above for the Arabian Gulf (Fig. 11). On the approach to Kuwait (A2), winds from the north transported fresh NO_x emissions from cities in Kuwait and Iraq to the ship and NO_x accounted for 81 % of NO_y. More aged air masses were found in other regions (A1, A3, and A4) with a roughly equal split between NO_x and HNO_3 (both 45 %–50 %) observed in A3 and A4. The major component of NO_z was HNO_3 in all regions, with significant but very variable contribution from organic nitrates, especially in A1 (13 ± 16 %) where the air masses originated from the eastern coast of Saudi Arabia, which ac-

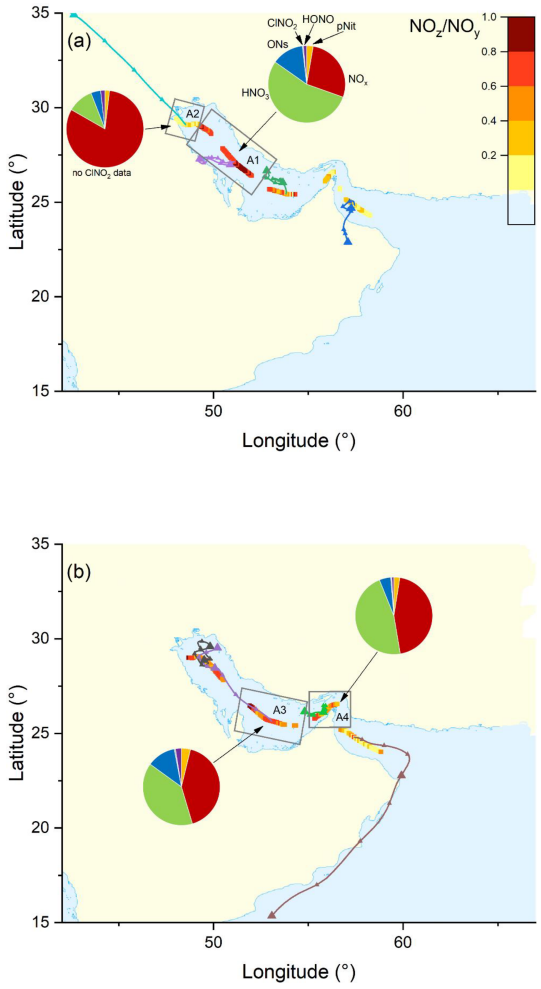

Figure 11. The NO_z / NO_y ratio over the Arabian Gulf during the **(a)** first and **(b)** second legs. Coloured lines are 2 d back-trajectories (HYSPLIT). The pie charts indicate the components of NO_y at various segments along the ship's track (ONs = organic nitrates, pNit = particulate nitrate). HNO_3 was calculated via $HNO_3 = NO_z - (ONs + pNit + ClNO_2 + HONO)$. The colours of the pie chart segments are assigned as follows (clockwise): pNit in yellow, NO_x in red, HNO_3 in green, ONs in blue, $ClNO_2$ in grey, and HONO in magenta.

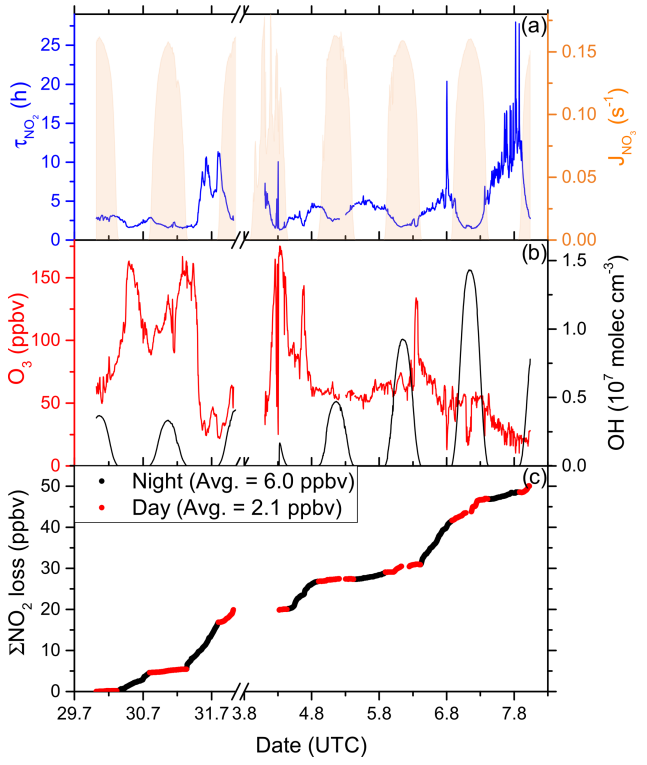

Figure 12. (a) Lifetime (τ) of NO_2 due to reactions with OH and O_3 in the *Arabian Gulf*, together with concentrations of O_3 and OH. The OH trace is an interpolation based on OH measurements and J_{O^1D} (see Sect. 3.3.3). Daytime hours are indicated via J_{NO_3}. **(b)** Cumulative loss of NO_2 during the displayed time frame, based on the calculated lifetimes and measured NO_2.

commodates numerous facilities for oil and gas extraction and processing, resulting in high levels of organic trace gases including alkanes, alkenes, and aromatics (Bourtsoukidis et al., 2019). Particulate nitrate contributed only minor amounts to NO_z in the Arabian Gulf, which reflects the high temperatures and resultant partitioning of nitrate into the gas phase. Other NO_z species contributed only weakly to the NO_z as indicated in Fig. 11.

3.3.3 Lifetime and sources of NO_x

Analogously to Sect. 3.1.3, we also determined NO_2 lifetimes and the cumulative loss of NO_2 in the Arabian Gulf. The results are presented in Fig. 12. Limited by the availability of OH data, these calculations include only the time period after 29 August 2017 on the first leg. In the same way as in Sect. 3.1.3, we used an interpolated OH data set in the following calculations.

In the Arabian Gulf, daytime NO_2 lifetimes (considering loss by OH) were generally between 2 and 4 h. Night-time lifetimes were in a similar range but also occasionally exceeded 10 h, e.g. when leaving the Arabian Gulf towards the Gulf of Oman and the Arabian Sea on the second leg, where O_3 mixing ratios fell below 20 ppbv. The average NO_2 lifetime was calculated to be 4.0 h.

Figure 12c shows that 50 ppbv of NO_2 was lost cumulatively throughout the period of measurements over the Arabian Gulf, with night-time losses (black data points) being more important than daytime losses (red data points). On average 6.0 ppbv NO_2 were lost per night and only 2.1 ppbv was lost per day. Large night-time compared to day-time losses are related to moderate OH levels in large parts of the Arabian Gulf (see Fig. 12b). The daytime average OH concentration was 2.4×10^6 molec. cm^{-3}, while on average 73 ppbv O_3 was present. The measured OH concentrations were generally low, given the NO_x and O_3 levels in the Ara-

bian Gulf, which may have resulted from its reactions with VOCs. With a loss rate constant of 11.6 s^{-1}, the Arabian Gulf was the AQABA region with the largest median OH reactivity (Pfannerstill et al., 2019), with 61 % of the total OH reactivity attributed to various measured VOCs. The daytime losses of NO_2 are therefore indirectly limited by the availability of VOCs from the oil and gas production (see above).

Via analysis of correlation between SO_2 and NO_2 (Fig. 13 and Table 2), we can assess the influence of shipping emissions on NO_x mixing ratios in the Arabian Gulf. In air masses recently influenced by NO_x emissions (NO_z / NO_y < 0.4), NO_x and SO_2 are only weakly correlated (slope $= 4.1 \pm 0.2$, $R = 0.41$), indicating that many different NO_x sources (i.e. not only shipping emissions) contribute. These might include vehicular traffic and industrial activity (e.g. production of nitrogen-based fertilisers Khan et al., 2016) in Kuwait City, the Iraqi city of Basra, and in Iranian harbours and offshore oil and gas terminals. Considering the limited NO_x lifetime, the land-based emission sources of NO_x from urban/industrialised areas gain in importance over plumes from nearby ships, when approaching the coast. In aged air masses, the slope of the NO_x versus SO_2 correlation is 0.11 ± 0.01 with a large correlation coefficient ($R = 0.72$). This indicates that in aged air masses, the NO_x levels are linked to SO_2 emissions, which is consistent with the photolysis of HONO being a major source of NO_x in the region. From the intercept (SO_2 mixing ratio = zero $= 0.0 \pm 0.3$ ppbv), we would expect negligible background levels of NO_z. Overall, shipping was an important source of NO_x in the Arabian Gulf, both through direct emissions and via photolysis of ship-related HONO.

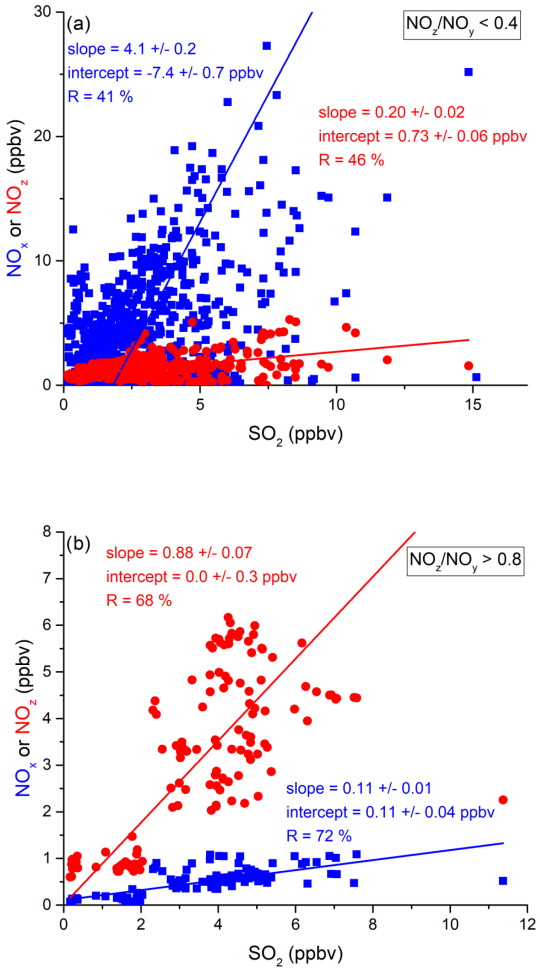

Figure 13. Correlation between SO_2 and NO_x or NO_z for **(a)** fresh and **(b)** aged NO_x emissions in the *Arabian Gulf*.

3.4 NO_x and NO_y and the role of ship-emission-related HONO formation during AQABA

In this section, we perform a steady-state analysis, assessing to what extent chemical source strengths can explain the background mixing ratios of NO_x observed during AQABA. Background conditions refer to NO_x mixing ratios found during periods when ship plumes were rarely encountered. "Background" NO_2 varied from region to region and was, for example, 50–150 pptv in the Mediterranean Sea. The required NO_x source strength (P, in molec. cm^{-3} s^{-1}) to maintain the observed NO_x levels is derived from the measured mixing ratios [NO_x] and the NO_2 reactivity (k^{NO_2}; see Sect. 3.1.3), whereby $P = P_{chem} + E$ is a combination of chemical production (P_{chem}) and direct emission (E). Notably, we neglect direct emissions under background conditions (i.e. $E = 0$) and assume that NO_x is only lost via the reaction of NO_2 with OH (i.e. $k^{NO_x} = k^{NO_2}$).

$$P = [NO_x] \cdot k^{NO_2} \quad (2)$$

Chemical processes that result in the formation of NO_x include the degradation of two gas-phase NO_z components, HONO and HNO_3, and the photolysis of particulate nitrate.

$$HONO + h\nu \rightarrow NO + OH \quad (R12)$$

$$OH + HNO_3 \rightarrow NO_3 + H_2O \quad (R13)$$

$$pNit + h\nu \rightarrow 2HONO + 1NO_x \quad (R14)$$

In a first step, we examine whether the HONO levels observed on AQABA can be explained by the photolysis of pNit in the PM_1 size range. This calculation is based on the assumption of a steady state for HONO established at noon through its photolytic loss and its production through the photolysis of pNit. Using average noon-time Mediterranean Sea concentrations for HONO (2.44×10^9 molec. cm^{-3}) and pNit (2.93×10^9 molec. cm^{-3}) and a photolysis rate J_{HONO} (1.45×10^{-3} s^{-1}), we calculate that a value for J_{pNit} of $\sim 1.21 \times 10^{-3}$ s^{-1} would be required in order to maintain the observed HONO concentrations. This is a factor of $\sim$ 5–6 higher than a reported value of $J_{pNit} \approx 2 \times 10^{-4}$ s^{-1}, based on observations over the western North Atlantic Ocean (Ye et al., 2016). It is, however, unclear whether the type and age

of particles examined by Ye et al. (2016) are comparable to those in AQABA. In addition, photolysable nitrate associated with particles that are > 1 µm diameter remain undetected by the AMS and could also contribute to the discrepancy between required and literature J_{pNit}.

Laboratory studies have demonstrated the conversion of NO_2 to HONO on BC particles, with a clear enhancement under UV irradiation (Acker et al., 2006; Elshorbany et al., 2009; Monge et al., 2010; Ma et al., 2013). Monge et al. (2010) postulated the transport of HONO and NO to remote low-NO_x areas, enabled via this heterogeneous mechanism. Besides the effect of irradiation, heterogeneous BC-assisted HONO and NO generation also shows a remarkable humidity dependence (Lammel and Perner, 1988; Kalberer et al., 1999; Kleffmann et al., 1999). Further information on the particulate-phase chemistry of HONO can be found in comprehensive reviews by Ma et al. (2013) and George et al. (2015). Sources of HONO during the AQABA campaign will be discussed in more detail in a separate publication.

Using Eq. (2), we now calculate what values of P_{chem} are required to maintain the background levels of NO_x observed and assess the individual contributions from Reactions (R12)–(R14) (results presented in Table 3). The analysis was restricted to data points where NO_z / NO_y was greater than 0.6 and to the 4 h time frame around local noon, in order to focus on aged air mass conditions during maximum photochemical activity. NO_2 reacting with O_3 was not considered a NO_x loss mechanism, due to the rapid reformation of NO_x by the photolysis of NO_3. For the pNit photolysis rate constant to form NO_x, we used $0.33 \cdot J_{\mathrm{pNit}}$ (from Ye et al., 2016), which accounts for the HONO / NO_x production ratio of 2 : 1. Additionally, we scaled J_{pNit} with J_{HONO} (normed to the average daytime maximum of J_{HONO}) to introduce diurnal variability. Due to limited data availability and rare occurrence of $NO_z / NO_y > 0.6$ (i.e. sampling of aged air) in the other regions, we performed this calculation for the Mediterranean Sea only. The results indicate that the measured HONO concentrations should result in a factor ca. 4.7 times larger NO_x production term than calculated via Eq. (2). Possible explanations for this include a positively biased HONO measurement or the underestimation of NO_x losses, e.g. due to undetected OH (despite the upper limit chosen in the interpolation). Our measurements and calculations, nonetheless, allow for the qualitative identification of HONO photolysis as a major source of daytime background NO_x levels during AQABA. The production rate from pNit photolysis can also account for ca. 64 % of the chemical NO_x generation, whereas the reaction of OH and HNO_3 forms an order of magnitude less NO_x.

Throughout AQABA, shipping emissions were responsible for fresh input of pollutant NO_x into the atmosphere. Our observations that levels of NO_x (with a lifetime of a few hours) were correlated with SO_2 (with lifetimes of more than a week) levels even in aged air masses and that HONO photolysis was an important source of NO may be reconciled by considering that HONO (and thus NO_x) production is driven by heterogeneous photochemistry on nitrate-containing particulate matter, the formation of which is associated with emissions of NO_x and SO_2 as well as black carbon. The latter has a lifetime in the boundary layer (defined by its deposition) of about a week or longer in the absence of precipitation and is thus comparable to that of SO_2. The slow, photochemically induced conversion of nitrate to HONO thus provides a long-lived source of NO_x and a link with SO_2, together with an explanation for the detection of short-lived HONO even in processed air masses in the eastern Mediterranean Sea. We emphasise that the analysis presented here focussed on the daytime chemistry of HONO. At night-time, a pseudo stationary state, independent of fresh NO_x input, has been observed by Wojtal et al. (2011) and explained with a reversible deposition of HONO on marine surfaces. This will, however, be insignificant during the day. Ship-derived HONO also has a substantial effect on the rates of photochemical O_3 formation in the remote marine boundary layer, largely as a result of higher RO_x production rates (Dai and Wang, 2021).

Table 3. Average required production rates to maintain the observed NO_x mixing ratios in aged air masses during the *Mediterranean Sea* transit and contributions from processes (R12)–(R14).

	Mediterranean Sea
$P_{\mathrm{chem}} \pm$ SD (10^5 molec. cm^{-3} s^{-1})	2.8 ± 2.2
$P(\mathrm{HONO} + h\nu) \pm$ SD (10^5 molec. cm^{-3} s^{-1})	13.1 ± 9.1
$P(\mathrm{pNit} + h\nu) \pm$ SD (10^5 molec. cm^{-3} s^{-1})	1.8 ± 0.4
$P(\mathrm{OH} + \mathrm{HNO_3}) \pm$ SD (10^5 molec. cm^{-3} s^{-1})	0.14 ± 0.06
Number of data points (5 min averages)	90

3.5 Inter-regional ozone production efficiency (OPE)

The OPE can be calculated from the relationship between O_x and NO_z where $O_x = O_3 + NO_2$, and the O_3 mixing ratios are augmented by those of NO_2, 95 % of which potentially photolyses to O_3 (Wood et al., 2009). Note that in any air mass where HNO_3 is a major component of NO_z, the derived OPE may represent an upper limit if HNO_3 is lost during transport from the NO_x source region to the measurement location. The NO_y / CO ratio has been used to estimate the impact of NO_z losses on the values of OPE obtained in this type of analysis (Nunnermacker et al., 2000) the rationale being that CO (like O_3) is a product of photochemical activity and relatively long lived, at least compared to NO_z. The high variability in the NO_y / CO ratio during AQABA is, however, indicative of local (non-photochemical) sources of CO (e.g. via combustion) and precludes use of this corrective procedure so that the values of OPE we present should be regarded as upper limits. An introduction into the OPE metric and on typical literature values is given in Sect. 1.

In Fig. 14 we plot O_x versus NO_z for which the NO_2 photolysis rate constant was $> 1 \times 10^{-3}$ s^{-1}, which restricts

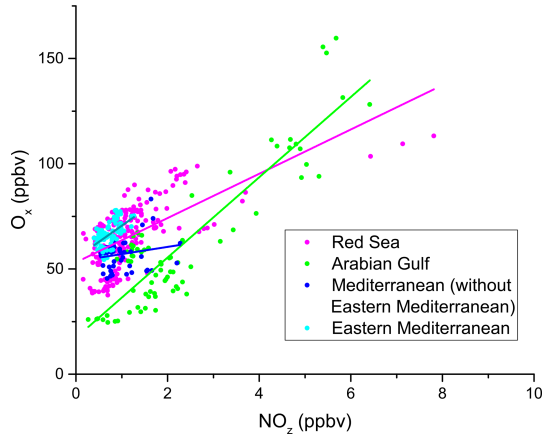

Figure 14. Correlation between O_x ($=O_3+NO_2$) and NO_z during AQABA, with the regions indicated via the colour code. Only daytime measurements were used in this analysis. The OPEs for AQABA and for the individual regions shown in Table 4 were derived from linear fits of these data points. A clear regional variability can be observed for O_x and NO_z mixing ratios. Elevated O_x and NO_z levels were measured in the Arabian Gulf and the Red Sea.

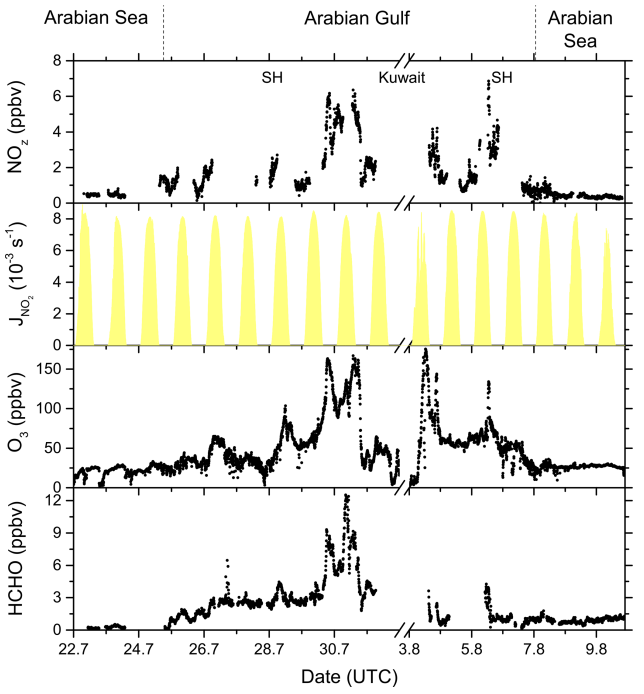

Figure 15. NO_z, O_3, and HCHO mixing ratios, together with NO_2 photolysis rates, during the transitions between the Arabian Sea and Arabian Gulf, as well as in the Arabian Gulf.

the analysis to hours of the day with active photochemistry. Regional OPE values are 10.5 ± 0.9 for the Red Sea, 19.1 ± 1.1 for the Arabian Gulf, and 15.4 ± 2.4 for the eastern Mediterranean Sea. The heterogeneity of NO_z and O_3 mixing ratios, i.e. the chemical conditions frequently varying between aged and plume situations (see Sect. 3.1), resulted in a low correlation coefficient in the western Mediterranean Sea ($R^2 = 0.19$), which precluded derivation of an OPE for this region and led us to restrict the Mediterranean Sea OPE analysis to the more homogenous eastern part (encompassing subregions M1–M5).

The range of OPE values measured during AQABA (10.5–19.1) is comparable to the value of 10, derived in the marine boundary layer (MBL) at Oki Islands, Japan, a site which is influenced by pollution arriving from the Korean peninsula and the Japanese mainland (Jaffe et al., 1996), but much lower than the value of 87 which was derived from observations off the coast of Newfoundland (Wang et al., 1996), where the median NO_x mixing ratio was < 100 pptv. As alluded to above, high values in remote locations may in part be a result of reactive nitrogen loss via deposition. By comparison, during AQABA the median NO_x mixing ratio was > 600 pptv, which together with the relatively low OPE indicates that the vast majority of the AQABA ship track cannot be considered representative of remote MBL conditions.

Figure 14 and Table 4 indicate that the Arabian Gulf, for which the highest O_3 levels in the entire campaign were found (up to 150 ppbv), also has the largest OPE, despite high median NO_x mixing ratios. The high OPE value, however, is consistent with the analysis of Pfannerstill et al. (2019), who used VOC and OH reactivity measurements to derive the fraction of OH that reacts with VOCs (fuelling the formation of RO_2, conversion of NO to NO_2, and thus O_3 formation) versus the fraction that reacted with NO_x (resulting in NO_z formation) to identify regions where O_3 formation was NO_x-limited, VOC-limited, or (as was generally the case) in a transition regime. Pfannerstill et al. (2019) indicated that formation of O_3 was favoured around the Arabian Peninsula where VOCs from petroleum extraction and processing industries were important sinks of OH. The highest net ozone production rates (NOPRs) during AQABA were also found in the Arabian Gulf where calculations of the rate of RO_2 induced oxidation of NO to NO_2 resulted in a median (over the diel cycle) value of NOPR = 32 ppbv per day which was driven by high noon-time mixing ratios of RO_2 (73 pptv in the Arabian Gulf) (Tadic et al., 2020). In contrast to the OPE, NOPR accounts for the total amount of O_3 produced in 1 d, considering production (governed by the formation of NO_2 via reactions of NO with HO_2 and RO_2) and loss (via photolysis and reaction with OH or HO_2). The OPE, on the other hand, focusses on the product side and assesses the competition between O_3 formation and sequestering into NO_z from a given initial level of NO_x. By approximating the O_3 production rate via the NO_2 formation from NO reactions with HO_2 and RO_2, the NOPR thus neglects the alternative branch leading to NO_z. In the other two regions, the correlation coefficients are notably smaller, due to the lower span in O_3 and NO_z, resulting in increased relative errors for the derived OPE values.

Table 4. Ozone production efficiencies (OPEs) for AQABA and the individual regions.

	AQABA	Eastern Med. Sea	Red Sea	Arabian Gulf
OPE	14.1 ± 0.7	15.4 ± 2.4	10.5 ± 0.9	19.1 ± 1.1
Correlation coeff. R (%)	65	55	65	89
$k^{OH}_{NO_x}/k^{OH}_{total}$ (%) [a]		1.0	2.0	7.5
O_3 (ppbv) [b]		58–73	42–81	23–108
NO_z (ppbv) [b]		0.5–1.0	0.5–2.1	0.9–4.9
NO_y / CO (%) [b,c]			1.4–7.0	1.9–14.6
OH_{max} (10^6 molec. cm^{-3})[(d)]		9.1	5.7	11.8

[a] Median. [b] 10–90 percentiles. [c] No CO data after 16 August 2017. [d] Average of daily OH peak concentrations; no data before 18 July 2017.

In Fig. 15 we plot a time series of NO_z mixing ratios during the transition from the Arabian Sea to the Arabian Gulf along with NO_2 photolysis rates, O_3, and formaldehyde (HCHO) which is formed during the photochemical processing of many VOCs (Fischer et al., 2003; Klippel et al., 2011; Wolfe et al., 2016; Wolfe et al., 2019) and which can therefore be used as a tracer for photochemical activity (Dodge, 1990; Altshuller, 1993; Garcia et al., 2006; Duncan et al., 2010; Parrish et al., 2012). The transition from low NO_z levels in the Arabian Sea to values up to ~ 7 ppbv in the Strait of Hormuz (SH) is accompanied by increases in both O_3 (up to 160 ppbv) and HCHO (up to 12.5 ppbv). Based on the analysis by Duncan et al. (2010), Tadic et al. (2020) calculated a median HCHO / NO_2 ratio of 9.3 for the Arabian Gulf, indicating that O_3 production in this region is NO_x limited. The high levels of NO_z, O_3, and HCHO in the Arabian Gulf result from the combination of intense solar radiation with high levels of reactive VOCs (Bourtsoukidis et al., 2019; Pfannerstill et al., 2019) and NO_x and are accompanied by the highest levels of gas-phase organic nitrates observed during AQABA, with absolute mixing ratios up to 2.5 ppbv on the approach to Kuwait. In conclusion, our NO_x / NO_y measurements and the OPE values derived from them confirm the exceptional photochemical activity in the Arabian Gulf.

4 Conclusions

During the AQABA campaign in the summer of 2017, we collected a unique NO_x and NO_y data set that covers the Mediterranean Sea, the Red Sea, and the Arabian Gulf, which are regions with only few previously published observational data sets. The highest median NO_x and NO_z mixing ratios were observed in the Arabian Gulf (NO_x: 1.6 ppbv; NO_z: 1.5 ppbv), followed by the Red Sea (NO_x: 1.0 ppbv; NO_z: 0.7 ppbv) and the Mediterranean Sea (NO_x: 0.3 ppbv; NO_z: 0.7 ppbv). Night-time losses of NO_2 exceeded daytime losses by factors of 2.8 and 2.9 in the Arabian Gulf and the Red Sea, respectively, whereas daytime losses were 2.5 times higher in the Mediterranean Sea, which is a result of consistently high daytime OH concentrations.

The derivation of NO_x lifetimes enabled us to calculate the NO_x source strength required to reproduce the observed mixing ratios and indicated that HONO photolysis was a significant source of NO_x in the Mediterranean Sea. The strong correlation between NO_x and SO_2 in air masses that were impacted by fresh emissions of NO_x indicated that ships are the dominant source of NO_x throughout the AQABA campaign. HONO may have been generated on particulate nitrate, possibly associated with black carbon that has been processed (to contain sulfate, organics, and nitrate) as the ship plumes evolve chemically.

The fractional contributions to NO_x of NO_y and the various components of NO_z were highly variable in the three regions. The lowest regional mean contribution of NO_x to NO_y (i.e. most aged air masses) was found in the Mediterranean Sea with 41 % compared to 47 % in the Red Sea and 46 % in the Arabian Gulf. Of the NO_z trace gases, HNO_3 represented the most important contribution to NO_y with 39 % in the Arabian Gulf, 25 % in the Red Sea, and 35 % in the Mediterranean Sea. A clear regional variability was observed for the contribution of organic nitrates, with the highest value (16 % in the Red Sea) related to the concurrent availability of precursor NO_x and VOCs from the oil and gas industry. Comparable figures were derived for the Arabian Gulf and the Mediterranean Sea, with 10 % and 11 %, respectively. pNit (particle diameter < 1 µm) contributed only a few percent, with the largest value (10 %) found in the Mediterranean Sea. HONO and $ClNO_2$ were generally only minor components (< 3 %) of NO_z. Future studies on the reactive nitrogen budget in the AQABA region might benefit from longer stationary measurements (e.g. to identify diurnal patterns), together with the detection of more speciated NO_z compounds (especially HNO_3 and ONs).

Data availability. The NO_x and NO_z data sets are available at https://doi.org/10.5281/zenodo.4746367 (Friedrich and Crowley, 2021). Other data sets (e.g. HONO, OH, SO_2) can be obtained via the person responsible on request.

Supplement. The supplement related to this article is available online at: https://doi.org/10.5194/acp-21-7473-2021-supplement.

Author contributions. NF analysed the NO_x and NO_y data sets and wrote the article. NF and JNC operated the TD-CRDS. PE and JNC provided CIMS measurements of SO_2 and $ClNO_2$. JSh, NS, and JNC performed and evaluated ONs measurements. JSc set up and processed data from the spectral radiometer. DD, BH, IT, and HF contributed NO, NO_2, HCHO, and CO measurements. MM, RR, ST, and HH provided OH concentrations. EYP, NW, and JW were responsible for the OH reactivity measurements. JB and FD performed measurements with the AMS and OPC instruments. HS, GL, and YC contributed the HONO data set. JL designed the AQABA campaign. All authors contributed to the writing of the article.

Competing interests. The authors declare that they have no conflict of interest.

Acknowledgements. The authors gratefully acknowledge the NOAA Air Resources Laboratory (ARL) for the provision of the HYSPLIT transport and dispersion model and READY website (https://www.ready.noaa.gov, last access: 10 May 2021) used in this publication. We thank the whole crew of the *Kommandor Iona* and Hays Ships for their support, as well as Marcel Dorf for organising the campaign.

Financial support. The article processing charges for this open-access publication were covered by the Max Planck Society.

Review statement. This paper was edited by Eleanor Browne and reviewed by two anonymous referees.

References

Acker, K., Febo, A., Trick, S., Perrino, C., Bruno, P., Wiesen, P., Moller, D., Wieprecht, W., Auel, R., Giusto, M., Geyer, A., Platt, U., and Allegrini, I.: Nitrous acid in the urban area of Rome, Atmos. Environ., 40, 3123–3133, https://doi.org/10.1016/j.atmosenv.2006.01.028, 2006.

Alahmadi, S., Al-Ahmadi, K., and Almeshari, M.: Spatial variation in the association between NO2 concentrations and shipping emissions in the Red Sea, Sci. Total Environ., 676, 131–143, https://doi.org/10.1016/j.scitotenv.2019.04.161, 2019.

Aldener, M., Brown, S. S., Stark, H., Williams, E. J., Lerner, B. M., Kuster, W. C., Goldan, P. D., Quinn, P. K., Bates, T. S., Fehsenfeld, F. C., and Ravishankara, A. R.: Reactivity and loss mechanisms of NO_3 and N_2O_5 in a polluted marine environment: Results from in situ measurements during New England Air Quality Study 2002, J. Geophys. Res.-Atmos., 111, D23S73, https://doi.org/10.1029/2006JD007252, 2006.

Alsharhan, A. S.: Petroleum geology and potential hydrocarbon plays in the Gulf of Suez rift basin, Egypt, AAPG Bull., 87, 143–180, 2003.

Altshuller, A. P.: Production of Aldehydes as Primary Emissions and from Secondary Atmospheric Reactions of Alkenes and Alkanes during the Night and Early Morning Hours, Atmos. Environ. A-Gen., 27, 21–32, https://doi.org/10.1016/0960-1686(93)90067-9, 1993.

Beirle, S., Platt, U., von Glasow, R., Wenig, M., and Wagner, T.: Estimate of nitrogen oxide emissions from shipping by satellite remote sensing, Geophys. Res. Lett., 31, L18102, https://doi.org/10.1029/2004gl020312, 2004.

Berresheim, H., Plass-Dülmer, C., Elste, T., Mihalopoulos, N., and Rohrer, F.: OH in the coastal boundary layer of Crete during MINOS: Measurements and relationship with ozone photolysis, Atmos. Chem. Phys., 3, 639–649, https://doi.org/10.5194/acp-3-639-2003, 2003.

Bohn, B., Corlett, G. K., Gillmann, M., Sanghavi, S., Stange, G., Tensing, E., Vrekoussis, M., Bloss, W. J., Clapp, L. J., Kortner, M., Dorn, H.-P., Monks, P. S., Platt, U., Plass-Dülmer, C., Mihalopoulos, N., Heard, D. E., Clemitshaw, K. C., Meixner, F. X., Prevot, A. S. H., and Schmitt, R.: Photolysis frequency measurement techniques: results of a comparison within the ACCENT project, Atmos. Chem. Phys., 8, 5373–5391, https://doi.org/10.5194/acp-8-5373-2008, 2008.

Bourtsoukidis, E., Ernle, L., Crowley, J. N., Lelieveld, J., Paris, J.-D., Pozzer, A., Walter, D., and Williams, J.: Non-methane hydrocarbon (C_2–C_8) sources and sinks around the Arabian Peninsula, Atmos. Chem. Phys., 19, 7209–7232, https://doi.org/10.5194/acp-19-7209-2019, 2019.

Bourtsoukidis, E., Pozzer, A., Sattler, T., Matthaios, V. N., Ernle, L., Edtbauer, A., Fischer, H., Könemann, T., Osipov, S., Paris, J. D., Pfannerstill, E. Y., Stönner, C., Tadic, I., Walter, D., Wang, N., Lelieveld, J., and Williams, J.: The Red Sea Deep Water is a potent source of atmospheric ethane and propane, Nat. Commun., 11, 447, https://doi.org/10.1038/s41467-020-14375-0, 2020.

Burkholder, J. B., Sander, S. P., Abbatt, J., Barker, J. R., Huie, R. E., Kolb, C. E., Kurylo, M. J., Orkin, V. L., Wilmouth, D. M., and Wine, P. H.: Chemical Kinetics and Photochemical Data for Use in Atmospheric Studies, Evaluation No. 18, JPL Publication 15-10, Jet Propulsion Laboratory, Pasadena, available at: http://jpldataeval.jpl.nasa.gov (last access: 10 May 2021), 2015.

Capaldo, K., Corbett, J. J., Kasibhatla, P., Fischbeck, P., and Pandis, S. N.: Effects of ship emissions on sulphur cycling and radiative climate forcing over the ocean, Nature, 400, 743–746, https://doi.org/10.1038/23438, 1999.

Celik, S., Drewnick, F., Fachinger, F., Brooks, J., Darbyshire, E., Coe, H., Paris, J.-D., Eger, P. G., Schuladen, J., Tadic, I., Friedrich, N., Dienhart, D., Hottmann, B., Fischer, H., Crowley, J. N., Harder, H., and Borrmann, S.: Influence of vessel characteristics and atmospheric processes on the gas and particle phase of ship emission plumes: in situ measurements in the Mediterranean Sea and around the Arabian Peninsula, Atmos. Chem. Phys., 20, 4713–4734, https://doi.org/10.5194/acp-20-4713-2020, 2020.

Chameides, W. L., Stedman, D. H., Dickerson, R. R., Rusch, D. W., and Cicerone, R. J.: No_x Production in Lightning, J. Atmos. Sci., 34, 143–149, https://doi.org/10.1175/1520-0469(1977)034<0143:Npil>2.0.Co;2, 1977.

Cooper, D. A.: Exhaust emissions from ships at berth, Atmos. Environ., 37, 3817–3830, https://doi.org/10.1016/S1352-2310(03)00446-1, 2003.

Dai, J. and Wang, T.: Impact of International Shipping Emissions on Ozone and $PM_{2.5}$: The Important Role of HONO and ClNO2, Atmos. Chem. Phys. Discuss. [preprint], https://doi.org/10.5194/acp-2020-1185, in review, 2021.

Dalsøren, S. B., Eide, M. S., Endresen, Ø., Mjelde, A., Gravir, G., and Isaksen, I. S. A.: Update on emissions and environmental impacts from the international fleet of ships: the contribution from major ship types and ports, Atmos. Chem. Phys., 9, 2171–2194, https://doi.org/10.5194/acp-9-2171-2009, 2009.

Daum, P. H., Kleinman, L., Imre, D. G., Nunnermacker, L. J., Lee, Y. N., Springston, S. R., Newman, L., and Weinstein-Lloyd, J.: Analysis of the processing of Nashville urban emissions on July 3 and July 18, 1995, J. Geophys. Res.-Atmos., 105, 9155–9164, https://doi.org/10.1029/1999jd900997, 2000.

Davis, D. D., Crawford, J., Chen, G., Chameides, W., Liu, S., Bradshaw, J., Sandholm, S., Sachse, G., Gregory, G., Anderson, B., Barrick, J., Bachmeier, A., Collins, J., Browell, E., Blake, D., Rowland, S., Kondo, Y., Singh, H., Talbot, R., Heikes, B., Merrill, J., Rodriguez, J., and Newell, R. E.: Assessment of ozone photochemistry in the western North Pacific as inferred from PEM-West A observations during the fall 1991, J. Geophys. Res.-Atmos., 101, 2111–2134, https://doi.org/10.1029/95jd02755, 1996.

Day, D. A., Dillon, M. B., Wooldridge, P. J., Thornton, J. A., Rosen, R. S., Wood, E. C., and Cohen, R. C.: On alkyl nitrates, O_3, and the "missing NO_y", J. Geophys. Res.-Atmos., 108, 4501, https://doi.org/10.1029/2003jd003685, 2003.

DeCarlo, P. F., Kimmel, J. R., Trimborn, A., Northway, M. J., Jayne, J. T., Aiken, A. C., Gonin, M., Fuhrer, K., Horvath, T., Docherty, K. S., Worsnop, D. R., and Jimenez, J. L.: Field-deployable, high-resolution, time-of-flight aerosol mass spectrometer, Anal. Chem., 78, 8281–8289, https://doi.org/10.1021/ac061249n, 2006.

Delaria, E. R., Vieira, M., Cremieux, J., and Cohen, R. C.: Measurements of NO and NO_2 exchange between the atmosphere and *Quercus agrifolia*, Atmos. Chem. Phys., 18, 14161–14173, https://doi.org/10.5194/acp-18-14161-2018, 2018.

Delaria, E. R. and Cohen, R. C.: A model-based analysis of foliar NO_x deposition, Atmos. Chem. Phys., 20, 2123–2141, https://doi.org/10.5194/acp-20-2123-2020, 2020.

Dickerson, R. R., Rhoads, K. P., Carsey, T. P., Oltmans, S. J., Burrows, J. P., and Crutzen, P. J.: Ozone in the remote marine boundary layer: A possible role for halogens, J. Geophys. Res.-Atmos., 104, 21385–21395, 1999.

Diesch, J.-M., Drewnick, F., Klimach, T., and Borrmann, S.: Investigation of gaseous and particulate emissions from various marine vessel types measured on the banks of the Elbe in Northern Germany, Atmos. Chem. Phys., 13, 3603–3618, https://doi.org/10.5194/acp-13-3603-2013, 2013.

Dodge, M. C.: Formaldehyde Production in Photochemical Smog as Predicted by 3 State-of-the-Science Chemical Oxidant Mechanisms, J. Geophys. Res.-Atmos., 95, 3635–3648, https://doi.org/10.1029/JD095iD04p03635, 1990.

Duncan, B. N., Yoshida, Y., Olson, J. R., Sillman, S., Martin, R. V., Lamsal, L., Hu, Y. T., Pickering, K. E., Retscher, C., Allen, D. J., and Crawford, J. H.: Application of OMI observations to a space-based indicator of NO_x and VOC controls on surface ozone formation, Atmos. Environ., 44, 2213–2223, https://doi.org/10.1016/j.atmosenv.2010.03.010, 2010.

Edtbauer, A., Stönner, C., Pfannerstill, E. Y., Berasategui, M., Walter, D., Crowley, J. N., Lelieveld, J., and Williams, J.: A new marine biogenic emission: methane sulfonamide (MSAM), dimethyl sulfide (DMS), and dimethyl sulfone ($DMSO_2$) measured in air over the Arabian Sea, Atmos. Chem. Phys., 20, 6081–6094, https://doi.org/10.5194/acp-20-6081-2020, 2020.

Eger, P. G., Friedrich, N., Schuladen, J., Shenolikar, J., Fischer, H., Tadic, I., Harder, H., Martinez, M., Rohloff, R., Tauer, S., Drewnick, F., Fachinger, F., Brooks, J., Darbyshire, E., Sciare, J., Pikridas, M., Lelieveld, J., and Crowley, J. N.: Shipborne measurements of $ClNO_2$ in the Mediterranean Sea and around the Arabian Peninsula during summer, Atmos. Chem. Phys., 19, 12121–12140, https://doi.org/10.5194/acp-19-12121-2019, 2019a.

Eger, P. G., Helleis, F., Schuster, G., Phillips, G. J., Lelieveld, J., and Crowley, J. N.: Chemical ionization quadrupole mass spectrometer with an electrical discharge ion source for atmospheric trace gas measurement, Atmos. Meas. Tech., 12, 1935–1954, https://doi.org/10.5194/amt-12-1935-2019, 2019b.

Elshorbany, Y. F., Kurtenbach, R., Wiesen, P., Lissi, E., Rubio, M., Villena, G., Gramsch, E., Rickard, A. R., Pilling, M. J., and Kleffmann, J.: Oxidation capacity of the city air of Santiago, Chile, Atmos. Chem. Phys., 9, 2257–2273, https://doi.org/10.5194/acp-9-2257-2009, 2009.

Elshorbany, Y. F., Steil, B., Brühl, C., and Lelieveld, J.: Impact of HONO on global atmospheric chemistry calculated with an empirical parameterization in the EMAC model, Atmos. Chem. Phys., 12, 9977–10000, https://doi.org/10.5194/acp-12-9977-2012, 2012.

Eyring, V., Isaksen, I. S. A., Berntsen, T., Collins, W. J., Corbett, J. J., Endresen, O., Grainger, R. G., Moldanova, J., Schlager, H., and Stevenson, D. S.: Transport impacts on atmosphere and climate: Shipping, Atmos. Environ., 44, 4735–4771, https://doi.org/10.1016/j.atmosenv.2009.04.059, 2010.

Fischer, H., Kormann, R., Klüpfel, T., Gurk, Ch., Königstedt, R., Parchatka, U., Mühle, J., Rhee, T. S., Brenninkmeijer, C. A. M., Bonasoni, P., and Stohl, A.: Ozone production and trace gas correlations during the June 2000 MINATROC intensive measurement campaign at Mt. Cimone, Atmos. Chem. Phys., 3, 725–738, https://doi.org/10.5194/acp-3-725-2003, 2003.

Fischer, H., Pozzer, A., Schmitt, T., Jöckel, P., Klippel, T., Taraborrelli, D., and Lelieveld, J.: Hydrogen peroxide in the marine boundary layer over the South Atlantic during the OOMPH cruise in March 2007, Atmos. Chem. Phys., 15, 6971–6980, https://doi.org/10.5194/acp-15-6971-2015, 2015.

Fried, A., McKeen, S., Sewell, S., Harder, J., Henry, B., Goldan, P., Kuster, W., Williams, E., Baumann, K., Shetter, R., and Cantrell, C.: Photochemistry of formaldehyde during the 1993 Tropospheric OH Photochemistry Experiment, J. Geophys. Res.-Atmos., 102, 6283–6296, https://doi.org/10.1029/96jd03249, 1997.

Friedrich, N. and Crowley, J. N.: Reactive nitrogen around the Arabian Peninsula and in the Mediterranean Sea during the 2017 AQABA ship campaign, Zenodo [dataset], https://doi.org/10.5281/zenodo.4746367, 2021.

Friedrich, N., Tadic, I., Schuladen, J., Brooks, J., Darbyshire, E., Drewnick, F., Fischer, H., Lelieveld, J., and Crowley, J. N.: Measurement of NO_x and NO_y with a thermal dissociation cavity ring-down spectrometer (TD-CRDS): instrument characterisation and first deployment, Atmos. Meas. Tech., 13, 5739–5761, https://doi.org/10.5194/amt-13-5739-2020, 2020.

Garcia, A. R., Volkamer, R., Molina, L. T., Molina, M. J., Samuelson, J., Mellqvist, J., Galle, B., Herndon, S. C., and Kolb, C. E.: Separation of emitted and photochemical formaldehyde in Mexico City using a statistical analysis and a new pair of gas-phase tracers, Atmos. Chem. Phys., 6, 4545–4557, https://doi.org/10.5194/acp-6-4545-2006, 2006.

Ge, B. Z., Sun, Y. L., Liu, Y., Dong, H. B., Ji, D. S., Jiang, Q., Li, J., and Wang, Z. F.: Nitrogen dioxide measurement by cavity attenuated phase shift spectroscopy (CAPS) and implications in ozone production efficiency and nitrate formation in Beijing, China, J. Geophys. Res.-Atmos., 118, 9499–9509, https://doi.org/10.1002/jgrd.50757, 2013.

George, C., Ammann, M., D'Anna, B., Donaldson, D. J., and Nizkorodov, S. A.: Heterogeneous Photochemistry in the Atmosphere, Chem. Rev., 115, 4218–4258, https://doi.org/10.1021/cr500648z, 2015.

Heland, J., Kleffmann, J., Kurtenbach, R., and Wiesen, P.: A new instrument to measure gaseous nitrous acid (HONO) in the atmosphere, Environ. Sci. Technol., 35, 3207–3212, https://doi.org/10.1021/es000303t, 2001.

Isakson, J., Persson, T. A., and Lindgren, E. S.: Identification and assessment of ship emissions and their effects in the harbour of G(o)over-circleteborg, Sweden, Atmos. Environ., 35, 3659–3666, https://doi.org/10.1016/S1352-2310(00)00528-8, 2001.

IUPAC: Task Group on Atmospheric Chemical Kinetic Data Evaluation, edited by: Ammann, M., Cox, R. A., Crowley, J. N., Herrmann, H., Jenkin, M. E., McNeill, V. F., Mellouki, A., Rossi, M. J., Troe, J., and Wallington, T. J., available at: http://iupac.pole-ether.fr/index.html (last access: 10 May 2021), 2020.

Jaffe, D. A., Honrath, R. E., Zhang, L., Akimoto, H., Shimizu, A., Mukai, H., Murano, K., Hatakeyama, S., and Merrill, J.: Measurements of NO, NO_y, CO and O_3 and estimation of the ozone production rate at Oki Island, Japan, during PEM-West, J. Geophys. Res.-Atmos., 101, 2037–2048, https://doi.org/10.1029/95jd01699, 1996.

Jimenez, J. L., Jayne, J. T., Shi, Q., Kolb, C. E., Worsnop, D. R., Yourshaw, I., Seinfeld, J. H., Flagan, R. C., Zhang, X. F., Smith, K. A., Morris, J. W., and Davidovits, P.: Ambient aerosol sampling using the Aerodyne Aerosol Mass Spectrometer, J. Geophys. Res.-Atmos., 108, 8425, https://doi.org/10.1029/2001jd001213, 2003.

Johansson, L., Jalkanen, J. P., and Kukkonen, J.: Global assessment of shipping emissions in 2015 on a high spatial and temporal resolution, Atmos. Environ., 167, 403–415, https://doi.org/10.1016/j.atmosenv.2017.08.042, 2017.

Kalberer, M., Ammann, M., Arens, F., Gaggeler, H. W., and Baltensperger, U.: Heterogeneous formation of nitrous acid (HONO) on soot aerosol particles, J. Geophys. Res.-Atmos., 104, 13825–13832, 1999.

Kercher, J. P., Riedel, T. P., and Thornton, J. A.: Chlorine activation by N_2O_5: simultaneous, in situ detection of $ClNO_2$ and N_2O5 by chemical ionization mass spectrometry, Atmos. Meas. Tech., 2, 193–204, https://doi.org/10.5194/amt-2-193-2009, 2009.

Khan, A. R., Al-Awadi, L., and Al-Rashidi, M. S.: Control of ammonia and urea emissions from urea manufacturing facilities of Petrochemical Industries Company (PIC), Kuwait, J. Air Waste Ma., 66, 609–618, https://doi.org/10.1080/10962247.2016.1145154, 2016.

Kleffmann, J., Becker, K. H., Lackhoff, M., and Wiesen, P.: Heterogeneous conversion of NO_2 on carbonaceous surfaces, Phys. Chem. Chem. Phys., 1, 5443–5450, https://doi.org/10.1039/a905545b, 1999.

Klippel, T., Fischer, H., Bozem, H., Lawrence, M. G., Butler, T., Jöckel, P., Tost, H., Martinez, M., Harder, H., Regelin, E., Sander, R., Schiller, C. L., Stickler, A., and Lelieveld, J.: Distribution of hydrogen peroxide and formaldehyde over Central Europe during the HOOVER project, Atmos. Chem. Phys., 11, 4391–4410, https://doi.org/10.5194/acp-11-4391-2011, 2011.

Ladstätter-Weißenmayer, A., Heland, J., Kormann, R., von Kuhlmann, R., Lawrence, M. G., Meyer-Arnek, J., Richter, A., Wittrock, F., Ziereis, H., and Burrows, J. P.: Transport and build-up of tropospheric trace gases during the MINOS campaign: comparision of GOME, in situ aircraft measurements and MATCH-MPIC-data, Atmos. Chem. Phys., 3, 1887–1902, https://doi.org/10.5194/acp-3-1887-2003, 2003.

Ladstatter-Weissenmayer, A., Kanakidou, M., Meyer-Arnek, J., Dermitzaki, E. V., Richter, A., Vrekoussis, M., Wittrock, F., and Burrows, J. P.: Pollution events over the East Mediterranean: Synergistic use of GOME, ground-based and sonde observations and models, Atmos. Environ., 41, 7262–7273, https://doi.org/10.1016/j.atmosenv.2007.05.031, 2007.

Lammel, G. and Perner, D.: The Atmospheric Aerosol as a Source of Nitrous-Acid in the Polluted Atmosphere, J. Aerosol Sci., 19, 1199–1202, https://doi.org/10.1016/0021-8502(88)90135-8, 1988.

Lange, L., Hoor, P., Helas, G., Fischer, H., Brunner, D., Scheeren, B., Williams, J., Wong, S., Wohlfrorn, K. H., Arnold, F., Strom, J., Krejci, R., Lelieveld, J., and Andreae, M. O.: Detection of lightning-produced NO in the midlatitude upper troposphere during STREAM 1998, J. Geophys. Res.-Atmos., 106, 27777–27785, https://doi.org/10.1029/2001jd900210, 2001.

Ledoux, F., Roche, C., Cazier, F., Beaugard, C., and Courcot, D.: Influence of ship emissions on NO_x, SO_2, O_3 and PM concentrations in a North-Sea harbor in France, J. Environ. Sci.-China, 71, 56–66, https://doi.org/10.1016/j.jes.2018.03.030, 2018.

Lelieveld, J., Hoor, P., Jöckel, P., Pozzer, A., Hadjinicolaou, P., Cammas, J.-P., and Beirle, S.: Severe ozone air pollution in the Persian Gulf region, Atmos. Chem. Phys., 9, 1393–1406, https://doi.org/10.5194/acp-9-1393-2009, 2009.

Lelieveld, J., Hadjinicolaou, P., Kostopoulou, E., Chenoweth, J., El Maayar, M., Giannakopoulos, C., Hannides, C., Lange, M. A., Tanarhte, M., Tyrlis, E., and Xoplaki, E.: Climate change and impacts in the Eastern Mediterranean and the Middle East, Climatic Change, 114, 667–687, https://doi.org/10.1007/s10584-012-0418-4, 2012.

Lenner, M.: Nitrogen-Dioxide in Exhaust Emissions from Motor-Vehicles, Atmos. Environ., 21, 37–43, https://doi.org/10.1016/0004-6981(87)90268-X, 1987.

Lewis, E. R. and Schwartz, S. E.: Sea salt aerosol production: mechanisms, methods, measurements and models: a critical review, Geophysical monograph, 152, American Geophysical Union, Washington, DC, xii, 413 pp., 2004.

Li, J. S., Parchatka, U., and Fischer, H.: Development of field-deployable QCL sensor for simultaneous detection of ambient N_2O and CO, Sensor Actuat. B-Chem, 182, 659–667, https://doi.org/10.1016/j.snb.2013.03.073, 2013.

Lin, W., Xu, X., Ge, B., and Liu, X.: Gaseous pollutants in Beijing urban area during the heating period 2007–2008: variability, sources, meteorological, and chemical impacts, Atmos. Chem. Phys., 11, 8157–8170, https://doi.org/10.5194/acp-11-8157-2011, 2011.

Liu, S. C., Trainer, M., Fehsenfeld, F. C., Parrish, D. D., Williams, E. J., Fahey, D. W., Hubler, G., and Murphy, P. C.: Ozone Production in the Rural Troposphere and the Implications for Regional and Global Ozone Distributions, J. Geophys. Res.-Atmos., 92, 4191–4207, https://doi.org/10.1029/JD092iD04p04191, 1987.

Logan, J. A.: Nitrogen-Oxides in the Troposphere – Global and Regional Budgets, J. Geophys. Res.-Oceans, 88, 785–807, https://doi.org/10.1029/JC088iC15p10785, 1983.

Longfellow, C. A., Ravishankara, A. R., and Hanson, D. R.: Reactive uptake on hydrocarbon soot: Focus on NO_2, J. Geophys. Res.-Atmos., 104, 13833–13840, 1999.

Ma, J. Z., Liu, Y. C., Han, C., Ma, Q. X., Liu, C., and He, H.: Review of heterogeneous photochemical reactions of NO_y on aerosol – A possible daytime source of nitrous acid (HONO) in the atmosphere, J. Environ. Sci., 25, 326–334, https://doi.org/10.1016/S1001-0742(12)60093-X, 2013.

Mallik, C., Tomsche, L., Bourtsoukidis, E., Crowley, J. N., Derstroff, B., Fischer, H., Hafermann, S., Hüser, I., Javed, U., Keßel, S., Lelieveld, J., Martinez, M., Meusel, H., Novelli, A., Phillips, G. J., Pozzer, A., Reiffs, A., Sander, R., Taraborrelli, D., Sauvage, C., Schuladen, J., Su, H., Williams, J., and Harder, H.: Oxidation processes in the eastern Mediterranean atmosphere: evidence from the modelling of HO_x measurements over Cyprus, Atmos. Chem. Phys., 18, 10825–10847, https://doi.org/10.5194/acp-18-10825-2018, 2018.

Mamane, Y., and Gottlieb, J.: Heterogeneous reaction of nitrogen oxides on sea salt and mineral particles – A single particle approach, J. Aerosol Sci., 21, 225–228, 1990.

Marmer, E. and Langmann, B.: Impact of ship emissions on the Mediterranean summertime pollution and climate: A regional model study, Atmos. Environ., 39, 4659–4669, https://doi.org/10.1016/j.atmosenv.2005.04.014, 2005.

Martinez, M., Harder, H., Kubistin, D., Rudolf, M., Bozem, H., Eerdekens, G., Fischer, H., Klüpfel, T., Gurk, C., Königstedt, R., Parchatka, U., Schiller, C. L., Stickler, A., Williams, J., and Lelieveld, J.: Hydroxyl radicals in the tropical troposphere over the Suriname rainforest: airborne measurements, Atmos. Chem. Phys., 10, 3759–3773, https://doi.org/10.5194/acp-10-3759-2010, 2010.

Metzger, S., Mihalopoulos, N., and Lelieveld, J.: Importance of mineral cations and organics in gas-aerosol partitioning of reactive nitrogen compounds: case study based on MINOS results, Atmos. Chem. Phys., 6, 2549–2567, https://doi.org/10.5194/acp-6-2549-2006, 2006.

Meusel, H., Tamm, A., Kuhn, U., Wu, D., Leifke, A. L., Fiedler, S., Ruckteschler, N., Yordanova, P., Lang-Yona, N., Pöhlker, M., Lelieveld, J., Hoffmann, T., Pöschl, U., Su, H., Weber, B., and Cheng, Y.: Emission of nitrous acid from soil and biological soil crusts represents an important source of HONO in the remote atmosphere in Cyprus, Atmos. Chem. Phys., 18, 799–813, https://doi.org/10.5194/acp-18-799-2018, 2018.

Monge, M. E., D'Anna, B., Mazri, L., Giroir-Fendler, A., Ammann, M., Donaldson, D. J., and George, C.: Light changes the atmospheric reactivity of soot, P. Natl. Acad. Sci. USA, 107, 6605–6609, https://doi.org/10.1073/pnas.0908341107, 2010.

Ninneman, M., Lu, S., Lee, P., McQueen, J., Huang, J. P., Demerjian, K., and Schwab, J.: Observed and Model-Derived Ozone Production Efficiency over Urban and Rural New York State, Atmosphere-Basel, 8, 126, https://doi.org/10.3390/atmos8070126, 2017.

Nunnermacker, L. J., Kleinman, L. I., Imre, D., Daum, P. H., Lee, Y. N., Lee, J. H., Springston, S. R., Newman, L., and Gillani, N.: NO_y lifetimes and O_3 production efficiencies in urban and power plant plumes: Analysis of field data, J. Geophys. Res.-Atmos., 105, 9165–9176, https://doi.org/10.1029/1999jd900753, 2000.

Nunnermacker, L. J., Weinstein-Lloyd, J., Kleinman, L., Daum, P. H., Lee, Y. N., Springston, S. R., Klotz, P., Newman, L., Neuroth, G., and Hyde, P.: Ground-based and aircraft measurements of trace gases in Phoenix, Arizona (1998), Atmos. Environ., 38, 4941–4956, https://doi.org/10.1016/j.atmosenv.2004.04.033, 2004.

Oertel, C., Matschullat, J., Zurba, K., Zimmermann, F., and Erasmi, S.: Greenhouse gas emissions from soils A review, Chem. Erde-Geochem., 76, 327–352, https://doi.org/10.1016/j.chemer.2016.04.002, 2016.

Olszyna, K. J., Bailey, E. M., Simonaitis, R., and Meagher, J. F.: O_3 and NO_y relationships at a rural Site, J. Geophys. Res.-Atmos., 99, 14557–14563, https://doi.org/10.1029/94jd00739, 1994.

Osthoff, H. D., Roberts, J. M., Ravishankara, A. R., Williams, E. J., Lerner, B. M., Sommariva, R., Bates, T. S., Coffman, D., Quinn, P. K., Dibb, J. E., Stark, H., Burkholder, J. B., Talukdar, R. K., Meagher, J., Fehsenfeld, F. C., and Brown, S. S.: High levels of nitryl chloride in the polluted subtropical marine boundary layer, Nat. Geosci., 1, 324–328, 2008.

Parrish, D. D., Ryerson, T. B., Mellqvist, J., Johansson, J., Fried, A., Richter, D., Walega, J. G., Washenfelder, R. A., de Gouw, J. A., Peischl, J., Aikin, K. C., McKeen, S. A., Frost, G. J., Fehsenfeld, F. C., and Herndon, S. C.: Primary and secondary sources of formaldehyde in urban atmospheres: Houston Texas region, Atmos. Chem. Phys., 12, 3273–3288, https://doi.org/10.5194/acp-12-3273-2012, 2012.

Pfannerstill, E. Y., Wang, N., Edtbauer, A., Bourtsoukidis, E., Crowley, J. N., Dienhart, D., Eger, P. G., Ernle, L., Fischer, H., Hottmann, B., Paris, J.-D., Stönner, C., Tadic, I., Walter, D., Lelieveld, J., and Williams, J.: Shipborne measurements of total OH reactivity around the Arabian Peninsula and its role in ozone chemistry, Atmos. Chem. Phys., 19, 11501–11523, https://doi.org/10.5194/acp-19-11501-2019, 2019.

Platt, U., Perner, D., Harris, G. W., Winer, A. M., and Pitts, J. N.: Observations of Nitrous-Acid in an Urban Atmosphere by Differential Optical-Absorption, Nature, 285, 312–314, https://doi.org/10.1038/285312a0, 1980.

Regelin, E., Harder, H., Martinez, M., Kubistin, D., Tatum Ernest, C., Bozem, H., Klippel, T., Hosaynali-Beygi, Z., Fischer, H., Sander, R., Jöckel, P., Königstedt, R., and Lelieveld, J.: HO_x measurements in the summertime upper troposphere over Europe: a comparison of observations to a box model

and a 3-D model, Atmos. Chem. Phys., 13, 10703–10720, https://doi.org/10.5194/acp-13-10703-2013, 2013.

Richter, A., Eyring, V., Burrows, J. P., Bovensmann, H., Lauer, A., Sierk, B., and Crutzen, P. J.: Satellite measurements of NO_2 from international shipping emissions, Geophys. Res. Lett., 31, L23110, https://doi.org/10.1029/2004gl020822, 2004.

Rickard, A. R., Salisbury, G., Monks, P. S., Lewis, A. C., Baugitte, S., Bandy, B. J., Clemitshaw, K. C., and Penkett, S. A.: Comparison of measured ozone production efficiencies in the marine boundary layer at two European coastal sites under different pollution regimes, J. Atmos. Chem., 43, 107–134, https://doi.org/10.1023/A:1019970123228, 2002.

Rolph, G., Stein, A., and Stunder, B.: Real-time environmental applications and display system: READY, Environ. Modell. Softw., 95, 210–228, https://doi.org/10.1016/j.envsoft.2017.06.025, 2017.

Romer, P. S., Duffey, K. C., Wooldridge, P. J., Allen, H. M., Ayres, B. R., Brown, S. S., Brune, W. H., Crounse, J. D., de Gouw, J., Draper, D. C., Feiner, P. A., Fry, J. L., Goldstein, A. H., Koss, A., Misztal, P. K., Nguyen, T. B., Olson, K., Teng, A. P., Wennberg, P. O., Wild, R. J., Zhang, L., and Cohen, R. C.: The lifetime of nitrogen oxides in an isoprene-dominated forest, Atmos. Chem. Phys., 16, 7623–7637, https://doi.org/10.5194/acp-16-7623-2016, 2016.

Roussel, P. B., Lin, X., Camacho, F., Laszlo, S., Taylor, R., Melo, O. T., Shepson, P. B., Hastie, D. R., and Niki, H.: Observations of ozone and precursor levels at two sites around Toronto, Ontario, during SONTOS 92, Atmos. Environ., 30, 2145–2155, https://doi.org/10.1016/1352-2310(95)00102-6, 1996.

Saxe, H. and Larsen, T.: Air pollution from ships in three Danish ports, Atmos. Environ., 38, 4057–4067, https://doi.org/10.1016/j.atmosenv.2004.03.055, 2004.

Sillman, S.: Ozone production efficiency and loss of NO_x in power plant plumes: Photochemical model and interpretation of measurements in Tennessee, J. Geophys. Res.-Atmos., 105, 9189–9202, https://doi.org/10.1029/1999jd901014, 2000.

Sinha, V., Williams, J., Crowley, J. N., and Lelieveld, J.: The Comparative Reactivity Method – a new tool to measure total OH Reactivity in ambient air, Atmos. Chem. Phys., 8, 2213–2227, https://doi.org/10.5194/acp-8-2213-2008, 2008.

Sobanski, N., Schuladen, J., Schuster, G., Lelieveld, J., and Crowley, J. N.: A five-channel cavity ring-down spectrometer for the detection of NO_2, NO_3, N_2O_5, total peroxy nitrates and total alkyl nitrates, Atmos. Meas. Tech., 9, 5103–5118, https://doi.org/10.5194/amt-9-5103-2016, 2016.

Stein, A. F., Draxler, R. R., Rolph, G. D., Stunder, B. J. B., Cohen, M. D., and Ngan, F.: NOAA'S HYSPLIT atmospheric transport and dispersion modeling system, B. Am. Meteorol. Soc., 96, 2059–2077, https://doi.org/10.1175/bams-d-14-00110.1, 2015.

Stickler, A., Fischer, H., Williams, J., de Reus, M., Sander, R., Lawrence, M. G., Crowley, J. N., and Lelieveld, J.: Influence of summertime deep convection on formaldehyde in the middle and upper troposphere over Europe, J. Geophys. Res.-Atmos., 111, D14308, https://doi.org/10.1029/2005JD007001, 2006.

Stutz, J., Kim, E. S., Platt, U., Bruno, P., Perrino, C., and Febo, A.: UV-visible absorption cross sections of nitrous acid, J. Geophys. Res.-Atmos., 105, 14585–14592, 2000.

Sun, L., Chen, T. S., Jiang, Y., Zhou, Y., Sheng, L. F., Lin, J. T., Li, J., Dong, C., Wang, C., Wang, X. F., Zhang, Q. Z., Wang, W. X., and Xue, L. K.: Ship emission of nitrous acid (HONO) and its impacts on the marine atmospheric oxidation chemistry, Sci. Total Environ., 735, 139355, https://doi.org/10.1016/j.scitotenv.2020.139355, 2020.

Sun, Y., Wang, L. L., Wang, Y. S., Zhang, D. Q., Quan, L., and Xin, J. Y.: In situ measurements of NO, NO_2, NO_y, and O_3 in Dinghushan (112° E, 23° N), China during autumn 2008, Atmos. Environ., 44, 2079–2088, https://doi.org/10.1016/j.atmosenv.2010.03.007, 2010.

Tadic, I., Crowley, J. N., Dienhart, D., Eger, P., Harder, H., Hottmann, B., Martinez, M., Parchatka, U., Paris, J.-D., Pozzer, A., Rohloff, R., Schuladen, J., Shenolikar, J., Tauer, S., Lelieveld, J., and Fischer, H.: Net ozone production and its relationship to nitrogen oxides and volatile organic compounds in the marine boundary layer around the Arabian Peninsula, Atmos. Chem. Phys., 20, 6769–6787, https://doi.org/10.5194/acp-20-6769-2020, 2020.

Thieser, J., Schuster, G., Schuladen, J., Phillips, G. J., Reiffs, A., Parchatka, U., Pöhler, D., Lelieveld, J., and Crowley, J. N.: A two-channel thermal dissociation cavity ring-down spectrometer for the detection of ambient NO_2, RO_2NO_2 and $RONO_2$, Atmos. Meas. Tech., 9, 553–576, https://doi.org/10.5194/amt-9-553-2016, 2016.

Trainer, M., Parrish, D. D., Buhr, M. P., Norton, R. B., Fehsenfeld, F. C., Anlauf, K. G., Bottenheim, J. W., Tang, Y. Z., Wiebe, H. A., Roberts, J. M., Tanner, R. L., Newman, L., Bowersox, V. C., Meagher, J. F., Olszyna, K. J., Rodgers, M. O., Wang, T., Berresheim, H., Demerjian, K. L., and Roychowdhury, U. K.: Correlation of Ozone with No_y in Photochemically Aged Air, J. Geophys. Res.-Atmos., 98, 2917–2925, https://doi.org/10.1029/92jd01910, 1993.

Večeřa, Z., Mikuška, P., Smolík, J., Eleftheriadis, K., Bryant, C., Colbeck, I., and Lazaridis, M.: Shipboard Measurements of Nitrogen Dioxide, Nitrous Acid, Nitric Acid and Ozone in the Eastern Mediterranean Sea, Water Air Soil Poll., 8, 117–125, https://doi.org/10.1007/s11267-007-9133-y, 2008.

Wang, J. H., Ge, B. Z., and Wang, Z. F.: Ozone Production Efficiency in Highly Polluted Environments, Current Pollution Reports, 4, 198–207, https://doi.org/10.1007/s40726-018-0093-9, 2018.

Wang, T., Carroll, M. A., Albercook, G. M., Owens, K. R., Duderstadt, K. A., Markevitch, A. N., Parrish, D. D., Holloway, J. S., Fehsenfeld, F. C., Forbes, G., and Ogren, J.: Ground-based measurements of NO_x and total reactive oxidized nitrogen (NO_y) at Sable Island, Nova Scotia, during the NARE 1993 summer intensive, J. Geophys. Res.-Atmos., 101, 28991–29004, https://doi.org/10.1029/96jd01090, 1996.

Wild, R. J., Edwards, P. M., Dube, W. P., Baumann, K., Edgerton, E. S., Quinn, P. K., Roberts, J. M., Rollins, A. W., Veres, P. R., Warneke, C., Williams, E. J., Yuan, B., and Brown, S. S.: A measurement of total reactive nitrogen, NO_y, together with NO_2, NO, and O_3 via cavity ring-down spectroscopy, Environ. Sci. Technol., 48, 9609–9615, https://doi.org/10.1021/es501896w, 2014.

Wild, R. J., Edwards, P. M., Bates, T. S., Cohen, R. C., de Gouw, J. A., Dubé, W. P., Gilman, J. B., Holloway, J., Kercher, J., Koss, A. R., Lee, L., Lerner, B. M., McLaren, R., Quinn, P. K., Roberts, J. M., Stutz, J., Thornton, J. A., Veres, P. R., Warneke, C., Williams, E., Young, C. J., Yuan, B., Zarzana, K. J., and

Brown, S. S.: Reactive nitrogen partitioning and its relationship to winter ozone events in Utah, Atmos. Chem. Phys., 16, 573–583, https://doi.org/10.5194/acp-16-573-2016, 2016.

Williams, E. J., Lerner, B. M., Murphy, P. C., Herndon, S. C., and Zahniser, M. S.: Emissions of NO_x, SO_2, CO, and HCHO from commercial marine shipping during Texas Air Quality Study (TexAQS) 2006, J. Geophys. Res.-Atmos., 114, D21306, https://doi.org/10.1029/2009jd012094, 2009.

Wojtal, P., Halla, J. D., and McLaren, R.: Pseudo steady states of HONO measured in the nocturnal marine boundary layer: a conceptual model for HONO formation on aqueous surfaces, Atmos. Chem. Phys., 11, 3243–3261, https://doi.org/10.5194/acp-11-3243-2011, 2011.

Wolfe, G. M., Kaiser, J., Hanisco, T. F., Keutsch, F. N., de Gouw, J. A., Gilman, J. B., Graus, M., Hatch, C. D., Holloway, J., Horowitz, L. W., Lee, B. H., Lerner, B. M., Lopez-Hilifiker, F., Mao, J., Marvin, M. R., Peischl, J., Pollack, I. B., Roberts, J. M., Ryerson, T. B., Thornton, J. A., Veres, P. R., and Warneke, C.: Formaldehyde production from isoprene oxidation across NO_x regimes, Atmos. Chem. Phys., 16, 2597–2610, https://doi.org/10.5194/acp-16-2597-2016, 2016.

Wolfe, G. M., Nicely, J. M., St. Clair, J. M., Hanisco, T. F., Liao, J., Oman, L. D., Brune, W. B., Miller, D., Thames, A., González Abad, G., Ryerson, T. B., Thompson, C. R., Peischl, J., McKain, K., Sweeney, C., Wennberg, P. O., Kim, M., Crounse, J. D., Hall, S. R., Ullmann, K., Diskin, G., Bui, P., Chang, C., and Dean-Day, J.: Mapping hydroxyl variability throughout the global remote troposphere via synthesis of airborne and satellite formaldehyde observations, P. Natl. Acad. Sci. USA, 116, 11171–11180, https://doi.org/10.1073/pnas.1821661116, 2019.

Womack, C. C., Neuman, J. A., Veres, P. R., Eilerman, S. J., Brock, C. A., Decker, Z. C. J., Zarzana, K. J., Dube, W. P., Wild, R. J., Wooldridge, P. J., Cohen, R. C., and Brown, S. S.: Evaluation of the accuracy of thermal dissociation CRDS and LIF techniques for atmospheric measurement of reactive nitrogen species, Atmos. Meas. Tech., 10, 1911–1926, https://doi.org/10.5194/amt-10-1911-2017, 2017.

Wood, E. C., Herndon, S. C., Onasch, T. B., Kroll, J. H., Canagaratna, M. R., Kolb, C. E., Worsnop, D. R., Neuman, J. A., Seila, R., Zavala, M., and Knighton, W. B.: A case study of ozone production, nitrogen oxides, and the radical budget in Mexico City, Atmos. Chem. Phys., 9, 2499–2516, https://doi.org/10.5194/acp-9-2499-2009, 2009.

Wu, D., Hu, Y. X., McCormick, M. P., Xu, K. M., Liu, Z. Y., Smith, B., Omar, A. H., and Chang, F. L.: Deriving Marine-Boundary-Layer Lapse Rate from Collocated CALIPSO, MODIS, and AMSR-E Data to Study Global Low-Cloud Height Statistics, IEEE Geosci. Remote Sens. Lett., 5, 649–652, https://doi.org/10.1109/Lgrs.2008.2002024, 2008.

Ye, C. X., Zhou, X. L., Pu, D., Stutz, J., Festa, J., Spolaor, M., Tsai, C., Cantrell, C., Mauldin, R. L., Campos, T., Weinheimer, A., Hornbrook, R. S., Apel, E. C., Guenther, A., Kaser, L., Yuan, B., Karl, T., Haggerty, J., Hall, S., Ullmann, K., Smith, J. N., Ortega, J., and Knote, C.: Rapid cycling of reactive nitrogen in the marine boundary layer, Nature, 532, 489–491, https://doi.org/10.1038/nature17195, 2016.

Zorn, S. R., Drewnick, F., Schott, M., Hoffmann, T., and Borrmann, S.: Characterization of the South Atlantic marine boundary layer aerosol using an aerodyne aerosol mass spectrometer, Atmos. Chem. Phys., 8, 4711–4728, https://doi.org/10.5194/acp-8-4711-2008, 2008.

Supplement of Atmos. Chem. Phys., 21, 7473–7498, 2021
https://doi.org/10.5194/acp-21-7473-2021-supplement

Atmospheric Chemistry and Physics
Open Access
EGU

Supplement of

Reactive nitrogen around the Arabian Peninsula and in the Mediterranean Sea during the 2017 AQABA ship campaign

Nils Friedrich et al.

Correspondence to: John N. Crowley (john.crowley@mpic.de)

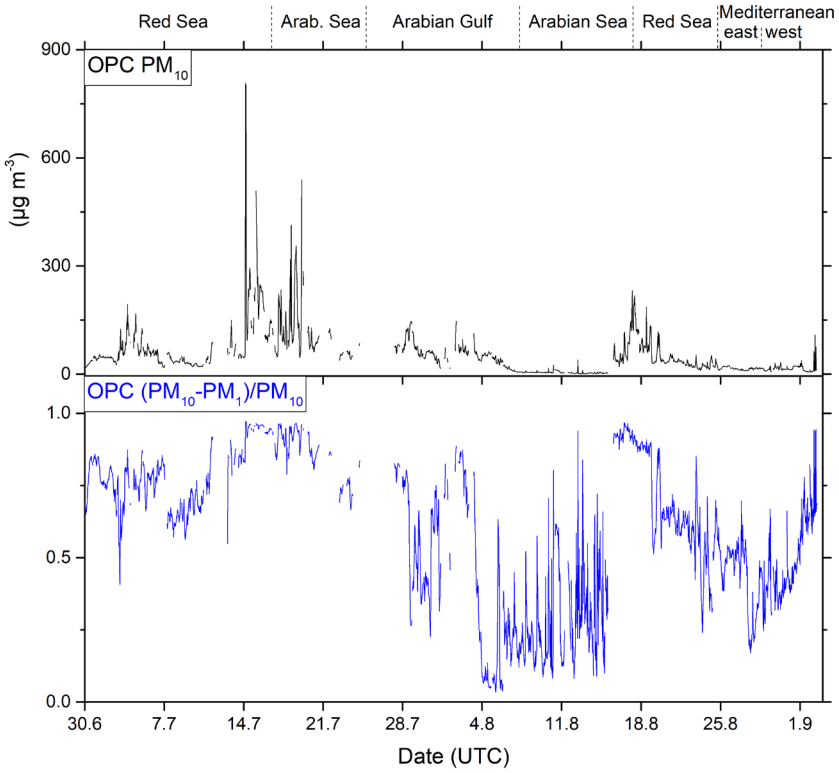

Figure S1: Total aerosol mass concentration during the AQABA campaign, as measured by an Optical Particle Counter in the PM_{10} size range. The contribution of coarse mode aerosol was estimated in form of the $(PM_{10}-PM_1)/PM_{10}$ ratio. Highest PM_{10} concentrations were on both legs observed in the transitional area between Red Sea and Arabian Sea, where coarse mode aerosol contributed ca. > 90 % to the total aerosol mass concentration.

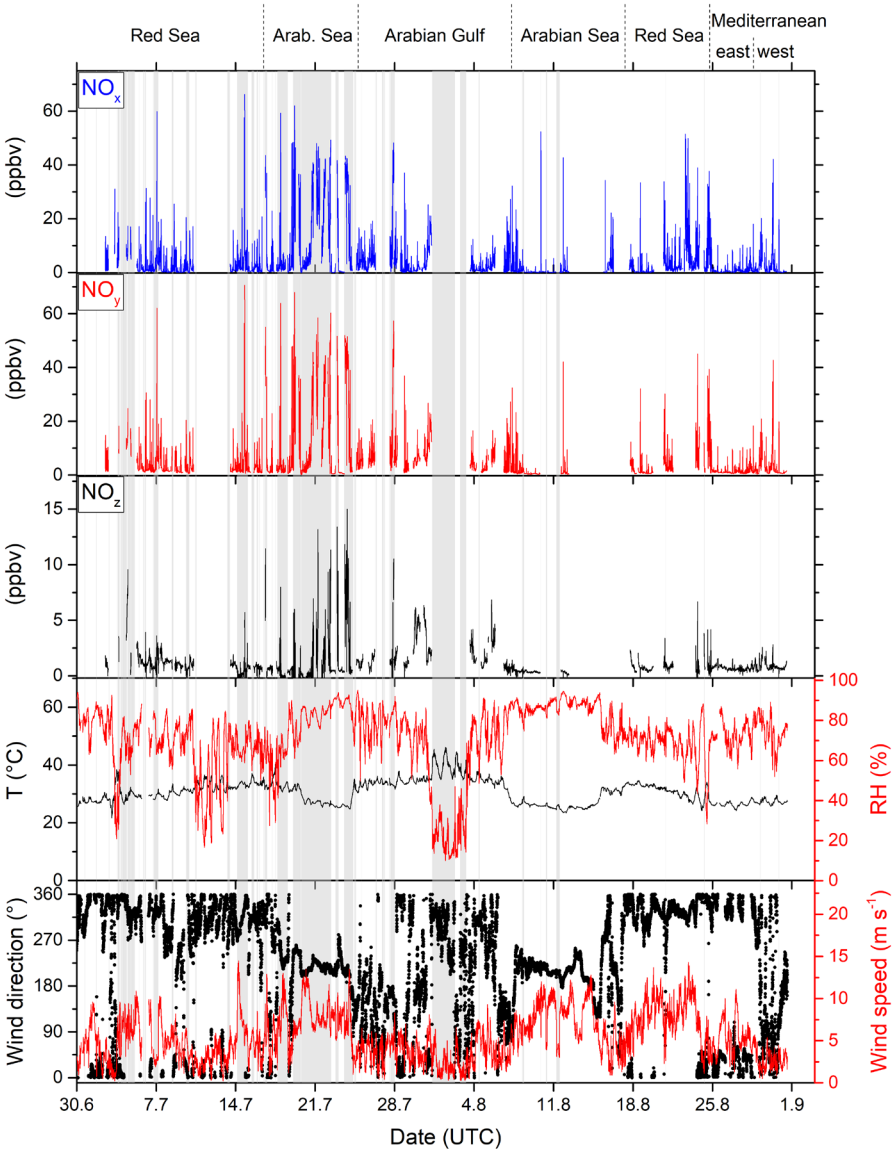

Figure S2: NO_x, NO_y and NO_z measured by TD-CRDS (5 minute averages). Periods during which the measurement was contaminated by the ship's stack are highlighted in grey. The first leg ended on the 31 July, the 2nd leg started on 3 August 2017 after anchorage in Kuwait. The two lowest panels indicate prevailing temperature, relative humidity, wind direction and wind speed.

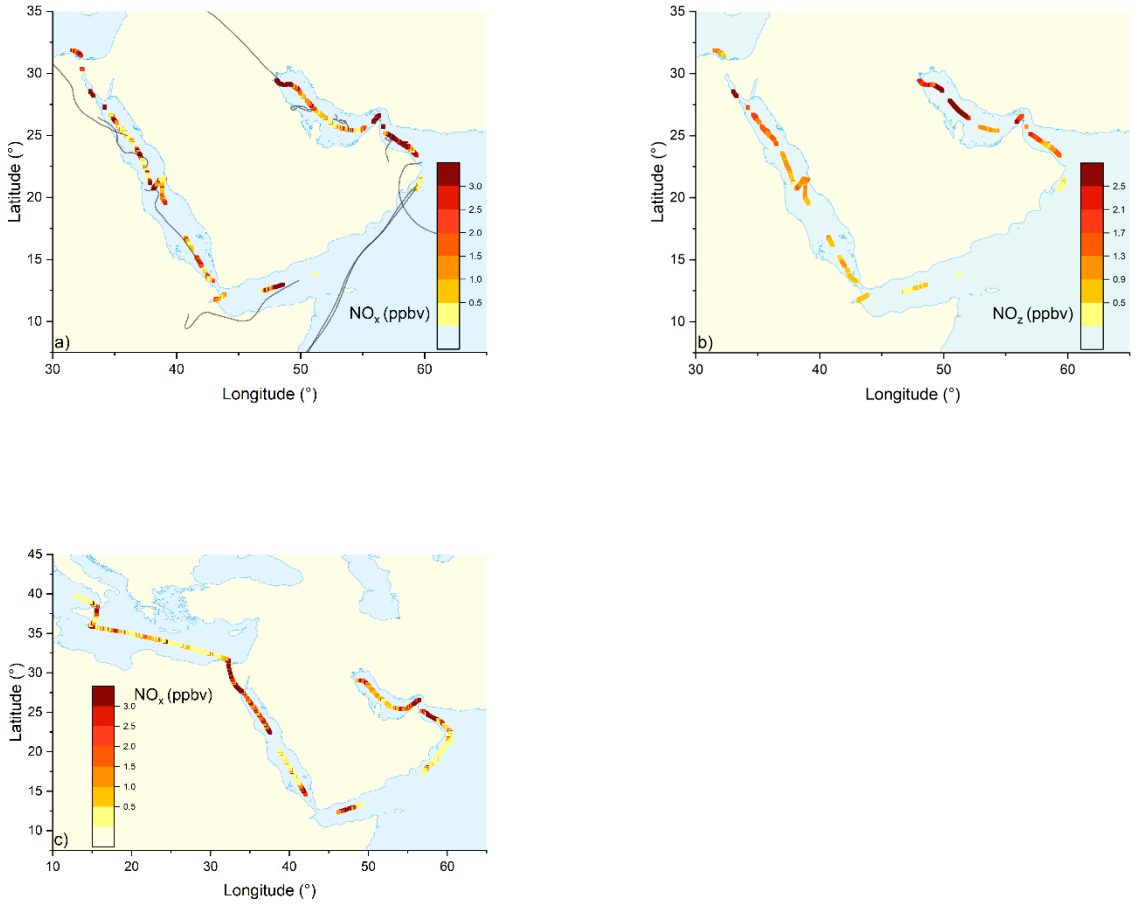

Figure S3: NO_x *(a)* and NO_z *(b)* mixing ratios during the first leg, and *(c)* NO_x mixing ratios during the second leg of AQABA. The data points are 30 min averages, periods contaminated with ship stack contamination (e.g. most of the Arabian Sea) have been removed. HYSPLIT back trajectories (48 hours) are indicated with grey lines in *(a)*. Elevated NO_z mixing ratios above 2.5 ppbv were encountered in the Arabian Gulf.

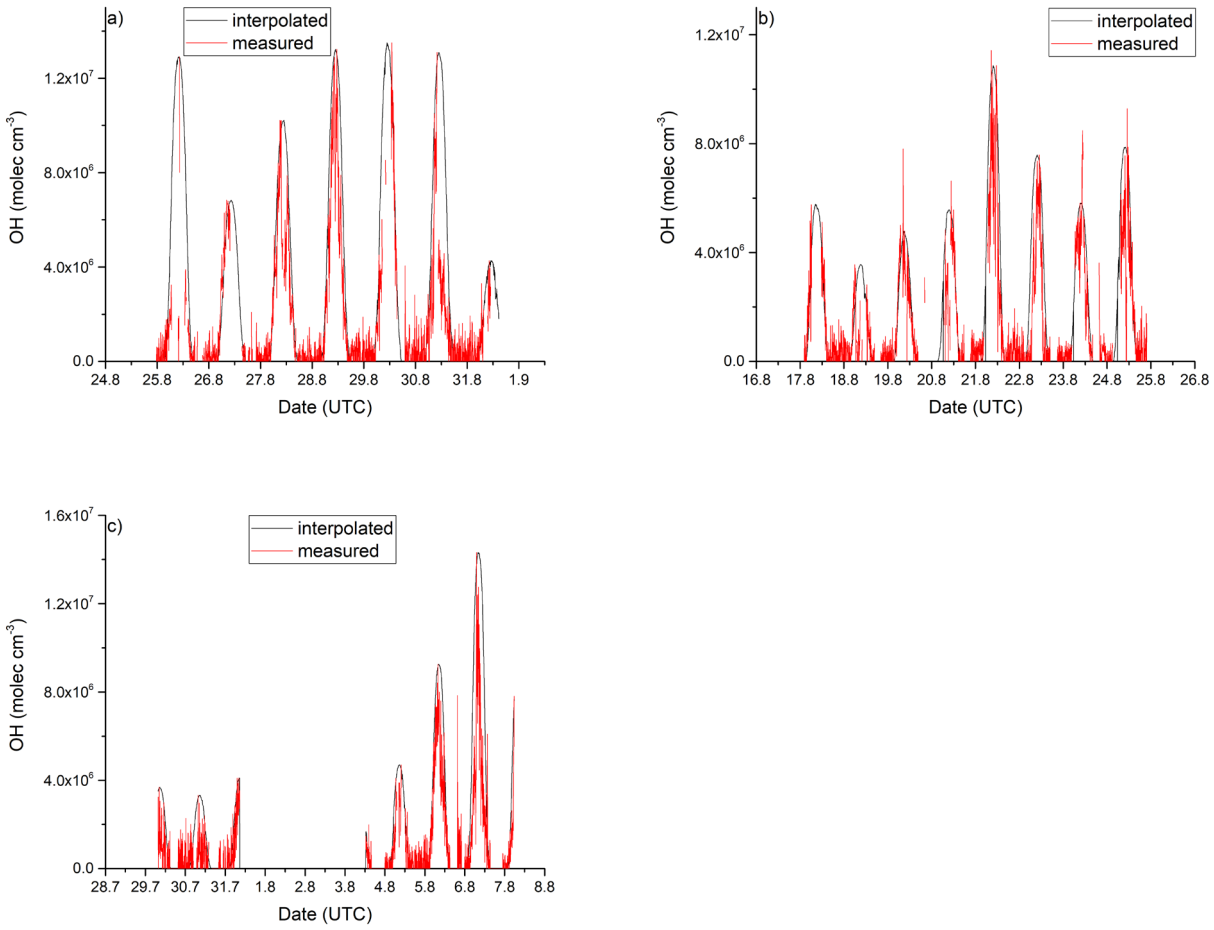

Figure S4: Comparison between measured OH concentrations and the interpolated trace based on J_{O1D} (see Sect. 3.1.3) in *(a)* the Mediterranean Sea, *(b)* the Red Sea, and *(c)* the Arabian Gulf.

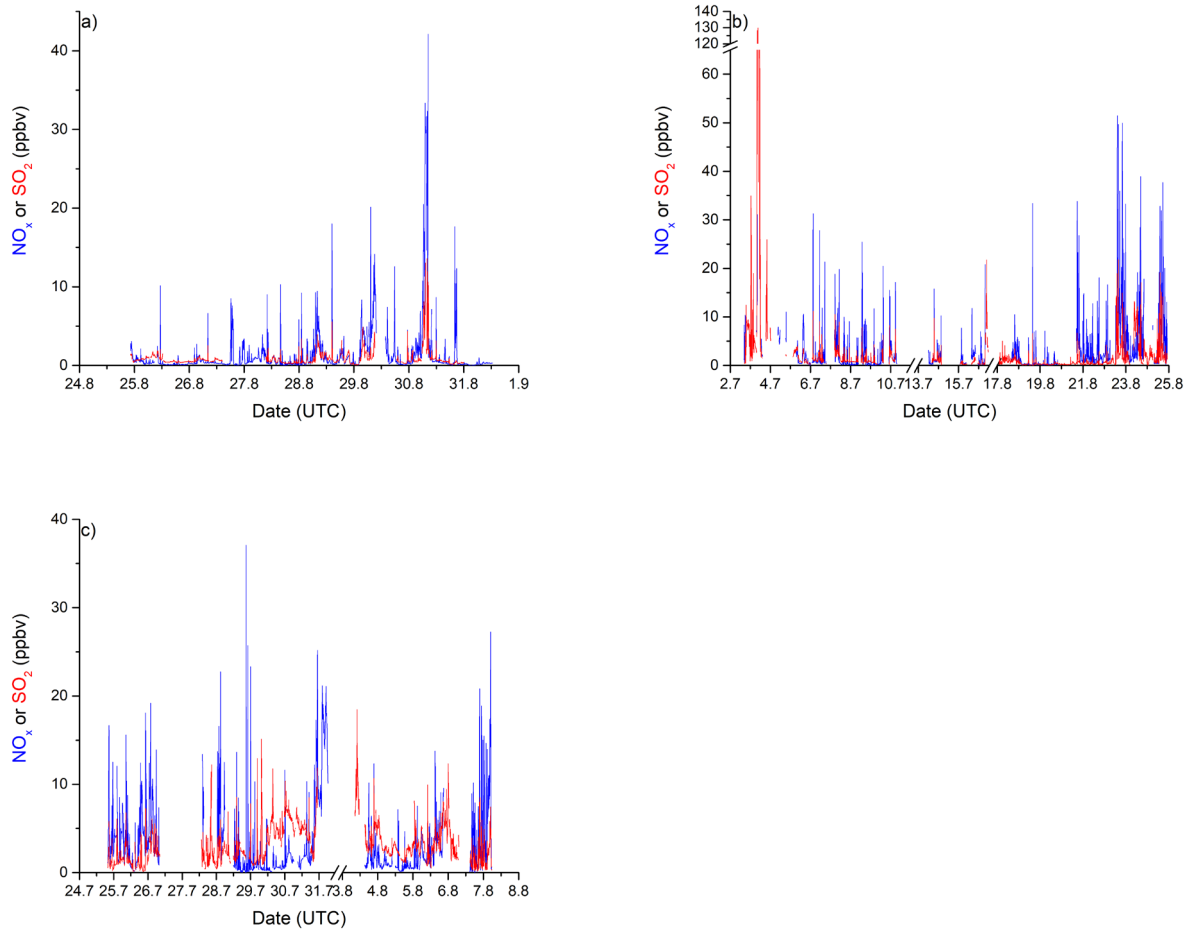

Figure S5: Time series of NO_x and SO_2 in *(a)* the Mediterranean Sea, *(b)* the Red Sea, and *(c)* the Arabian Gulf.

7 Reactive nitrogen budget and organic nitrate yields in a chamber study of the nighttime oxidation of isoprene by NO_3.

The thesis author conducted the TD-CRDS measurements during the NO3ISOP campaign, performed the presented analyses, and wrote the section. Additional data sets from other instruments were used upon approval and are listed together with their respective owning institutions below (see Section 7.2.4 for more details on the respective methods):

- *HNO_3, HONO, isoprene, MVK+MACR, HO_2, O_3, INP, IHN: Forschungszentrum Jülich, Germany.*
- *Organic nitrates: Reed College, United States.*
- *NO_3, N_2O_5: ICARE CNRS, France; MPI for Chemistry, Germany.*

7.1 Introduction

Isoprene is the most abundant biogenic VOC (BVOC) emitted into the earth's atmosphere, contributing about 50 % to the overall 10^{15} g yearly BVOC emissions (Guenther et al., 2012; Messina et al., 2016; Granier et al., 2019). The emission rate of isoprene from vegetation depends positively on light intensity and temperature so that isoprene mixing ratios increase in the late afternoon, when the main sink (reaction with the OH-radical) slows down (Warneke et al., 2004). In the early evening, isoprene accumulates during continued emission into the developing shallow boundary layer, where its main nighttime sink becomes reaction with the nitrate radical (NO_3) (Starn et al., 1998; Stroud et al., 2002; Brown et al., 2009). The nighttime chemistry of NO_x leading to the formation of NO_3 is further discussed in Section 2.5. Models of isoprene chemistry indicate that 40-50 % of isoprene nitrates originate from the NO_3-initiated degradation of isoprene at night (Horowitz et al., 2007; Xie et al., 2013), which accounts for ca. 6 % of the total isoprene oxidation (von Kuhlmann et al., 2004; Horowitz et al., 2007). These studies focussed on the comparison with observational data sets from the south-eastern United States, and therefore apply for regions with concurrent elevated BVOC and anthropogenic emissions, providing the required sources of isoprene and NO_x.

Essential features of the NO_3-initated oxidation of isoprene are displayed in Figure 7 (adapted from Schwantes et al. (2015) and IUPAC (2020)). Similar mechanistic schemes have also been presented in reviews by Ng et al. (2017) and Wennberg et al. (2018). Note that of the four possible peroxy radicals only those formed from addition to the 1- and 4- position are considered (these are the most important) and that interchange between peroxy radicals via dissociation and re-formation (see below and Vereecken et al. (2021)) is disregarded for the sake of clarity of presentation. The addition of the nitrate radical to the 1-position of isoprene is favoured by a factor of ca. 6 over the 4-position (IUPAC, 2020). Internal addition (i.e. in the 2- or the 3-position) is neglectable, due to the missing allylic nature of the radicals formed after NO_3 addition, compared to the external branches. Theoretical considerations have found that the relative energy gain from the reaction of isoprene with NO_3 is e.g. 1.9 times larger when resulting in the 1-subsituted (30.7 kcal mol^{-1}) instead of the 2-subsituted radical (15.9 kcal mol^{-1}) (Suh et al., 2001). In the initial step of the isoprene oxidation, two isomeric nitrooxyperoxy radicals are therefore formed, with the peroxy group either located in the β (β-NISOPO2) or δ (δ-NISOPO2) position relative to the nitrate functionality. Studies of Schwantes et al. (2015) indicate a ca. 1.2:1 ratio between the δ- and the β-isomers. These two isomers can undergo a series of subsequent reactions. Alkoxy radicals (β/δ-NISOPO) are produced in the reaction with

NO or NO_3. The reaction with another peroxy radical (RO_2) enables the formation of alkoxy radicals, alcohols (β/δ-ISOPCNO3), methyl vinyl ketone (MVK) and the aldehyde NC4CHO. For the RO_2 + RO_2 self-reaction, Kwan et al. (2012) found that the branch leading to carbonyls and alcohols (ca. 59-77 %) is favoured over the formation of two alkoxy radicals (ca. 19-38 %) or an organic peroxide (ROOR; ca. 3-4 %). MVK and NC4CHO are formed from the respective alkoxy radicals. In the presence of hydroperoxyl radicals (HO_2) hydroperoxides (e.g. β/δ-NISOPOOH) are formed. In the context of estimating the reactive nitrogen budget, apart from MVK all the products of the isoprene oxidation by NO_3 retain a nitrate group, which enables their detection via TD-CRDS.

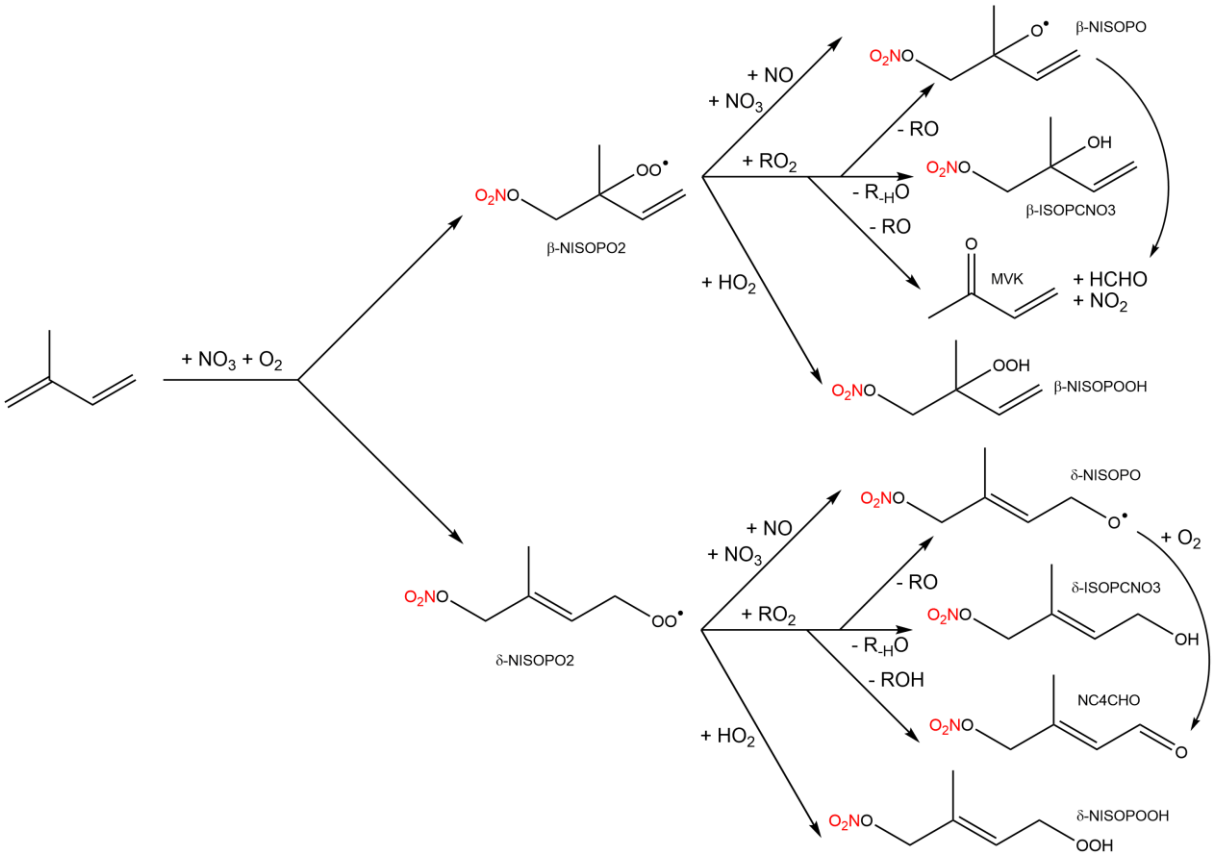

Figure 7: Reaction scheme showing the primary products of the isoprene oxidation by NO_3, based on works from Schwantes et al. (2015) and IUPAC (2020). Functional groups which are expected to form NO_2 molecules in the inlet of the TD-CRDS are marked in red. Abbreviations for the dominant organic product species shown are based on the nomenclature used in the Master Chemical Mechanism (MCM, version 3.3.1) (Saunders et al., 2003; Jenkin et al., 2015). Only organic products are shown in the scheme (except for the dissociating NO_2 during the MVK formation), for visual clarity.

The first-generation products shown in Figure 7 are prone to further react with OH and O_3, due to the remaining double bond, leading to more oxidised nitrates or carbonyl species (e.g. glyoxal) and ultimately to CO and CO_2. These complex reactions, however, are outside the scope of this work and the reader is referred to Jenkin et al. (2015) and Wennberg et al. (2018). Furthermore, the analyses in this section are limited to the unspeciated sum of organic nitrates,

as detected via TD-CRDS. In summary, Jenkin et al. (2015) estimated that 40 % of the molecules retain their nitrate functionality in the OH-initiated degradation of the first-generation isoprene-nitrates, whereas O_3-initiated reactions result in 65 % of the second-generation products possessing a nitrate group.

Recent theoretical calculations by Vereecken et al. (2021) have shown that the oxygen addition leading to the formation of the initial RO_2 radicals (NISOPO2) is reversible, allowing interconversion between several nitrated RO_2 species. From the subsequently formed alkoxy radicals (NISOPO), new pathways resulting in nitrated RO_2 radials with epoxy functions have been found, which supress the production of MVK. Additional competing pathways from RO radicals include isomerisation and chain terminations, resulting in the release of NO_2. Implementing the epoxide-forming reactions also allowed reconciling model predictions with experimental data sets of RO_2 and MVK from the same campaign discussed in this section (Vereecken et al., 2021).

The NO_3 initiated oxidation of isoprene can also lead to the formation of secondary organic aerosol (SOA) with yields (= mass of formed aerosol divided by the mass of consumed isoprene) between ca. 4 % and 24 % reported from chamber studies (Ng et al., 2008; Rollins et al., 2009) and between 2 % and 27 % from analysis of aircraft-based measurements of the nitrate fraction of the sampled aerosol (Brown et al., 2009; Fry et al., 2018). Ng et al. (2008) estimate that 2-3 Tg yr^{-1} of the yearly SOA mass is produced from NO_3 + isoprene. By comparison, overall isoprene contributes ca. 14 Tg yr^{-1} of SOA (Henze et al., 2008), including also products of the oxidation by OH and O_3. At nighttime, products of isoprene and NO_3 can account for up to ca. 85 % of particulate organic nitrate mass concentrations (Lee et al., 2016).

Detailed insight of the mechanism for formation of gas-phase products and SOA from the NO_3-initiated oxidation of isoprene was the goal of the NO3ISOP campaign, conducted at the SAPHIR chamber of the Forschungszentrum Jülich in summer 2018. Publications from the NO3ISOP campaign deal with the evolution of NO_3 reactivity (Dewald et al., 2020), the composition and volatility of the multi-generation products (Wu et al., 2020), and the partitioning of organic nitrates between the gas- and the particulate-phase (Brownwood et al., 2021). In this study, the reactive nitrogen budget is examined by combining measurements of NO_x (=NO+NO_2), NO_y (=NO_x+NO_z), HNO_3 and other NO_z species (sum of organic nitrates, N_2O_5, NO_3, and HONO) and to box model results. Additionally, yields of organic nitrates (ONs) relative to the consumed isoprene and NO_z yields relative to the loss in NO_x are determined.

7.2 Methods

7.2.1 NO3ISOP campaign

The NO3ISOP campaign took place over a four week period (summer 2018) at the SAPHIR chamber of the Forschungszentrum Jülich (see Section 7.2.2), in which a total of 22 experiments were conducted. In the first 11 experiments the focus was on the gas-phase, while the last 11 experiments were performed with addition of seed-aerosol (ammonium sulfate) in order to stimulate SOA formation. A list of the experimental conditions for the gas-phase experiments performed is shown in Table 3. Results from the particulate-phase experiments are not presented in this work. An analysis of these data sets would require differentiating between gas- and particle-phase nitrates (pNit). As presented in Friedrich et al. (2020) (i.e. Section 5), however, the pNit channel of the TD-CRDS suffers from humidity-induced release of previously deposited NO_x from the charcoal denuder surface, resulting in a positive bias of unknown extent.

In typical experiments, NO_2 mixing ratios below 10 ppbv were introduced into the chamber together with 70-120 ppbv of O_3 to generate NO_3 radicals, achieving a NO_3 production rate of ca. 1.2 ppbv hr^{-1} (at 25 °C, 95 ppbv O_3, and 4 ppbv NO_2) . Isoprene levels were usually between 1 and 4 ppbv. Water vapor was added in three experiments (3-7 August 2018), resulting in relative humidities of up to 60 %. On 6 and 12 August 2018, the chamber roof was opened during ca. half of the experiment in order to study the photo-oxidation of the isoprene-nitrates formed during the dark phase. The addition of CO on 12 August 2018 had the goal of scavenging OH radicals and limiting the degradation of the isoprene + NO_3 products to photolysis reactions. Photo-oxidation of isoprene was investigated on 3 August 2018 by starting under sunlight irradiation. HO_2 production was promoted on 9 August 2018 through the ozonolysis of propene and again the scavenging of OH by CO, with an expected shift towards the RO_2 + HO_2 branch described in Section 7.1. Lower mixing ratios of NO_2, O_3 and isoprene were used in slow oxidation experiments on 7 and 10 August 2018 to stimulate RO_2 isomerisation. In contrast, fast oxidation conditions were established on 8 and 13 August 2018, stimulating the self-reaction of two RO_2 molecules.

Table 3: Experimental conditions during the experiments of the NO3ISOP campaign with only gas-phase chemistry.

Day in 2018	NO_2 range (ppbv)	O_3 range (ppbv)	max. isoprene (ppbv)	max. RH (%)	Remarks
31 July	1-6	90-120	0	0	
1 August	2-5	90-120	1.2	0	
2 August	2-7	90-120	2.5	0	
3 August	3-6	80-100	2.6	55	day to night transition
6 August	1-6	90-110	3.2	60	night to day transition
7 August	3-5	50-60	2.4	14	
8 August	14-32	80-120	10	0	
9 August	2-7	70-120	4.2	0	addition of propene and CO
10 August	4-5	40-70	2.8	0	
12 August	4-13	70-110	3.5	0	addition of CO night to day transition
13 August	12-27	80-110	8.3	0	

7.2.2 SAPHIR chamber

The atmospheric simulation chamber SAPHIR (Simulation of Atmospheric PHotochemistry In a large Reaction chamber) is located at the Forschungszentrum Jülich in Germany and consists of a double-wall FEP foil, which is supported by a metal frame. The space between the FEP foils is flushed permanently with nitrogen to avoid diffusion of ambient air into and contamination of the simulated atmosphere. With a length of 18 m and a diameter of 5 m the chamber defines a 270 m^3 reaction volume and possesses a surface area of 324 m^2. A shutter system allows the chamber to be fully darkened or exposed to natural sunlight. The chamber is operated at ambient temperature and at an overpressure of ~30 Pa, compared to ambient pressure. A replenishment flow of synthetic air is necessary to counteract leaks and flow into instruments, leading to a typical dilution rate during NO3ISOP of ca. 1.4 x 10^{-5} s^{-1} (Dewald et al., 2020). The chamber was flushed overnight with synthetic air (generated from nitrogen and oxygen of purity 6.0) before each experiment. Homogenous mixing of the simulated atmosphere is achieved by two, Teflon coated ventilators. Further characteristics of the SAPHIR chamber are described in e.g. Rohrer et al. (2005) and Wegener et al. (2007).

7.2.3 TD-CRDS measurements during the NO3ISOP campaign

During the NO3ISOP campaign, NO_x and NO_z were measured with the TD-CRDS instrument described in detail in Friedrich et al. (2020) (i.e. Section 5). This section therefore focusses on the unique technical features of the deployment at the NO3ISOP campaign, mainly required for the coupling to the SAPHIR chamber. For experiments in the dark, concentrations of NO are suppressed by the presence of O_3 and the TD-CRDS measurements of NO_x are considered equivalent to NO_2, as confirmed by two other independent CRDS-based NO_2 data sets and the continuous monitoring of NO with a chemiluminescence detector (CLD), permanently installed at SAPHIR. The instrument was located inside an air-conditioned container below the chamber. The quartz-tubing of the TD-inlet was mounted in a custom metal frame and connected to a port at the bottom of the SAPHIR chamber via a short length of PFA tubing (0.95 cm inner diameter) (see Figure 8). An additional PFA inlet line protruded ca. 50 cm into the chamber so that the air entered the TD-region after passing through only ~1.5 m PFA. This approach guaranteed a short residence time (ca. 2.1 s) of air samples in the ambient temperature part of the inlet, and was contrived to minimise retention of sticky molecules such as e.g. HNO_3.

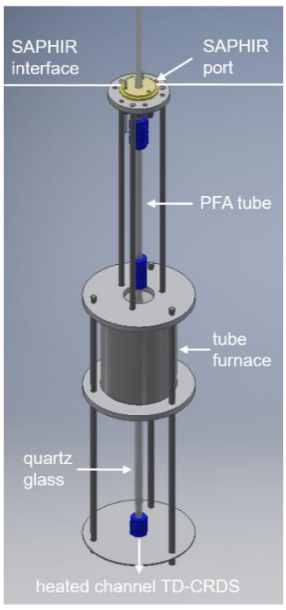

Figure 8: Heated inlet of the TD-CRDS and connection to the SAPHIR chamber. The PFA sampling line before the heated section extended another ca. 0.5 m into the gas volume of the chamber.

7.2.4 Other instrumentation

A variety of data sets from other instruments were used in the following analysis. HNO_3 was detected with a chemical ionisation mass spectrometer, using CO_3^- anions as primary ions (abbreviated as "CO_3^--CIMS" in this work), at a time resolution of 0.5 s. The minimum

detection limit of 0.66 pptv is achieved at an integration time of 40 s, and an accuracy of ca. 35 % has been estimated for HNO_3 measurements with this instrument (Khattatov, 2019). Calibrations were performed via two parallel approaches: a) gravimetric observation of the HNO_3 source's weight loss, and b) collection of gaseous HNO_3 in an aqueous solution followed by ion chromatography.

ONs were measured with a thermal dissociation, CRDS instrument ("Reed-CRDS"). The Reed-CRDS detects ONs with an uncertainty of 10 % (Brownwood et al., 2021), and a detection limit of 0.66 ppbv (Keehan et al., 2020). Due to the single-channel CRDS detection and the cycling between non-heated/heated inlets at different temperatures (ambient temperature, 130 °C, 385 °C, and 700 °C), the time resolution is limited to ca. 8 minutes.

Unified final data sets for NO_3 and N_2O_5 were derived from two CRDS instruments, the 5C-CRDS (Sobanski et al., 2016a) and the NOAA-CRDS (Dubé et al., 2006; Fuchs et al., 2008; Wagner et al., 2009) (NOAA = National Oceanic and Atmospheric Administration). In both setups, NO_3 is detected at wavelength of ca. 662 nm and N_2O_5 is thermally converted to NO_3 prior to detection in a second CRDS channel. For each experiment, the final traces were chosen based on data quality and the agreement with the expected temperature-dependent equilibrium between the two species. The 5C-CRDS detects NO_3 and N_2O_5 with detection limits of 1.5 pptv and 3.5 pptv, respectively, whereas total uncertainties amount 25 % and 28 %. Detection limits (1s, 1σ) for the NOAA-CRDS are 0.25 pptv (NO_3) and 0.9 pptv (N_2O_5); total uncertainties have been estimated as 25 % for NO_3 and between -8 % and + 11 % for N_2O_5, respectively.

HONO measurements were performed with a LOPAP instrument (= long path absorption photometer). This technique relies on photometric detection of a forming azo dye and is characterised by an accuracy of 10 %, a detection limit of 1-2 pptv, and a time resolution of ca. 5 minutes (Heland et al., 2001; Kleffmann et al., 2002; Rohrer et al., 2005).

Mixing ratios of isoprene and of the sum of MVK and methacrolein were derived from a proton transfer reaction time-of-flight mass spectrometer (Vocus PTR-ToF-MS; Krechmer et al. (2018)). An empirical correction factor of 0.7 (for dry days) for isoprene was determined based on parallel measurements with another PTR-ToF-MS and on changes in NO_3 and OH reactivity following the injection of isoprene into the chamber.

HO_2 was measured indirectly via laser induced fluorescence (LIF), subsequent to the conversion to OH by the addition of NO (Holland et al., 2003; Fuchs et al., 2011). This measurement was characterised by a time resolution of 47 s, a 1σ precision of 0.5 x 10^7 cm^{-3},

and a 1σ accuracy of 18 % (Novelli et al., 2021). O_3 was detected via UV-absorption, with a time resolution of 10 s, a detection limit of 1 ppbv, and an uncertainty of 5 %.

Uncalibrated signal counts for ISOPCNO3 and NISOPOOH were provided by a high-resolution time-of-flight CIMS (HR-ToF-CIMS, Aerodyne Research), employing Br^- primary ions, equipped with a custom inlet to facilitate sampling of highly oxidised molecules (HOMs) and HO_2 (Albrecht et al., 2019; Wu et al., 2020).

7.2.5 Box model calculations

The box model used in the following analysis has been previously presented in Dewald et al. (2020). Numerical simulations were conducted in the FACSIMILE/CHEKMAT environment with a time resolution of 1 minute (Curtis and Sweetenham, 1987). The development of the box model was focused on reproducing the measured NO_3 reactivity and used the reaction scheme of the isoprene oxidation by NO_3, O_3 and OH from the Master Chemical Mechanism (MCM, version 3.3.1) (Saunders et al., 2003; Jenkin et al., 2015), together with the currently recommended rate constant for the NO_3 + isoprene reaction from IUPAC (2020). Chemistry of organic nitrate products has been simplified in order to allow computations in the FACSIMILE/CHEKMAT environment. Therefore, comparisons in this work are limited to the sum of organic nitrates in the model, assuming that second-generation products retain their nitrate functionality, and the abundancies of individual organic nitrate species are not assessed. All reactions included and their rate constants can be found in Section 9. Model runs were constrained to the injected concentrations of NO_2, O_3 and isoprene, as well as to environmental parameters (temperature, pressure). The model accounts for dilution due to the replenishment flow of the chamber and for the wall losses of NO_3 and N_2O_5.

Results from a budget calculation (recently described in Brownwood et al. (2021)) were employed to derive exclusively the amounts of isoprene which were consumed in the reaction with NO_3. Briefly, the losses of isoprene due to ozonolysis (using measured O_3 and the IUPAC (2020) recommended rate coefficient for isoprene + O_3) and dilution (based on the replenishment flow of the chamber) were subtracted from the total isoprene loss detected via proton transfer reaction mass spectrometry. OH concentrations were below the detection limit in all discussed experiments and the loss due to OH was hence not included in the calculation of consumed isoprene. The estimate for isoprene lost in the reaction with NO_3 therefore represents an upper limit. An uncertainty of 10 % or 0.5 ppbv (whatever is larger) was assigned to this value. On average, 82 % of the total isoprene loss was attributed to reaction with NO_3.

7.3 Results

7.3.1 NO_z composition and comparison with other measurements and box model

To illustrate measurement procedures and data analysis a first focus is set on an experiment conducted on the 2 August 2018 in which the chamber shutters were permanently closed.

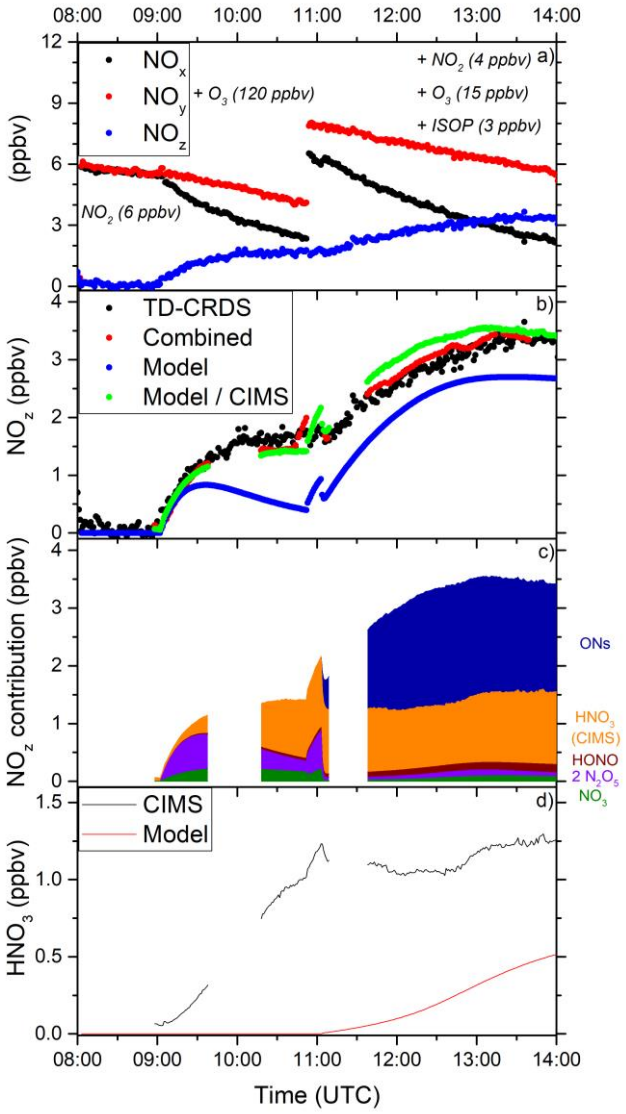

Figure 9: Exemplary slow oxidation experiment (dry, only gas phase) from 2 August 2018. *(a)* Time series of NO_x, NO_y and NO_z along three injections, where isoprene was only introduced during the last injection. *(b)* Comparison of the measured NO_z mixing ratios with a combined value from other measurements of individual NO_z species, with a box model, and with a combination of box model results and HNO_3 measurements. *(c)* Composition of NO_z, according to the box model and the HNO_3 measurement. *(d)* Comparison of measured and modelled HNO_3 identifying an additional source of HNO_3 during the isoprene-free injection.

During the course of the experiment, three gas-injections were performed. At 08:00 UTC ca. 6 ppbv of NO_2 were injected into the chamber, resulting in identical readings in the NO_x and NO_y cavities (Figure 9a) which decayed due to dilution until 09:00 UTC. After the injection of

ca. 120 ppbv O_3 at 09:00 UTC, the signals from the NO_x and NO_y cavities deviated, indicating formation of NO_z. This was mainly due to the formation of NO_3 and N_2O_5 but also due to an apparent chamber source of HNO_3 in the presence of ozone (see below and Figure 9d). At 11:00 UTC ca. 3 ppbv of isoprene were injected, together with a refill of NO_2 and O_3 to their initial values. The subsequent increase of the NO_z mixing ratio up to 3.4 ppbv can be attributed mainly to the ONs generated (see below and Figure 9c). 7.9 ppbv NO_y was present in the SAPHIR chamber at the time of the third injection at 11 UTC (of NO_2, O_3 and isoprene).

Figure 9b compares the TD-CRDS measurements of NO_z (black trace) with values derived from other instruments (red trace) which include NO_3 and N_2O_5 (times 2) from the 5C-CRDS, HONO from the LOPAP, HNO_3 from the CO_3^--CIMS and ONs from the Reed-CRDS. Due to the low time resolution of the Reed-CRDS (12 minutes), their data were interpolated onto the 1 minute time resolution used in the analysis. Correlation between the NO_z measured by the TD-CRDS and the summed NO_z value is shown in Figure 10a, yielding a slope of 0.91 ± 0.01, an intercept of 0.18 ± 0.02 ppbv, and a correlation coefficient R^2 of 99 %.

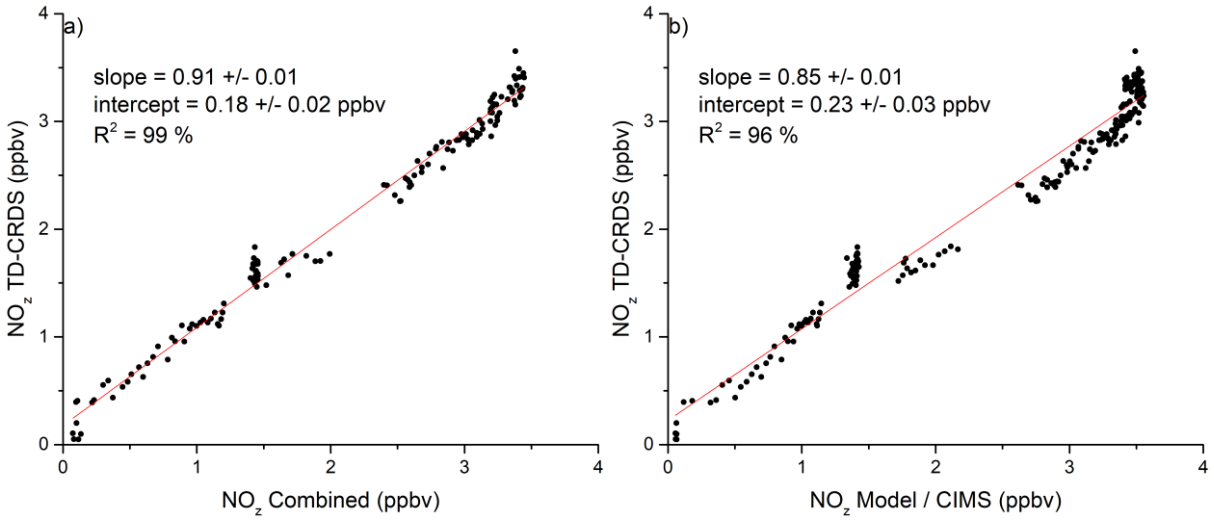

Figure 10: Correlation between the NO_z mixing ratios derived from the TD-CRDS and *(a)* the combined value from other measurements of NO_z species (HNO_3, NO_3, N_2O_5, ONs and HONO), and *(b)* the box model results combined with the measured HNO_3.

The statistical uncertainty in the slope of 0.01 (derived from the bivariate fit), however, is surpassed by the systematic uncertainty stemming from the measurement uncertainties of the individual instruments. This systematic uncertainty has been estimated as 0.21 by propagation of the relative uncertainties of "NO_z TD-CRDS" and "NO_z Combined". The relative uncertainty in the summed NO_z value is variable in time due to changes in the NO_z composition, leading to an averaged value of 17 %. Within combined uncertainty, the two measurements therefore agree (slope = 0.91 ± 0.21).

Additionally, NO_z mixing ratios were calculated from a box model run (blue trace in Figure 9b), which was originally designed to replicate isoprene, NO_3, and the NO_3 reactivity during the experiment. The model clearly underestimates the NO_z formation especially during the isoprene-free injection. As shown in Figure 9d, the poor agreement between model and measurement can be attributed to a model underestimation of HNO_3. Especially during the early stages of the experiment where ~1 ppbv were measured and the model prediction was close to zero. At the end of the experiment (at 14 UTC), the model still underestimated HNO_3 by 40 %. This is related to a chamber wall source of HNO_3 in the presence of NO_2 and O_3, e.g. resulting from the heterogeneous conversion of N_2O_5 to HNO_3 (see Section 7.3.4), which is not included in the model. Constraining the model with HNO_3 measurements results in much better agreement (green trace in Figure 9b). Figure 10b displays a slope of 0.85 ± 0.01, an intercept of 0.23 ± 0.03 ppbv, and a correlation coefficient R^2 of 96 %.

For this data set, Figure 9c shows that HNO_3 and N_2O_5 contribute substantially to NO_z, especially before the isoprene injection, whereas NO_3 and HONO play a minor role. At ca. 13 UTC, when the injected isoprene was largely consumed, NO_z was composed of 53 ± 9 % ONs, 36 ± 13 % HNO_3, 3.7 ± 0.8 % N_2O_5, 4 ± 1 % NO_3, and 3.6 ± 0.6 % HONO (according to measurement of individual NO_z species), respectively.

7.3.2 Organic nitrates (ONs) comparison between TD-CRDS and Reed-CRDS

The focus of the discussion is now shifted towards the organic nitrates formed during the last injection of the experiment on 2 August 2018 (described in Section 7.3.1). ONs mixing ratios were calculated from measured NO_z by subtracting the measured mixing ratios of inorganic NO_z (i.e. ONs = NO_z – (HNO_3 + HONO + 2 N_2O_5 + NO_3)), and compared to the ONs from the Reed-CRDS. Figure 11 indicates good agreement both before (in the absence of ONs) and after the addition of isoprene. The bivariate fit of the correlation plot (Figure 11b) yields a slope of 0.90 ± 0.04, a y-axis intercept of 0.07 ± 0.05 ppbv, and a correlation coefficient R^2 of 98 %. For the first ca. 30 minutes after the isoprene injection, ONs concentrations could not be derived from the NO_z measurements due to a gap in the HNO_3 data. Due to the low amounts of ONs formed and the propagation of errors from five different measurements involved in the derivation of ONs mixing ratios from the TD-CRDS, this slope is associated with a relatively large systematic uncertainty of 0.39. The agreement between the two ONs time series in Figure 11a, however, serves to confirm the general applicability of quantifying ONs formation, following isoprene injections, from measurements of NO_z and individual inorganic NO_z

species. This method will be further used in Section 7.3.3 to calculate yields of ONs, relative to the isoprene lost via reaction with NO_3.

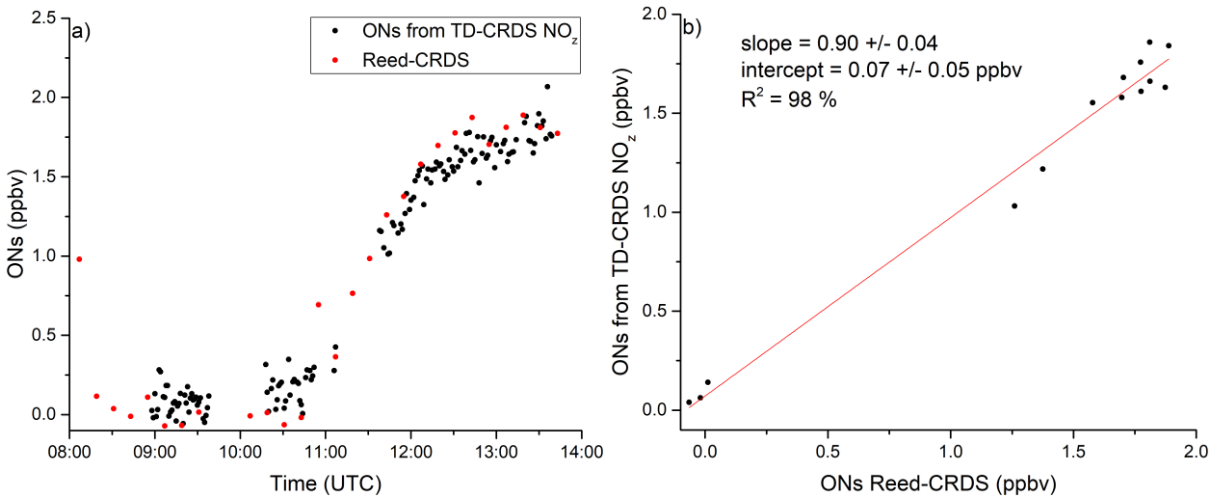

Figure 11: Comparison between ONs derived from the TD-CRDS NO_z mixing ratios and from the measurements of the Reed-CRDS. *(a)* Time series showing a parallel increase in ONs after the injection of isoprene at 11 UTC. *(b)* Correlation plot for data points after 10:19 UTC.

7.3.3 ONs yields relative to isoprene consumed in the reaction with NO_3

In this section, ONs mixing ratios derived from the NO_z measurements of the TD-CRDS (as described in Section 7.3.2) are used to determine the yield of ONs relative to the number of isoprene molecules lost in the reaction with the nitrate radical. The consumed isoprene due to reaction with NO_3 (plotted on the x-axes in Figure 12), i.e. not due to ozonolysis or dilution, was calculated from a separate box model which incorporates measurements of isoprene and O_3 (see Section 7.2.5). In Figure 12, correlation plots between ΔONs (i.e. the increase in ONs mixing ratios from the beginning to the end of the respective time frame) and ΔIsoprene consumed are presented for all analysed gas-phase experiments. ONs yields were obtained from bivariate fits (York, 1966) of these data sets. Determining ONs yields was not possible for three days due to missing HNO_3 data (3, 7, and 9 August 2018). Additionally, the original TD-CRDS-measured ΔNO_z is given, in order to allow the impact of subtracting other NO_z species on the final ΔONs trace to be assessed. Chemically, ΔNO_z constitutes a combination of the mixing ratio changes in each individual NO_z species (see Eq. 7).

$$\Delta NO_z = \Delta ONs + \Delta HNO_3 + 2 \cdot \Delta N_2O_5 + \Delta NO_3 + \Delta HONO \qquad \text{Eq. 7}$$

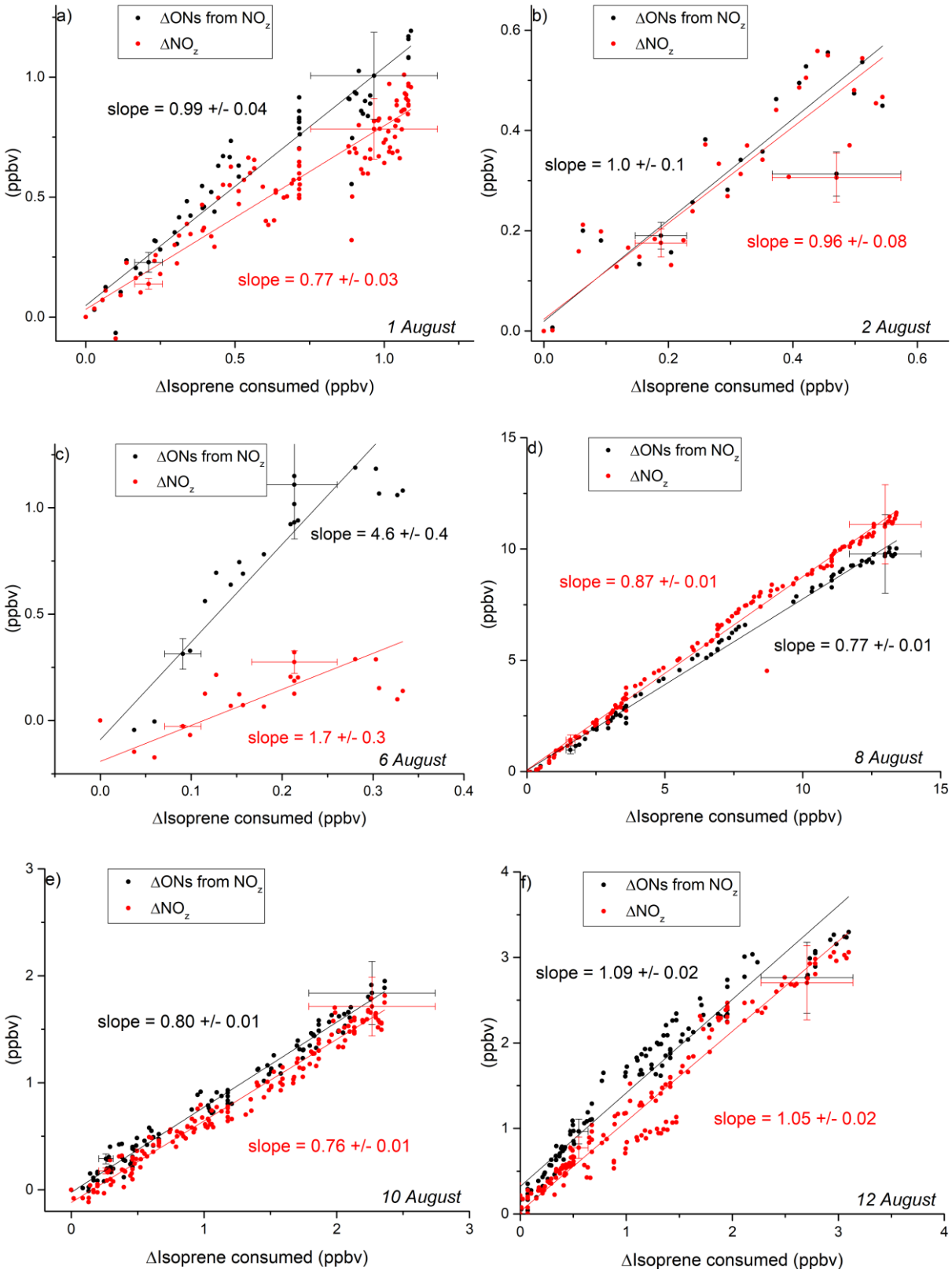
a)
ΔONs from NOz
ΔNOz
slope = 0.99 +/- 0.04
slope = 0.77 +/- 0.03
1 August
(ppbv)
ΔIsoprene consumed (ppbv)
b)
ΔONs from NOz
ΔNOz
slope = 1.0 +/- 0.1
slope = 0.96 +/- 0.08
2 August
(ppbv)
ΔIsoprene consumed (ppbv)
c)
ΔONs from NOz
ΔNOz
slope = 4.6 +/- 0.4
slope = 1.7 +/- 0.3
6 August
(ppbv)
ΔIsoprene consumed (ppbv)
d)
ΔONs from NOz
ΔNOz
slope = 0.87 +/- 0.01
slope = 0.77 +/- 0.01
8 August
(ppbv)
ΔIsoprene consumed (ppbv)
e)
ΔONs from NOz
ΔNOz
slope = 0.80 +/- 0.01
slope = 0.76 +/- 0.01
10 August
(ppbv)
ΔIsoprene consumed (ppbv)
f)
ΔONs from NOz
ΔNOz
slope = 1.09 +/- 0.02
slope = 1.05 +/- 0.02
12 August
(ppbv)
ΔIsoprene consumed (ppbv)

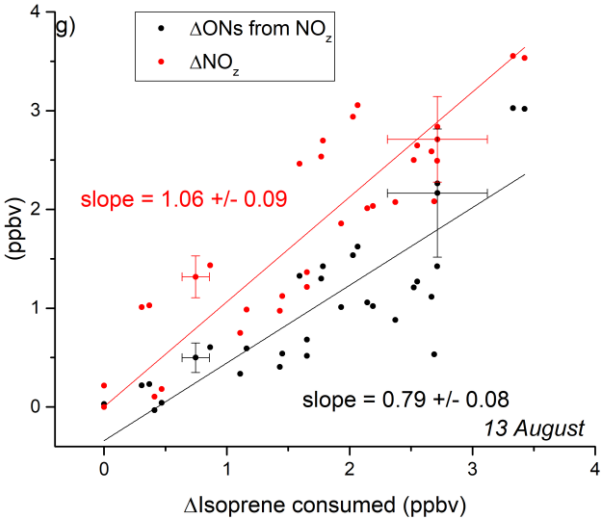

Figure 12: Changes in ONs and NO_z mixing ratios plotted against the amount of consumed isoprene. Yields of ONs relative to lost isoprene (in the reaction with NO_3) can be obtained from the slopes of these graphs. Slopes are given together with their statistical uncertainty (based on the result of the bivariate fit of the data points). In each graph, illustrative error bars are displayed for two ΔONs and ΔNO_z data points. The presented experiments were performed on 1 August *(a)*, 2 August *(b)*, 6 August *(c)*, 8 August *(d)*, 10 August *(e)*, 12 August *(f)*, and 13 August 2018 *(g)*.

The subtraction of non-ONs NO_z species influences the derived slopes by varying extents. In four experiments (2, 8, 10, and 12 August) the slope is adjusted by less than 11 %, whereas large corrections (> 25 %) are necessary in the other three experiments (1, 6, and 13 August). The difference between ΔONs and ΔNO_z can be primarily explained by changes in HNO_3 mixing ratios, relative to ΔNO_z. Constant high mixing ratios of HNO_3, however, would not have an effect on the resulting values for ΔONs. On 1 and 6 August 2018, negative trends in HNO_3 led to significant upward corrections in the ONs yields, compared to ΔNO_z.

An interesting feature can be observed in the data set from 12 August 2018 (see Figure 12f). On this day, two separate time frames were combined and displayed together on one scale, by i.e. resetting ΔONs/ΔNO_z and ΔIsoprene consumed to zero after the gap between the two time frames. In the ΔNO_z data set, ca. 20 points between 0.5 and 1 ppbv deviate significantly from the fit line of the entire experiment, but continue parallel to the slope line. This behaviour was caused by a sudden drop in N_2O_5 of 0.2 ppbv (equalling 0.4 ppbv NO_z) during an injection of NO_2, O_3 and isoprene. Interestingly, this change in the NO_z composition is not represented in the ΔONs data set, as the subtraction of the measured N_2O_5 (x2) from NO_z compensates the interference. This simple and illustrative example serves to highlight the applicability and robustness associated with the chosen method of deriving ONs from NO_z, and the merit of NO_z measurements in estimating the abundancies of missing NO_z species, when data sets for all other important components (here HNO_3 and N_2O_5) are available.

Quantitative results from the ONs yields analysis are listed and put into context in Table 4. In Shenolikar (2021), yields were presented for individual injections. Averages of these individual yields have been listed in the last column of Table 4. HONO mixing ratios were not available for the experiments from 6 August 2018 onwards, but are expected to have a negligible effect on ΔONs.

Table 4: Organic nitrate yields derived from TD-CRDS measurements of NO_z, together with the associated statistical (based on the fit results) and systematic uncertainties (see Section 7.3.3). Yields are compared to results from other CRDS instruments measuring ONs during the NO3ISOP campaign, as reported in Brownwood et al. (2021) and Shenolikar (2021).

Day in 2018	ΔONs (ppbv)	ONs yield	R^2 (%)	Statistical uncertainty	Systematic uncertainty SU_Y	Yield reported by Brownwood et al. (2021)	Yield reported by Shenolikar (2021)
1 August	1.1	0.99	92	0.04	0.28	-	0.36
2 August	0.6	1.0	82	0.1	0.26	-	0.44
6 August	1.4	(4.6)	84	0.4	1.5	0.90	0.88
8 August	10.4	0.77	99	0.01	0.16	1.01	0.80
10 August	1.9	0.80	98	0.01	0.21	0.94	0.71
12 August	3.6	1.09	94	0.02	0.24	1.12	1.05
13 August	2.4	0.79	71	0.08	0.27	1.19	0.78

The uncertainties of the ONs yields (SU_Y) were estimated based on the uncertainties of the involved measurements (see Eq. 8-Eq. 11). Uncertainties in the changes of NO_z and NO_z species (used in Eq. 11) were calculated by multiplying the change in the respective variable with the relative uncertainties quoted in Sections 7.2.3 and 7.2.4. The final SU_Y might therefore constitute an upper limit, as the mixing ratio differences are not necessarily associated with the same relative uncertainties as the absolute mixing ratios. For example a constant offset in a measurement would still allow the correct determination of a mixing ratio change, whereas an uncertainty caused by a non-linear response to a mixing ratio increase (e.g. inlet losses, concentration-dependent biases) would also add uncertainty to the differences. The systematic uncertainty in ΔIsoprene consumed (=ΔISOP) has been estimated as 10 % or at a minimum of 0.5 ppbv by Brownwood et al. (2021). For experiments with low ΔISOP, such as e.g. 2 August 2018, this would lead to relative uncertainties in ΔISOP (= $SU_{\Delta ISOP}$ / ΔISOP) of close to or above 100 %. In Brownwood et al. (2021), however, this definition was employed for

experiments with a minimum ΔISOP of 2.3 ppbv, equalling a relative uncertainty of 22 %. For the results presented in this work, the relative uncertainty was therefore calculated according to Brownwood et al. (2021), but only up to a maximum of 22 %. This cap applied to the experiments on 1, 2, and 6 August 2018.

$$Y = \frac{\Delta ONs}{\Delta ISOP} \quad \text{Eq. 8}$$

$$\Delta ONs = \Delta NO_z - \Delta HNO_3 - \Delta NO_3 - 2 \cdot \Delta N_2O_5 - \Delta HONO \quad \text{Eq. 9}$$

$$SU_Y = \sqrt{\left(\frac{SU_{\Delta ONs}}{\Delta ONs}\right)^2 + \left(\frac{SU_{\Delta ISOP}}{\Delta ISOP}\right)^2} \cdot Y \quad \text{Eq. 10}$$

$$SU_{\Delta ONs} = \sqrt{{SU_{\Delta NO_z}}^2 + {SU_{\Delta HNO_3}}^2 + {SU_{\Delta NO_3}}^2 + 2 \cdot {SU_{\Delta N_2O_5}}^2 + {SU_{\Delta HONO}}^2} \quad \text{Eq. 11}$$

Resulting ONs yields, derived from TD-CRDS-measured NO_z, were in a range between 77 % and 460 %. The experiment on 6 August 2018, for which an obviously false yield of 4.6 was derived, however, was the only experiment discussed in this analysis performed under humid conditions. Additionally, only a ca. 30 minutes long time frame was available for analysis, due to gaps in the HNO_3 data set and failure of the TD-CRDS instrument during the course of the experiment. The respective time frame was also coincident with the final phase of an injection, where ONs were reaching a plateau, resulting in a NO_z increase of only ca. 300-400 pptv. Figure 12c illustrates that a parallel 1 ppbv decrease in HNO_3 overshadows the ONs formation, leading to an increase of the derived ONs yield by a factor of 2.7. Under humid conditions, the CO_3^--CIMS may suffer from an interference from NO_3^- anions (e.g. in form of particulate nitrates). Nitrates released from the chamber wall, however, would be expected to also cause a response in the NO_y signal of the TD-CRDS. HNO_3 and nitrates desorbing from inlet surfaces of the CO_3^--CIMS, under exposure to water, would therefore be a likely explanation of the observed behaviour. Considering these instrumental issues, the experiment on 6 August 2018 was excluded from further analysis.

Previous experimental studies, which did not correct for isoprene losses by O_3 and OH, report yields between ca. 60 % and 90 % (IUPAC, 2020). Correcting the yield for ozonolysis of isoprene might therefore be an explanation for results above 90 %, compared to these literature studies. Additionally, the literature studies were performed under differing experimental conditions (pressures, reagent concentrations) in setups using flow tubes (Berndt and Boge,

1997), aircraft platforms (Perring et al., 2009), or smaller volume chambers than SAPHIR (Barnes et al., 1990; Kwan et al., 2012; Schwantes et al., 2015). The final ONs yield will also to some extent depend on the fate of the initial RO_2 radical (see Section 7.1), favoured by the chemical composition in each individual experiment. The lowest ONs yields were determined for 8 and 13 August 2018 (77 % and 79 %). These experiments were designed as fast oxidation experiments (see Section 7.2.1), promoting RO_2 + RO_2 self-reactions. The lower yields are thus consistent with the expected increase in MVK production. Recently proposed lower yields of MVK (from isoprene oxidation by NO_3) due to the competing formation of epoxidised nitrates (Vereecken et al., 2021) would also be consistent with this conclusion, as these nitrates are susceptible to NO_2 elimination, lowering the ONs yield likewise. For the experiment on 13 August 2018, the CalTech (California Institute of Technology) mechanism by Wennberg et al. (2018) would predict 250 to 400 % higher MVK + methacrolein mixing ratios, compared to a mechanism which incorporates epoxidation reactions (Vereecken et al., 2021). Note that NO_2 release from ONs results in ONs yields below 100 %, but should not affect the yield of NO_z relative to NO_x lost (see Section 7.3.4).

A similarly low yield of 80 %, however, was also observed in the experiment on 10 August 2018. An evaluation, in how far variability in the ONs yields can be explained either by diverging chemical regimes or by instrumental uncertainties, is therefore required. In Figure 13, the derived ONs yields are displayed against the average NO_3 production rates generated throughout the respective experiments. As described in Section 7.2.1, fast oxidation experiments (i.e. production rates of ca. 6 ppbv/hr) were performed to promote RO_2 + RO_2 reactions, whereas the RO_2 + NO_3 branch was expected to dominate at moderate production rates of ca. 2 ppbv/hr. Promoting the isomerisation of initial RO_2 radicals was the aim in slow oxidation experiments. A clear trend in ONs yields, depending on the NO_3 production rate, cannot be observed in the presented data sets. Some reproducibility in the ONs yields, however, seems to be apparent when regarding the lower yields during fast oxidation experiments (see above). Figure 13 also demonstrates that the experiments during NO3ISOP were conducted under divergent chemical conditions, prohibiting the meaningful determination of an average ONs yield for the campaign.

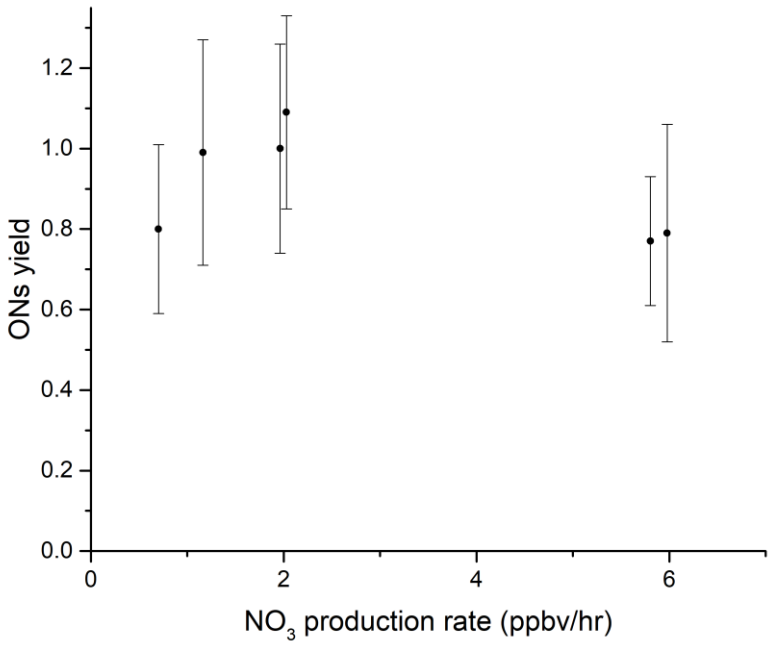

Figure 13: ONs yields and systematic uncertainties relative to the average production rate of NO_3 during the respective experiments.

The mean HO_2/NO_3 ratio (see Figure 14a) was calculated to elucidate whether these different experimental setups led to different chemical regimes, i.e. changing the impact of the RO_2 + RO_2 and the RO_2 + HO_2 reaction pathways, which might be able to explain variability in ONs yields. Figure 14a, shows that ONs yields below 80 % were both observed under higher ($HO_2/NO_3 > 0.6$) and lower HO_2-conditions ($HO_2/NO_3 < 0.4$). Nonetheless, a small trend might be observable, leading to quantitative ONs formation rather during experiments with low HO_2/NO_3 ratios (see Figure 14a), contradicting the expected higher yields under RO_2 + HO_2 favouring conditions. In contrast to atmospheric conditions, RO_2 concentrations were up to 10 times larger than HO_2 concentrations, leading to an additional potential RO_2 interference in the HO_2 measurement (Vereecken et al., 2021). The model of Vereecken et al. (2021) was able to reconcile measured and modelled HO_2 by adding a 7 % interference from RO_2.

The ratio of uncalibrated signal counts for the ONs products NISOPOOH and ISOPCNO3 is presented in Figure 14b, in order to investigate the reaction branches in terms of their product species. Increased formation of the hydroperoxide NISOPOOH would indicate predominance of RO_2 + HO_2 reactions, whereas the alcohol ISOPCNO3 can serve as a proxy species for RO_2 + RO_2 reactions (see Section 7.1). The minimal NISOPOOH / ISOPCNO3 ratio of 2 indicates that RO_2 + RO_2 dominance was achieved in none of the discussed experiments, making it unlikely that differences in the fate of RO_2 are responsible for the observed variability in the

ONs yield. Modelling studies have confirmed that $RO_2 + HO_2$ and $RO_2 + NO_3$ were the most important loss processes for RO_2 (together on average accountable for ca. 85 % of the RO_2 loss) in the experiments on 10, 12, and 13 August 2018 (Vereecken et al., 2021), despite varying the NO_3 production rate between 0.7 and 6.0 ppbv/hr.

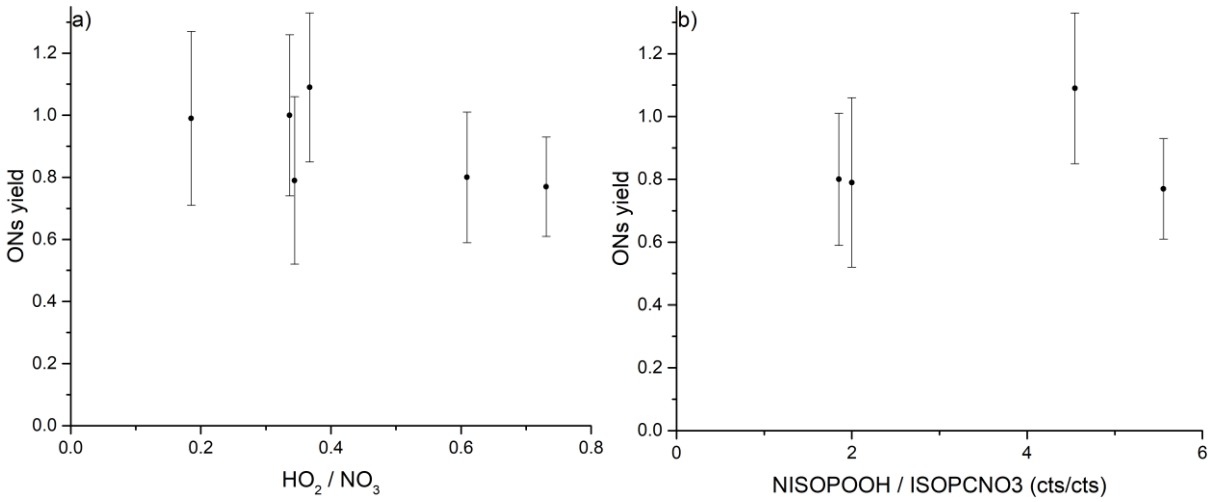

Figure 14: ONs yields plotted against *(a)* the average HO_2/NO_3 and *(b)* the NISOPOOH / ISOPCNO3 ratio. NISOPOOH and ISOPCNO3 serve as proxy species for the $RO_2 + HO_2$ and the $RO_2 + RO_2$ pathways. A clear trend in the yields depending on these two experimental parameters cannot be identified.

Another indication of a shift towards $RO_2 + RO_2$ chemistry would be a pronounced formation of MVK. In Figure 15a, the ONs yields are displayed against the change in the MVK + methacrolein mixing ratio (relative to consumed isoprene). An obvious trend in relation to this product-based parameter is again not observable, with ONs yields below 80 % occurring both at the highest (8.7 %) and the lowest (6.7 %) MVK + methacrolein yield. This calculation, however, is unfortunately also limited to four days due to missing data from the Vocus PTR-ToF-MS.

In contrast, Figure 15b demonstrates that ONs yields close to or above 100 % are usually associated with large corrections (relative to the ONs formation), caused by negative trends in the HNO_3 mixing ratios (which are subtracted from NO_z). In conclusion, the variability in ONs yields is presumably a result of concentration-dependent systematic uncertainties inherent in the determination of ONs mixing ratios from NO_z, which are largely related to the HNO_3 contribution. An unambiguous association with changes in the chemical regimes could not be identified in the analysis discussed above.

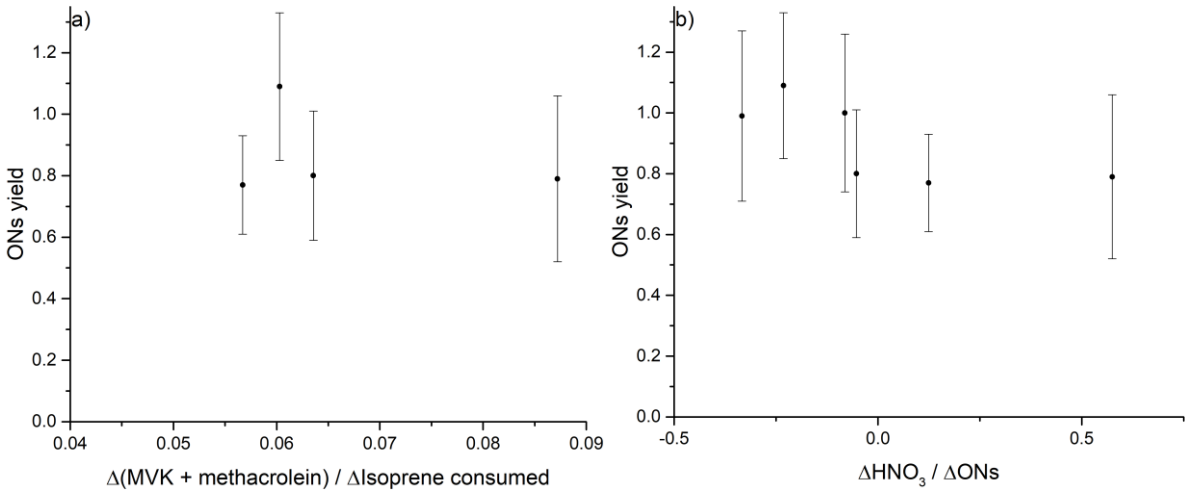

Figure 15: *(a)* Relationship between the measured ONs yields and the formation of MVK and methacrolein, relative to the isoprene lost. *(b)* Impact of the HNO_3 correction for NO_z (relative to the ONs formation) on the resulting ONs yields.

ONs yields are now contrasted to the results from the other CRDS instruments measuring ONs during the NO3ISOP campaign (see Table 4). Yields reported in Shenolikar (2021) were systematically low in the first two experiments (1 and 2 August 2018). This instrument suffered from multiple technical issues, especially during the initial phase of the campaign. These included memory effects when switching between sampling and zeroing due to isoprene nitrates sticking to inlet surfaces, and the unexpected dissociation of these nitrates in the lower temperature (448 K) channel, designated for peroxy nitrates. Additionally, this instrument suffered from a partial detection of HNO_3 under dry conditions (Dewald et al., 2021).

Yields reported by Brownwood et al. (2021) are generally higher than those from the TD-CRDS (specifically on 8 and 10 August 2018; see Table 4). This discrepancy can be explained (at least in part) by a correction for wall losses of ONs, applied to all experimental data sets presented in Brownwood et al. (2021). For this correction, a wall loss rate constant of 2.2×10^{-5} s^{-1} was employed (Rollins et al., 2009), which was, however, determined under humid conditions (ca. 25 % RH) in an earlier experiment at the SAPHIR chamber (conducted in 2007), from the decay of ONs mixing ratios after complete consumption of isoprene. Figure 16 illustrates that ONs wall losses are likely overestimated when applying a wall loss rate constant of 2.2×10^{-5} s^{-1} to data obtained in dry experiments.

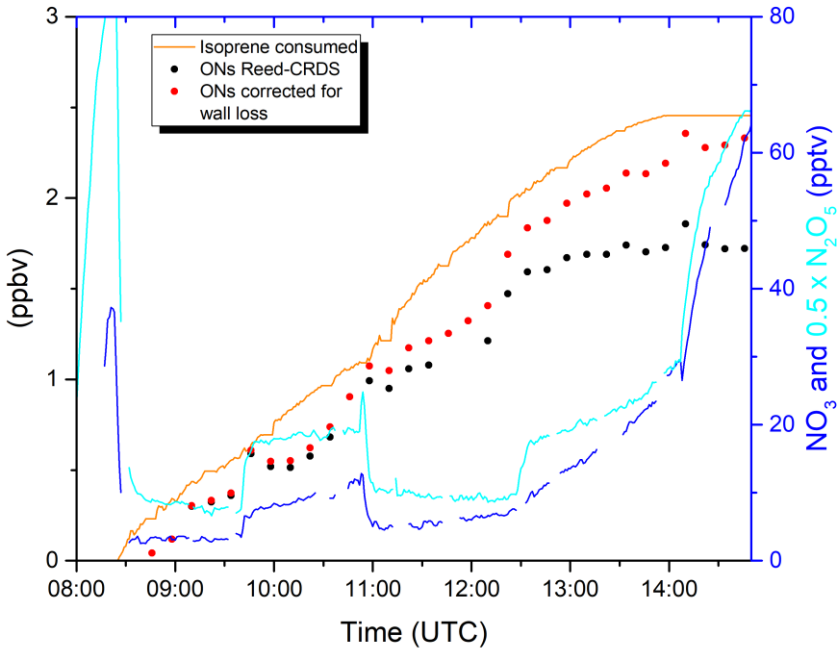

Figure 16: Comparison of originally-measured ONs by the Reed-CRDS and the trace after correcting for wall losses of ONs. Mixing ratios of consumed isoprene, NO_3, and N_2O_5 are included to illustrate that additional formation of ONs is unlikely after the near-complete consumption of isoprene (at ca. 13:45 UTC).

By ca. 13:45 UTC, the consumption of isoprene via reaction with NO_3 can be considered as complete. The corresponding increases of NO_3 from 7 to 63 pptv, and of N_2O_5 from 18 to 132 pptv, within the last ca. 2.5 hours of the depicted time frame indicate that no further ONs are produced during this phase of the experiment. Similar amounts of NO_2 (ca. 1 ppbv) and O_3 (ca. 10 ppbv) were added to the chamber at 11 UTC and 14 UTC. At 11 UTC, the newly-formed NO_3 and N_2O_5 molecules are quickly depleted by additional isoprene, whereas a sharp increase can be observed after the injection at 14 UTC, highlighting the shift in the fate of NO_3 following the complete consumption of isoprene. Measured ONs by the Reed-CRDS are constant at 1.7 ppbv after 13:30 UTC, regardless of the short spike at ca. 14 UTC due to the reinjection of NO_2 and O_3. At the same time, the ONs trace corrected for wall losses continues to increase from 2.0 ppbv to 2.3 ppbv, and does not appear to level-off even an hour after the complete consumption of isoprene. The divergence between the two ONs time series, however, already emerges during the first half of the experiment, under the presence of isoprene and during the formation of ONs, leading to a ca. 20 % higher final ΔONs (until 13:30 UTC). In conclusion, ONs wall losses are presumably slow under dry conditions, unless the process is compensated by the formation of dinitrates, which appears to be unlikely due to the build-up in NO_3 and N_2O_5. Figure S5 in Brownwood et al. (2021) shows that five out of seven experiments at 0 %

RH were characterised by ONs yields above 100 %, highlighting the potential overestimation of ONs wall losses when applying the rate constant derived by Rollins et al. (2009) under dry conditions.

The analysis presented in this section overall demonstrated the applicability of NO_z measurements in the determination of ONs yields and showed that the results are comparable to previous literature on the isoprene + NO_3 system. It was found that ONs yield variability was caused by instrumental uncertainties rather than by changes in the product distribution of the isoprene oxidation. Additionally, the impact of ONs wall losses in experiments without addition of water was discussed.

7.3.4 Reactive nitrogen budget

The simultaneous detection of NO_x and NO_z by the TD-CRDS enables examination of the reactive nitrogen budget in the NO_3-initiated oxidation of isoprene, which requires correction of the measured mixing ratios for dilution and accounting for the wall losses of NO_3 and N_2O_5. NO_z yields relative to NO_x were specifically not corrected for wall losses of ONs, as the findings in Section 7.3.3 have led to the assumption that these are likely to be small in the absence of humidity. For experiments carried out under dry conditions during the NO3ISOP campaign, Dewald et al. (2020) determined NO_3 and N_2O_5 wall loss rate constants (in the absence of isoprene) of $k_{wall,NO3} = 1.6 \times 10^{-3}$ s^{-1} and $k_{wall,N2O5} = 3.3 \times 10^{-4}$ s^{-1}. As N_2O_5 was often present at higher mixing ratios and, as it contains two NO_x molecules its loss to the walls can contribute significantly to loss of reactive nitrogen (see Figure 9c). In the presence of 2 ppbv of isoprene, the loss rate of NO_3 is 3.2×10^{-2} s^{-1} (using the IUPAC (2020) rate coefficient for NO_3 + isoprene of $2.95 \times 10^{-12}\exp(-450/T)$ cm^3 molec^{-1} s^{-1}). The lifetime of NO_3 due to reaction with isoprene is ca. 30 s, whereas the lifetime due to wall loss is ca. 10 minutes. In the presence of isoprene, the wall loss of NO_3 therefore is reduced in importance. Nonetheless, each NO_3 or N_2O_5 molecule lost to the chamber wall lowers the yield of NO_z relative to lost NO_x. Dewald et al. (2020) have demonstrated that a box model which omits these wall losses overpredicts NO_3 mixing ratios by a factor of three and N_2O_5 mixing ratios by a factor of two, after the isoprene injection on 2 August 2018.

The wall loss rate constants of NO_3 and N_2O_5 were hence included into the box model (see Section 7.2.5) and the summed losses of NO_3 and N_2O_5 (multiplied by two) were added to the measured NO_z mixing ratios at each time step. The effect of these corrections is presented in Figure 17, where data from the first injection (5-12 ppbv NO_2, 70-110 ppbv O_3, and 0-3 ppbv

isoprene) on 12 August 2018 is analysed. About 3.5 ppbv of isoprene were injected into the chamber at the beginning of this experiment. Median mixing ratios of NO_3 and N_2O_5 were 18 pptv and 111 pptv, respectively. The dilution correction increases the NO_z yield by about 15 % in this example (see Figure 17), while wall losses of N_2O_5 and NO_3 add another 27 %. Dilution has a noticeable effect on the NO_z yield as it leads to an increase in NO_x losses and a decrease in the NO_z formation rate. N_2O_5 loss is the predominant wall loss process, contributing with an average of 85 % to the overall wall loss correction. All slopes in Figure 17 are characterised by correlation coefficients (R^2) of greater than 99 %. After applying both corrections, a NO_z yield of 0.95 (per NO_x consumed) is obtained, compared to 0.53 without correction. Clearly, substantial amounts of reactive nitrogen are lost at the chamber walls during these experiments (see Figure 17 and Table 5), despite the predominance of the NO_3 loss via reaction with isoprene. Implementing the rate coefficient for the wall loss reactions into the box model, however, allowed estimation of the effect of these processes. It needs to be highlighted again that, as shown by Dewald et al. (2020), considering wall losses is essential for successfully replicating measured NO_3 and N_2O_5 mixing ratios with the box model, also during time frames where substantial amounts of isoprene were part of the simulated atmosphere.

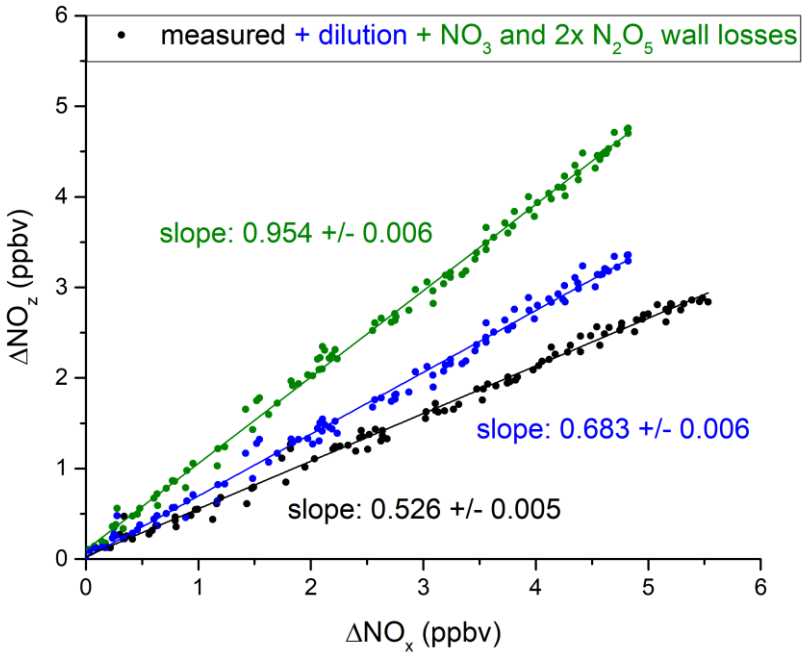

Figure 17: Effect of corrections for dilution and wall losses of NO_3 and N_2O_5 on the derived NO_z yields relative to consumed NO_x (first injection on 12 August 2018). The cumulatively lost NO_3 and N_2O_5 was estimated using box model calculations (with wall loss rates as published in Dewald et al. (2020)) and then added to the ΔNO_z measured via TD-CRDS, at each time step.

For all dry, gas-phase-only injections during the NO3ISOP campaign where NO_z data was available, the NO_z yields after applying the corrections for loss of NO_3/N_2O_5 and dilution are displayed in Figure 18, as a histogram, and in Table 5. The NO_z yield corrections are also listed in Table 5. NO_z yields in a range between 74 % and 182 % were derived from the TD-CRDS data sets. The three injections (of NO_2 and O_3) for which yields above 100 % were calculated (fourth injections on 8 and 13 August 2018 and fifth injection on 10 August 2018; see Figure 18) were performed after the complete consumption of isoprene. Subsequently, a large increase in HNO_3 was observable (up to 40 ppbv on 13 August 2018), indicating that HNO_3 previously deposited to the chamber walls (or formed in the heterogeneous loss of N_2O_5) is released which results in apparent NO_z yields of >1 per NO_2 added. On average, the yield was 90 ± 7 % (± standard deviation), when omitting yields above 100 %.

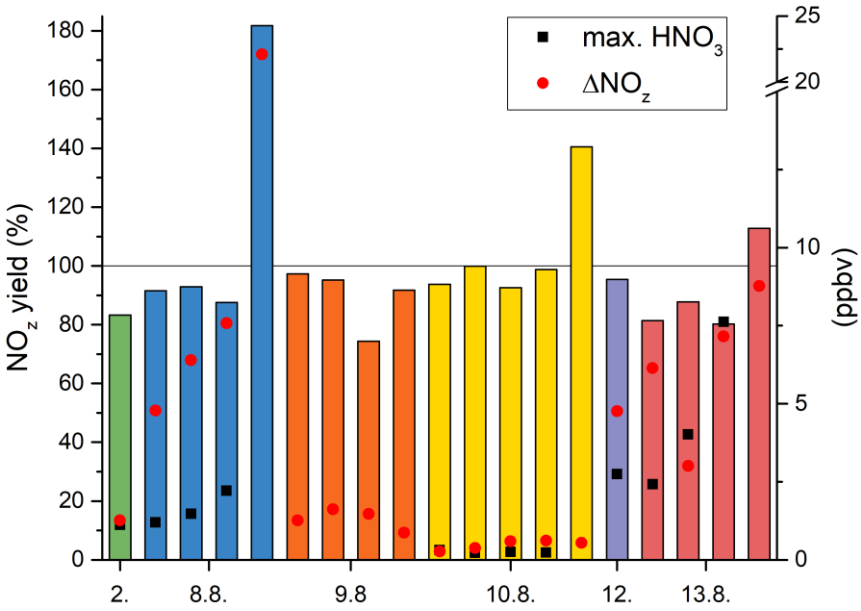

Figure 18: NO_z yields relative to the consumed NO_x after correcting for dilution and wall losses of NO_3 and N_2O_5. Black and red data points signify the maximum mixing ratios of HNO_3 and the increase in NO_z during the respective injections. Reasons for NO_z yields above 1 in late stages of several experiments (i.e. after complete consumption of isoprene) are discussed in Section 7.3.4.

Similar behaviour can be observed in reversed direction on the 2 August 2018 experiment, where the formation of HNO_3 apparently discontinues after the injection of isoprene (see Figure 9d). This source of HNO_3 is further explored using a modified box model run, where all N_2O_5 molecules lost to the walls (with the $k_{wall,N2O5}$ quoted above) were assumed to form two gas phase molecules of HNO_3, which again are subject to wall losses. For $k_{wall,HNO3}$, an optimum value of 8.0×10^{-5} s^{-1} was obtained by minimising the average relative deviation between the

change in modelled and measured HNO_3 mixing ratios after 11 UTC. The results of this simulation are presented in Figure 19.

Introducing the heterogeneous conversion of N_2O_5 to HNO_3 into the box model allowed replication of the shape of the measured HNO_3 before the isoprene injection at 11 UTC, in contrast to the previous box model run displayed in Figure 9d. Nonetheless, the absolute amount of HNO_3 formed without isoprene chemistry is neither predicted correctly when including a wall loss of HNO_3, nor without including this process. The observation that even stoichiometric conversion of N_2O_5 cannot explain enough HNO_3 indicates the release of additional HNO_3 or other nitrates from the chamber walls.

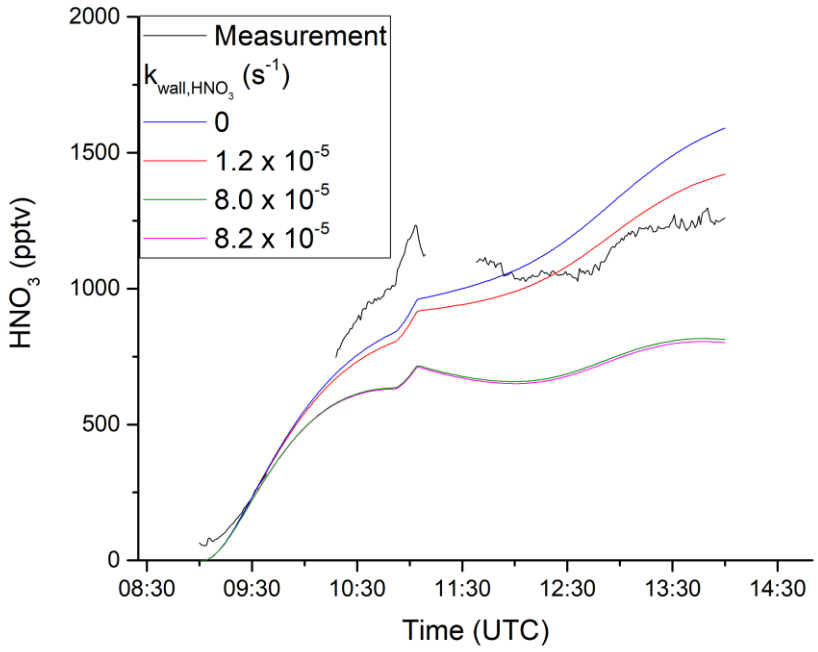

Figure 19: Comparison of measured and box model calculated HNO_3 on 2 August 2018. Box model simulations have been performed with and without considering wall losses of HNO_3. Each N_2O_5 lost to the walls was assumed to form two molecules of HNO_3.

Table 5: NO_z yields for the injections presented in Figure 18, together with the effect of the NO_3/N_2O_5 wall loss correction, the statistical results of the fit, and information on the underlying chemical composition (concerning HNO_3 and NO_z).

Day in 2018	Injection Nr.	ΔNO_z corrected (ppbv)	Max. HNO_3 (ppbv)	NO_z yield increase through NO_3/N_2O_5 wall loss correction (%)	Corrected NO_z yield (%)	Statistical uncertainty (%)	R^2 (%)
2 August	2	1.3	1.1	13	83	2	97
8 August	1	4.8	1.2	23	92	1	99
	2	6.4	1.5	21	93	1	99
	3	7.6	2.2	30	88	1	99
	4	22.1	-	95	182	2	99
9 August	1	1.3	-	10	97	2	98
	2	1.6	-	6	95	1	99
	3	1.5	-	8	74	1	98
	4	0.9	-	13	92	3	98
10 August	1	0.3	0.3	9	94	12	70
	2	0.4	0.2	23	100	6	92
	3	0.6	0.3	13	93	3	96
	4	0.6	0.2	31	99	4	94
	5	0.5	-	43	141	11	93
12 August	1	4.8	2.7	27	95	1	100
13 August	1	6.1	2.4	12	81	1	100
	2	3.0	4.0	15	88	2	99
	3	7.2	7.6	25	80	2	99
	4	8.7	-	42	113	2	99

After injection of isoprene, however, the model with HNO_3 wall loss, using the optimised rate constant (green trace), agrees with the measurement of the CO_3^--CIMS on the formation of additional ca. 0.2-0.3 ppbv of HNO_3, whereas HNO_3 doubles in the blue trace from 0.8 ppbv to 1.6 ppbv. The concurrent heterogeneous chemistry of N_2O_5 and loss of HNO_3 can therefore

explain the observed behaviour of HNO_3 under the declining presence of isoprene in the chamber. Another indication supporting this conclusion can be found in the time frame between 11:00 UTC and 12:45 UTC, where HNO_3 was constant at ca. 1 ppbv or exhibited even a small decline. Here, the presence of isoprene (maximum 2.3 ppbv) favoured the NO_3 + isoprene channel, supressing the formation and consequent conversion of N_2O_5. The blue trace demonstrates that the remaining N_2O_5 formation and the release of OH (reacting with NO_2) would allow a continuing increase in HNO_3 during the isoprene-rich phase, if HNO_3 would not also be prone to adsorb on the chamber wall.

Considering the NO_z yields reported in Table 5, these findings can confirm that yields between 80 % and 100 % are likely not biased strongly by HNO_3 released from the wall and not formed from the NO_2 injected during the respective experiments, as usually time frames were analysed where at least isoprene > 0.5 to 1 ppbv was present. Exceptions were discussed earlier, in which isoprene was not refilled in final injections towards the end of the experiments.

Figure 19 also includes a model run which uses a $k_{wall,HNO3}$ of 1.2×10^{-5} s^{-1} (red trace), as previously reported for the SAPHIR chamber by Karl (2004). This model run, however, fails to reproduce the decline in HNO_3 following the injection of isoprene (similar to the wall-loss-free simulation), and hence underestimates wall losses of HNO_3. The surface characteristics of the chamber are likely to not be constant over years and to depend on previous experiments, i.e. the chemical history of the chamber, as well as the individual experimental conditions, explaining the apparent increase in $k_{wall,HNO3}$ over time.

Another literature value of 8.2×10^{-5} s^{-1} (magenta trace), derived for a similarly large chamber (200 m^3) by harmonising experimental data and a custom box model approach (Bloss et al., 2005), exhibits agreement with the optimised $k_{wall,HNO3}$ and hence also allows simulating the correct change in HNO_3 after 11 UTC. To a certain degree the chamber setups might be comparable, as in both the walls are made of FEP, the air is homogenised using fans, and experiments were conducted under dry conditions. Values for $k_{wall,HNO3}$ derived via model optimisation in the way described in this section, however, can only serve as estimates due to the dependence on the accuracy of the HNO_3 measurements, the modelled isoprene + NO_3 product chemistry (forming OH), and the stoichiometry of the heterogeneous N_2O_5 conversion.

Wall losses of HNO_3 are also a plausible explanation for variability in the NO_z yields presented in Table 5. As shown in Figure 20, a negative trend in the NO_z yields with increasing maximum HNO_3 mixing ratios can be observed. By forcing a linear fit through a y-intercept at 1, an

empirical relationship between NO_z yield and maximum HNO_3 can be obtained: per 1 ppbv HNO_3 present, 3.4 % NO_z are lost, compared to the potential stoichiometric conversion of NO_x into NO_z. Incomplete conversion of HNO_3 into NO_x in the TD-CRDS inlet would also explain the behaviour displayed in Figure 20. The complete conversion has been, however, previously demonstrated in Friedrich et al. (2020) (i.e. Section 5).

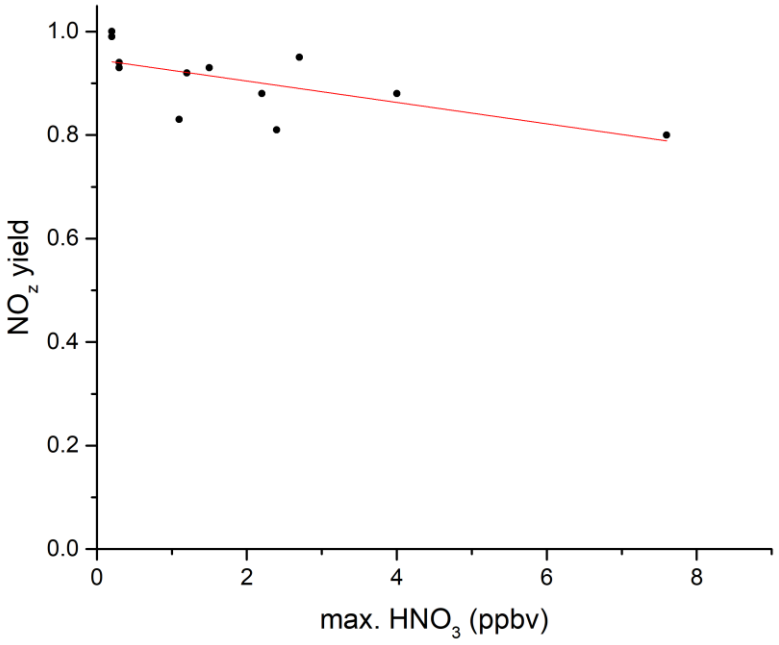

Figure 20: Negative trend in the observed NO_z yields with increasing maximum mixing ratio in HNO_3, indicating HNO_3 wall losses as a potential source for depletion in NO_x which is not associated with an equal increase in detectable NO_z.

In conclusion, the variability in the NO_z yields and frequent occurrence of numbers below unity are likely to be related to the wall losses and sources of HNO_3, depending on the ancillary composition of the simulated atmospheric mixture. Quantifying these would require additional characterisation experiments of the SAPHIR chamber, where e.g. HNO_3 is introduced into the chamber without any further trace gases or chamber surface processes are monitored depending on individual concentrations of NO_2, O_3, isoprene, and water. Respective investigations are unfortunately outside the scope of the data sets collected during the NO3ISOP campaign. Besides HNO_3 losses and sources, the "missing" NO_z yield might additionally be caused by remaining dry losses of isoprene-nitrates. The detectable reactive nitrogen budget is hence biased by a combination of all these three processes.

7.4 Conclusion

In this section, data sets from eight different experiments at the SAPHIR chamber during the NO3ISOP campaign were presented and analysed. By comparison with ancillary measurements of individual NO_z species and with box model calculations, the NO_z composition was elucidated and the NO_z measurements via TD-CRDS were validated. ONs yields were in a range between 77 % and 109 % per isoprene lost due to the reaction with NO_3. The variability of the ONs yields could not be attributed to changes in the fate of the initially formed RO_2 radicals, but rather to instrumental uncertainties stemming from the correction of NO_z for underlying trends in the HNO_3 mixing ratios. A mean NO_z yield (relative to NO_x) of 90 ± 7 % was derived, using the box model to correct for wall losses of NO_3 and N_2O_5, and neglecting wall losses of isoprene-derived nitrates. Finally, heterogeneous conversion of N_2O_5 at the walls was identified as a potential source for HNO_3 in the SAPHIR chamber. NO_z yields below unity are likely caused by wall losses of HNO_3.

8 Outlook

This work presented a comprehensive characterisation of a newly developed TD-CRDS instrument together with analyses of campaign data sets from ship-based measurements around the Arabian Peninsula and from chamber simulations exploring the dark oxidation of isoprene by NO_3. Instrument-wise, the re-release of previously deposited NO_y, caused by water, from the denuder surface was a key finding. The AQABA campaign was characterised by frequent changes between the sampling of polluted and aged air masses, resulting in contrasting NO_z/NO_y ratios depending on the region and on the air mass origins. HNO_3 was identified as the predominant NO_z component in the investigated Middle East regions, with organic nitrates contributing nearly equally strong when VOC emissions from nearby oil and gas production played a role. Shipping emissions affected the reactive nitrogen budget during the entire AQABA cruise, leading to unexpectedly high production of the short-lived HONO even under the occasionally encountered maritime background conditions. Organic nitrates were formed with high yields (usually > 80 %) during the NO3ISOP chamber experiments. The parallel measurements of NO_x and NO_z helped to identify the role of chamber wall chemistry of HNO_3 and N_2O_5 in perturbing the quantitative sequestering of NO_x.

Future enhancements of the TD-CRDS should involve optimisation of the optical detection system with new mirrors to lower the detection limits and to allow assessing the reactive nitrogen budget in remote locations. Increasing the length of the oven might enable operating the heated inlet at lower nominal temperatures. Development of regeneration techniques for the denuder would be warranted in order to continue quantifying the pNit fraction of NO_y. Future field deployments of the instrument would benefit from reliable supporting measurements of HNO_3 and organic nitrates. A stationary measurement platform would facilitate the collection of additional diel profiles in the NO_y budget, which would yield further interesting findings on the shift in the reactive nitrogen budget during the transition from OH- to NO_3-initiated tropospheric oxidation at the end of the day.

9 Appendix

S1: Chemical reactions and kinetic parameters included in the FACSIMILE box model. Note, that the reaction numeration is not consistent with the reactions in the publication. Abbreviations of chemical species are based on MCM 3.3.

k1 : N2O5 = NO3 + NO2
k2 : NO2 + NO3 = N2O5
k3 : NO + NO3 = NO2 + NO2
k4 : NO2 + O3 = NO3 + O2
k5 : NO + O3 = NO2 + O2
k6 : OH + O3 = HO2
k7 : HO2 + O3 = OH
k8 : OH + HO2 =
k9 : OH + NO2 = HNO3
k10 : OH + NO3 = HO2 + NO2
k11 : NO3 + ISO = NISOPO2
k12*0.3 : O3 + ISO = CH2OOE + MACR
k12*0.2 : O3 + ISO = CH2OOE + MVK
k12*0.3 : O3 + ISO = HCHO + MACROOA
k12*0.2 : O3 + ISO = HCHO + MVKOOA
k13*0.288 : OH + ISO = CISOPA
k13*0.238 : OH + ISO = CISOPC
k13*0.022 : OH + ISO = ISOP34O2
k13*0.020 : OH + ISO = ME3BU3ECHO + HO2
k13*0.042 : OH + ISO = PE4E2CO + HO2
k13*0.288 : OH + ISO = TISOPA
k13*0.102 : OH + ISO = TISOPC
k14*0.706 : NISOPO2 + HO2 = NISOPOOH
k15 : NISOPO2 + NO3 = NISOPO + NO2
k16*0.2 : NISOPO2 = ISOPCNO3
k16*0.2 : NISOPO2 = NC4CHO
k16*0.6 : NISOPO2 = NISOPO
k101 : NISOPO = NC4CHO + HO2
k17*0.22 : CH2OOE = CH2OO
k17*0.51 : CH2OOE = CO
k17*0.27 : CH2OOE = HO2 + CO + OH
k18 : NO3 + MACR = MACO3 + HNO3
k19*0.12 : O3 + MACR = HCHO + MGLYOOB
k19*0.88 : O3 + MACR = MGLYOX + CH2OOG
k20*0.45 : OH + MACR = MACO3
k20*0.47 : OH + MACR = MACRO2
k20*0.08 : OH + MACR = MACROHO2
k21*0.5 : O3 + MVK = MGLOOA + HCHO
k21*0.5 : O3 + MVK = MGLYOX + CH2OOB
k22*0.3 : OH + MVK = HMVKAO2
k22*0.7 : OH + MVK = HMVKBO2
k17*0.255 : MACROOA = C3H6
k17*0.255 : MACROOA = CH3CO3 + HCHO + HO2
k17*0.22 : MACROOA = MACROO
k17*0.27 : MACROOA = OH + CO + CH3CO3 + HCHO
k17*0.255 : MVKOOA = C3H6
k17*0.255 : MVKOOA = CH3O2 + HCHO + CO + HO2
k17*0.22 : MVKOOA = MVKOO
k17*0.27 : MVKOOA = OH + MVKO2
3.5E-12*0.2*M : CISOPA = CISOPAO2
3E-12*0.2*M : CISOPA = ISOPBO2
2E-12*0.2*M : CISOPC = CISOPCO2
3.5E-12*0.2*M : CISOPC = ISOPDO2
k14 : ISOP34O2 + HO2 = ISOP34OOH
k15 : ISOP34O2 + NO3 = ISOP34O + NO2
2.65E-12*RO2*0.1 : ISOP34O2 = HC4CHO
2.65E-12*RO2*0.8 : ISOP34O2 = ISOP34O
2.65E-12*RO2*0.1 : ISOP34O2 = ISOPDOH
9.73E-11 : ISOP34OOH + OH = HC4CHO + OH

k17 : ISOP34O = MACR + HCHO + HO2
1.04E-10*0.829 : HC4CHO + OH = C58O2
1.04E-10*0.171 : HC4CHO + OH = HC4CO3
k14*0.56 : HC4CO3 + HO2 =
k14*0.44 : HC4CO3 + HO2 = MACR + HO2 + OH
k15*1.6 : HC4CO3 + NO3 = MACR + HO2 + NO2
1E-11*RO2 : HC4CO3 = MACR + HO2
k29*4.0 : CO2C3CHO + NO3 = CO2C3CO3 + HNO3
7.15E-11 : CO2C3CHO + OH = CO2C3CO3
k104 : ME3BU3ECHO + NO3 = NC526O2
1.6E-17*0.33 : ME3BU3ECHO + O3 = CH2OOC + CO2C3CHO
1.6E-17*0.67 : ME3BU3ECHO + O3 = HCHO + CO2C3OOB
7.3E-11*0.712 : ME3BU3ECHO + OH = C530O2
7.3E-11*0.288 : ME3BU3ECHO + OH = ME3BU3ECO3
k17*0.82 : CO2C3OOB = C4CO2O2 + OH
k17*0.18 : CO2C3OOB = CO2C3OO
1.2E-15 : CO2C3OO + CO =
1E-15 : CO2C3OO + NO2 = NO3
k14*0.625 : C4CO2O2 + HO2 =
k15 : C4CO2O2 + NO3 = NO2
8.8E-12*RO2 : C4CO2O2 =
1.2E-14 : PE4E2CO + NO3 = NC51O2
1E-17*0.43 : PE4E2CO + O3 = CH2OOB + CO2C3CHO
1E-17*0.57 : PE4E2CO + O3 = HCHO + CO2C3OOA
2.71E-11 : PE4E2CO + OH = C51O2
k14*0.44 : CO2C3CO3 + HO2 = CH3COCH2O2 + OH
k14*0.56 : CO2C3CO3 + HO2 =
k15*1.74 : CO2C3CO3 + NO3 = CH3COCH2O2 + NO2
1E-11*RO2 : CO2C3CO3 = CH3COCH2O2
1.36E-13*exp(1250/T)*0.15 : CH3COCH2O2 + HO2 = OH
1.36D-13*exp(1250/TEMP)*0.85 : CH3COCH2O2 + HO2 =
k15 : CH3COCH2O2 + NO3 = NO2
2*(3.5E-13*8E-12)^0.5*RO2*0.2 : CH3COCH2O2 = ACETOL
2*(3.5E-13*8E-12)^0.5*RO2*0.6 : CH3COCH2O2 =
2*(3.5E-13*8E-12)^0.5*RO2*0.2 : CH3COCH2O2 = MGLYOX
k14*0.706 : C51O2 + HO2 =
k15 : C51O2 + NO3 = NO2
8.4E-13*RO2 : C51O2 =
k105 : TISOPA = ISOPAO2
3E-12*0.2*M : TISOPA = ISOPBO2
k105 : TISOPC = ISOPCO2
3.5E-12*0.2*M : TISOPC = ISOPDO2
k14*0.706 : CISOPAO2 + HO2 = ISOPAOOH
k15 : CISOPAO2 + NO3 = CISOPAO + NO2
k106 : CISOPAO2 = C536O2
k106 : CISOPAO2 = C5HPALD1 + HO2
5.22E15*exp(-9838/T) : CISOPAO2 = CISOPA
2.4E-12*0.8*RO2 : CISOPAO2 = CISOPAO
2.4E-12*0.1*RO2 : CISOPAO2 = HC4ACHO
2.4E-12*0.1*RO2 : CISOPAO2 = ISOPAOH
k17*0.37 : CISOPAO =
k17*0.63 : CISOPAO = HC4CCHO + HO2
k14*0.706 : CISOPCO2 + HO2 = ISOPCOOH
k15 : CISOPCO2 + NO3 = CISOPCO + NO2
k107 : CISOPCO2 = C537O2
k107 : CISOPCO2 = C5HPALD2 + HO2
3.06E15*exp(-10254/T) : CISOPCO2 = CISOPC
2E-12*0.8*RO2 : CISOPCO2 = CISOPCO
2E-12*0.1*RO2 : CISOPCO2 = HC4CCHO
2E-12*0.1*RO2 : CISOPCO2 = ISOPAOH
9.73E-11 : ISOP34OOH + OH = HC4CHO + OH
k15 : NC526O2 + NO3 = NO2
9.20E-14*RO2 : NC526O2 =
k17*0.18 : CH2OOC = CH2OO
k17*0.82 : CH2OOC = HO2 + CO + OH
k29*4.0 : CO2C3CHO + NO3 = HNO3
7.15E-11 : CO2C3CHO + OH =
k14*0.706 : C530O2 + HO2 =

k15 : C530O2 + NO3 = NO2
9.20E-14*RO2 : C530O2 =
k29*0.44 : M3BU3ECO3 + HO2 = C45O2 + OH + NO2
k14*0.56 : M3BU3ECO3 + HO2 =
k15*1.6 : M3BU3ECO3 + NO3 = C45O2 + NO2
1.00D-11*RO2 : M3BU3ECO3 = C45O2
k14*0.625 : C45O2 + HO2 =
k15 : C45O2 + NO3 = NO2
1.30E-12*RO2 : C45O2 =
k14*0.706 : NC51O2 + HO2 =
k15 : NC51O2 + NO3 = NO2
8.80E-13*RO2 : NC51O2 =
k17*0.30 : CISOPCO = C527O2
k17*0.52 : CISOPCO = HC4ACHO + HO2
k17*0.18 : CISOPCO = HO2 + M3F
k17*0.19 : CISOPAO = C526O2
k17*0.63 : CISOPAO = HC4CCHO + HO2
k17*0.18 : CISOPAO = HO2 + M3F
k14*0.706 : C536O2 + HO2 =
k15 : C536O2 + NO3 = NO2
9.20E-14*RO2 : C536O2 =
3.00E7*exp(-5300/T) : C536O2 = CO + OH
k29*4.25 : C5HPALD1 + NO3 = OH + HNO3
2.4E-17*0.73 : C5HPALD1 + O3 = MGLYOOA
2.40E-17*0.27 : C5HPALD1 + O3 = MGLYOX
5.20E-11 : C5HPALD1 + OH = OH
k14*0.706 : C537O2 + HO2 =
k15 : C537O2 + NO3 = NO2
9.20E-14*RO2 : C537O2 =
3.00E7*exp(-5300/T) : C537O2 = CO + OH
k29*4.25 : C5HPALD2 + NO3 = OH + HNO3
2.4E-17*0.27 : C5HPALD2 + O3 = GLYOOC
2.4E-17*0.73 : C5HPALD2 + O3 = GLYOX
5.2E-11 : C5HPALD2 + OH = OH
k14*0.706 : C527O2 + HO2 =
k15 : C527O2 + NO3 = NO2
8.8E-13*RO2 : C527O2 =
3.00E7*exp(-5300/T) : C527O2 = CO + OH
1.9E-11 : M3F + NO3 = NO2
2.0E-17 : M3F + O3 =
9.0E-11 : M3F + OH = HO2
k14*0.706 : C526O2 + HO2 =
k15 : C526O2 + NO3 = NO2
9.20E-14*RO2 : C526O2 =
3.00E7*exp(-5300/T) : C526O2 = CO + OH
k14*0.706 : ISOPAO2 + HO2 = ISOPAOOH
k15 : ISOPAO2 + NO3 = NO2 + ISOPAO
k23*0.1 : ISOPAO2 = HC4ACHO
k23*0.8 : ISOPAO2 = ISOPAO
k23*0.1 : ISOPAO2 = ISOPAOH
k83*0.1 : ISOPAO2 + NO = ISOPANO3
k83*0.9 : ISOPAO2 + NO = ISOPAO + NO2
k14*0.706 : ISOPBO2 + HO2 = ISOPBOOH
k15 : ISOPBO2 + NO3 = ISOPBO + NO2
k24*0.8 : ISOPBO2 = ISOPBO
k24*0.2 : ISOPBO2 = ISOPBOH
k83*0.066 : ISOPBO2 + NO = ISOPBNO3
k83*0.934 : ISOPBO2 + NO = ISOPBO + NO2
k14*0.706 : ISOPCO2 + HO2 = ISOPCOOH
k15 : ISOPCO2 + NO3 = NO2 + ISOPCO
k25*0.1 : ISOPCO2 = HC4CCHO
k25*0.1 : ISOPCO2 = ISOPAOH
k25*0.8 : ISOPCO2 = ISOPCO
k83*0.1 : ISOPCO2 + NO = ISOPCNO3
k83*0.9 : ISOPCO2 + NO = ISOPCO + NO2
k14*0.706 : ISOPDO2 + HO2 = ISOPDOOH
k15 : ISOPDO2 + NO3 = ISOPDO + NO2
k26*0.1 : ISOPDO2 = HCOC5

k26*0.8 : ISOPDO2 = ISOPDO
k26*0.1 : ISOPDO2 = ISOPDOH
k84*0.05 : ISOPAOOH + OH = HC4ACHO
k84*0.93 : ISOPAOOH + OH = IEPOXA + OH
k84*0.02 : ISOPAOOH + OH = ISOPAO2
k85 : ISOPANO3 + O3 =
k97 : ISOPANO3 + OH = INAO2
k17*0.25 : ISOPAO = C524O2
k17*0.75 : ISOPAO = HC4CCHO + HO2
k29*4.25 : HC4ACHO + NO3 = HC4ACO3 + HNO3
k86 : HC4ACHO + O3 =
k87*0.52 : HC4ACHO + OH = C58O2
k87*0.49 : HC4ACHO + OH = HC4ACO3
k88*0.5 : ISOPAOH + OH = HC4ACHO + HO2
k88*0.5 : ISOPAOH + OH = HC4CCHO + HO2
k89*0.92 : ISOPBOOH + OH = IEPOXB + OH
k89*0.08 : ISOPBOOH + OH = ISOPBO2
k90 : ISOPBNO3 + O3 =
k91*0.72 : ISOPBNO3 + OH = INB1O2
k91*0.28 : ISOPBNO3 + OH = INB2O2
k17 : ISOPBO = MVK + HCHO + HO2
k92 : ISOPBOH + OH = ISOPBO
k84*0.05 : ISOPCOOH + OH = HC4CCHO + OH
k84*0.93 : ISOPCOOH + OH = IEPOXC + OH
k84*0.02 : ISOPCOOH + OH = ISOPCO2
k17*0.75 : ISOPCO = HC4ACHO + HO2
k17*0.25 : ISOPCO = HC4CCHO + HO2
k29*4.25 : HC4CCHO + NO3 = HC4CCO3 + HNO3
k86 : HC4CCHO + O3 =
k87*0.52 : OH + HC4CCHO = C57O2
k87*0.48 : OH + HC4CCHO = HC4CCO3
k93*0.22 : OH + ISOPDOOH = HCOC5 + OH
k93*0.75 : OH + ISOPDOOH = IEPOXB + OH
k93*0.03 : OH + ISOPDOOH = ISOPDO2
k90 : ISOPDNO3 + O3 =
k94 : ISOPDNO3 + OH = INDO2
k17 : ISOPDO = MACR + HCHO + HO2
k95 : OH + HCOC5 = C59O2
k96 : OH + ISOPDOH = HCOC5
k27 : NISOPOOH + OH = NC4CHO + OH
k28 : ISOPCNO3 + OH = INCO2
k29*4.25 : NC4CHO + NO3 = NC4CO3 + HNO3
k30*0.52 : NC4CHO + OH = C510O2
k30*0.48 : NC4CHO + OH = NC4CO3
k103*0.5 : NC4CHO + O3 = NOA + GLYOOC
k103*0.5 : NC4CHO + O3 = GLYOX + NOAOOA
k17*0.11 : GLYOOC = GLYOO
k17*0.89 : GLYOOC = OH + HO2 + CO + CO
k17*0.11 : NOAOOA = NOAOO
k17*0.89 : NOAOOA = OH + NO2 + MGLYOX
k31 : CH2OO + CO = HCHO
k32 : CH2OO + NO2 = HCHO + NO3
k17*0.35 : CH3C2H2O2 = CH3CO3 + HCHO
k17*0.65 : CH3C2H2O2 = HCHO + CH3O2 + CO
k33*0.44 : MACO3 + HO2 = CH3C2H2O2
k33*0.66 : MACO3 + HO2 =
k15*1.74 : MACO3 + NO3 = CH3C2H2O2 + NO2
k34*0.7 : MACO3 = CH3C2H2O2
k34*0.3 : MACO3 =
k17*0.18 : MGLYOOB =
17*0.82 : MGLYOOB = OH + CO + CH3CO3
k29*2.4 : MGLYOX + NO3 = CH3CO3 + CO + HNO3
k35 : MGLYOX + OH = CH3CO3 + CO
k17*0.37 : CH2OOG = CH2OO
k17*0.47 : CH2OOG = CO
k17*0.16 : CH2OOG = HO2 + CO + OH
k14*0.625 : MACRO2 + HO2 =
k15 : MACRO2 + NO3 = NO2

k36 : MACRO2 =
k14*0.625 : MACROHO2 + HO2 =
k15 : MACROHO2 + NO3 = NO2
k37 : MACROHO2 =
k38*0.35 : NO3 + C3H6 = PRONO3AO2
k38*0.65 : NO3 + C3H6 = PRONO3BO2
k14*0.520*0 : PRONO3AO2 + HO2 =
k15 : PRONO3AO2 + NO3 = NO2
k56 : PRONO3AO2 =
k14*0.520*0 : PRONO3BO2 + HO2 =
k15 : PRONO3BO2 + NO3 = NO2
k57 : PRONO3BO2 =
k39*0.5 : O3 + C3H6 = CH2OOB + CH3CHO
k39*0.5 : O3 + C3H6 = CH3CHOOA + HCHO
k59 : CO + OH = HO2
k40 : HO2 + NO3 = OH + NO2
k17*0.24 : CH3CHOOA = CH3CHOO
k17*0.36 : CH3CHOOA = CH3O2 + CO + OH
k17*0.2 : CH3CHOOA = CH3O2 + HO2
k17*0.2 : CH3CHOOA =
k31 : CH3CHOO + CO = CH3CHO
k32 : CH3CHOO + NO2 = CH3CHO + NO3
k58*0.87 : OH + C3H6 = HYPROPO2
k58*0.13 : OH + C3H6 = IPROPOLO2
k14*0.52 : HYPROPO2 + HO2 =
k15 : HYPROPO2 + NO3 = NO2
k43 : HYPROPO2 =
k14*0.52 : IPROPOLO2 + HO2 =
k15 : IPROPOLO2 + NO3 = NO2
k25 : IPROPOLO2 =
k33 : CH3CO3 + HO2 =
k40 : CH3CO3 + NO3 = NO2 + CH3O2
k41*0.3 : CH3CO3 =
k41*0.7 : CH3CO3 = CH3O2
k17*0.2 : MGLOOA = CH3CO3 + HCHO + HO2
k17*0.36 : MGLOOA = OH + CO + CH3CO3
k17*0.44 : MGLOOA =
k17*0.24 : CH2OOB = CH2OO
k17*0.4 : CH2OOB = CO
k17*0.36 : CH2OOB = HO2 + CO + OH
k14*0.625 : HMVKAO2 + HO2 =
k15 : HMVKAO2 + NO3 = NO2
k42 : HMVKAO2 =
k14*0.625 : HMVKBO2 + HO2 =
k15 : HMVKBO2 + NO3 = NO2
k43 : HMVKBO2 =
k31 : MACROO + CO = MACR
k32 : MACROO + NO2 = MACR + NO3
k44 : CH3O2 + HO2 =
k45 : CH3O2 + HO2 = HCHO
k46 : CH3O2 + NO3 = CH3O +NO2
k47*0.5 : CH3O2 = CH3OH
k47*0.5 : CH3O2 = HCHO
k31 : MVKOO + CO = MVK
k32 : MVKOO + NO2 = MVK + NO3
k14*0.625 : MVKO2 + HO2 =
k15 : MVKO2 + NO3 = NO2
k42 : MVKO2 =
k48 : BCARY + NO3 = NBCO2
k15 : NBCO2 + NO3 =
k49 : BCARY + O3 = BCAOO
k49 : BCARY + O3 = BCBOO
k50 : BCARY + O3 =
k51 : BCAOO = BCSOZ
k52 : BCBOO = BCSOZ
k14*0.706*0 : INCO2 + HO2 =
k15*0 : INCO2 + NO3 = NO2
k53*0 : INCO2 =

k33*0.44 : NC4CO3 + HO2 = NOA + CO + HO2 + OH
k33*0.66*0 : NC4CO3 + HO2 =
k15*1.74 : NC4CO3 + NO3 = NOA + CO + HO2 + NO2
k54*0.3*0 : NC4CO3 =
k54*0.7 : NC4CO3 = NOA + HO2 + CO
k102 : NOA + OH = MGLYOX + NO2
k14*0.706*0 : C510O2 + HO2 =
k15*0 : C510O2 + NO3 = NO2
k55*0 : C510O2 =
k14*0.706*0 : INAO2 + HO2 =
k15*0 : INAO2 + NO3 = NO2
k24*0 : INAO2 =
k14*0.706*0 : C524O2 + HO2 =
k15*0 : C524O2 + NO3 = NO2
k53*0 : C524O2 =
k98 : HC4ACO3 + HO2 =
k15*1.74 : HC4ACO3 + NO3 =
k54 : HC4ACO3 =
k14*0.706*0 : C58O2 + HO2 =
k15*0 : C58O2 + NO3 = NO2
k55*0 : C58O2 =
k99*0.5 : OH + IEPOXB = IEB1O2
k99*0.5 : OH + IEPOXB = IEB2O2
k14*0.706*0 : INB1O2 + HO2 =
k15*0 : INB1O2 + NO3 =
k53*0 : INB1O2 =
k14*0.706*0 : INB2O2 + HO2 =
k24*0 : INB2O2 =
k100*0.719 : OH + IEPOXC = IEC1O2
k100*0.281 : OH + IEPOXC =
k98 : HC4CCO3 + HO2 =
k15*1.74 : HC4CCO3 + NO3 = NO2
k54 : HC4CCO3 =
k14*0.706*0 : INDO2 + HO2 =
k15*0 : INDO2 + NO3 = NO2
k24*0 : INDO2 =
k14*0.706*0 : C57O2 + HO2 =
k15*0 : C57O2 + NO3 = NO2
k55*0 : C57O2 =
k14*0.706*0 : C59O2 + HO2 =
k15*0 : C59O2 + NO3 = NO2
k55*0 : C59O2 =
k14*0.706 : IEB1O2 + HO2 =
k15 : IEB1O2 + NO3 = NO2
k55 : IEB1O2 =
k14*0.706 : IEB2O2 + HO2 =
k15 : IEB2O2 + NO3 =
k43 : IEB2O2 =
k14*0.706 : IEC1O2 + HO2 =
k15 : IEC1O2 + NO3 = NO2
k55 : IEC1O2 =
k60 : CO + NO3 =
k61 : HCHO + NO3 = HNO3 + CO + HO2
k62 : OH + HCHO = HO2 + CO
k63 : O = O3
k64 : O = O3
k65 : O + O3 =
k66 : O + NO = NO2
k67 : O + NO2 = NO
k68 : O + NO2 = NO3
k69 : O1D = O
k70 : O1D = O
k71 : O1D = OH + OH
k72 : OH + H2O2 = HO2
k73 : HO2 + HO2 = H2O2
k74 : OH + NO = HONO
k75 : HO2 + NO = OH + NO2
k76 : HO2 + NO2 = HO2NO2

```
k77                    : HO2NO2 + OH = NO2
k78                    : OH + HONO = NO2
k79                    : OH + HNO3 = NO3
k82                    : HO2NO2 = HO2 + NO2
k59                    : Y + OH = HO2
k80                    : SHONO = HONO
k81                    : SHCHO = HCHO
kWall1                 : O3 =
kWall3                 : N2O5 =
kWall1                 : H2O2 =
kWall1                 : HO2 =
kWall1                 : HONO =
kWall1                 : HNO3 =
khet1                  : N2O5 =
khet2                  : NO3 =
kWall2                 : NO3 =
kDil                   : All molecules
* ---------------------------------------
*Rate equations
k1 = ((1.3e-3*(T/300)^-3.5*exp(-11000/T))*M*
(9.7e14*(T/300)^0.1*exp(-11080/T)))/((1.3e-3*
(T/300)^-3.5*exp(-11000/T))*M+(9.7e14*(T/300)^0.1*
exp(-11080/T)))*10^(log10(0.35)/(1+(log10((1.3e-3*(T/300)^-3.5
*exp(-11000/T))*M/(9.7e14*(T/300)^0.1*exp(-11080/T)))
/(0.75-1.27*log10(0.35)))^2))
k2 = ((3.6e-30*(T/300)^-4.1)*M*(1.9e-12*(T/300)^0.2))
/((3.6e-30*(T/300)^-4.1)*M+(1.9e-12*(T/300)^0.2))*
10^(log10(0.35)/(1+(log10((3.6e-30*(T/300)^-4.1)*
M/(1.9e-12*(T/300)^0.2))/(0.75-1.27*log10(0.35)))^2))
k3 = 1.8E-11*exp(110/T)
k4 = 1.4E-13 * exp (-2470/T)
k5 = 2.07E-12 * exp (-1400/T)
k6 = 1.70E-12*exp(-940/T)
k7 = 2.03E-16*(T/300)^4.57*exp(693/T)
k8 = 4.8E-11*exp(250/T)
k9 = ((3.2e-30*(T/300)^-4.5)*M*(3.0e-11))/
((3.2e-30*(T/300)^-4.5)*M+(3.0e-11))*10^(log10(0.41)/
(1+(log10((3.2e-30*(T/300)^-4.5)*M/(3.0e-11))/
(0.75-1.27*log10(0.41)))^2))
k10 = 2E-11
k11 = 2.95E-12 * exp (-450/T)
k12 = 1.03E-14 * exp (-1995/T)
k13 = 2.7E-11 * exp (390/T)
k14 = 2.91E-13 * exp(1300/T)
k15 = 2.3E-12
k16 = 1.3E-12*RO2
k17 = 1E6
k18 = 3.4E-15
k19 = 1.4E-15*exp(-2100/T)
k20 = 8.0E-12*exp(380/T)
k21 = 8.5E-16*exp(-1520/T)
k22 = 2.6E-12*exp(610/T)
k23 = 2.4E-12*RO2
k24 = 8E-13*RO2
k25 = 2E-12*RO2
k26 = 2.9E-12*RO2
k27 = 1.03E-10
k28 = 6.93E-11
k29 = 1.4E-12*exp(-1860/T)
k30 = 4.16E-11
k31 = 1.2E-15
k32 = 1E-15
k33 = 5.2E-13*exp(980/T)
k34 = 1E-11*RO2
k35 = 1.9E-12*exp(575/T)
k36 = 9.2E-14*RO2
k37 = 1.4E-12*RO2
k38 = 4.6E-13*exp(-1155/T)
```

k39 = 5.5E-15*exp(-1880/T)
k40 = 4E-12
k41 = 2*(3.5E-13*2.9E-12*exp(500/T))^0.5*RO2
k42 = 2E-12*RO2
k43 = 8.8E-13*RO2
k44 = 3.8E-13*exp(780/T)*(1-1/(1+498*exp(-1160/T)))
k45 = 3.8E-13*exp(780/T)*(1/(1+498*exp(-1160/T)))
k46 = 1.2E-12
k47 = 2*1.03E-13*exp(365/T)*RO2*0.5*(1-7.18*exp(-885/T))
k48 = 1.9E-11
k49 = 0.435*1.2E-14
k50 = 0.13*1.2E-14
k51 = 8E1
k52 = 1.2E2
k53 = 2.9E-12*RO2
k54 = 1E-11*RO2
k55 = 9.2E-14*RO2
k56 = 6E-13*0.2*RO2
k57 = 4E-14*0.2*RO2
k58 = ((8e-27*(T/300)^-3.5)*M*(3.0e-11*(T/300)^-1))/
((8e-27*(T/300)^-3.5)*M+(3.0e-11*(T/300)^-1))*
10^(log10(0.5)/(1+(log10((8e-27*(T/300)^-3.5)*M/
(3.0e-11*(T/300)^-1))/(0.75-1.27*log10(0.5)))^2))
k59 = 1.44E-13*(1+(M/4.2E19))
k60 = 4E-19
k61 = 5.5E-16
k62 = 5.4E-12 * exp (135/T)
k63 = 5.6E-34*0.8*M*(T/300)^-2.6*0.2*M
k64 = 6.0E-34*0.2*M*(T/300)^-2.6*0.2*M
k65 = 8.0E-12 * exp (-2060/T)
k66 = 5E-11*(T/300)^-0.3
k67 = 5.5E-12 * exp (188/T)
k68 = ((1.3e-31*(T/300)^-1.5)*M*(2.3e-11*(T/300) 0.24))/
((1.3e-31*(T/300)^-1.5)*M+(2.3e-11*(T/300)^0.24))*
10^(log10(0.6)/(1+(log10((1.3e-31*(T/300)^-1.5)*M/
(2.3E-11*(T/300)^0.24))/(0.75-1.27*log10(0.6)))^2))
k69 = 3.2E-11*exp(67/T)*0.2*M
k70 = 2.0E-11*exp(130/T)*0.8*M
k71 = 2.14E-10*H2O
k72 = 2.9E-12*exp(-160/T)
k73 = 2.20E-13*(1+(1.40E-21*exp(2200/T)*H2O))*exp(600/T)
k74 = ((7.4e-31*(T/300)^-2.4)*M*(3.3e-11*(T/300)^-0.3))/
((7.4e-31*(T/300)^-2.4)*M+(3.3e-11*(T/300)^-0.3))*
10^(log10(0.81)/(1+(log10((7.4e-31*(T/300)^-2.4)*M/
(3.3e-11*(T/300)^-0.3))/(0.75-1.27*log10(0.81)))^2))
k75 = 3.45E-12*exp(270/T)
k76 = ((1.4e-31*(T/300)^-3.1)*M*(4.0e-12))/
((1.4e-31*(T/300)^-3.1)*M+(4.0e-12))*10^(log10(0.4)/
(1+(log10((1.4e-31*(T/300)^-3.1)*M/(4.0e-12))/
(0.75-1.27*log10(0.4)))^2))*0
k77 = 3.2e-13*exp(690/T)
k78 = 2.5e-12*exp(260/T)
k79 = 2.40E-14*exp(460/T) + ((6.50E-34*exp(1335/T)*M)/
(1+(6.50E-34*exp(1335/T)*M/2.70E-17*exp(2199/T))))
k80 = ((1E9*O3)/M)*NO2*0.008*exp(-3950/T)
k81 = 1*3.1E13*(0.21+0.026*RH)*exp(-2876/T)*0
k82 = ((4.1e-5*exp(-10650/T))*M*(6.0e15*exp(-11170/T)))/
((4.1e-5*exp(-10650/T))*M+(6.0e15*exp(-11170/T)))*
10^(log10(0.4)/(1+(log10((4.1e-5*exp(-10650/T))*M/
(6.0e15*exp(-11170/T)))/(0.75-1.27*log10(0.4)))^2))
k83 = 2.7E-12*exp(360/T)
k84 = 1.54E-10
k85 = 5.3E-17
k86 = 2.4E-17
k87 = 4.52E-11
k88 = 9.3E-11
k89 = 5E-11
k90 = 1.06E-16

k91 = 1.36E-11
k92 = 3.85E-11
k93 = 1.15E-10
k94 = 2.54E-11
k95 = 3.81E-11
k96 = 7.38E-11
k97 = 6.96E-11
k98 = 5.2E-13*exp(980/T)
k99 = 9.05E-12
k100 = 1.5E-11
k101 = 2.50E-14*exp(-300/T)*0.2*M
k102 = 1.3E-13
k103 = 2.4E-17
k104 = 3.3E-13
k105 = 2.5E-12*exp(-480/T)*0.2*M
k106 = 8.14E9*exp(-8591/T)*exp(1.00E8/T^3)*0.5
k107 = 2.20E10*exp(-8174/T)*exp(1.00E8/T^3)*0.5
khet1 = (0*het*(1.46E4*(T/108)^0.5)*SAS)/4
khet2 = (0*het*(1.46E4*(T/62)^0.5)*SAS)/4

10 References

Albrecht, S. R., Novelli, A., Hofzumahaus, A., Kang, S., Baker, Y., Mentel, T., Wahner, A., and Fuchs, H.: Measurements of hydroperoxy radicals (HO2) at atmospheric concentrations using bromide chemical ionisation mass spectrometry, Atmospheric Measurement Techniques, 12, 891-902, 10.5194/amt-12-891-2019, 2019.

Anderson, D. Z., Frisch, J. C., and Masser, C. S.: Mirror Reflectometer Based on Optical Cavity Decay Time, Applied Optics, 23, 1238-1245, Doi 10.1364/Ao.23.001238, 1984.

Avnery, S., Mauzerall, D. L., Liu, J. F., and Horowitz, L. W.: Global crop yield reductions due to surface ozone exposure: 2. Year 2030 potential crop production losses and economic damage under two scenarios of O-3 pollution, Atmospheric Environment, 45, 2297-2309, 10.1016/j.atmosenv.2011.01.002, 2011.

Barnes, I., Bastian, V., Becker, K. H., and Tong, Z.: KINETICS AND PRODUCTS OF THE REACTIONS OF NO3 WITH MONOALKENES, DIALKENES, AND MONOTERPENES, Journal of Physical Chemistry, 94, 2413-2419, 10.1021/j100369a041, 1990.

Barthelmie, R. J., and Pryor, S. C.: Implications of ammonia emissions for fine aerosol formation and visibility impairment - A case study from the Lower Fraser Valley, British Columbia, Atmospheric Environment, 32, 345-352, Doi 10.1016/S1352-2310(97)83466-8, 1998.

Berden, G., Peeters, R., and Meijer, G.: Cavity ring-down spectroscopy: Experimental schemes and applications, International Reviews in Physical Chemistry, 19, 565-607, 2000.

Berndt, T., and Boge, O.: Gas-phase reaction of NO3 radicals with isoprene: A kinetic and mechanistic study, International Journal of Chemical Kinetics, 29, 755-765, 10.1002/(sici)1097-4601(1997)29:10<755::aid-kin4>3.0.co;2-l, 1997.

Bloss, C., Wagner, V., Bonzanini, A., Jenkin, M. E., Wirtz, K., Martin-Reviejo, M., and Pilling, M. J.: Evaluation of detailed aromatic mechanisms (MCMv3 and MCMv3.1) against environmental chamber data, Atmos Chem Phys, 5, 623-639, DOI 10.5194/acp-5-623-2005, 2005.

Brown, S. S.: Absorption spectroscopy in high-finesse cavities for atmospheric studies, Chemical Reviews, 103, 5219-5238, 2003.

Brown, S. S., Dibb, J. E., Stark, H., Aldener, M., Vozella, M., Whitlow, S., Williams, E. J., Lerner, B. M., Jakoubek, R., Middlebrook, A. M., DeGouw, J. A., Warneke, C., Goldan, P. D., Kuster, W. C., Angevine, W. M., Sueper, D. T., Quinn, P. K., Bates, T. S., Meagher, J. F., Fehsenfeld, F. C., and Ravishankara, A. R.: Nighttime removal of NOx in the summer marine boundary layer, Geophysical Research Letters, 31, Artn L07108;10.1029/2004gl019412, 2004.

Brown, S. S., Degouw, J. A., Warneke, C., Ryerson, T. B., Dube, W. P., Atlas, E., Weber, R. J., Peltier, R. E., Neuman, J. A., Roberts, J. M., Swanson, A., Flocke, F., McKeen, S. A., Brioude, J., Sommariva, R., Trainer, M., Fehsenfeld, F. C., and Ravishankara, A. R.: Nocturnal isoprene oxidation over the Northeast United States in summer and its impact on reactive nitrogen partitioning and secondary organic aerosol, Atmospheric Chemistry and Physics, 9, 3027-3042, 2009.

Brown, S. S., Dube, W. P., Peischl, J., Ryerson, T. B., Atlas, E., Warneke, C., de Gouw, J. A., Hekkert, S. t. L., Brock, C. A., Flocke, F., Trainer, M., Parrish, D. D., Feshenfeld, F. C., and Ravishankara, A. R.: Budgets for nocturnal VOC oxidation by nitrate radicals aloft during the 2006 Texas Air Quality Study, Journal of Geophysical Research-Atmospheres, 116, 10.1029/2011jd016544, 2011.

Brownwood, B., Turdziladze, A., Hohaus, T., Wu, R., Mentel, T. F., Carlsson, P. T. M., Tsiligiannis, E., Hallquist, M., Andres, S., Hantschke, L., Reimer, D., Rohrer, F., Tillmann, R., Winter, B., Liebmann, J., Brown, S. S., Kiendler-Scharr, A., Novelli, A., Fuchs, H., and Fry, J. L.: Gas-Particle Partitioning and SOA Yields of Organonitrate Products from NO3-Initiated Oxidation of Isoprene under Varied Chemical Regimes, ACS Earth and Space Chemistry, 10.1021/acsearthspacechem.0c00311, 2021.

Carsey, T. P., Churchill, D. D., Farmer, M. L., Fischer, D. J., Pszenny, A. A., Ross, V. B., Saltzmann, E. S., SpringerYoung, M., and Bonsang, B.: Nitrogen oxides and ozone production in the North Atlantic marine boundary layer, Journal of Geophysical Research-Atmospheres, 102, 10653-10665, Doi 10.1029/96jd03511, 1997.

Carslaw, D. C., Murrells, T. P., Andersson, J., and Keenan, M.: Have vehicle emissions of primary NO2 peaked?, Faraday Discussions, 189, 439-454, 10.1039/c5fd00162e, 2016.

Chameides, W. L., Stedman, D. H., Dickerson, R. R., Rusch, D. W., and Cicerone, R. J.: Nox Production in Lightning, Journal of the Atmospheric Sciences, 34, 143-149, Doi 10.1175/1520-0469(1977)034<0143:Npil>2.0.Co;2, 1977.

Chebbi, A., and Carlier, P.: Carboxylic acids in the troposphere, occurrence, sources, and sinks: A review, Atmospheric Environment, 30, 4233-4249, Doi 10.1016/1352-2310(96)00102-1, 1996.

Chen, L., Zhu, J., Liao, H., Yang, Y., and Yue, X.: Meteorological influences on PM2.5 and O-3 trends and associated health burden since China's clean air actions, Science of the Total Environment, 744, ARTN 140837;10.1016/j.scitotenv.2020.140837, 2020.

Crounse, J. D., Nielsen, L. B., Jorgensen, S., Kjaergaard, H. G., and Wennberg, P. O.: Autoxidation of Organic Compounds in the Atmosphere, J Phys Chem Lett, 4, 3513-3520, 10.1021/jz4019207, 2013.

Crutzen, P.: A discussion of the chemistry of some minor constituents in the stratosphere and troposphere, Pure and Applied Geophysics, 106-108, 1385-1399, 1973.

Curtis, A. R., and Sweetenham, W. P.: Facsimile, Atomic Energy Research Establishment, Report R-12805, 1987, 1987.

Dai, J., and Wang, T.: Impact of International Shipping Emissions on Ozone and PM2.5: The Important Role of HONO and ClNO2, Atmos. Chem. Phys. Discuss., 2021, 1-29, 10.5194/acp-2020-1185, 2021.

Day, D. A., Wooldridge, P. J., Dillon, M. B., Thornton, J. A., and Cohen, R. C.: A thermal dissociation laser-induced fluorescence instrument for in situ detection of NO_2, peroxy nitrates, alkyl nitrates, and HNO_3, Journal of Geophysical Research-Atmospheres, 107, doi:10.1029/2001jd000779, 2002.

Dewald, P., Liebmann, J. M., Friedrich, N., Shenolikar, J., Schuladen, J., Rohrer, F., Reimer, D., Tillmann, R., Novelli, A., Cho, C. M., Xu, K. M., Holzinger, R., Bernard, F., Zhou, L., Mellouki, W., Brown, S. S., Fuchs, H., Lelieveld, J., and Crowley, J. N.: Evolution of NO3 reactivity during the oxidation of isoprene, Atmos Chem Phys, 20, 10459-10475, 10.5194/acp-20-10459-2020, 2020.

Dewald, P., Dörich, R., Schuladen, J., Lelieveld, J., and Crowley, J. N.: Impact of ozone and inlet design on the detection of isoprene-derived organic nitrates by thermal dissociation cavity ring-down spectroscopy (TD-CRDS), Atmos. Meas. Tech. Discuss., 2021, 1-35, 10.5194/amt-2021-128, 2021.

Dibb, J. E., Scheuer, E., Whitlow, S. I., Vozella, M., Williams, E., and Lerner, B. M.: Ship-based nitric acid measurements in the gulf of Maine during New England Air Quality Study 2002, Journal of Geophysical Research-Atmospheres, 109, Artn D20303;10.1029/2004jd004843, 2004.

Driscoll, C. T., Lambert, K. F., and Chen, L.: Acidic Deposition: Sources and Ecological Effects, in: Acid in the Environment: Lessons Learned and Future Prospects, edited by: Visgilio, G. R., and Whitelaw, D. M., Springer US, Boston, MA, 27-58, 2007.

Dubé, W. P., Brown, S. S., Osthoff, H. D., Nunley, M. R., Ciciora, S. J., Paris, M. W., McLaughlin, R. J., and Ravishankara, A. R.: Aircraft instrument for simultaneous, in situ measurement of NO3 and N2O5 via pulsed cavity ring-down spectroscopy, Review of Scientific Instruments, 77, doi: 10.1063/1.2176058, 2006.

Duncan, B. N., Yoshida, Y., Olson, J. R., Sillman, S., Martin, R. V., Lamsal, L., Hu, Y. T., Pickering, K. E., Retscher, C., Allen, D. J., and Crawford, J. H.: Application of OMI observations to a space-based indicator of NOx and VOC controls on surface ozone formation, Atmospheric Environment, 44, 2213-2223, 10.1016/j.atmosenv.2010.03.010, 2010.

Ehhalt, D. H., Dorn, H. P., and Poppe, D.: The Chemistry of the Hydroxyl Radical in the Troposphere, P Roy Soc Edinb B, 97, 17-34, Doi 10.1017/S0269727000005273, 1990.

Faustini, A., Rapp, R., and Forastiere, F.: Nitrogen dioxide and mortality: review and meta-analysis of long-term studies, Eur Respir J, 44, 744-753, 10.1183/09031936.00114713, 2014.

Finlayson-Pitts, B. J., and Pitts, J. N.: Chemistry of the Upper and Lower Atmosphere, Academic Press, San Diego, 2000.

Franco, B., Blumenstock, T., Cho, C., Clarisse, L., Clerbaux, C., Coheur, P. F., De Maziere, M., De Smedt, I., Dorn, H. P., Emmerichs, T., Fuchs, H., Gkatzelis, G., Griffith, D. W. T., Gromov, S., Hannigan, J. W., Hase, F., Hohaus, T., Jones, N., Kerkweg, A., Kiendler-Scharr, A., Lutsch, E., Mahieu, E., Novelli, A., Ortega, I., Paton-Walsh, C., Pommier, M., Pozzer, A., Reimer, D., Rosanka, S., Sander, R., Schneider, M., Strong, K., Tillmann, R., Van Roozendael, M., Vereecken, L., Vigouroux, C., Wahner, A., and Taraborrelli, D.: Ubiquitous atmospheric production of organic acids mediated by cloud droplets, Nature, 593, 233-+, 10.1038/s41586-021-03462-x, 2021.

Friedrich, N., Tadic, I., Schuladen, J., Brooks, J., Darbyshire, E., Drewnick, F., Fischer, H., Lelieveld, J., and Crowley, J. N.: Measurement of NOx and NOy with a thermal dissociation cavity ring-down spectrometer (TD-CRDS): instrument characterisation and first deployment, Atmos. Meas. Tech., 13, 5739-5761, 10.5194/amt-13-5739-2020, 2020.

Fry, J. L., Brown, S. S., Middlebrook, A. M., Edwards, P. M., Campuzano-Jost, P., Day, D. A., Jimenez, J. L., Allen, H. M., Ryerson, T. B., Pollack, I., Graus, M., Warneke, C., de Gouw, J. A., Brock, C. A., Gilman, J., Lerner, B. M., Dube, W. P., Liao, J., and Welti, A.: Secondary organic aerosol (SOA) yields from NO3 radical + isoprene based on nighttime aircraft power plant plume transects, Atmospheric Chemistry and Physics, 18, 11663-11682, 10.5194/acp-18-11663-2018, 2018.

Fuchs, H., Dube, W. P., Cicioira, S. J., and Brown, S. S.: Determination of inlet transmission and conversion efficiencies for in situ measurements of the nocturnal nitrogen oxides, NO3, N2O5 and NO2, via pulsed cavity ring-down spectroscopy, Analytical Chemistry, 80, 6010-6017, 2008.

Fuchs, H., Bohn, B., Hofzumahaus, A., Holland, F., Lu, K. D., Nehr, S., Rohrer, F., and Wahner, A.: Detection of HO2 by laser-induced fluorescence: calibration and interferences from RO2 radicals, Atmospheric Measurement Techniques, 4, 1209-1225, 2011.

Fuchs, H., Hofzumahaus, A., Rohrer, F., Bohn, B., Brauers, T., Dorn, H. P., Haseler, R., Holland, F., Kaminski, M., Li, X., Lu, K., Nehr, S., Tillmann, R., Wegener, R., and Wahner, A.: Experimental evidence for efficient hydroxyl radical regeneration in isoprene oxidation, Nature Geoscience, 6, 1023-1026, 10.1038/Ngeo1964, 2013.

Galloway, J. N., Dentener, F. J., Capone, D. G., Boyer, E. W., Howarth, R. W., Seitzinger, S. P., Asner, G. P., Cleveland, C. C., Green, P. A., Holland, E. A., Karl, D. M., Michaels, A. F., Porter, J. H., Townsend, A. R., and Vorosmarty, C. J.: Nitrogen cycles: past, present, and future, Biogeochemistry, 70, 153-226, DOI 10.1007/s10533-004-0370-0, 2004.

Gierczak, T., Jimenez, E., Riffault, V., Burkholder, J. B., and Ravishankara, A. R.: Thermal decomposition of HO2NO2 (peroxynitric acid, PNA): Rate coefficient and determination of the enthalpy of formation, Journal of Physical Chemistry A, 109, 586-596, 10.1021/jp046632f, 2005.

Granier, C., Darras, S., Denier van der Gon, H., Doubalova, J., N., E., Galle, B., Gauss, M., Guevara, M., Jalkanen, J.-P., Kuenen, J., Liousse, C., Quack, B., Simpson, D., and Sindelarova, K.: The Copernicus Atmosphere Monitoring Service global and regional emissions (April 2019 version), Copernicus Atmosphere Monitoring Service (CAMS) report, 10.24380/d0bn-kx16, 2019.

Grewe, V., Dahlmann, K., Matthes, S., and Steinbrecht, W.: Attributing ozone to NOx emissions: Implications for climate mitigation measures, Atmospheric Environment, 59, 102-107, 10.1016/j.atmosenv.2012.05.002, 2012.

Grewe, V., Matthes, S., and Dahlmann, K.: The contribution of aviation NOx emissions to climate change: are we ignoring methodological flaws?, Environ. Res. Lett., 14, ARTN 121003;10.1088/1748-9326/ab5dd7, 2019.

Guenther, A. B., Jiang, X., Heald, C. L., Sakulyanontvittaya, T., Duhl, T., Emmons, L. K., and Wang, X.: The Model of Emissions of Gases and Aerosols from Nature version 2.1 (MEGAN2.1): an extended and updated framework for modeling biogenic emissions, Geoscientific Model Development, 5, 1471-1492, 10.5194/gmd-5-1471-2012, 2012.

Guerreiro, C. B. B., Foltescu, V., and de Leeuw, F.: Air quality status and trends in Europe, Atmospheric Environment, 98, 376-384, 10.1016/j.atmosenv.2014.09.017, 2014.

Haagensmit, A. J.: Chemistry and Physiology of Los-Angeles Smog, Ind Eng Chem, 44, 1342-1346, DOI 10.1021/ie50510a045, 1952.

Heland, J., Kleffmann, J., Kurtenbach, R., and Wiesen, P.: A new instrument to measure gaseous nitrous acid (HONO) in the atmosphere, Environmental Science & Technology, 35, 3207-3212, DOI 10.1021/es000303t, 2001.

Henze, D. K., Seinfeld, J. H., Ng, N. L., Kroll, J. H., Fu, T. M., Jacob, D. J., and Heald, C. L.: Global modeling of secondary organic aerosol formation from aromatic hydrocarbons: high- vs. low-yield pathways, Atmos Chem Phys, 8, 2405-2420, DOI 10.5194/acp-8-2405-2008, 2008.

Herbelin, J. M., Mckay, J. A., Kwok, M. A., Ueunten, R. H., Urevig, D. S., Spencer, D. J., and Benard, D. J.: Sensitive Measurement of Photon Lifetime and True Reflectances in an Optical Cavity by a Phase-Shift Method, Applied Optics, 19, 144-147, Doi 10.1364/Ao.19.000144, 1980.

Holland, F., Hofzumahaus, A., Schafer, R., Kraus, A., and Patz, H. W.: Measurements of OH and HO2 radical concentrations and photolysis frequencies during BERLIOZ, Journal of Geophysical Research-Atmospheres, 108, 10.1029/2001jd001393, 2003.

Horowitz, L. W., Liang, J. Y., Gardner, G. M., and Jacob, D. J.: Export of reactive nitrogen from North America during summertime: Sensitivity to hydrocarbon chemistry, Journal of Geophysical Research-Atmospheres, 103, 13451-13476, Doi 10.1029/97jd03142, 1998.

Horowitz, L. W., Fiore, A. M., Milly, G. P., Cohen, R. C., Perring, A., Wooldridge, P. J., Hess, P. G., Emmons, L. K., and Lamarque, J.-F.: Observational constraints on the chemistry of isoprene nitrates over the eastern United States, J. Geophys. Res., 112, D12S08-, 2007.

Hosaynali Beygi, Z., Fischer, H., Harder, H. D., Martinez, M., Sander, R., Williams, J., Brookes, D. M., Monks, P. S., and Lelieveld, J.: Oxidation photochemistry in the Southern Atlantic boundary layer: unexpected deviations of photochemical steady state, Atmospheric Chemistry and Physics, 11, 8497-8513, doi:10.5194/acp-11-8497-2011, 2011.

IPCC: Climate Change 2013: The Physical Science Basis. Contribution of Working Group I to the Fifth Assessment Report of the Intergovernmental Panel on Climate Change, Cambridge, United Kingdom and New York, NY, USA, 1585 pp, 2013.

Itahashi, S., Yumimoto, K., Kurokawa, J. I., Morino, Y., Nagashima, T., Miyazaki, K., Maki, T., and Ohara, T.: Inverse estimation of NOx emissions over China and India 2005?2016: contrasting recent trends and future perspectives, Environ. Res. Lett., 14, ARTN 124020;10.1088/1748-9326/ab4d7f, 2019.

IUPAC: Task Group on Atmospheric Chemical Kinetic Data Evaluation, (Ammann, M., Cox, R.A., Crowley, J.N., Herrmann, H., Jenkin, M.E., McNeill, V.F., Mellouki, A., Rossi, M. J., Troe, J. and Wallington, T. J.) http://iupac.pole-ether.fr/index.html., 2020.

Jenkin, M. E., Young, J. C., and Rickard, A. R.: The MCM v3.3.1 degradation scheme for isoprene, Atmos. Chem. Phys., 15, 11433-11459, 10.5194/acp-15-11433-2015, 2015.

Karl, M.: Modellierung atmosphärisch-chemischer Reaktionen in der Tageslicht-Atmosphären-Simulationskammer SAPHIR, PhD, Universität Münster, Münster, 2004.

Keehan, N. I., Brownwood, B., Marsavin, A., Day, D. A., and Fry, J. L.: A thermal-dissociation-cavity ring-down spectrometer (TD-CRDS) for the detection of organic nitrates in gas and particle phases, Atmospheric Measurement Techniques, 13, 6255-6269, 10.5194/amt-13-6255-2020, 2020.

Khan, M. A. H., Cooke, M. C., Utembe, S. R., Archibald, A. T., Derwent, R. G., Xiao, P., Percival, C. J., Jenkin, M. E., Morris, W. C., and Shallcross, D. E.: Global modeling of the nitrate radical (NO3) for present and pre-industrial scenarios, Atmospheric Research, 164, 347-357, 10.1016/j.atmosres.2015.06.006, 2015.

Khattatov, T.: Development, calibration and deployment of an airborne chemical ionization mass spectrometer for trace gas measurements, PhD, Fakultät für Mathematik und Naturwissenschaften, Bergische Universität Wuppertal, Wuppertal, 2019.

Kim, S., Huey, L. G., Stickel, R. E., Tanner, D. J., Crawford, J. H., Olson, J. R., Chen, G., Brune, W. H., Ren, X., Lesher, R., Wooldridge, P. J., Bertram, T. H., Perring, A., Cohen, R. C., Lefer, B. L., Shetter, R. E., Avery, M., Diskin, G., and Sokolik, I.: Measurement of HO_2NO_2 in the free troposphere during the intercontinental chemical transport experiment - North America 2004, Journal of Geophysical Research-Atmospheres, 112, doi:10.1029/2006jd007676, 2007.

Kleffmann, J., Heland, J., Kurtenbach, R., Lorzer, J., and Wiesen, P.: A new instrument (LOPAP) for the detection of nitrous acid (HONO), Environmental Science and Pollution Research, 48-54, 2002.

Kleinman, L. I.: Low and High Nox Tropospheric Photochemistry, Journal of Geophysical Research-Atmospheres, 99, 16831-16838, Doi 10.1029/94jd01028, 1994.

Krechmer, J., Lopez-Hilfiker, F., Koss, A., Hutterli, M., Stoermer, C., Deming, B., Kimmel, J., Warneke, C., Holzinger, R., Jayne, J., Worsnop, D., Fuhrer, K., Gonin, M., and de Gouw, J.: Evaluation of a New Reagent-Ion Source and Focusing Ion–Molecule Reactor for Use in Proton-Transfer-Reaction Mass Spectrometry, Analytical Chemistry, 90, 12011-12018, 10.1021/acs.analchem.8b02641, 2018.

Kwan, A. J., Chan, A. W. H., Ng, N. L., Kjaergaard, H. G., Seinfeld, J. H., and Wennberg, P. O.: Peroxy radical chemistry and OH radical production during the NO3-initiated oxidation of isoprene, Atmospheric Chemistry and Physics, 12, 7499-7515, 10.5194/acp-12-7499-2012, 2012.

Lamarque, J. F., Kyle, G. P., Meinshausen, M., Riahi, K., Smith, S. J., van Vuuren, D. P., Conley, A. J., and Vitt, F.: Global and regional evolution of short-lived radiatively-active gases and aerosols in the Representative Concentration Pathways, Climatic Change, 109, 191-212, 10.1007/s10584-011-0155-0, 2011.

Lammel, G., and Grassl, H.: Greenhouse effect of NOx, Environ Sci Pollut R, 2, 40-45, Doi 10.1007/Bf02987512, 1995.

Lammel, G., and Cape, J. N.: Nitrous acid and nitrite in the atmosphere, Chemical Society Reviews, 25, 361-+, DOI 10.1039/cs9962500361, 1996.

Lange, L., Hoor, P., Helas, G., Fischer, H., Brunner, D., Scheeren, B., Williams, J., Wong, S., Wohlfrorn, K. H., Arnold, F., Strom, J., Krejci, R., Lelieveld, J., and Andreae, M. O.: Detection of lightning-produced NO in the midlatitude upper troposphere during STREAM 1998, Journal of Geophysical Research-Atmospheres, 106, 27777-27785, Doi 10.1029/2001jd900210, 2001.

Lee, B. H., Mohr, C., Lopez-Hilfiker, F. D., Lutz, A., Hallquist, M., Lee, L., Romer, P., Cohen, R. C., Iyer, S., Kurten, T., Hu, W. W., Day, D. A., Campuzano-Jost, P., Jimenez, J. L., Xu, L., Ng, N. L., Guo, H. Y., Weber, R. J., Wild, R. J., Brown, S. S., Koss, A., de Gouw, J., Olson, K., Goldstein, A. H., Seco, R., Kim, S., McAvey, K., Shepson, P. B., Starn, T., Baumann, K., Edgerton, E. S., Liu, J. M., Shilling, J. E., Miller, D. O., Brune, W., Schobesberger, S., D'Ambro, E. L., and Thornton, J. A.: Highly functionalized organic nitrates in the southeast United States: Contribution to secondary organic aerosol and reactive nitrogen budgets, Proceedings of the National Academy of Sciences of the United States of America, 113, 1516-1521, 10.1073/pnas.1508108113, 2016.

Leighton, P. A.: Photochemistry of Air Pollution, Academic Press, New York, 1961.

Lelieveld, J., Evans, J. S., Fnais, M., Giannadaki, D., and Pozzer, A.: The contribution of outdoor air pollution sources to premature mortality on a global scale, Nature, 525, 367-+, 10.1038/nature15371, 2015.

Lelieveld, J., Gromov, S., Pozzer, A., and Taraborrelli, D.: Global tropospheric hydroxyl distribution, budget and reactivity, Atmospheric Chemistry and Physics, 16, 12477-12493, 2016.

Lenner, M.: Nitrogen-Dioxide in Exhaust Emissions from Motor-Vehicles, Atmospheric Environment, 21, 37-43, Doi 10.1016/0004-6981(87)90268-X, 1987.

Leser, H., Honninger, G., and Platt, U.: MAX-DOAS measurements of BrO and NO2 in the marine boundary layer, Geophysical Research Letters, 30, 10.1029/2002GL015811, 2003.

Levy, H.: Normal Atmosphere - Large Radical and Formaldehyde Concentrations Predicted, Science, 173, 141-&, 1971.

Li, D. J.: Emissions of NO and NH3 from a Typical Vegetable-Land Soil after the Application of Chemical N Fertilizers in the Pearl River Delta, Plos One, 8, ARTN e59360;10.1371/journal.pone.0059360, 2013.

Li, Y., Schichtel, B. A., Walker, J. T., Schwede, D. B., Chen, X., Lehmann, C. M. B., Puchalski, M. A., Gay, D. A., and Collett, J. L.: Increasing importance of deposition of reduced nitrogen in the United States, Proceedings of the National Academy of Sciences of the United States of America, 113, 5874-5879, 10.1073/pnas.1525736113, 2016.

Lightfoot, P. D., Cox, R. A., Crowley, J. N., Destriau, M., Hayman, G. D., Jenkin, M. E., Moortgat, G. K., and Zabel, F.: Organic Peroxy-radicals - Kinetics, Spectroscopy and Tropospheric Chemistry, Atmospheric Environment Part A-general Topics, 26, 1805-1961, 1992.

Likens, G. E., Butler, T. J., Claybrooke, R., Vermeylen, F., and Larson, R.: Long-term monitoring of precipitation chemistry in the US: Insights into changes and condition, Atmospheric Environment, 245, ARTN 118031;10.1016/j.atmosenv.2020.118031, 2021.

Logan, J. A., Prather, M. J., Wofsy, S. C., and McElroy, M. B.: Tropospheric Chemistry - a Global Perspective, Journal of Geophysical Research-Oceans and Atmospheres, 86, 7210-7254, 1981.

Logan, J. A.: Nitrogen-Oxides in the Troposphere - Global and Regional Budgets, Journal of Geophysical Research-Oceans, 88, 785-807, DOI 10.1029/JC088iC15p10785, 1983.

Matsumoto, J., Hirokawa, J., Akimoto, H., and Kajii, Y.: Direct measurement of NO2 in the marine atmosphere by laser-induced fluorescence technique, Atmospheric Environment, 35, 2803-2814, Doi 10.1016/S1352-2310(01)00078-4, 2001.

Messina, P., Lathiere, J., Sindelarova, K., Vuichard, N., Granier, C., Ghattas, J., Cozic, A., and Hauglustaine, D. A.: Global biogenic volatile organic compound emissions in the ORCHIDEE and MEGAN models and sensitivity to key parameters, Atmospheric Chemistry and Physics, 16, 14169-14202, 10.5194/acp-16-14169-2016, 2016.

Mills, I. C., Atkinson, R. W., Kang, S., Walton, H., and Anderson, H. R.: Quantitative systematic review of the associations between short-term exposure to nitrogen dioxide and mortality and hospital admissions, Bmj Open, 5, ARTN e006946;10.1136/bmjopen-2014-006946, 2015.

Monks, P. S.: Gas-phase radical chemistry in the troposphere, Chemical Society Reviews, 34, 376-395, 10.1039/b307982c, 2005.

Muller, K. P., and Rudolph, J.: Measurements of Peroxyacetylnitrate in the Marine Boundary-Layer over the Atlantic, Journal of Atmospheric Chemistry, 15, 361-367, Doi 10.1007/Bf00115405, 1992.

Nakamura, K., Kondo, Y., Chen, G., Crawford, J. H., Takegawa, N., Koike, M., Kita, K., Miyazaki, Y., Shetter, R. E., Lefer, B. L., Avery, M., and Matsumoto, J.: Measurement of NO2 by the photolysis conversion technique during the Transport and Chemical Evolution Over the Pacific (TRACE-P) campaign, Journal of Geophysical Research-Atmospheres, 108, Artn 4752;10.1029/2003jd003712, 2003.

Nault, B. A., Garland, C., Pusede, S. E., Wooldridge, P. J., Ullmann, K., Hall, S. R., and Cohen, R. C.: Measurements of $CH_3O_2NO_2$ in the upper troposphere, Atmospheric measurement techniques, 8, 987-997, doi:10.5194/amt-8-987-2015, 2015.

Ng, N. L., Kwan, A. J., Surratt, J. D., Chan, A. W. H., Chhabra, P. S., Sorooshian, A., Pye, H. O. T., Crounse, J. D., Wennberg, P. O., Flagan, R. C., and Seinfeld, J. H.: Secondary organic aerosol (SOA) formation from reaction of isoprene with nitrate radicals (NO3), Atmospheric Chemistry and Physics, 8, 4117-4140, 2008.

Ng, N. L., Brown, S. S., Archibald, A. T., Atlas, E., Cohen, R. C., Crowley, J. N., Day, D. A., Donahue, N. M., Fry, J. L., Fuchs, H., Griffin, R. J., Guzman, M. I., Herrmann, H., Hodzic, A., Iinuma, Y., Jimenez, J. L., Kiendler-Scharr, A., Lee, B. H., Luecken, D. J., Mao, J. Q., McLaren, R., Mutzel, A., Osthoff, H. D., Ouyang, B., Picquet-Varrault, B., Platt, U., Pye, H. O. T., Rudich, Y., Schwantes, R. H., Shiraiwa, M., Stutz, J., Thornton, J. A., Tilgner, A., Williams, B. J., and Zaveri, R. A.: Nitrate radicals and biogenic volatile organic compounds: oxidation, mechanisms, and organic aerosol, Atmospheric Chemistry and Physics, 17, 2103-2162, 10.5194/acp-17-2103-2017, 2017.

Novelli, A., Cho, C., Fuchs, H., Hofzumahaus, A., Rohrer, F., Tillmann, R., Kiendler-Scharr, A., Wahner, A., and Vereecken, L.: Experimental and theoretical study on the impact of a nitrate group on the chemistry of alkoxy radicals, Physical Chemistry Chemical Physics, 23, 5474-5495, 10.1039/d0cp05555g, 2021.

Oertel, C., Matschullat, J., Zurba, K., Zimmermann, F., and Erasmi, S.: Greenhouse gas emissions from soils A review, Chemie Der Erde-Geochemistry, 76, 327-352, 10.1016/j.chemer.2016.04.002, 2016.

Okeefe, A., and Deacon, D. A. G.: Cavity Ring-down Optical Spectrometer for Absorption-Measurements Using Pulsed Laser Sources, Review of Scientific Instruments, 59, 2544-2551, Doi 10.1063/1.1139895, 1988.

Orphal, J., Fellows, C. E., and Flaud, P. M.: The visible absorption spectrum of NO3 measured by high-resolution Fourier transform spectroscopy, Journal of Geophysical Research-Atmospheres, 108, Art. Nr. 4077, doi:10.1029/2002JD002489, 2003.

Osthoff, H. D., Sommariva, R., Baynard, T., Pettersson, A., Williams, E. J., Lerner, B. M., Roberts, J. M., Stark, H., Goldan, P. D., Kuster, W. C., Bates, T. S., Coffman, D., Ravishankara, A. R., and Brown, S. S.: Observation of daytime N2O5 in the marine boundary layer during New England Air Quality Study - Intercontinental Transport and Chemical Transformation 2004, Journal of Geophysical Research-Atmospheres, 111, 2006.

Osthoff, H. D., Roberts, J. M., Ravishankara, A. R., Williams, E. J., Lerner, B. M., Sommariva, R., Bates, T. S., Coffman, D., Quinn, P. K., Dibb, J. E., Stark, H., Burkholder, J. B., Talukdar, R. K., Meagher, J., Fehsenfeld, F. C., and Brown, S. S.: High levels of nitryl chloride in the polluted subtropical marine boundary layer, Nature Geoscience, 1, 324-328, 10.1038/ngeo177, 2008.

Perring, A. E., Bertram, T. H., Wooldridge, P. J., Fried, A., Heikes, B. G., Dibb, J., Crounse, J. D., Wennberg, P. O., Blake, N. J., Blake, D. R., Brune, W. H., Singh, H. B., and Cohen, R. C.: Airborne observations of total $RONO_2$: new constraints on the yield and lifetime of isoprene nitrates, Atmospheric Chemistry and Physics, 9, 1451-1463, 2009.

Perring, A. E., Pusede, S. E., and Cohen, R. C.: An observational perspective on the atmospheric impacts of alkyl and multifunctional nitrates on ozone and secondary organic aerosol, Chemical Reviews, 113, 5848-5870, doi:10.1021/cr300520x, 2013.

Peters, E., Wittrock, F., Grossmann, K., Friess, U., Richter, A., and Burrows, J. P.: Formaldehyde and nitrogen dioxide over the remote western Pacific Ocean: SCIAMACHY and GOME-2 validation using ship-based MAX-DOAS observations, Atmospheric Chemistry and Physics, 12, 11179-11197, 10.5194/acp-12-11179-2012, 2012.

Peterson, M. C., and Honrath, R. E.: NOx and NOy over the northwestern North Atlantic: Measurements and measurement accuracy, Journal of Geophysical Research-Atmospheres, 104, 11695-11707, Doi 10.1029/1998jd100088, 1999.

Poppe, D., Wallasch, M., and Zimmermann, J.: The Dependence of the Concentration of Oh on Its Precursors under Moderately Polluted Conditions - a Model Study, Journal of Atmospheric Chemistry, 16, 61-78, Doi 10.1007/Bf00696625, 1993.

Reed, C., Evans, M. J., Di Carlo, P., Lee, J. D., and Carpenter, L. J.: Interferences in photolytic NO2 measurements: explanation for an apparent missing oxidant?, Atmospheric Chemistry and Physics, 16, 4707-4724, 10.5194/acp-16-4707-2016, 2016.

Rickard, A. R., Salisbury, G., Monks, P. S., Lewis, A. C., Baugitte, S., Bandy, B. J., Clemitshaw, K. C., and Penkett, S. A.: Comparison of measured ozone production efficiencies in the marine boundary layer at two European coastal sites under different pollution regimes, Journal of Atmospheric Chemistry, 43, 107-134, Doi 10.1023/A:1019970123228, 2002.

Rohrer, F., Bohn, B., Brüning, D., Johnen, F.-J., Wahner, A., and Kleffmann, J.: Characterisation of the photolytic HONO-source in the atmosphere simulation chamber SAPHIR, ACP, 5, 2189-2201, 2005.

Rohrer, F., Lu, K. D., Hofzumahaus, A., Bohn, B., Brauers, T., Chang, C. C., Fuchs, H., Haseler, R., Holland, F., Hu, M., Kita, K., Kondo, Y., Li, X., Lou, S. R., Oebel, A., Shao, M., Zeng, L. M., Zhu, T., Zhang, Y. H., and Wahner, A.: Maximum efficiency in the hydroxyl-radical-based self-cleansing of the troposphere, Nature Geoscience, 7, 559-563, 10.1038/Ngeo2199, 2014.

Rollins, A. W., Kiendler-Scharr, A., Fry, J. L., Brauers, T., Brown, S. S., Dorn, H. P., Dubé, W. P., Fuchs, H., Mensah, A., Mentel, T. F., Rohrer, F., Tillmann, R., Wegener, R., Wooldridge, P. J., and Cohen, R. C.: Isoprene oxidation by nitrate radical: alkyl nitrate and secondary organic aerosol yields, Atmospheric Chemistry and Physics, 9, 6685-6703, 10.5194/acp-9-6685-2009, 2009.

Rollins, A. W., Smith, J. D., Wilson, K. R., and Cohen, R. C.: Real Time In Situ Detection of Organic Nitrates in Atmospheric Aerosols, Environmental Science & Technology, 44, 5540-5545, 10.1021/es100926x, 2010.

Russell, A. G., Winner, D. A., Harley, R. A., Mccue, K. F., and Cass, G. R.: Mathematical-Modeling and Control of the Dry Deposition Flux of Nitrogen-Containing Air-Pollutants, Environmental Science & Technology, 27, 2772-2782, DOI 10.1021/es00049a016, 1993.

Saunders, S. M., Jenkin, M. E., Derwent, R. G., and Pilling, M. J.: Protocol for the development of the Master Chemical Mechanism, MCM v3 (Part A): tropospheric degradation of non-aromatic volatile organic compounds, Atmospheric Chemistry and Physics, 3, 161-180, 2003.

Schumann, U., and Huntrieser, H.: The global lightning-induced nitrogen oxides source, Atmospheric Chemistry and Physics, 7, 3823-3907, DOI 10.5194/acp-7-3823-2007, 2007.

Schwantes, R. H., Teng, A. P., Nguyen, T. B., Coggon, M. M., Crounse, J. D., St Clair, J. M., Zhang, X., Schilling, K. A., Seinfeld, J. H., and Wennberg, P. O.: Isoprene NO_3 Oxidation Products from the RO_2 + HO_2 Pathway, Journal of Physical Chemistry A, 119, 10158-10171, 10.1021/acs.jpca.5b06355, 2015.

Seinfeld, J. H., and Pandis, S. N.: Atmospheric Chemistry and Physics: From Air Pollution to Climate Change, John Wiley and Sons, Inc., Hoboken, New Jersey, 2016.

Shenolikar, J.: Nighttime radical NOx chemistry by CRD, Chemistry Department, Johannes Gutenberg-Universität Mainz, Mainz, 2021.

Shindell, D. T., Faluvegi, G., Koch, D. M., Schmidt, G. A., Unger, N., and Bauer, S. E.: Improved Attribution of Climate Forcing to Emissions, Science, 326, 716-718, 10.1126/science.1174760, 2009.

Sobanski, N., Schuladen, J., Schuster, G., Lelieveld, J., and Crowley, J. N.: A five-channel cavity ring-down spectrometer for the detection of NO_2, NO_3, N_2O_5, total peroxy nitrates and total alkyl nitrates, Atmospheric Measurement Techniques, 9, 5103-5118, 10.5194/amt-9-5103-2016, 2016a.

Sobanski, N., Tang, M. J., Thieser, J., Schuster, G., Pöhler, D., Fischer, H., Song, W., Sauvage, C., Williams, J., Fachinger, J., Berkes, F., Hoor, P., Platt, U., Lelieveld, J., and Crowley, J. N.: Chemical and meteorological influences on the lifetime of NO_3 at a semi-rural mountain site during PARADE, Atmospheric Chemistry and Physics, 16, 4867-4883, 10.5194/acp-16-4867-2016, 2016b.

Spicer, C. W.: Nitrogen-Oxide Reactions in the Urban Plume of Boston, Science, 215, 1095-1097, DOI 10.1126/science.215.4536.1095, 1982.

Starn, T. K., Shepson, P. B., Bertman, S. B., Riemer, D. D., Zika, R. G., and Olszyna, K.: Nighttime isoprene chemistry at an urban-impacted forest site, J Geophys Res-Atmos, 103, 22437-22447, Doi 10.1029/98jd01201, 1998.

Stavrakou, T., Muller, J. F., Boersma, K. F., van der A, R. J., Kurokawa, J., Ohara, T., and Zhang, Q.: Key chemical NOx sink uncertainties and how they influence top-down emissions of nitrogen oxides, Atmospheric Chemistry and Physics, 13, 9057-9082, 10.5194/acp-13-9057-2013, 2013.

Stephens, E. R., and Price, M. A.: Atmospheric Photochemical Reactions in a Tube Flow Reactor, Atmospheric Environment, 3, 573-&, Doi 10.1016/0004-6981(69)90047-X, 1969.

Stroud, C. A., Roberts, J. M., Williams, E. J., Hereid, D., Angevine, W. M., Fehsenfeld, F. C., Wisthaler, A., Hansel, A., Martinez-Harder, M., Harder, H., Brune, W. H., Hoenninger, G., Stutz, J., and White, A. B.: Nighttime isoprene trends at an urban forested site during the 1999 Southern Oxidant Study, J Geophys Res-Atmos, 107, Artn 4291;10.1029/2001jd000959, 2002.

Stutz, J., Kim, E. S., Platt, U., Bruno, P., Perrino, C., and Febo, A.: UV-visible absorption cross sections of nitrous acid, Journal of Geophysical Research-Atmospheres, 105, 14585-14592, 2000.

Suh, I., Lei, W. F., and Zhang, R. Y.: Experimental and theoretical studies of isoprene reaction with NO3, Journal of Physical Chemistry A, 105, 6471-6478, 10.1021/jp0105950, 2001.

Takashima, H., Irie, H., Kanaya, Y., and Syamsudin, F.: NO2 observations over the western Pacific and Indian Ocean by MAX-DOAS on Kaiyo, a Japanese research vessel, Atmospheric Measurement Techniques, 5, 2351-2360, 10.5194/amt-5-2351-2012, 2012.

Takiguchi, Y., Takami, A., Sadanaga, Y., Lun, X. X., Shimizu, A., Matsui, I., Sugimoto, N., Wang, W., Bandow, H., and Hatakeyama, S.: Transport and transformation of total reactive nitrogen over the East China Sea, Journal of Geophysical Research-Atmospheres, 113, Artn D10306;10.1029/2007jd009462, 2008.

Thieser, J., Schuster, G., Phillips, G. J., Reiffs, A., Parchatka, U., Pöhler, D., Lelieveld, J., and Crowley, J. N.: A two-channel, thermal dissociation cavity-ringdown spectrometer for the detection of ambient NO_2, RO_2NO_2 and $RONO_2$, Atmos. Meas. Tech., 9, 553-576, 10.5194/amt-9-553-2016, 2016.

van Vuuren, D. P., Edmonds, J., Kainuma, M., Riahi, K., Thomson, A., Hibbard, K., Hurtt, G. C., Kram, T., Krey, V., Lamarque, J. F., Masui, T., Meinshausen, M., Nakicenovic, N., Smith, S. J., and Rose, S. K.: The representative concentration pathways: an overview, Climatic Change, 109, 5-31, 10.1007/s10584-011-0148-z, 2011.

Vandaele, A. C., Hermans, C., Simon, P. C., Carleer, M., Colin, R., Fally, S., Merienne, M. F., Jenouvrier, A., and Coquart, B.: Measurements of the NO_2 absorption cross-section from 42 000 cm^{-1} to 10 000 cm^{-1} (238-1000 nm) at 220 K and 294 K, Journal of Quantitative Spectroscopy & Radiative Transfer, 59, 171-184, 1998.

Večeřa, Z., Mikuška, P., Smolík, J., Eleftheriadis, K., Bryant, C., Colbeck, I., and Lazaridis, M.: Shipboard Measurements of Nitrogen Dioxide, Nitrous Acid, Nitric Acid and Ozone in the Eastern Mediterranean Sea, Water, Air, & Soil Pollution: Focus, 8, 117-125, 10.1007/s11267-007-9133-y, 2008.

Vereecken, L., Carlsson, P. T. M., Novelli, A., Bernard, F., Brown, S. S., Cho, C., Crowley, J. N., Fuchs, H., Mellouki, W., Reimer, D., Shenolikar, J., Tillmann, R., Zhou, L., Kiendler-Scharr, A., and Wahner, A.: Theoretical and experimental study of peroxy and alkoxy radicals in the NO3-initiated oxidation of isoprene, Physical Chemistry Chemical Physics, 23, 5496-5515, 10.1039/D0CP06267G, 2021.

Veres, P. R., Roberts, J. M., Wild, R. J., Edwards, P. M., Brown, S. S., Bates, T. S., Quinn, P. K., Johnson, J. E., Zamora, R. J., and de Gouw, J.: Peroxynitric acid (HO_2NO_2) measurements during the UBWOS 2013 and 2014 studies using iodide ion chemical ionization mass spectrometry, Atmos. Chem. Phys., 15, 8101-8114, 10.5194/acp-15-8101-2015, 2015.

von Kuhlmann, R., Lawrence, M. G., Poschl, U., and Crutzen, P. J.: Sensitivities in global scale modeling of isoprene, Atmos Chem Phys, 4, 1-17, DOI 10.5194/acp-4-1-2004, 2004.

Wagner, C., Schuster, G., and Crowley, J. N.: An aerosol flow tube study of the interaction of N_2O_5 with calcite, Arizona dust and quartz, Atmospheric Environment, 43, 5001-5008, 2009.

Warneke, C., de Gouw, J. A., Goldan, P. D., Kuster, W. C., Williams, E. J., Lerner, B. M., Jakoubek, R., Brown, S. S., Stark, H., Aldener, M., Ravishankara, A. R., Roberts, J. M., Marchewka, M., Bertman, S., Sueper, D. T., McKeen, S. A., Meagher, J. F., and Fehsenfeld, F. C.: Comparison of daytime and nighttime oxidation of biogenic and anthropogenic VOCs along the New England coast in summer during New England Air Quality Study 2002, Journal of Geophysical Research-Atmospheres, 109, 2004.

Watson, J. G., Chow, J. C., Lurmann, F. W., and Musarra, S. P.: Ammonium-Nitrate, Nitric-Acid, and Ammonia Equilibrium in Wintertime Phoenix, Arizona, J Air Waste Manage, 44, 405-412, 1994.

Wayne, R. P., Barnes, I., Biggs, P., Burrows, J. P., Canosa-Mas, C. E., Hjorth, J., Lebras, G., Moortgat, G. K., Perner, D., Poulet, G., Restelli, G., and Sidebottom, H.: The Nitrate Radical - Physics, Chemistry, and the Atmosphere, Atmospheric Environment, 25, 1-203, 1991.

Wegener, R., Brauers, T., Koppmann, R., Bares, S. R., Rohrer, F., Tillmann, R., Wahner, A., Hansel, A., and Wisthaler, A.: Simulation chamber investigation of the reactions of ozone with short-chained alkenes, J Geophys Res-Atmos, 112, Artn D13301;10.1029/2006jd007531, 2007.

Wennberg, P. O., Bates, K. H., Crounse, J. D., Dodson, L. G., McVay, R. C., Mertens, L. A., Nguyen, T. B., Praske, E., Schwantes, R. H., Smarte, M. D., St Clair, J. M., Teng, A. P., Zhang, X., and Seinfeld, J. H.: Gas-Phase Reactions of Isoprene and Its Major Oxidation Products, Chemical Reviews, 118, 3337-3390, 10.1021/acs.chemrev.7b00439, 2018.

Wild, R. J., Edwards, P. M., Dube, W. P., Baumann, K., Edgerton, E. S., Quinn, P. K., Roberts, J. M., Rollins, A. W., Veres, P. R., Warneke, C., Williams, E. J., Yuan, B., and Brown, S. S.: A measurement of total reactive nitrogen, NOy, together with NO_2, NO, and O_3 via cavity ring-down spectroscopy, Environmental Science & Technology, 48, 9609-9615, doi:10.1021/es501896w, 2014.

Wu, R., Vereecken, L., Tsiligiannis, E., Kang, S., Albrecht, S. R., Hantschke, L., Zhao, D., Novelli, A., Fuchs, H., Tillmann, R., Hohaus, T., Carlsson, P. T. M., Shenolikar, J., Bernard, F., Crowley, J. N., Fry, J. L., Brownwood, B., Thornton, J. A., Brown, S. S., Kiendler-Scharr, A., Wahner, A., Hallquist, M., and Mentel, T. F.: Molecular composition and volatility of multi-generation products formed from isoprene oxidation by nitrate radical, Atmos. Chem. Phys. Discuss., 2020, 1-37, 10.5194/acp-2020-1180, 2020.

Xie, Y., Paulot, F., Carter, W. P. L., Nolte, C. G., Luecken, D. J., Hutzell, W. T., Wennberg, P. O., Cohen, R. C., and Pinder, R. W.: Understanding the impact of recent advances in isoprene photooxidation on simulations of regional air quality, Atmos Chem Phys, 13, 8439-8455, 10.5194/acp-13-8439-2013, 2013.

York, D.: Least-Squares Fitting of a Straight Line, Canadian Journal of Physics, 44, 1079-1086, DOI 10.1139/p66-090, 1966.

Yuba, A., Sadanaga, Y., Takami, A., Hatakeyama, S., Mosui, Y., Ohara, T., Yonemura, S., Kato, S., Kajii, Y., and Bandow, H.: Concentration variations of total reactive nitrogen and total nitrate during transport to Fukue Island and to Cape Hedo, Japan in the marine boundary layer, Atmospheric Environment, 97, 471-478, 10.1016/j.atmosenv.2014.04.010, 2014.

Zel'dovich, Y. B.: The Oxidation of Nitrogen in Combustion Explosions, Acta Physicochimica U. S. S. R., 21, 577-628, 1946.

Zhang, Y., West, J. J., Mathur, R., Xing, J., Hogrefe, C., Roselle, S. J., Bash, J. O., Pleim, J. E., Gan, C. M., and Wong, D. C.: Long-term trends in the ambient PM2.5- and O-3-related mortality burdens in the United States under emission reductions from 1990 to 2010, Atmospheric Chemistry and Physics, 18, 15003-15016, 10.5194/acp-18-15003-2018, 2018.